A Search for Scalar Resonances in the Mass Range $66 - 110$ GeV/c^2 Produced in pp Collisions at $\sqrt{s} = 13$ TeV and Observed in the Two Photon Final State

by

Andy Chen

A dissertation submitted in partial fulfillment
of the requirements for the degree of
Doctor of Philosophy
(Physics)
in The University of Michigan
2023

Doctoral Committee:

Professor Dante Amidei, Chair
Assistant Professor Alex Gorodetsky
Professor Dragan Huterer
Professor Aaron Pierce
Associate Professor Thomas Schwarz

Andy Chen

andych@umich.edu

ORCID iD: 0000-0001-9973-7966

© Andy Chen 2023

DEDICATION

For the continuous and never-ending curiosity of mankind.

ACKNOWLEDGEMENTS

As my graduate career comes to a close, I wish to recognize all the family members, friends, and mentors that have helped me along my educational path.

First and foremost, I must thank my graduate research advisor Dante Amidei for launching me into the large and welcoming ATLAS group both at UM and at CERN. His patient support and prompt advice from start to end has undeniably been the root of my success in the numerous projects and opportunities I have taken on during my time as a graduate student.

Despite the unforeseen circumstances during my visit to CERN in 2020, the amount of knowledge I learned from scientists and researchers as well as the experiences I shared with colleagues was unimaginable. From the slopes of Chamonix to the caves of Jura, my hardware project supervisors, Siyuan Sun and Liang Guan, offered me invaluable advice and wisdom even when outside the walls of CERN.

I would like to express my sincere gratitude to my research partner, Christopher Robyn Hayes, for his unending guidance throughout my graduate studies. I have been fortunate enough to have such an incredible mentor who has taken the time to encourage, challenge, and support me not only throughout our long analysis journeys but also during our long cycling journeys through the country roads of Ann Arbor.

Finally, I would like to acknowledge all of my collaborators who have generously shared their time and insights with me, without whom this work would not have been possible. I thank them each for playing a significant part of my journey and for making this entire graduate experience truly unforgettable.

TABLE OF CONTENTS

DEDICATION ii

ACKNOWLEDGEMENTS iii

LIST OF FIGURES viii

LIST OF TABLES xx

LIST OF ABBREVIATIONS xxv

ABSTRACT xxxiii

CHAPTER

I. Introduction 1

II. Theoretical Background 4

2.1 The Standard Model of Particle Physics 5
2.1.1 The Fundamental Particles 5
2.1.2 The Strong Interaction 6
2.1.3 The Electroweak Interaction 7
2.2 The Standard Model Higgs Boson 9
2.2.1 Scalar Production Modes and Cross Sections 9
2.2.2 Scalar Decays to Diphoton 10
2.3 The Higgs Boson Beyond the Standard Model 14
2.3.1 Two Higgs Doublet Model 14
2.3.2 Production and Decay of the Higgs in Type-I 2HDM 16
2.3.3 BSM Higgs in Recent Experimental Searches 19

III. Experimental Apparatus 23

3.1 The Large Hadron Collider 24
3.1.1 Proton Accelerator Chain 25

3.1.2 Energy and Luminosity . . . 27
3.2 The ATLAS Detector . . . 29
3.2.1 Coordinate System and Kinematic Description . . . 29
3.2.2 Solenoid and Toroidal Magnets . . . 30
3.2.3 Inner Tracking Detectors . . . 32
3.2.4 Electromagnetic and Hadronic Calorimeters . . . 33
3.2.5 Muon Spectrometer . . . 38
3.2.6 Trigger System . . . 39
3.2.7 Forward Detectors . . . 40

IV. Photon Reconstruction and Identification . . . 44

4.1 Electron and Photon Reconstruction . . . 46
4.1.1 Topocluster Reconstruction . . . 46
4.1.2 Track Reconstruction . . . 47
4.1.3 Track Matching . . . 48
4.1.4 Conversion Vertex Reconstruction . . . 49
4.1.5 Supercluster Reconstruction . . . 50
4.1.6 Identification and Isolation . . . 51
4.2 Parton Jets Faking Photons . . . 53
4.3 Primary Vertex Reconstruction . . . 54

V. Scalar Resonance Search Strategy . . . 55

5.1 Scalar Resonance Models . . . 57
5.2 Outline of Analysis Methodology . . . 60

VI. Generation, Selection, and Categorization of Diphoton Events 62

6.1 Monte Carlo Samples . . . 63
6.1.1 New Scalar Resonance Signal Samples . . . 63
6.1.2 QCD Continuum Background Samples . . . 64
6.1.3 $Z \to ee$ Resonance Background Samples . . . 65
6.1.4 Sample Post-Processing . . . 66
6.2 Proton-proton Collision Datasets . . . 68
6.3 Diphoton Event Selection . . . 71
6.3.1 Vertex Selection . . . 71
6.3.2 Identification Selection . . . 71
6.3.3 Isolation Selection . . . 72
6.3.4 Kinematic Selection . . . 76
6.3.5 Photon Conversion Categorization . . . 80
6.3.6 Elimination of Ambiguous Electron Fakes . . . 84
6.3.7 Classification of Diphoton Events . . . 92
6.3.8 Selection Efficiency . . . 102

VII. Signal and Background Modeling . . . 106

7.1 Signal Modeling . . . 107
7.1.1 Signal Shape . . . 107
7.1.2 Signal Shape Uncertainties . . . 118
7.2 Fiducial Volume and Correction Factors . . . 125
7.2.1 Fiducial Volume Definition . . . 125
7.2.2 C_X and A_X Factors . . . 127
7.2.3 Systematic Variations on the C_X Factors . . . 131
7.3 Background Modeling . . . 140
7.3.1 Non-resonant Background Components . . . 140
7.3.2 Full Background Continuum Shape . . . 162
7.3.3 Resonant Background from Drell-Yan Electron Fakes 182

VIII. Results for Diphoton Decays of Higgs-like Scalars . . . 202

8.1 Statistical Methods . . . 203
8.2 Summary of Systematic Variations . . . 208
8.3 Expected Model and Limits . . . 210
8.4 Observed Limits and Results . . . 217
8.4.1 Distributions of $m_{\gamma\gamma}$ in Data . . . 217
8.4.2 Resonance Discovery p-value . . . 220
8.4.3 Limits on Fiducial and Total Cross-Section . . . 223

IX. Conclusion . . . 227

APPENDIX . . . 229

A. Muon Spectrometer Phase II Upgrade: sMDT Chambers . . 230

A.1 Infrastructure and Workflow . . . 234
A.2 Preparation of Materials . . . 236
A.2.1 Tube Straightness Measurement . . . 236
A.2.2 Aluminum Tube Preparation . . . 236
A.2.3 End-Plug Preparation . . . 238
A.3 Tube Assembly . . . 240
A.3.1 Wiring Station . . . 240
A.3.2 Swaging Station . . . 241
A.3.3 Assembly procedure . . . 242
A.4 Quality Assurance and Quality Control Tests . . . 244
A.4.1 Visual Inspection . . . 244
A.4.2 Gas Tightness Test . . . 244
A.4.3 Length and Wire Tension Measurements . . . 246
A.4.4 Dark current measurement . . . 249

A.4.5 Negative HV Treatment 253
A.5 Tube Production Database 254
A.6 Conclusion 256

BIBLIOGRAPHY 257

LIST OF FIGURES

Figure

2.1 The Feynman diagram representation of dominant Higgs boson production processes at the LHC in the lower diphoton invariant mass regime. The curly edges denote gluons g, wavy edges denote vector bosons V, straight edges with embedded arrows denote quarks q, and dashed edges denote Higgs bosons. 10

2.2 Higgs boson decay channels listed in the order of decreasing branching ratio. 12

2.3 Higgs boson to diphoton diagram drawn with an abbreviated 3-point vertex. 13

2.4 The cross section of the BSM (here labeled as NP), Higgs scalar relative to that of the SM Higgs boson. The curves are based on a scalar mass of $m_h = 80\,\text{GeV}$ and a mixing angle of $\tan\beta = 2$ [24]. . 17

2.5 Branching ratios of the BSM Higgs scalar. The curves are based on a scalar mass of $m_h = 80\,\text{GeV}$ and a mixing angle of $\tan\beta = 2$ [24]. 18

2.6 Allowed (α, β) parameter space for the BSM Higgs scalar after combining the measurements from Higgs signal strength and the results from direct searches for light scalar at LEP and LHC [24]. The allowable regions for potential scalars of mass $m_h = 90\,\text{GeV}$ and $100\,\text{GeV}$ are colored by the red and blue bands, respectively. 20

2.7 The expected and observed exclusion limits (95% CL) from CMS on the production cross section times branching ratio into two photons for a BSM Higgs boson relative to the expected SM Higgs boson using both Run 1 and early Run 2 datasets from the LHC [47]. The inner (green) and the outer (yellow) band indicate the regions containing 68% and 95% respectively, of the distribution of limits expected under the SM background-only hypothesis. 21

3.1 An aerial view of the LHC on the border of France and Switzerland [29]. 24

3.2 A diagram of the accelerator complex at CERN [80]. Protons are first accelerated in the LINAC2 (now replaced by LINAC4) and subsequently boosted by the PSB (here labeled as Booster), the PS, and the SPS before finally being injected into the main LHC ring. . . . 26

3.3 A cut-away representation of the particle trackers and detectors in the ATLAS detector [40]. 29
3.4 A diagram of the two magnet systems in the ATLAS detector: the solenoid and the outer toroidal magnets. The scale of this diagram matches that of Figure 3.3. 31
3.5 A cross-sectional diagram of the inner detector in the ATLAS detector with its three main components: the pixel detector, the SCT, and the TRT. 32
3.6 A cut-away representation of the EM and hadronic calorimeter in the barrel region of the ATLAS detector. 34
3.7 A cross-sectional diagram of the EM calorimeter in the ATLAS detector. 35
3.8 A cross-sectional diagram of the hadronic calorimeter in the ATLAS detector. 37
3.9 A cut-away view of the entire muon system in the ATLAS detector. 39
3.10 The placement of the three main forward detectors (LUCID, ZDC, and ALFA) along the beamline on either side of the IP. The locations of the LHC dipole and quadrupole magnets along with the ATLAS TAS and TAN collimators are also shown for positional reference. . 41
3.11 The pair of Roman pots with each of the electronic components (left) and the scintillating-fiber stack in each Roman pot (right). 43
4.1 A diagram of the superclustering algorithm for electron and photon reconstruction [14]. Seed clusters are shown in red, and satellite clusters are shown in blue. 51
4.2 A flowchart showing the logic of the ambiguity resolution for a particle object initially reconstructed both as an electron and a photon [14]. An "innermost hit" is a hit in the pixel detector nearest the beamline along the track trajectory, E/p is the ratio of the supercluster energy to the measured momentum of the matched track, R_{conv} is the radial position of the conversion vertex, and R_{firstHit} is the smallest radial position of a hit in the track or tracks that make a conversion vertex. 52
5.1 The search for a new scalar resonance in the diphoton decay channel. The backgrounds are modeled using both data and MC samples. The "bump-hunt" is performed by fitting the signal shape modeled from simulation along the diphoton invariant mass spectrum. 56
6.1 The isolation selection efficiencies and the ratios between the signal to background sensitivity $S/\sqrt{B}$ for each MC campaign and each m_X using events in the range $m_X \pm 2 \cdot \sigma_{\text{CB},X}$. The efficiencies compare the use of official photon isolation working points to no photon isolation criteria. 75
6.2 The diphoton invariant mass spectrum after applying the trigger and kinematic selection of $E_{\text{T}} > 22\,\text{GeV}$ on each photon which causes the "turn-on" effect in the diphoton invariant mass range $40\,\text{GeV} < m_{\gamma\gamma} < 60\,\text{GeV}$. 77

6.3 The diphoton invariant mass spectrum of the diphoton background continuum with various sets of relative kinematic cuts applied on the photon transverse energies. 78
6.4 The selection efficiencies and the ratios between the signal to background sensitivity $S/\sqrt{B}$ for each MC campaign and each m_X using events in the range $m_X \pm 2 \cdot \sigma_{\mathrm{CB},X}$. The efficiencies compare the use of various sets of relative kinematic cuts applied on the photon E_{T} to the nominal $E_{\mathrm{T}} > 22\,\mathrm{GeV}$ cuts. 79
6.5 The predicted diphoton invariant mass distribution separated by photon conversion categories. The effects of the continuum background using the MC Sherpa $\gamma\gamma$ signal region with the data $\gamma j + jj$ nominal control region as described in Section 7.3.1.3 and the fake photon background from $Z \to ee$ decays are shown in each distribution. A scale factor of 1.25 is applied to the UU category histograms to separate them visually from those for the UC category. 86
6.6 The expected limit on the diphoton invariant mass distribution in the low-mass regime from a previous ATLAS diphoton resonance search [55]. The limit in the region around the Z boson worsens due to the impact of the background from DY electrons faking photons. . . . 87
6.7 The 2D distribution of photon ambiguity BDT scores for the leading and subleading photon candidates in the PowhegPy8 ggH at $m_X = 100\,\mathrm{GeV}$, the PowhegPy8 $Z \to ee$, and the Sherpa2 $\gamma\gamma$ sample for each photon conversion category. 88
6.8 The score distribution and complementary cumulative distribution of the photon ambiguity BDT score $\xi_{\texttt{minBDTscore}}$ for the PowhegPy8 gluon-gluon fusion (ggH) at $m_X = 100\,\mathrm{GeV}$, PowhegPy8 $Z \to ee$, and Sherpa $\gamma\gamma$ samples for each photon conversion category. 89
6.9 The predicted diphoton invariant mass distribution for events that pass and fail the ambiguiity BDT selection criteria separated by photon conversion categories. The effects of the continuum background using the MC Sherpa $\gamma\gamma$ signal region with the data $\gamma j + jj$ nominal control region as described in Section 7.3.1.3 and the fake photon background from $Z \to ee$ decays are shown in each distribution. A scale factor of 1.25 is applied to the UU category histograms to separate them visually from those for the UC category. 91
6.10 The distribution of diphoton BDT training variables for each signal production mode at $m_X = 100\,\mathrm{GeV}$, the Sherpa2 $\gamma\gamma$ background, and the PowhegPy8 $Z \to ee$ background. The distribution for each sample is normalized separately for shape comparison. 95
6.11 The distributions of diphoton BDT scores for the training and validation subsets. 96

6.12 The distribution of the diphoton BDT event-level scores for each signal production mode at all four mass points $m_X = 60, 80, 100, 120\,\text{GeV}$, the Sherpa2 $\gamma\gamma$ background, the nominal data control region, and the PowhegPy8 $Z \to ee$ background. The production modes in the cut efficiency is both luminosity weighted and SM-like cross-section weighted while the backgrounds are separately normalized to unity. 98
6.13 The cumulative distribution of the diphoton BDT event-level scores using the score as the lower bound for each signal production mode at all four mass points $m_X = 60, 80, 100, 120\,\text{GeV}$, the Sherpa2 $\gamma\gamma$ background, the nominal data control region, and the PowhegPy8 $Z \to ee$ background. The production modes in the cut efficiency is both luminosity weighted and SM-like cross-section weighted while the backgrounds are separately normalized to unity. 99
6.14 The relative signal sensitivity for each production mode after applying the diphoton BDT score criteria relative to no criteria applied. 99
6.15 The total and relative selection efficiencies for each MC campaign and each m_X using events in the range $m_X \pm 2 \cdot \sigma_{\text{CB},X}$ using the final analysis selections. The total selection efficiencies are calculated with sequential application of the final analysis selections. The relative selection efficiencies are calculated by comparing each analysis selection to the previous selection. 104
7.1 The global mass-parameterized fit to the $m_{\gamma\gamma}$ distributions of the merged NWA signals weighted by SM-like Higgs cross-sections using a DSCB function in each model-dependent category. The bottom panels show the pulls of the fit. 110
7.2 The mass-parameterized linear fit to the Δm_X parameter of the merged NWA signals weighted by SM-like Higgs cross-sections in each model-dependent category. The blue shaded bands indicate the possible range of parameters based on the error of the likelihood fit. The points are the values and associated errors derived from single mass point DSCB fits. 111
7.3 The mass-parameterized linear fit to the σ_{CB} parameter of the merged NWA signals weighted by SM-like Higgs cross-sections in each model-dependent category. The blue shaded bands indicate the possible range of parameters based on the error of the likelihood fit. The points are the values and associated errors derived from single mass point DSCB fits. 112
7.4 The mass-parameterized linear fit to the α_{low} parameter of the merged NWA signals weighted by SM-like Higgs cross-sections in each model-dependent category. The blue shaded bands indicate the possible range of parameters based on the error of the likelihood fit. The points are the values and associated errors derived from single mass point DSCB fits. 113

7.5 The mass-parameterized linear fit to the α_{high} parameter of the merged NWA signals weighted by SM-like Higgs cross-sections in each model-dependent category. The blue shaded bands indicate the possible range of parameters based on the error of the likelihood fit. The points are the values and associated errors derived from single mass point DSCB fits. 114
7.6 The global mass-parameterized fit to the $m_{\gamma\gamma}$ distributions of the merged NWA signals weighted by SM-like Higgs cross-sections using a DSCB function in each model-dependent category. The bottom panels show the pulls of the fit. 116
7.7 The mass-parameterized linear fit to the Δm_X, σ_{CB}, α_{low}, and α_{high} parameters of the ggH signal in each model-independent category. The blue shaded bands indicate the possible range of parameters based on the error of the likelihood fit. The points are the values and associated errors derived from single mass point DSCB fits. . . 117
7.8 Systematic uncertainties associated with the photon energy scale and photon energy resolution as a function of m_X, computed for each UU model-dependent category. 120
7.9 Systematic uncertainties associated with the photon energy scale and photon energy resolution as a function of m_X, computed for each UC model-dependent category. 121
7.10 Systematic uncertainties associated with the photon energy scale and photon energy resolution as a function of m_X, computed for each CC model-dependent category. 122
7.11 Systematic uncertainties associated with the photon energy scale and photon energy resolution as a function of m_X, computed for each model-independent category. 124
7.12 Profile distributions of (a) track and (b) calorimeter isolation with respect to truth isolation for a resonance at $m_X = 100\,\text{GeV}$. 2D distributions of (c) track and (d) calorimeter isolation with respect to truth isolation for ggH resonance at $m_X = 100\,\text{GeV}$. Dotted cyan line indicates the truth and reconstruction isolation cuts where the bottom left quadrant passes selection cuts. 127
7.13 The inclusive category correction factor (C_X) comparing the number of events passing the full set of selection cuts with the number of events passing the fiducial volume criteria for each mass point and each production mode. 128
7.14 The inclusive category correction factor (C_X) relative to the value for the merged production mode. 129
7.15 The acceptance factor (A_X) comparing the number of events passing the fiducial volume criteria with the total number of events for each mass point and each production mode. 130

7.16 The inclusive category acceptance factor (A_X) times correction factor (C_X) comparing the number of events passing the full set of selection cuts with the total number of events for each mass point and each production mode. 130
7.17 Experimental uncertainties on the C_X factor associated with the trigger scale factor, the pile-up reweighting, the photon identification efficiency, the photon isolation efficiency, the photon energy resolution, the photon energy scale, and the data-driven (DD) photon isolation correction for the model-dependent method. 134
7.18 Experimental uncertainties on the C_X factor associated with the trigger scale factor, the pile-up reweighting, the photon identification efficiency, the photon isolation efficiency, the photon energy resolution, the photon energy scale, and the data-driven (DD) photon isolation correction for the model-independent method. 138
7.19 The $\gamma\gamma$, γj, and jj component yields for each model-dependent category determined by the 2x2D sideband method as a function of the diphoton mass. 147
7.20 The $\gamma\gamma$, γj, and jj component fractions for each model-dependent category determined by the 2x2D sideband method as a function of the diphoton mass. 148
7.21 The $\gamma\gamma$, γj, and jj component yields for each model-independent category determined by the 2x2D sideband method as a function of the diphoton mass. 149
7.22 The $\gamma\gamma$, γj, and jj component fractions for each model-independent category determined by the 2x2D sideband method as a function of the diphoton mass. 149
7.23 Components of the event weight shown as a distribution with respect to the truth invariant mass for the Sherpa2 $\gamma\gamma$ samples in the fully inclusive category. The two mass slices are combined with no stitch weighting applied and is composed of all three MC campaigns (mc16a, mc16d, and mc16e). 152
7.24 The irreducible background with (red) and without (black) weighting on the slices for the UU3 category. The ratio to the fit (green) on the weighted shape is shown for comparison. 154
7.25 The irreducible background with (red) and without (black) weighting on the slices for the UU category. The ratio to the fit (green) on the weighted shape is shown for comparison. 156
7.26 Reducible background shapes from data in L′4 shown with the expected contribution for prompt diphoton events from Sherpa2 $\gamma\gamma$ MC simulation in L′4 for each model-dependent category. 158

7.27 Reducible background shapes obtained from the data in the different L′ variations for each model-dependent category. All distributions are normalized to unity to compare shapes with the nominal control region (L′4). The Tight-Antitight control region, which has no additional L′ requirement, is also shown in red for comparison but is not used in this analysis. The bottom panel shows the ratio comparing each control region to L′4. 160
7.28 Reducible background shapes from data in L′4 shown with the expected contribution for prompt diphoton events from Sherpa2 $\gamma\gamma$ MC simulation in L′4 for each model-independent category. 161
7.29 Reducible background shapes obtained from the data in the different L′ variations for each model-independent category. All distributions are normalized to unity to compare shapes with the nominal control region (L′4). The Tight-Antitight control region, which has no additional L′ requirement, is also shown in red for comparison but is not used in this analysis. The bottom panel shows the ratio comparing each control region to L′4. 161
7.30 Full background template constructed from MC signal region $\gamma\gamma$ component and the L′4 data control region reducible γj component for each model-dependent category. The contributions of the $\gamma\gamma$ component are separately shown in dark blue to emphasize its contribution to the full template shown in light blue. The bottom panel shows the ratio between the full template and the $\gamma\gamma$ component. . 163
7.31 Full background template of the $\gamma\gamma$, γj, and jj component for each model-dependent category. 164
7.32 Full background template constructed from MC signal region $\gamma\gamma$ component and the L′4 data control region reducible γj component for each model-independent category. The contributions of the $\gamma\gamma$ component are separately shown in dark blue to emphasize its contribution to the full template shown in light blue. The bottom panel shows the ratio between the full template and the $\gamma\gamma$ component. . 166
7.33 Full background template of the $\gamma\gamma$, γj, and jj component for each model-independent category. 166
7.34 Relative spurious signal (SS) systematic estimated on the smoothed full background continuum templates obtained for each model-dependent category. The dashed lines are used for illustrating the 50% background uncertainty. Functions that have a relative spurious signal greater than 100% have been excluded for plotting purposes. . . . 172
7.35 Absolute number of spurious signal events as a function of m_X estimated on the smoothed $\gamma\gamma + \gamma j$ templates obtained for each model-dependent category for the chosen fit function. 174
7.36 Absolute number of spurious signal events as a function of m_X estimated on the smoothed $\gamma\gamma + \gamma j$ template variations obtained for each model-dependent category for the chosen fit function. 176

7.37 Spurious signal relative to the expected statistical uncertainty in the data obtained from the smoothed template variations for each model-dependent category for the chosen fit function. 177
7.38 Relative spurious signal (SS) systematic estimated on the smoothed full background continuum templates obtained for each model-independent category. The dashed lines are used for illustrating the 50% background uncertainty. Functions that have a relative spurious signal greater than 100% have been excluded for plotting purposes. . . . 179
7.39 Absolute number of spurious signal events as a function of m_X estimated on the smoothed $\gamma\gamma + \gamma j$ templates obtained for each model-independent category for the chosen fit function. 180
7.40 Absolute number of spurious signal events as a function of m_X estimated on the smoothed $\gamma\gamma + \gamma j$ template variations obtained for each model-independent category for the chosen fit function. . . . 181
7.41 Spurious signal relative to the expected statistical uncertainty in the data obtained from the smoothed template variations for each model-independent category for the chosen fit function. 181
7.42 Invariant mass distributions (normalized to unity) of electrons pairs (black), pairs made of a leading truth-matched electron reconstructed as a photon and subleading truth-matched electron reconstructed as an electron (red), and pairs made of a leading truth-matched electron reconstructed as an electron and subleading truth-matched electron reconstructed as a photon (blue). The unconverted (a) and converted (b) photons are obtained through a $Z \to ee$ simulation sample. . . 183
7.43 Cumulative distribution functions of discrete invariant mass distributions of electrons pairs (black) and electron with fake leading photon (red) or fake subleading photon (blue) pairs in unconverted (a) and converted (b) photon category, obtained on a $Z \to ee$ simulation sample. 185
7.44 Invariant mass distributions (normalized to unity) of electron with fake photon (blue) and transformed electron (red) pairs in leading (a) and subleading (b) cases for unconverted photons, obtained on a $Z \to ee$ simulation sample. 185
7.45 Invariant mass distributions (normalized to unity) of electron with fake photon (blue) and transformed electron (red) pairs in leading (a) and subleading (b) cases for converted photons, obtained on a $Z \to ee$ simulation sample. 186
7.46 Invariant mass distributions (normalized to unity) of diphoton pair (blue) and transformed electrons pairs obtained with summed up shifts (red) in the UU (a), UC (b), CU (c) and CC (d) categories, obtained on a $Z \to ee$ simulation sample. 187

7.47 The fit of the resonant and non-resonant backgrounds in the (a) unconverted photon γe spectrum, (b) unconverted photon $e\gamma$ spectrum, (c) the converted photon γe spectrum and the (d) the converted photon $e\gamma$ spectrum from the control region data. The non-resonant background subtraction in these invariant mass distributions is performed before calculation of the leading and subleading fake rates in data. 189
7.48 Invariant mass dependence of the leading (a) and subleading (b) unconverted photon fake rates as measured in $Z \to ee$ simulation, before (blue) and after (red) applying the Smirnov transformation. 190
7.49 Invariant mass dependence of the leading (a) and subleading (b) converted photon fake rates as measured in $Z \to ee$ simulation, before (blue) and after (red) applying the Smirnov transformation. 190
7.50 Invariant mass dependence of the leading (left) and subleading (right) converted (top) and unconverted (bottom) photon fake rates, as measured in data. The red lines represent the fit in the mass window. 193
7.51 Invariant mass dependence of correlation factor α in UU (a), UC (b), CU (c) and CC (d) categories, obtained on a $Z \to ee$ simulation sample. The red lines represent the fit in the mass window. 194
7.52 Invariant mass distributions per diphoton BDT category in UU (a), UC (b), CU (c) and CC (d) photon conversion categories, integrals are normalized to unity, obtained on a $Z \to ee$ simulation sample. 195
7.53 Invariant mass dependence of normalization factor f in UU (a), UC (b), CU (c) and CC(d) conversion categories, given for each diphoton BDT category, used to obtain expected number of fake photons in data. The red lines represent the fit in the mass window. 196
7.54 Drell-Yan invariant mass templates, that are derived from ee events in data, (red) and the expected diphoton background component (blue) in the UU (a), UC (b), CU (c) and CC (d) categories, obtained from the $Z \to ee$ simulation sample and normalized to the Run2 luminosity. 198
7.55 DY invariant mass templates describing the expected diphoton background component in the UU (a), UC (b), CU (c) and CC (d) categories, inclusive across the diphoton BDT categories, with individual systematic variations of the mean, width and normalization. The different sources of uncertainties are added in quadrature. 201
8.1 The $m_{\gamma\gamma}$ distribution from each resonant and non-resonant background for each model-dependent category. The $\gamma\gamma$ contribution is taken from the Sherpa MC samples, the γj and jj contribution from data-driven control regions, and the $Z \to ee$ contribution from the data-driven template. 212

8.2 Expected limit on the total production cross-section times branching ratio to two photons for a Higgs-like resonance as a function of the resonance mass m_X for the model-dependent method. Central values of the expected and observed limit from the recent CMS analysis [48] and the expected limit from the previous ATLAS analysis [55] using 80.4 fb^{-1} scaled to 139.5 fb^{-1} are shown for comparison. The expected limit here considers all systematic uncertainties and an integrated luminosity of 139.5 fb^{-1}. 213
8.3 The $m_{\gamma\gamma}$ distribution from each resonant and non-resonant background for each model-independent category. The $\gamma\gamma$ contribution is taken from the Sherpa MC samples, the γj and jj contribution from data-driven control regions, and the $Z \to ee$ contribution from the data-driven template. 214
8.4 Expected limit on the fiducial production cross-section times branching ratio to two photons for a Higgs-like resonance as a function of the resonance mass m_X for the model-independent method. The expected limit here considers all systematic uncertainties and an integrated luminosity of 139.5 fb^{-1}. 215
8.5 Expected limit on the total production cross-section times branching ratio to two photons for a Higgs-like resonance as a function of the resonance mass m_X for the model-independent method. Central values of the expected and observed limit from the recent CMS analysis [48] and the expected limit from the previous ATLAS analysis [55] using 80.4 fb^{-1} scaled to 139.5 fb^{-1} are shown for comparison. The expected limit here considers all systematic uncertainties and an integrated luminosity of 139.5 fb^{-1}. 216
8.6 Data distributions of $m_{\gamma\gamma}$ overlaid with background-only fits for each model-dependent category. The bottom panels correspond to the difference between data and the the fit. 218
8.7 Data distributions of $m_{\gamma\gamma}$ overlaid with background-only fits for each model-independent category. The bottom panels correspond to the difference between data and the the fit. 219
8.8 The observed p-value for the background-only hypothesis in the logarithmic scale as a function of the resonance mass m_X using the model-dependent method. 221
8.9 The observed p-value for the background-only hypothesis in the logarithmic scale as a function of the resonance mass m_X using the model-independent method. 222
8.10 The expected and observed limits on the total production cross section $\sigma_{\text{fid}} \cdot \text{BR}(X \to \gamma\gamma)$ of a scalar resonance as a function of the resonance mass m_X in the 66 – 110 GeV diphoton invariant mass range for the model-dependent method. The green and yellow bands show the $\pm 1\sigma$ and $\pm 2\sigma$ uncertainties on the expected limit. 223

8.11 The expected and observed limits on the total production cross section for the model-dependent method overlaid with results from other similar scalar resonance searches. The resonance search previously performed by A Toroidal LHC Apparatus (ATLAS) [55] is shown in red. The resonance search recently performed by the Compact Muon Solenoid (CMS) [48] is shown in blue. The green and yellow bands show the $\pm 1\sigma$ and $\pm 2\sigma$ uncertainties on the expected limit. 224
8.12 The expected and observed limits on the fiducial production cross section $\sigma_{\text{fid}} \cdot \text{BR}(X \to \gamma\gamma)$ of a scalar resonance as a function of the resonance mass m_X in the 66 – 110 GeV diphoton invariant mass range for the model-independent method. The green and yellow bands show the $\pm 1\sigma$ and $\pm 2\sigma$ uncertainties on the expected limit. 225
8.13 The expected and observed limits on the total production cross section for the model-independent method overlaid with results from other similar scalar resonance searches. The resonance search previously performed by ATLAS [55] is shown in red. The resonance search recently performed by CMS [48] is shown in blue. The green and yellow bands show the $\pm 1\sigma$ and $\pm 2\sigma$ uncertainties on the expected limit. 226
A.1 A cross-sectional diagram of the muon spectrometer in the barrel region of the ATLAS detector in the $x - y$ plane. 231
A.2 A cross-sectional diagram of the muon spectrometer in the barrel and end-cap regions of the ATLAS detector in the $y - z$ plane. 231
A.3 One of the 96 sMDT chambers consisting of approximately 500 individual sMDT tubes. The tubes are mostly constructed at MSU and tested at UM. Each sMDT chamber is constructed and tested at UM before being delivered to CERN. 232
A.4 Tube straightness measurement station with the digital microscope aimed at the middle of the aluminum tube sitting on the V-bar. . . 237
A.5 The fraction of aluminum tubes delivered in 2020 and 2021 that pass various tube straightness criteria. 237
A.6 Tube design with an exploded view of the end-plug components [68]. All length measurements are in mm. 239
A.7 Setup used to string the tungsten-rhenium wire through the aluminum tube. 240
A.8 Setup used stretch the wire and hold the wire at the nominal tension. 241
A.9 The rotary swaging head for creating grooves around the tube at the end-plug o-ring locations. 242
A.10 Set up of the tube leak test station. The tube is placed inside the vacuum vessel and pressurized with Helium to 3 bar absolute. . . . 245
A.11 Helium gas input connected to a sMDT tube placed inside the vacuum vessel for the gas tightness test. 245
A.12 Testing station for tube length and wire tension measurements. . . 246
A.13 Distribution of the measured length of the tubes built at UM. . . . 247
A.14 Circuit for wire tension test. 247

A.15 Distribution of wire tension in the tubes built at UM. 249
A.16 HV test and dark current measurement setup. 250
A.17 Cross section of the tube mounting diagram for the dark current test station. 250
A.18 HV test stand with a total capacity of 48 tubes. The CAEN SY5527 mainframe with the CAEN GECO monitoring program is running on the connected computer. 251
A.19 Examples of one tube that recovered from initial high dark current measurements and one that developed higher and higher dark current over time. Note the different scales. 252
A.20 Distribution of the final dark current measurement and the burn-in time for the tubes built at UM. The three peaks in the burn-in time distribution correspond to the most common test lengths used for measuring the dark current: day time (just a few hours), overnight (typically about 15-16 hours) and over the weekend (normally around 64 hours). 253

LIST OF TABLES

Table

2.1 The elementary particles of the SM with their respective masses [98]. The neutrino leptons are massless under the SM, but the experimentally constrained masses of the flavor eigenstates are listed here. . . 5

2.2 The cross section of Higgs-like production modes at $\sqrt{s} = 13\,\text{TeV}$. Values correspond to the expected cross section of the SM Higgs-like boson at various masses [73]. 11

2.3 The branching fractions of Higgs-like decay channels. Values correspond to the expected branching fractions of the SM Higgs-like boson at various masses [73]. 12

2.4 The coupling between complex scalar doublets and SM particles in various 2HDM types. 16

5.1 The recommended SM-like Higgs boson cross section and branching ratios values at $\sqrt{s} = 13\,\text{TeV}$ for the ggH, VBF, ttH, WH, and ZH production modes at various mass points m_X provided by the LHC Higgs Working Group [73]. 58

5.2 A list of steps in the resonance search analysis methodology. The usage of how each step is used in each category for the model-dependent and model-independent methods is briefly summarized. The role of the MC samples and LHC datasets is also shown for each step. . . 61

6.1 The signal samples of the five Higgs production modes with the largest SM-like cross sections considered in this analysis. The available simulated mass points and event statistics for each of the three MC campaign is listed for each production mode. All signals are generated using the NWA such that $\Gamma_X = 4\,\text{MeV}$. 64

6.2 Prompt diphoton background samples generated with the AFII fast detector simulation. The total events given here are the number of events generated and reconstructed at AOD level. The filter efficiency measures the fraction of events from the generator-level sample that are present in the final simulated sample. 65

6.3 The $Z \to ee$ samples used to study the DY background arising from electrons faking photons. The event totals presented here are the number of events generated and reconstructed at the AOD level. The Sherpa slices cover the region of $m_{ee} > 40\,\text{GeV}$ and are sliced in $\max(H_\text{T}, p_\text{T}(V))$ at the parton level, where the boson transverse momentum $p_\text{T}(V)$ is worked out from the two parton-level leptons and the parton-level H_T is given by the scalar p_T sum of all parton-level jets with $p_\text{T} > 20\,\text{GeV}$. The k-factor, defined as the cross-section ratio $\sigma_\text{NNLO}/\sigma_\text{Generator}$ for the relevant mass dilepton mass range, is also given here [32]. 67
6.4 The unprescaled diphoton L1 and HLT triggers used per data-taking period with their associated integrated luminosity. 70
6.5 The prescaled diphoton L1 and HLT triggers used per data-taking period with their associated integrated luminosity. 70
6.6 The percentage of events containing photons reconstructed as unconverted or converted in simulated $Z \to ee$ and $X \to \gamma\gamma$ samples and the relative significance per photon conversion category $f_i^{X\to\gamma\gamma}/\sqrt{f_i^{Z\to ee}}$ for all three MC campaigns combined. An average event count is taken between the signal samples with $m_X = 80\,\text{GeV}$ and $100\,\text{GeV}$ to approximate the expected event count for a signal sample at $m_X = 90\,\text{GeV}$. The FoM for this 4-category scheme is 1.804. 84
6.7 The fraction of events containing ambiguous photons in each photon conversion category in simulated Sherpa2 $\gamma\gamma$, PowhegPy8 ggH, and PowhegPy8 $Z \to ee$ samples. 85
6.8 The correlation matrix between the diphoton invariant mass $m_{\gamma\gamma}$ and variables highly correlated with it in the signal and background samples used for training the diphoton BDT. 92
6.9 The correlation matrix between variables in the signal and background samples used for training the diphoton BDT. Dashed entries (-) indicate negligible to no correlation between corresponding variables. 96
6.10 The normalized importance values for each variable based on its frequency of usage to split a decision tree node. The variable importance is weighted by the signal to background separation gain squared and by the number of events in the node of a given variable. 97
6.11 The fractions of events for each production mode estimated at $m_X = 90\,\text{GeV}$ and the number of background events per GeV at $m_{\gamma\gamma} = 90\,\text{GeV}$ for each diphoton BDT class. 101
6.12 Relative sensitivities for each of the 9 categories using both photon conversion categorization and diphoton BDT classification. 102
6.13 Summary of the final analysis selections and categorization. 103
6.14 Event cutflow using the final analysis selections measured in data for 2015, 2016, 2017, and 2018. Fractions of events for each photon conversion category is also given below the analyis selection cutflow. 105

7.1 The m_X-parameterizations of the DSCB function parameters describing the signal shape for each model-dependent category. In these fits, n_{high} and n_{low} are set to fixed values. 115
7.2 The m_X-parameterizations of the DSCB function parameters describing the signal shape for each model-independent category. In these fits, n_{high} and n_{low} are set to fixed values. 118
7.3 Parameterizations of the DSCB function describing the signal shape that result from the global fit to signal templates where the photon energy scale and resolutions are varied up and down. The parameters are derived in each UU model-dependent category. 120
7.4 Parameterizations of the DSCB function describing the signal shape that result from the global fit to signal templates where the photon energy scale and resolutions are varied up and down. The parameters are derived in each UC model-dependent category. 121
7.5 Parameterizations of the DSCB function describing the signal shape that result from the global fit to signal templates where the photon energy scale and resolutions are varied up and down. The parameters are derived in each CC model-dependent category. 122
7.6 Parameterizations of the DSCB function describing the signal shape that result from the global fit to signal templates where the photon energy scale and resolutions are varied up and down. The parameters are derived in each model-independent category. 124
7.7 Parametrization of the experimental uncertainties on the C_X factor as function of m_X in each photon conversion categories and expressed for the luminosity of the data. The parameterization for each photon conversion category is taken as the envelope over the diphoton BDT categories. 135
7.8 Parametrization of the experimental uncertainties on the C_X factor as function of m_X in each photon conversion categories and expressed for the luminosity of the data. 139
7.9 The variables used to determine the definitions of the Loose, Tight [45], and LoosePrime photon ID selections. 142
7.10 The photon isolation and ID efficiencies for true photons from Sherpa2 $\gamma\gamma$ samples in the [60, 120] GeV mass range for each model-dependent category. The efficiencies are determined with respect to the leading and subleading photon candidates of true diphoton events that pass the full event selection except the photon isolation and having the ID criteria replaced with L′4 ID requirements. The uncertainty on these efficiencies comes from the MC statistical uncertainty. 145
7.11 The $\gamma\gamma$, γj, and jj fractions in the [60, 120] GeV mass range, obtained using the 2x2D sideband method for each model-dependent category. The first error term reflects the statistical uncertainty, and the second error term reflects the systematic uncertainties derived from the L′ variations. 146

7.12 The photon isolation and ID efficiencies for true photons from Sherpa2 $\gamma\gamma$ samples in the [60, 120] GeV mass range for each model-dependent category. The efficiencies are determined with respect to the leading and subleading photon candidates of true diphoton events that pass the full event selection except the photon isolation and having the ID criteria replaced with L′4 ID requirements. The uncertainty on these efficiencies comes from the MC statistical uncertainty. 150
7.13 The $\gamma\gamma$, γj, and jj fractions in the [60, 120] GeV mass range, obtained using the 2x2D sideband method for each model-dependent category. The first error term reflects the statistical uncertainty, and the second error term reflects the systematic uncertainties derived from the L′ variations. 150
7.14 Stitching factors applied as an overall weight to the Sherpa2 $\gamma\gamma$ 90 − 175 GeV slice before being combined with the 50 − 90 GeV slice to reduce the transition discontinuity at 90 GeV. The factor is found using a maximum likelihood fit using a fifth order polynomial for each model-dependent category in each of the three MC campaigns. 153
7.15 Stitching factors applied as an overall weight to the Sherpa2 $\gamma\gamma$ 90 − 175 GeV slice before being combined with the 50 − 90 GeV slice to reduce the transition discontinuity at 90 GeV. The factor is found using a maximum likelihood fit using a fifth order polynomial for each model-independent category in each of the three MC campaigns. 156
7.16 The expected number of events for each of the diphoton background continuum components for each model-dependent category in the diphoton invariant mass range $62\,\text{GeV} < m_{\gamma\gamma} < 120\,\text{GeV}$. 165
7.17 The expected number of events for each of the diphoton background continuum components for each model-independent category in the diphoton invariant mass range $62\,\text{GeV} < m_{\gamma\gamma} < 120\,\text{GeV}$. 165
7.18 The output of the spurious signal test run on the smoothed templates built from Sherpa $\gamma\gamma$ and the γj reweighting. The information per analysis category indicates the fit function chosen, the size of the spurious signal in event count, the size of the spurious signal divided by the background statistical uncertainty, the 2σ error on the size of the spurious signal divided by the background uncertainty, and number of free parameters in the fit function. 173
7.19 Parameterization of the spurious signal in this search, N_{SS}, as function of m_X, obtained for the background modeling for each model-dependent category and expressed for the luminosity of the data. 175
7.20 Parameterization of the spurious signal in this search, N_{SS}, as function of m_X, obtained for the background modeling template variations for each model-dependent category and expressed for the luminosity of the data. 178

7.21 The output of the spurious signal test run on the smoothed templates built from Sherpa $\gamma\gamma$ and the γj reweighting. The information per analysis category indicates the fit function chosen, the size of the spurious signal in event count, the size of the spurious signal divided by the background statistical uncertainty, the 2σ error on the size of the spurious signal divided by the background uncertainty, and number of free parameters in the fit function. 179
7.22 Parameterization of the spurious signal in this search, N_{SS}, as function of m_X, obtained for the background modeling for each model-independent category and expressed for the luminosity of the data. 180
7.23 Parameterization of the spurious signal in this search, N_{SS}, as function of m_X, obtained for the background modeling template variations for each model-independent category and expressed for the luminosity of the data. 181
7.24 Absolute (and relative) uncertainties in GeV on the DY shape for each category. The material distortion giving the highest deviation is also shown. 200
7.25 Absolute (and relative) uncertainties in number of events on the DY normalization for each category. The material distortion giving the highest deviation is also shown. 200
8.1 Summary of the main sources of systematic uncertainty on the scalar resonance cross section limit for the model-dependent method. . . 208
8.2 Summary of the main sources of systematic uncertainty on the scalar resonance cross section limit for the model-independent method. . 209
8.3 The estimated contribution from each resonant and non-resonant background in the $62-120\,\text{GeV}$ $m_{\gamma\gamma}$ range for the model-dependent method. 210
8.4 The estimated contribution from each resonant and non-resonant background in the $62-120\,\text{GeV}$ $m_{\gamma\gamma}$ range for the model-independent method. 214
A.1 UM tube room stations. 234
A.2 Nominal parameters for sMDT tube materials and nominal criteria for test measurements. 235

LIST OF ABBREVIATIONS

2HDM Two Higgs Doublet Model

AFII ATLFAST-II

ALFA Absolute Luminosity For ATLAS

ALICE A Large Ion Collider Experiment

ALP axion-like particle

ATLAS A Toroidal LHC Apparatus

BDT gradient-boosted decision tree

BIL Barrel-Inner-Large

BIS Barrel-Inner-Small

BML Barrel-Middle-Large

BMS Barrel-Middle-Small

BOL Barrel-Outer-Large

BOS Barrel-Outer-Small

BSM beyond the standard model

CC converted-converted

CC1 converted-converted diphoton BDT class 1

CC2 converted-converted diphoton BDT class 2

CC3 converted-converted diphoton BDT class 3

CDF cumulative distribution function

CERN the European Organization for Nuclear Research

CMS the Compact Muon Solenoid

CP charge-parity

CSC Cathode Strip Chamber

CU converted-unconverted

DAQ data acquisition

DSCB double-sided Crystal Ball

DY Drell-Yan

EM electromagnetic

EWSB electroweak symmetry breaking

FASER the ForwArd Search ExpeRiment

FCal Forward Calorimeter

FCNC flavor-changing neutral currents

FFT fast Fourier Transform

FoM figure of merit

GECO GEneral COntrol

ggH gluon-gluon fusion

GPR Gaussian Process Regression

GP Gaussian Process

GUI graphical user interface

HCal hadronic calorimeter

HEC Hadronic End-cap Calorimeter

HGam Higgs working group for $H \to \gamma\gamma$ related analyses

HL-LHC High Luminosity LHC

HLT High Level Trigger

HV high voltage

ID identification

IHEP the Institute for High-Energy Physics

I/O input/output

IP interaction point

IPA isopropyl alcohol

KS Kolmogorov–Smirnov

LAr liquid argon

LEP the Large Electron-Positron collider

LHC Large Hadron Collider

LHCb the LHC-beauty experiment

LHCf the LHC-forward experiment

LINAC4 the 4th generation linear accelerator

LO leading order

LS2 Long Shutdown 2

LS3 Long Shutdown 3

LUCID the LUminosity measurement using Cerenkov Integrating Detector

L1 Level-1

L2 Level-2

MC Monte Carlo

MDT Monitored Drift Tube

Mifa Mifa Aluminium B.V.

MoEDAL the Monopole and Exotics Detector At the LHC

MPI the Max Planck Institute for Physics, Munich

MSU Michigan State University

MVA multivariate analysis

MxAOD mini xAOD

NLO next-to-leading order

NNLO next-to-next-to-leading order

NP new physics

NRF normal-conducting radio-frequency

NWA narrow width approximation

PBT polybutylene terephthalate

PDF parton distribution function

PMT photomultiplier tube

POM polyoxymethylene

pp proton-proton

pQCD perturbative QCD

PS Proton Synchrotron

PSB Proton Synchrotron Booster

QAQC quality assurance and quality control

QCD quantum chromodynamics

ROOT Rapid Object-Oriented Technology

RPC Resistive Plate Chamber

R&D research and development

SCFH standard cubic feet per hour

SCT semi-conductor tracker

SM standard model

sMDT small-diameter Monitored Drift Tube

SND the Scattering and Neutrino Detector

SPS Super Proton Synchrotron

TAS Target Absorber Secondary

TGC Thin Gap Chamber

TMVA ROOT multivariate analysis

TOTEM the TOTal Elastic and diffractive cross section Measurement experiment

tRPC thin Resistive Plate Chamber

TRT transition radiation tracker

ttH top-associated production

UC unconverted-converted

UC1 unconverted-converted diphoton BDT class 1

UC2 unconverted-converted diphoton BDT class 2

UC3 unconverted-converted diphoton BDT class 3

UM the University of Michigan, Ann Arbor

US United States

UU unconverted-unconverted

UU1 unconverted-unconverted diphoton BDT class 1

UU2 unconverted-unconverted diphoton BDT class 2

UU3 unconverted-unconverted diphoton BDT class 3

VBF vector boson fusion

VEV vacuum expectation value

VH Higgs-strahlung

WH Higgs-strahlung from a $W^{\pm}$ boson

ZH Higgs-strahlung from a Z boson

ABSTRACT

We report on the search for new Higgs-like particles with SM-like scalar couplings produced in pp collisions with a mass in the range of 66 – 110 GeV/c^2 and decaying to two photons. The search is conducted in the pp collision data collected by the ATLAS detector during the Run 2 data-taking period of the LHC. Using an integrated luminosity of 139.5 fb^{-1} at a pp center-of-mass energy of $\sqrt{s} = 13$ TeV recorded in 2015 – 2018, we develop and apply techniques in this data to find and identify narrow width resonances predicted by theories with an extended Higgs sector. No significant signals are observed, and the cross section times branching ratio for a SM-like Higgs-like scalar decaying to two photons is limited to be less than the experimental sensitivity of this search, approximately 50 fb over the mass range of 66 – 110 GeV/c^2. A less restrictive model-independent search that focuses on only the dominant scalar production mode similarly finds no signals, and the cross section times branching ratio is limited to less than approximately 70 fb in the same mass range.

CHAPTER I

Introduction

The recipe for the basic building blocks of the universe has undergone many revisions in the last few millennia, starting from the theory of the atom by Democritus and Leucippus in 5 BCE and arriving currently at the standard model (SM) of particle physics. The SM mathematically describes three of the four fundamental forces of nature — the electromagnetic, weak, and strong — as well as the most elementary particles that participate in each of the forces. This model also has extensive experimental confirmation, including the observation of the predicted Higgs boson in 2012 [7] [39]. Although the subsequent studies of this object are consistent with the SM, the Higgs boson still remains an object of mystery in its nature, origin, and role within the universe. Neither the theory nor the existing measurements on this discovered particle exclude the possibility of other undiscovered Higgs-like particles with similar interactions.

Many extensions to the SM have been proposed in attempt to enlarge the SM theory. These theories, collectively called beyond the standard model (BSM) extensions, allow for the existence of additional elementary particles that can couple with SM particles. For example, Two Higgs Doublet Models (2HDMs) provide at least one more Higgs-like particle that exhibits similar coupling characteristics to SM particles as the SM Higgs boson [28]. Although experiments and analyses in the past have

excluded a subset of these theories and ruled out regions of parameter space in the remaining ones [24] [56], additional particle collision data at high energies can be used to push the sensitivity frontier further in hopes of revealing these new particles. Thus, the study of the Higgs boson and its potential variants can provide new insights to help build a better understanding of Higgs physics and probe for new physics [90].

The high energy particle collisions necessary to create and observe the Higgs boson occur at the Large Hadron Collider (LHC), where protons collide at a center-of-mass energy of $E_{\mathrm{CM}} = 13$ TeV [31]. The collisions are detected and measured using the ATLAS detector which uses state-of-the-art energy calorimetry and particle tracking technology to perform measurements on the collision products with very high energy and spatial resolution [40]. In this thesis, we will use the data collected by the ATLAS detector during the Run 2 data-taking period to search for new Higgs-like bosons with SM-like scalar couplings and decaying to two photons, focusing on the low diphoton invariant mass regime below the SM Higgs boson mass of 125 GeV/c^2. We will describe why the two photon state of the Higgs boson decay is a compelling experimental signature and why the background of this final state can be drastically reduced compared to other multi-particle final states at the LHC. We will use statistical tools such as Gaussian Process Regression (GPR), gradient-boosted decision tree (BDT) classifiers, and categorization schemes to improve the modeling of background SM interactions and to separate them from predicted BSM activity.

This thesis is organized as follows. The SM is reviewed in Chapter 2 where fundamental particles and their interactions, the production and decay of the Higgs boson, and possible extensions to the SM theory are explored. The technology used in the ATLAS experiment to pursue a search for a new Higgs-like particle is described in Chapter 3. The information collected from the ATLAS particle detector is processed using the procedures and methods outlined in Chapter 4 to reconstruct particles relevant to the two photon decay channel of a Higgs-like particle. The analysis strategy

for performing a search in the diphoton decay channel are summarized in Chapter 5. The Monte Carlo (MC) samples and datasets used in this analysis along with the selection criteria and categorization schemes used on the diphoton events are described in Chapter 6. The statistical methods and analytical models used to describe the signal and background shapes are detailed in Chapter 7. The final cross section limits set on the production of a Higgs-like scalar in the low diphoton invariant mass regime using the LHC full Run 2 dataset are summarized in Chapter 8.

Additional work performed on the ATLAS muon spectrometer is described in the Appendix. The construction and testing of the upgraded small-diameter Monitored Drift Tube (sMDT) technology at the University of Michigan, Ann Arbor (UM) for the muon tracker is given in Appendix 10.

CHAPTER II

Theoretical Background

The SM of particle physics is extremely successful at describing the behaviour and interactions between particles. The model is succinct enough to allow its mathematical form be written on a key-chain. Yet, the theory is also robust enough to provide a thorough description of the fundamental particles, from the production and propagation of light across the primordial universe to the radioactive decay of man-made elements.

A summary of the quarks, leptons, and gauge bosons comprising the SM is outlined in Section 2.1. The production modes of the SM Higgs boson and its decay into various final states with an emphasis on the two photon decay channel is described in Section 2.2. The well-motivated 2HDM that extends the SM with additional Higgs-like particles is discussed afterwards in Section 2.3.

Type		Particle	Symbol	Mass [MeV/c^2]
Fermions	*Quark*	up	u	2.2
		charm	c	1275
		top	t	173000
		down	d	4.7
		strange	s	95
		bottom	b	4180
	Lepton	electron	e	0.511
		muon	μ	106
		tau	τ	1777
		electron neutrino	ν_e	$< 2 \times 10^{-6}$
		muon neutrino	ν_μ	$< 2 \times 10^{-6}$
		tau neutrino	ν_τ	$< 2 \times 10^{-6}$
Bosons	*Vector*	gluon	g	0
		photon	γ	0
		Z boson	Z	91188
		$W^\pm$ boson	$W^\pm$	80379
	Scalar	Higgs boson	H	125180

Table 2.1: The elementary particles of the SM with their respective masses [98]. The neutrino leptons are massless under the SM, but the experimentally constrained masses of the flavor eigenstates are listed here.

2.1 The Standard Model of Particle Physics

The SM is composed of point-like Dirac fermions [52] interacting via the gauge bosons. The elementary particles along with their respective masses are listed in Table 2.1.

2.1.1 The Fundamental Particles

The fundamental particles in the SM are classified as fermions or bosons based on their intrinsic spin: fermions have half-integer spins while bosons have integer spins. For the fermions, these spin-1/2 particles are categorized as quarks or leptons. The quarks can be paired into three generations of down-type and up-type quarks: the

down d with the up u, the strange s with the charm c, and the bottom b with the top t flavor, respectively. The down-type quarks from each generation have a fractional electric charge of $-1/3$ while the up-type quarks have $+2/3$. The leptons can also be paired into three generations: the electron e, muon μ, and tau τ, each paired with their respective neutrino ν_e, ν_μ, and ν_τ. The electron-like leptons from each generation have -1 electric charge while the neutrinos are electrically neutral. The generations of quarks and leptons are listed in increasing mass with the exception of the neutrinos. Under the SM, the neutrino leptons are allowed to be massless. However, experimental evidence has shown that the they are very small, and each flavor of neutrino is a linear combination of the three mass eigenstates.

For the bosons, the spin-0 particles are labeled as scalar bosons while the non-zero spin particles are labeled as vector bosons. The only scalar boson is the Higgs boson H while the vector bosons are the photon γ, gluons g, and weak gauge bosons $W^\pm$ and Z. The SM bosons are electrically neutral except for the $W^\pm$ which has an electric charge of ± 1. The photon and gluons are all massless while the Higgs boson and weak gauge bosons are among the most massive of elementary particles.

2.1.2 The Strong Interaction

The strong force is responsible for the short-range interactions between the gluons and the quarks [57]. These two types of particles are called partons when in a bound state, with the exception of the top quark which decays far too quickly to participate in a bound state. The bound quarks are usually found in composite subatomic particles called hadrons, which include baryons, such as the proton and neutron, and mesons, such as the pion. The gluons mediate the strong force between quarks through the constant exchange of gluons to bind the quarks into hadrons.

Quarks are not usually observed independently, but they can be interpreted as individual point-like scattering partons in high energy environments such as a particle

collider. The probability of a hadron containing a particular flavor of quark or gluon at a given momentum is encoded in the parton distribution functions (PDFs). When a scattering event ejects a quark from a pair of colliding hadrons, the freely propagating quark quickly undergoes a hadronization process where additional quarks and gluons are pair-produced from the vacuum and combine to form hadrons. These hadrons populate a collimated spray of particles called a hadronic jet whose momentum and energy are those of the original quark. These jets dominate as the final states emerging from hadron colliders.

2.1.3 The Electroweak Interaction

The electroweak force is the unified description of the long-range electromagnetic and short-range weak interactions. The electroweak sector is described by the $SU(2) \times U(1)$ symmetry group with four generators which give rise to the massless electroweak gauge bosons: the three weak isospin bosons W_1, W_2, and W_3 and the weak hypercharge boson Y. These four bosons mediate the electroweak force between fermions.

Just as an unmagnetized and symmetric ferromagnetic system will fall into a more energetically-favored and asymmetric magnetized state as the temperature of the system decreases, the electroweak system experienced symmetry breaking in the early universe as the temperature cooled. The SM Higgs field acquires a non-zero vacuum expectation value (VEV) at a critical temperature, causing the Higgs mechanism to induce electroweak symmetry breaking (EWSB) and transform the four degrees of freedom in the Higgs field into the massive Higgs boson and three would-be massless Nambu-Goldstone bosons. The electroweak gauge bosons then coalesce into the weak bosons and the photon after this symmetry breaking: linear combinations of W_1 and W_2 become the electrically charged $W^{\pm}$ mass eigenstates, and linear combinations of W_3 and Y become the electrically neutral Z and γ mass eigenstates. The $W^{\pm}$

and Z each absorb one of the would-be Nambu-Goldstone bosons to become the massive weakly-interacting bosons. Yukawa-type couplings enable the Higgs boson to interact with quarks and leptons, allowing both hadronic and leptonic colliders to produce interactions involving the Higgs sector of the SM.

After symmetry breaking, the electroweak sector is left with only the unbroken $U_{\mathrm{EM}}(1)$ symmetry group whose single generator is represented by the γ which does not directly interact with the Higgs boson. The photon mediates the electromagnetic (EM) interaction between all electrically charged particles through the exchange of photons. This electrically neutral boson also acts as the intermediate particle in the annihilation and creation of oppositely charged quark and lepton pairs. The weak bosons mediate the weak interaction between all the quarks and leptons through the exchange of $W^{\pm}$ and Z bosons. These bosons act as the intermediate particle for fermion transformations both across and within generations of quarks and leptons.

The Higgs boson remains as a poorly understood scalar that is studied at accelerators. The possibility of a Higgs sector more complex than the single field described by the SM is the subject of this thesis.

2.2 The Standard Model Higgs Boson

A search for a Higgs-like scalar as predicted by the SM begins with an understanding of how scalars, including the SM Higgs, are produced in high energy collisions and how their decays are subsequently observed in particle detectors. Higgs boson production processes can occur for various initial states composed of SM particles. These initial state particles are accelerated by and undergo high energy collisions at existing hadronic and leptonic particle colliders. The Higgs boson is transient: it decays very quickly and can only be observed in the final state SM particles that emerge from its decay. The final states that correspond to possible Higgs boson decay channels are used to find evidence of its existence.

2.2.1 Scalar Production Modes and Cross Sections

Since the LHC is mainly a proton-proton collider, the production modes for the Higgs boson in this study involve gluons and quarks in the initial state. By using Feynman diagrams which encode the mathematics of SM interactions into a series expansion with a graphical representation, the possible production modes for the Higgs boson at the LHC can be illustrated visually using edges to represent propagating particles and vertices to represent interactions for cross section calculations. The Higgs boson can be produced through the collision of gluons via ggH and top-associated production (ttH) modes as shown in Figures 2.1a and 2.1c, respectively. On the other hand, the Higgs boson can also be produced through the collision of quarks via Higgs-strahlung (VH) — a process where a Higgs boson is radiated off of a weak gauge boson — and vector boson fusion (VBF) modes as shown in Figures 2.1b and 2.1d, respectively. The VH production mode can be further differentiated as either Higgs-strahlung from a $W^{\pm}$ boson (WH) or Higgs-strahlung from a Z boson (ZH).

Each Higgs boson production mode is associated with a cross section σ measured in units of barns b, or equivalently $10^{-28}\,\mathrm{m}^2$, which describes the likelihood that a

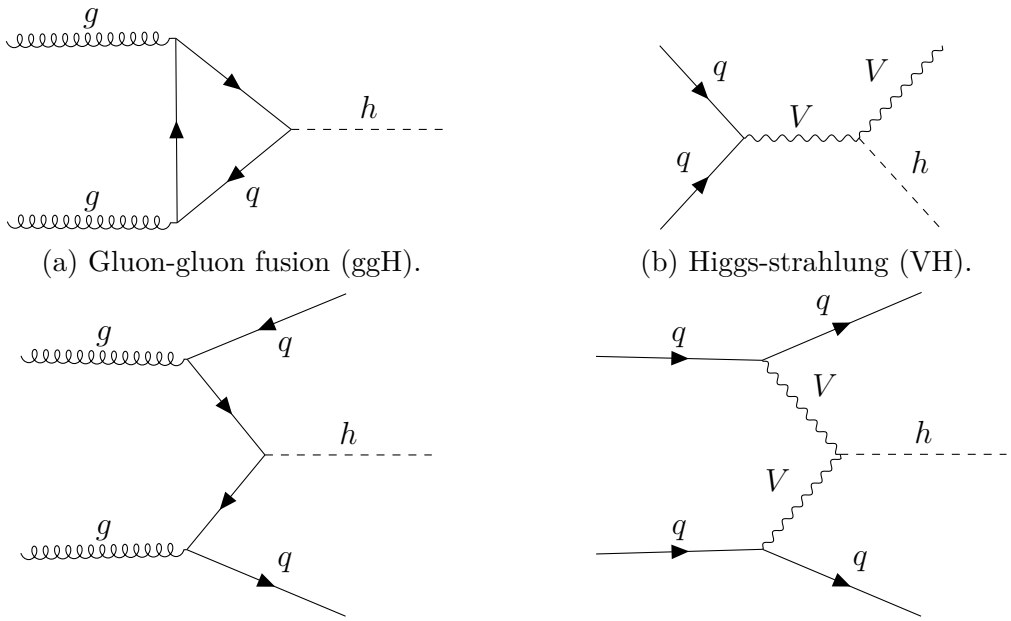

(a) Gluon-gluon fusion (ggH).

(b) Higgs-strahlung (VH).

(c) Top-associated production (ttH).

(d) Vector boson fusion (VBF).

Figure 2.1: The Feynman diagram representation of dominant Higgs boson production processes at the LHC in the lower diphoton invariant mass regime. The curly edges denote gluons g, wavy edges denote vector bosons V, straight edges with embedded arrows denote quarks q, and dashed edges denote Higgs bosons.

given process will occur. Since the cross section of a process is calculated solely from its associated Feynman diagrams with the appropriate PDFs, the cross section of a particular production mode is independent of other production modes. The cross section values for the dominant Higgs production modes shown in Figure 2.1 are calculated for the SM Higgs boson at 125 GeV/c^2 in the last row of Table 2.2 [73]. Since this analysis searches for Higgs-like particles with SM-like scalar couplings in the lower mass range, the expected cross section values at various mass points in this range are also listed.

2.2.2 Scalar Decays to Diphoton

The decay channels of the SM Higgs include dibosons and dijets in their final state. The Feynman diagrams for some of these two particle decays are illustrated in Figure 2.2. Each decay channel occupies some fraction, known as the branching fraction or

Mass [GeV]	Cross Section [pb]				
	ggH	VBF	ttH	WH	ZH
60	155.5	6.924	3.483	11.70	6.183
70	117.2	6.301	2.113	7.920	4.279
80	92.40	5.748	1.590	5.538	3.073
90	75.07	5.258	1.154	3.977	2.261
100	62.35	4.822	0.9146	2.926	1.704
110	52.68	4.434	0.6675	2.194	1.309
120	45.14	4.086	0.5598	1.679	1.024
125	41.98	3.925	0.4987	1.475	0.9095

Table 2.2: The cross section of Higgs-like production modes at $\sqrt{s} = 13\,\text{TeV}$. Values correspond to the expected cross section of the SM Higgs-like boson at various masses [73].

branching ratio, of the total number of decays. The branching ratio of two photon decay channels for a SM Higgs boson at 125 GeV/c^2 is listed in the last row of Table 2.3 [73]. The expected branching ratios of the diphoton decay at various mass points in the lower mass range are also listed for reference in this low mass range search. Despite having a relatively smaller branching ratio compared to other two particle decay channels as shown in Table 2.3, the diphoton channel provides a search channel that avoids the overwhelming hadronic SM background processes at the LHC. In fact, many studies on the SM Higgs have been done in the much "cleaner" diphoton decay channel. The diphoton channel was also one of the final states used to present the Higgs boson excess in 2012 [7] [39].

For bosonic decays of the Higgs boson, the top quark loop as shown in Figures 2.2d and 2.2e is the most dominant. However, the mass of the top quark is larger compared to that of the Higgs boson, suppressing the top quark loop interaction in favor of the weak boson loop interaction shown in Figures 2.2b and 2.2c for the Higgs boson decay. Since the Higgs boson does not directly interact with the massless photon, loop diagrams with two photon final states as shown in Figures 2.2b, 2.2c, and 2.2d are often represented as an effective three-point vertex for brevity as shown

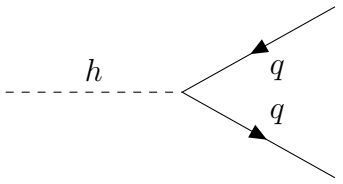

(a) Tree-level diquark decay.

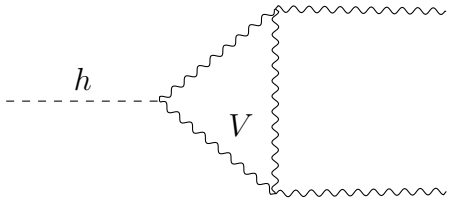

(b) Diboson decay via vector boson loop using 3-point vertices.

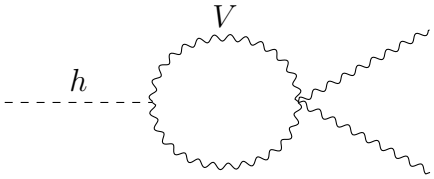

(c) Diboson decay via vector boson loop using a 4-point vertex.

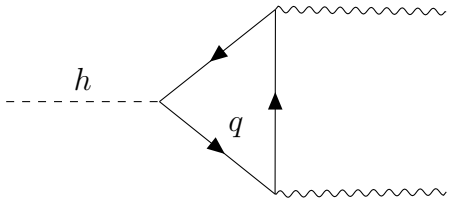

(d) Diboson decay via quark loop.

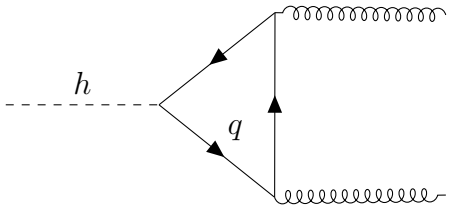

(e) Digluon decay via quark loop.

Figure 2.2: Higgs boson decay channels listed in the order of decreasing branching ratio.

Mass [GeV]	Branching Fraction		
	bb	gg	$\gamma\gamma$
60	0.8515	2.731e-2	4.849e-4
70	0.8421	3.509e-2	6.871e-4
80	0.8312	4.443e-2	9.369e-4
90	0.8185	5.511e-2	1.242e-3
100	0.7986	6.648e-2	1.602e-3
110	0.7545	7.642e-2	1.981e-3
120	0.6607	8.023e-2	2.265e-3
125	0.5907	7.820e-2	2.315e-3

Table 2.3: The branching fractions of Higgs-like decay channels. Values correspond to the expected branching fractions of the SM Higgs-like boson at various masses [73].

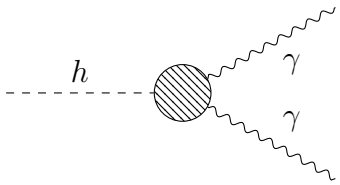

Figure 2.3: Higgs boson to diphoton diagram drawn with an abbreviated 3-point vertex.

in Figure 2.3.

2.3 The Higgs Boson Beyond the Standard Model

Although the SM only includes one Higgs scalar boson, many BSM theories allow for and predict additional Higgs-like scalar particles that interact with SM particles. Some of the more compelling models that extend the SM Higgs sector include the composite Higgs [21], axion-like particle (ALP) singlets [77], and the 2HDM [56] and its variations [25]. This section will focus on the properties and implications of the 2HDM.

2.3.1 Two Higgs Doublet Model

The 2HDM is a set of theories where a second complex scalar doublet is introduced into the Higgs sector of the SM and produces additional Higgs-like particles. This extension in its most general form leads to a scalar potential with 14 parameters that allow for possible charge-parity (CP)-conserving, CP-violating, and charge-violating properties [28]. The large number of parameters in this model gives rise to many different types of 2HDMs.

With two scalar fields Φ_1 and Φ_2, the Higgs field now has eight degrees of freedom. Spontaneously breaking the gauge symmetry of these fields produces five scalar fields and three would-be Nambu-Goldstone fields. These fields then mix to produce five scalar bosons and three would-be Nambu-Goldstone bosons which are absorbed by the $W^{\pm}$ and Z bosons to give them mass through the Higgs mechanism. The five remaining scalar bosons present themselves as a pair of charged scalars $H^{\pm}$, two neutral CP-even scalars h and H, and one CP-odd pseudoscalar A. The charged scalars and the pseudoscalar are presented here as mass eigenstates, but the two neutral scalars are not necessarily mass eigenstates. The SM Higgs boson H^{SM} mass eigenstate with a mass of approximately 125 GeV/c^2 corresponds to a potential mix

of the two neutral scalars:

$$H^{\mathrm{SM}} = h\sin(\beta-\alpha) + H\cos(\beta-\alpha) \tag{2.1}$$

where α is the mixing angle between the two neutral scalars, and β is the mixing angle between the charged scalars. The neutral CP-even BSM Higgs scalar h^{BSM} mass eigenstate is represented by the remaining orthogonal combination of H and h.

After constraining the model with discrete $\mathbb{Z}^2$ symmetries, CP conservation, and flavor-changing neutral currents (FCNC) forbiddance, the 2HDMs are reduced to four different types: type-I, type-II, X (lepton-specific), and Y (flipped). The number of parameters in the extended Higgs sector is now reduced to six: the four scalar masses $m_{H^\pm}$, m_H, m_h, and m_A, the ratio of the vacuum expectation values $\tan(\beta) = v_2/v_1$, and the mixing angle α. The types of 2HDM are characterized by how the new scalar fields interact with the up-type u^i, down-type d^i, and electron-like e^i SM particles where i indexes the generation. The descriptions of 2HDM types are summarized in Table 2.4 and provided below:

Type-I All charged fermions only couple to the second doublet in the Type-I 2HDM which follows from enforcing a $\mathbf{\Phi}_1 \to -\mathbf{\Phi}_1$ discrete symmetry.

Type-II Up-type quarks only couple to the second doublet while down-type quarks and charged leptons couple to the first doublet in the Type-II 2HDM which follows from enforcing a $\mathbf{\Phi}_1 \to -\mathbf{\Phi}_1$, $d^i \to -d^i$, $e^i \to -e^i$ discrete symmetry.

X (lepton-specific) All quarks only couple to the second doublet while charged leptons couple to the first doublet in the X 2HDM which follows from enforcing a $\mathbf{\Phi}_1 \to -\mathbf{\Phi}_1$, $e^i \to -e^i$ discrete symmetry.

2HDM Type	up-type u^i	down-type d^i	charged leptonic e^i
Type I	$\mathbf{\Phi}_2$	$\mathbf{\Phi}_2$	$\mathbf{\Phi}_2$
Type II	$\mathbf{\Phi}_2$	$\mathbf{\Phi}_1$	$\mathbf{\Phi}_1$
X (lepton-specific)	$\mathbf{\Phi}_2$	$\mathbf{\Phi}_2$	$\mathbf{\Phi}_1$
Y (flipped)	$\mathbf{\Phi}_2$	$\mathbf{\Phi}_1$	$\mathbf{\Phi}_2$

Table 2.4: The coupling between complex scalar doublets and SM particles in various 2HDM types.

Y (flipped) Up-type quarks and charged leptons only couple to the second doublet while down-type quarks couple to the first doublet in the Y 2HDM which follows from enforcing a $\mathbf{\Phi}_1 \to -\mathbf{\Phi}_1$, $d^i \to -d^i$ discrete symmetry.

2.3.2 Production and Decay of the Higgs in Type-I 2HDM

The Type-I 2HDM establishes the same coupling strengths between the SM particles and both CP-even Higgs scalars up to a multiplicative factor. Under certain circumstances in the 2HDM, the decay of the BSM Higgs scalar to diphotons has a large branching fraction. Thus, this thesis will focus on the the production of a BSM Higgs boson in the Type-I 2HDM via proton-proton (pp) collisions and its decay to two photons.

The coupling constant for each of the two Higgs scalars with gauge bosons (V) and fermions (u, d, l) are functions of the mixing angles α and β:

$$\xi_h^{u,d,l} = \frac{\cos\alpha}{\sin\beta} \tag{2.2}$$

$$\xi_h^V = \sin(\beta - \alpha) \tag{2.3}$$

$$\xi_H^{u,d,l} = \frac{\sin\alpha}{\sin\beta} \tag{2.4}$$

$$\xi_H^V = \cos(\beta - \alpha) \tag{2.5}$$

In the limit where $\alpha \to \beta$, the coupling of H to SM bosons and fermions match that of the SM Higgs boson exactly as shown by Equation 2.1. The scalar h is described

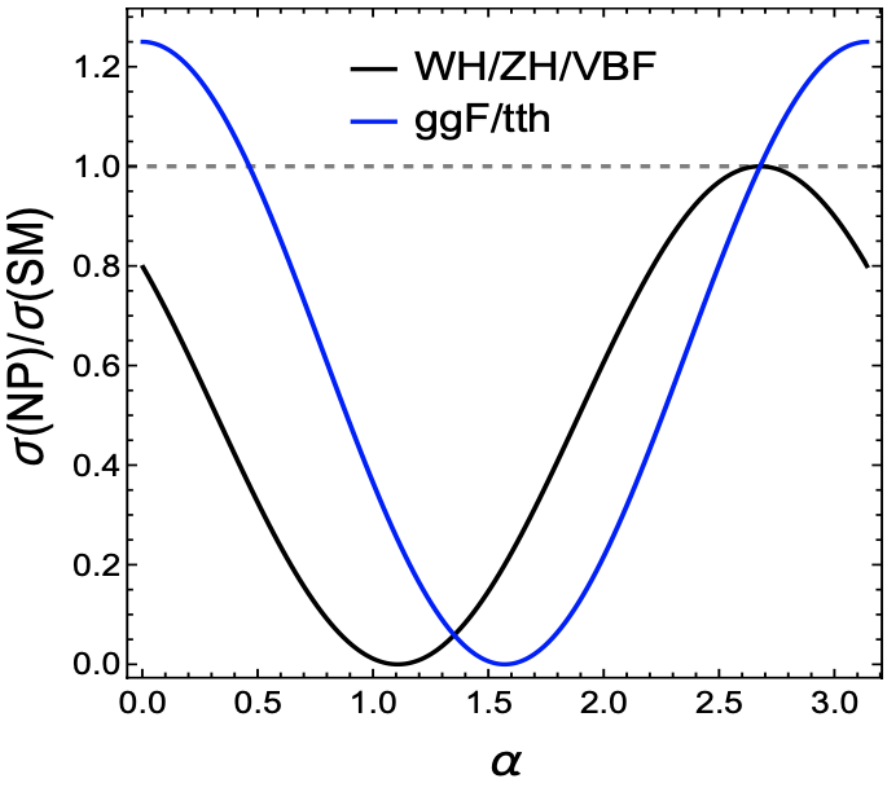

Figure 2.4: The cross section of the BSM (here labeled as NP), Higgs scalar relative to that of the SM Higgs boson. The curves are based on a scalar mass of $m_h = 80\,\text{GeV}$ and a mixing angle of $\tan\beta = 2$ [24].

as fermiophilic since the scaling factor for bosonic coupling vanishes (Equation 2.3). This limit is known as the alignment limit and results in a relatively inert second Higgs doublet $\mathbf{\Phi}_2$ where the coupling between the BSM Higgs scalar and the SM particles is restricted to only fermions. As a result, the VH and VBF production modes become suppressed, and the ggH and ttH modes become more promising modes to explore as indicated by Figure 2.4 at $\alpha = \beta \approx 1.11$.

On the other hand, in the limit where $\alpha \to \pi/2$, the scaling factor for the tree-level coupling of h to SM fermions vanishes (Equation 2.2). This limit is known as the fermiophobic limit where the ggH and ttH modes are now suppressed in favor of the VH and VBF modes. The decay channels of h now show fermionic suppression and cause the diphoton decay channel to become dominant as shown in Figure 2.5.

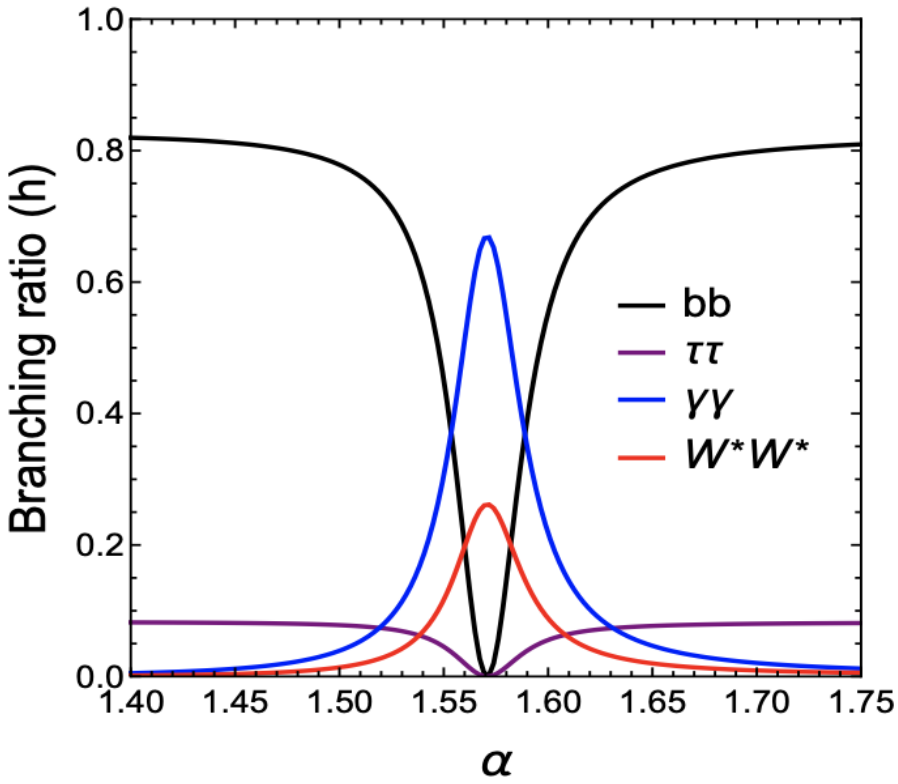

Figure 2.5: Branching ratios of the BSM Higgs scalar. The curves are based on a scalar mass of $m_h = 80\,\text{GeV}$ and a mixing angle of $\tan\beta = 2$ [24].

2.3.3 BSM Higgs in Recent Experimental Searches

Past studies performed by the Large Electron-Positron collider (LEP) [91], ATLAS [42] [55], and CMS [46] [47] collaborations have set some constraints on the existence of new light scalars. These limits are expressed as constraints on the (α, β) parameter space at a given mass. The upper limits on the cross section for the BSM Higgs scalar from direct and inclusive searches have constrained the mixing angle parameter space to regions near the alignment limit and ruled out some narrow regions at the fermiophobic limit as shown in Figure 2.6. However, large regions of parameter space still remain to be explored.

Interestingly, the CMS cross section limits on a BSM Higgs-like scalar in the two photon decay channel have shown a slight excess with respect to the SM prediction [47]. Their results from using the LHC early Run-2 dataset produce the excess at a mass of approximately 95.3 GeV/c^2 with a local significance of 2.8 standard deviations[1] as shown in Figure 2.7. The need to follow up on this experimental observation further motivates the search presented in this thesis. The rest of this thesis will detail the methods, procedures, and results of a Higgs-like scalar resonance search in the diphoton invariant mass regime between 66 – 110 GeV/c^2 using the full LHC Run-2 dataset. The lower bound of 66 GeV/c^2 is motivated by avoidance of the "turn-on" region due to the online trigger used in the data collection as described later in Section 6. The upper bound of 110 GeV/c^2 allows the search to use techniques that are optimized for characterizing shape features and background processes found in the range below the SM Higgs mass at $m_{\text{SM Higgs}} \approx 125$ GeV/c^2. Scalar searches at ranges below [85] and above [83] the mass regime of 66 – 110 GeV/c^2 are also performed using their respective set of specialized techniques, but the methodology and results of those searches will not be discussed in this thesis.

[1] CMS has recently released a new measurement in March 2023 with a somewhat weaker significance [48].

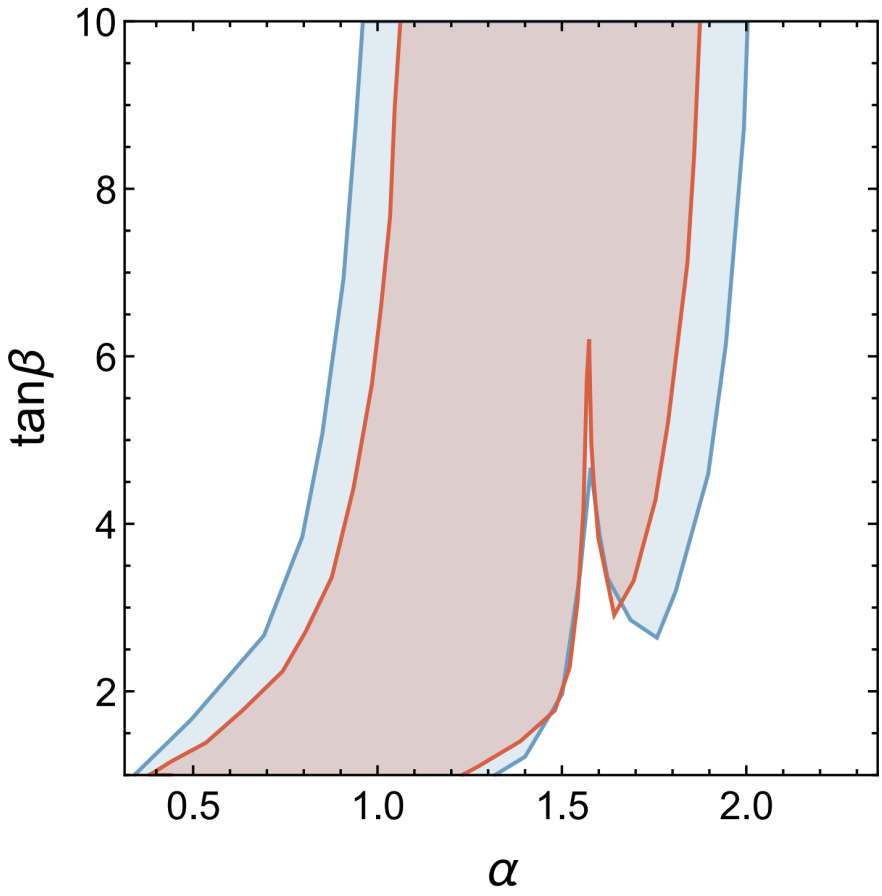

Figure 2.6: Allowed (α, β) parameter space for the BSM Higgs scalar after combining the measurements from Higgs signal strength and the results from direct searches for light scalar at LEP and LHC [24]. The allowable regions for potential scalars of mass $m_h = 90\,\text{GeV}$ and $100\,\text{GeV}$ are colored by the red and blue bands, respectively.

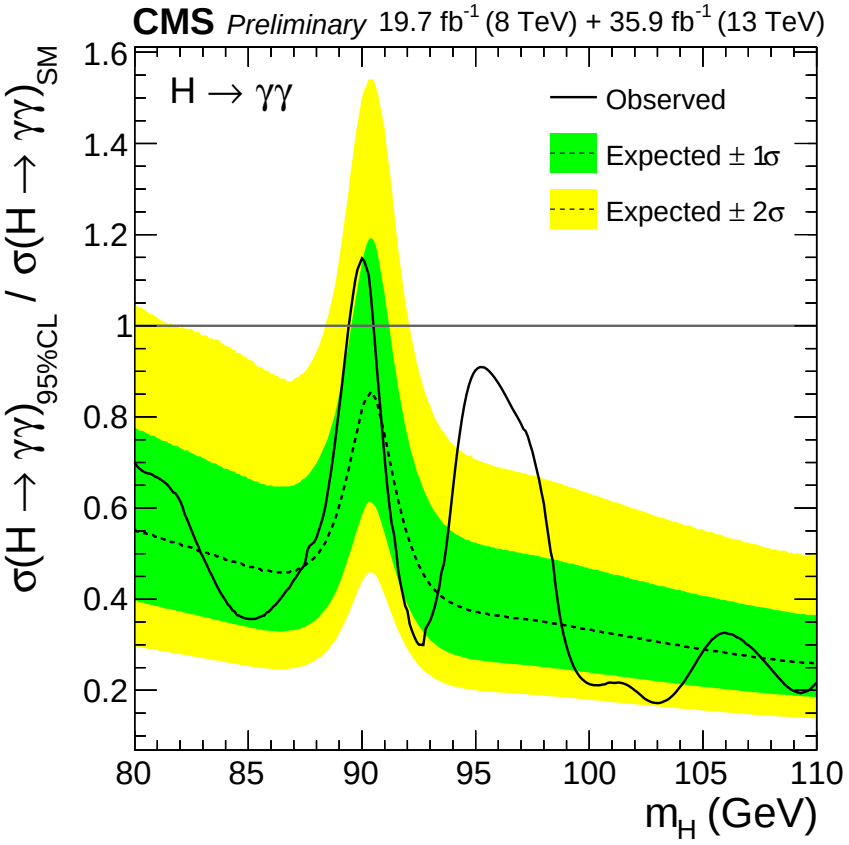

Figure 2.7: The expected and observed exclusion limits (95% CL) from CMS on the production cross section times branching ratio into two photons for a BSM Higgs boson relative to the expected SM Higgs boson using both Run 1 and early Run 2 datasets from the LHC [47]. The inner (green) and the outer (yellow) band indicate the regions containing 68% and 95% respectively, of the distribution of limits expected under the SM background-only hypothesis.

Henceforth, H will be used to represent the SM Higgs boson, and h and X will be used interchangeably to represent the BSM Higgs-like scalar. Additionally, we will set $c = 1$ such that the units of mass and energy will both be expressed in GeV for brevity.

CHAPTER III

Experimental Apparatus

The experimental apparatus used for high energy particle physics has seen great strides in innovation and improvement in measurement accuracy since the first cyclotron invented at the University of California, Berkeley in the 1930s [70]. Not only has the development of particle accelerators led to a better understanding of particle physics, but they also have seen remarkable applications in the nuclear medical field as particle sources for radiation therapy [93], in the biochemistry field as light sources for crystallography [102], and in the applied materials field as ion implantation beams for semi-conductor manufacturing [88].

The large and steady increase in beam energies and improvement in detector technology allows proton collisions to occur at a center-of-mass energy of $\sqrt{s} = 13$ TeV at the the European Organization for Nuclear Research (CERN) LHC and to be studied using the sophisticated ATLAS detector. The multiple subsystems used by the LHC to accelerate protons to high energy are outlined in Section 3.1. The luminosity — a measure of the particle interaction rate — of the proton beam as well as the bunch structure of the beam will be described. The ATLAS detector components and how they operate in order to collect precision measurements on high energy particles are detailed in Section 3.2.

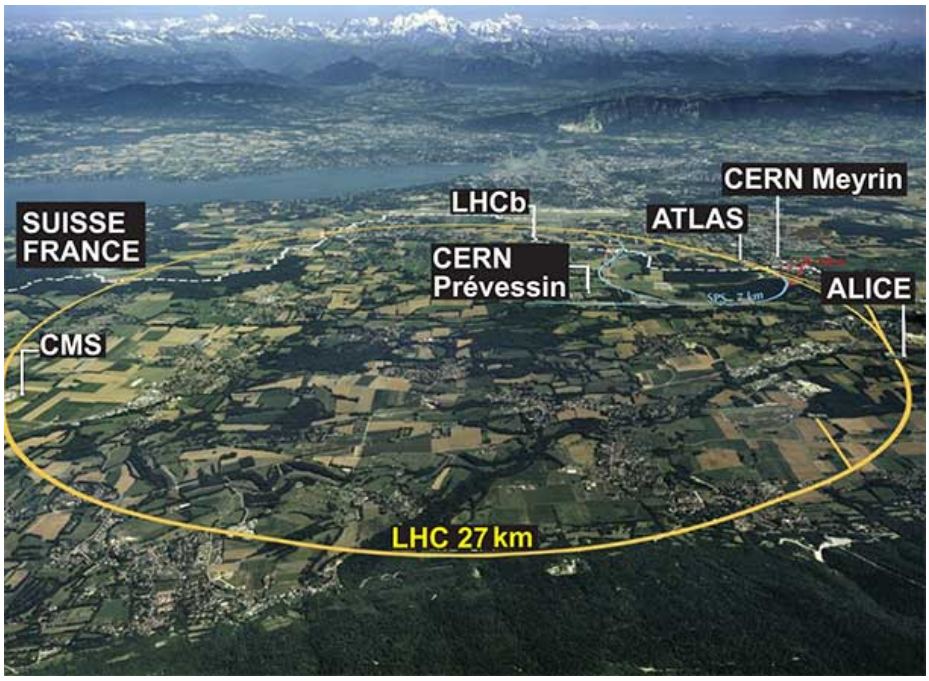

Figure 3.1: An aerial view of the LHC on the border of France and Switzerland [29].

3.1 The Large Hadron Collider

Designed and approved in the 1990s and built in the 2000s, the LHC is the largest and highest energy particle accelerator in the world as of 2023. The underground tunnel, originally used for the LEP collider in the 1990s, now houses the main 2.8 m wide LHC beam pipe rings that span 27 km in circumference [72]. This ring is located 125 m below the surface of the Earth in Switzerland and France as shown in Figure 3.1.

The main ring consists of approximately 1200 dipole magnets that keep the proton beams on their circular path and approximately 400 quadrupole magnets that keep the beam focused [89]. Additional high order multipole magnets are used near the intersection points to focus the beam further for collision and throughout the main ring to correct for magnetic field imperfections. Normal-conducting radio-frequency (NRF) cavities are used throughout the ring to accelerate each counter-rotating proton beam to 6.5 TeV.

3.1.1 Proton Accelerator Chain

The protons are first prepared by a series of smaller accelerators that successively increase the energy of the particles before their injection into the main ring [31]. The the 4th generation linear accelerator (LINAC4) generates negative hydrogen ions composed of one proton and two electrons and accelerates them to an energy of 160 MeV [51]. The ions are then fed to the Proton Synchrotron Booster (PSB) where the electrons are stripped and the remaining protons are accelerated to 2 GeV [78]. The protons are then injected into the Proton Synchrotron (PS) to be accelerated to 26 GeV and into the Super Proton Synchrotron (SPS) to a penultimate energy of 450 GeV [31]. Finally, the protons are injected into the main LHC ring and accelerated to 6.5 TeV for each of the two counter-rotating beams.

The entire process starting from the LINAC4 and ending with the final injection into the main ring as illustrated in Figure 3.2 takes place over a period of several minutes. Once in the main LHC ring, the protons are accumulated into bunches, accelerated to their peak energy over a period of 20 minutes, and circulated up to 24 hours for proton collisions at four intersection points. Each of the two counter-rotating beams consists of up to 2808 proton bunches [20]. Bunch crossings between the two proton beams occur at 25 ns intervals. The large number of protons in each bunch, approximately 10^{11} protons, will lead to multiple particle collisions (pileup) during each bunch crossing. The interaction pileup μ ranges in $10 - 65$ interactions per bunch crossing with an average of $\langle\mu\rangle = 33.7$ pp interactions per crossing during the entirety of Run 2 [17].

Each beam crossing point houses an experiment and its detector: ATLAS [40], CMS [38], the LHC-beauty experiment (LHCb) [74], and A Large Ion Collider Experiment (ALICE) [2]. Five smaller experiments — the TOTal Elastic and diffractive cross section Measurement experiment (TOTEM) [99], the Monopole and Exotics Detector At the LHC (MoEDAL) [81], the LHC-forward experiment (LHCf) [75],

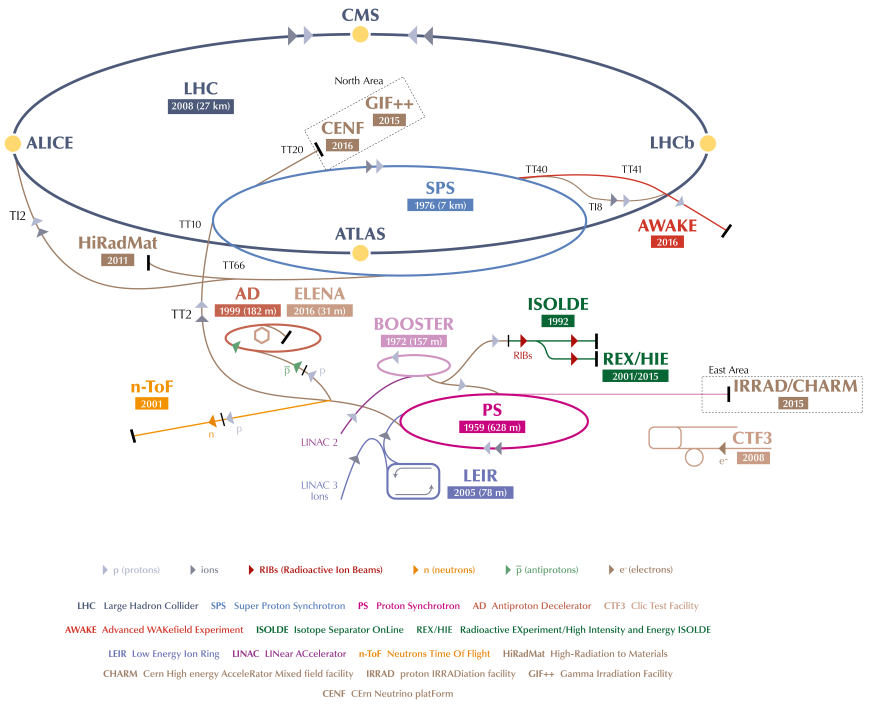

Figure 3.2: A diagram of the accelerator complex at CERN [80]. Protons are first accelerated in the LINAC2 (now replaced by LINAC4) and subsequently boosted by the PSB (here labeled as Booster), the PS, and the SPS before finally being injected into the main LHC ring.

the Scattering and Neutrino Detector (SND) [97], and the ForwArd Search ExpeRiment (FASER) [53] — are designed for specific SM measurements and BSM searches.

3.1.2 Energy and Luminosity

As mentioned in Section 2.2.1, the likelihood of two particles undergoing elastic or inelastic scattering can be characterized by the cross section σ of the interaction. With a given interaction cross section, the rate of collisions at the collider is given by

$$R = L(t) \cdot \sigma \tag{3.1}$$

where $L(t)$ is the instantaneous luminosity which measures the number of particles that an accelerator can send through a cross sectional unit as a function of time. The total number of collisions delivered by an accelerator is then given by

$$N_{\text{collisions}} = \sigma \cdot L_{\text{int}} = \sigma \cdot \int L(t)\ dt \tag{3.2}$$

where L_{int} is the integrated luminosity in units of inverse cross section representing the ratio between the number of collisions and the interaction cross section. The processes of interest in this study have very small cross sections on the order of 1 femtobarn (fb) which is equivalent to $10^{-39}\,\text{cm}^2$. To observe one such interaction would require an integrated luminosity of $10^{39}\,\text{cm}^{-2}$ or, equivalently and more conveniently, 1 inverse femtobarn (fb^{-1}).

In Run 2, the two beams were maintained at a center of mass energy of $\sqrt{s} =$ 6.5 TeV each for a total of $\sqrt{s} = 13$ TeV. An average instantaneous luminosity of $L = 1 \times 10^{34}\,\text{cm}^{-2}\,\text{s}^{-1}$ during operation and a total integrated luminosity of $\int L = 140.1\,\text{fb}^{-1}$ was provided by the LHC during the data-taking periods of 2015 – 2018 [17]. Further upgrades from Long Shutdown 2 (LS2) after Run 2 increased the total center of mass energy to $\sqrt{s} = 13.6$ TeV and an instantaneous luminosity of $2 - 3 \times$

$10^{34}\,\mathrm{cm}^{-2}\,\mathrm{s}^{-1}$ for Run 3 currently underway [37].

3.2 The ATLAS Detector

As a general-purpose particle detector, the ATLAS experiment as shown in Figure 3.3 is able to detect elementary particles and collect data from the pp collisions provided by the LHC [40]. The detector is designed to reconstruct a large portion of each collision outcome, including the mass, momentum, energy, and charge of each particle streaming from a single interaction event. After data collection and collision event quality control is performed, an integrated luminosity of $\int L\, dt = 139.4\,\text{fb}^{-1}$ is available from Run 2 to be used in the search for a diphoton resonance [17].

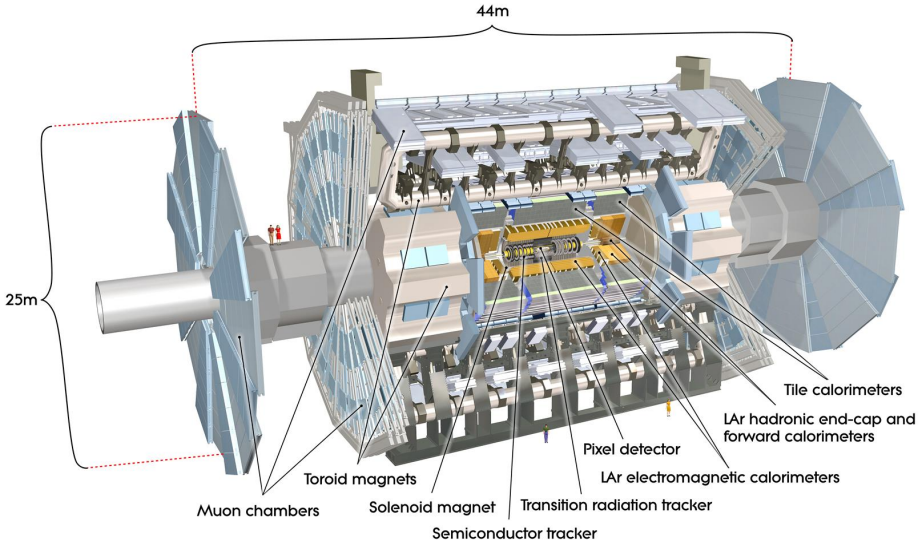

Figure 3.3: A cut-away representation of the particle trackers and detectors in the ATLAS detector [40].

3.2.1 Coordinate System and Kinematic Description

A coordinate system must first be established for the ATLAS detector to provide a frame of reference for the measurements on the detected particles. The Cartesian coordinate system for the detector is defined such that the positive x-axis points towards the center of the main LHC ring, the positive y-axis points upwards towards the surface of the Earth, and the positive z-axis points along the counter-clockwise

direction of the LHC beam path when viewed from above the ground. The A side of the detector is defined to be the side with positive z while the C side is with negative z.

With the z-axis along the beam path, the azimuthal angle ϕ is measured around the beam axis and the polar angle is measured from the beam axis. In pp collisions, it is convenient to redefine the polar angle θ as pseudorapidity η:

$$\eta \equiv -\ln\left[\tan\left(\frac{\theta}{2}\right)\right]. \tag{3.3}$$

The ATLAS detector is sensitive over the range $|\eta| < 3.2$ corresponding to $\theta \in [0.08148, \pi - 0.08148]$ [40].

Several measurements are made in the plane perpendicular to the beam axis, such as transverse mass m_{T}, transverse momentum p_{T}, and transverse energy E_{T}. These transverse quantities play an important role in the analysis of data collected at particle beam colliders since the component of any measurement along the beamline can be attributed to the residual movement of the particles in the z direction while the transverse components are always associated with the particle interaction. The angular distance ΔR in the pseudorapidity-azimuthal angle space is defined as

$$\Delta R = \sqrt{\Delta\eta^2 + \Delta\phi^2}. \tag{3.4}$$

3.2.2 Solenoid and Toroidal Magnets

Several particle detection systems use magnetic spectroscopy to measure particle momentum. The magnet system consists of four components as shown in Figure 3.4: the inner solenoid, the barrel toriodal magnets, and the two sets of endcap toroidal magnets. The solenoid bends the trajectory of charged particles as they traverse the tracking systems before reaching the EM and hadronic calorimeters. The toroidal

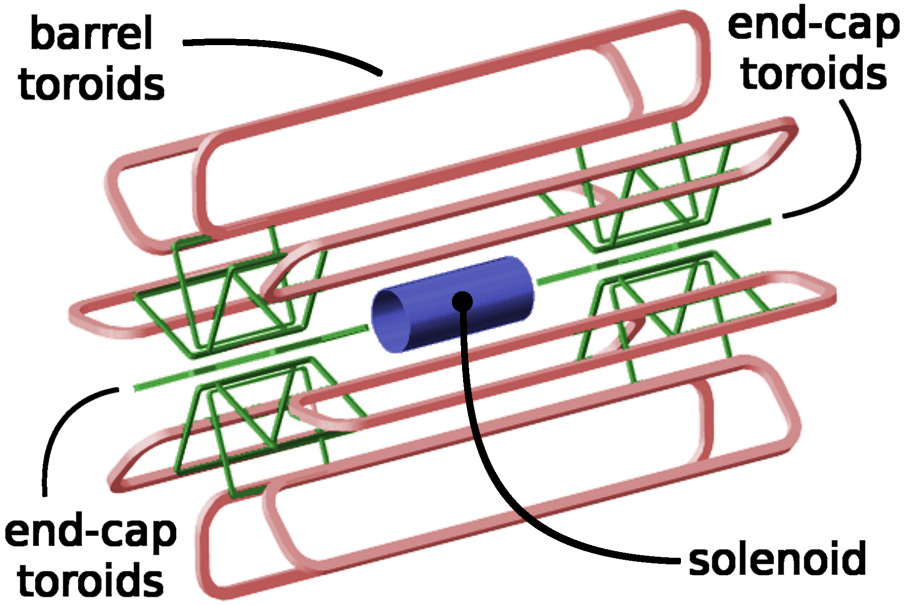

Figure 3.4: A diagram of the two magnet systems in the ATLAS detector: the solenoid and the outer toroidal magnets. The scale of this diagram matches that of Figure 3.3.

magnets work together with the solenoid to bend the trajectory of muons as they are tracked through the muon spectrometer.

The solenoid surrounds the inner detector and produces a 2 T magnetic field [40]. This system measures 5.8 m in length and 2.5 m in diameter with a thickness of 0.1 m. Its thickness is minimized so the subsequent calorimeter thickness can be optimized to achieve the desired calorimeter performance.

The three toroidal magnet systems lie outside the calorimeters and contain the muon system described in Section 3.2.5. The eight large superconducting barrel loops and two sets of eight end-cap magnets produce a non-uniform magnetic field strength that varies between $2 - 4$ T for bending muon trajectories. The entire barrel magnet system measures 25.3 m in length with an inner diameter of 9.4 m and outer diameter of 20.1 m. Each of the endcap magnet system measures 5.0 m in length with an inner diameter of 1.65 m and outer diameter of 10.7 m.

3.2.3 Inner Tracking Detectors

The inner tracking detectors make precise measurements on the locations of charged particles when they first emerge from the *pp* collision in order to reconstruct their trajectories and momenta. These measurements also help locate potential vertices where photons from the collisions convert to charged particles.

The inner detector is a concentric cylindrical series of detectors and trackers consisting of three layers as shown in Figure 3.5: the pixel detector, the semi-conductor tracker (SCT), and the transition radiation tracker (TRT), listed in the order of increasing radial distance from the beam pipe at $R = 0$. The detector spans a length of 3.5 m and a diameter of 2.3 m.

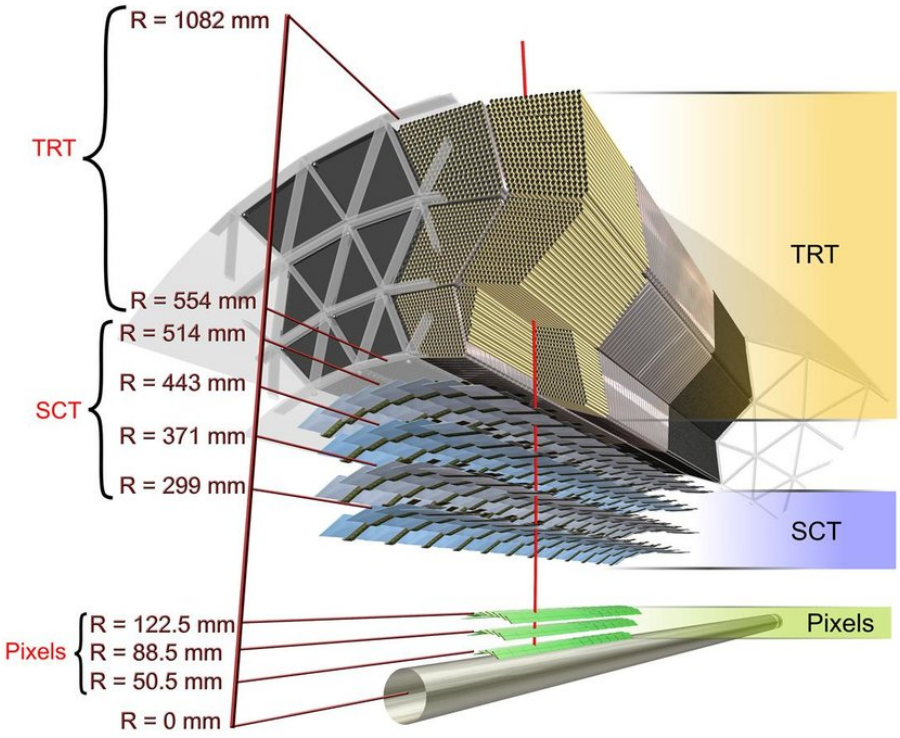

Figure 3.5: A cross-sectional diagram of the inner detector in the ATLAS detector with its three main components: the pixel detector, the SCT, and the TRT.

The pixel detector has three concentric barrel layers and three end-cap disks [40]. Each layer is composed of oxygenated n-type silicon wafer detecting material measuring 250 µm thick and contains 1744 modules of size 2 cm × 6 cm with around 47000 pixels of size 50 µm × 400 µm and around 5000 pixels of size 50 µm × 600 µm per module. The entire pixel detector has > 80 million readout channels, making up over half of the total readout of the ATLAS detector. The pixel detector achieves resolutions of 10 µm in the $R-\phi$ direction for each barrel layer and end-cap disk as well as 115 µm in the z direction for each barrel layer and in the R direction for each end-cap disk.

The SCT contains four double layers of silicon strips of size 80 µm × 12 cm totalling 6.3 million readout channels [40]. This precision tracking system achieves resolutions of 17 µm in the $r-\phi$ direction for each barrel layer and end-cap disk as well as 580 µm in the z direction for each barrel layer and in the r direction for each end-cap disk.

The TRT contains approximately 3×10^5 drift tubes (also known as straws) each measuring 4 mm in diameter and up to 144 cm in length [40]. Each straw is filled with an ionizing gas mixture composed of xenon and argon with a high voltage axial wire. This tracking system achieves resolutions of 130 µm for each barrel layer and end-cap disk.

3.2.4 Electromagnetic and Hadronic Calorimeters

The calorimeter system consists of an EM calorimeter and a hadronic calorimeter (HCal) as shown in Figure 3.6. These calorimeters are designed to stop the particles such that most of their energy is deposited into these detectors. The first calorimeter is sensitive to electrons and photons, both of which can result from the decay of particles ejected from the hadronic collision. The latter calorimeter is sensitive to the heavier particles that result from hadronization and hadronic jets.

Both calorimeters are sampling calorimeters where alternating layers of absorbing material and active medium induce the showering of particles and sample the energy

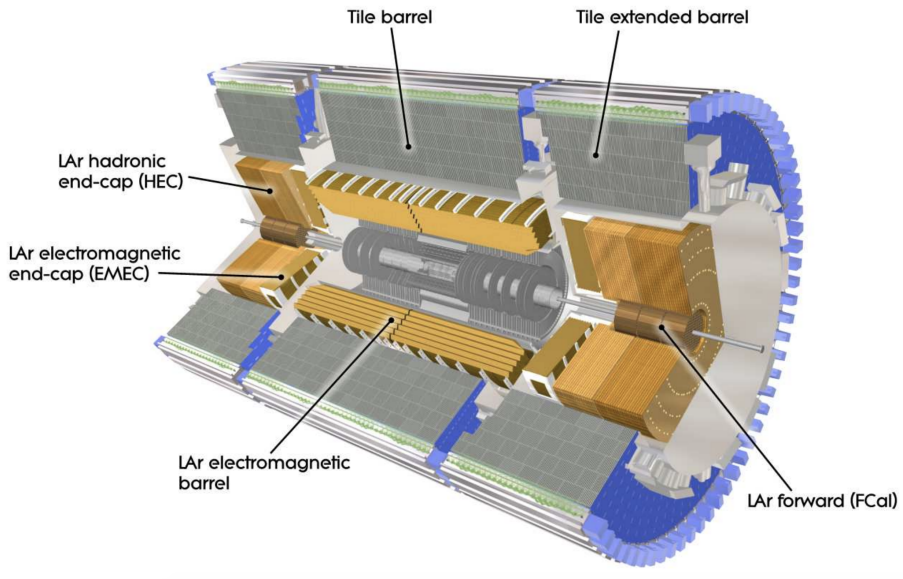

Figure 3.6: A cut-away representation of the EM and hadronic calorimeter in the barrel region of the ATLAS detector.

of the resulting particle showers, respectively, to provide energy measurements. Each calorimeter system is composed of a barrel and an end-cap on each side, and both systems have full azimuthal symmetry and coverage around the beam axis.

Electromagnetic calorimeter In the EM calorimeter, material is placed in the path of charged particles and photons to facilitate bremsstrahlung — the radiation of photons from high-energy charged particles — and e^+e^- pair production from high-energy photons. The culmination of these interactions produces a shower of EM particles within the calorimeter. The number of particles in the shower is detected in the active medium and is proportional to the shower energy. The EM calorimeter is composed of lead and steel accordion shaped electrode cells with liquid argon (LAr) in the intermediate spacing of the plates as shown in Figure 3.7 [40]. The dense material is used for its short EM radiation lengths to increase the possibility of creating EM showers, and the LAr is used as the active medium to measure the energy deposited in the shower. The calorimeter has a pseudorapidity coverage of $0 < |\eta| < 1.52$ for the barrel part and of $1.37 < |\eta| < 3.2$ for the two end-caps.

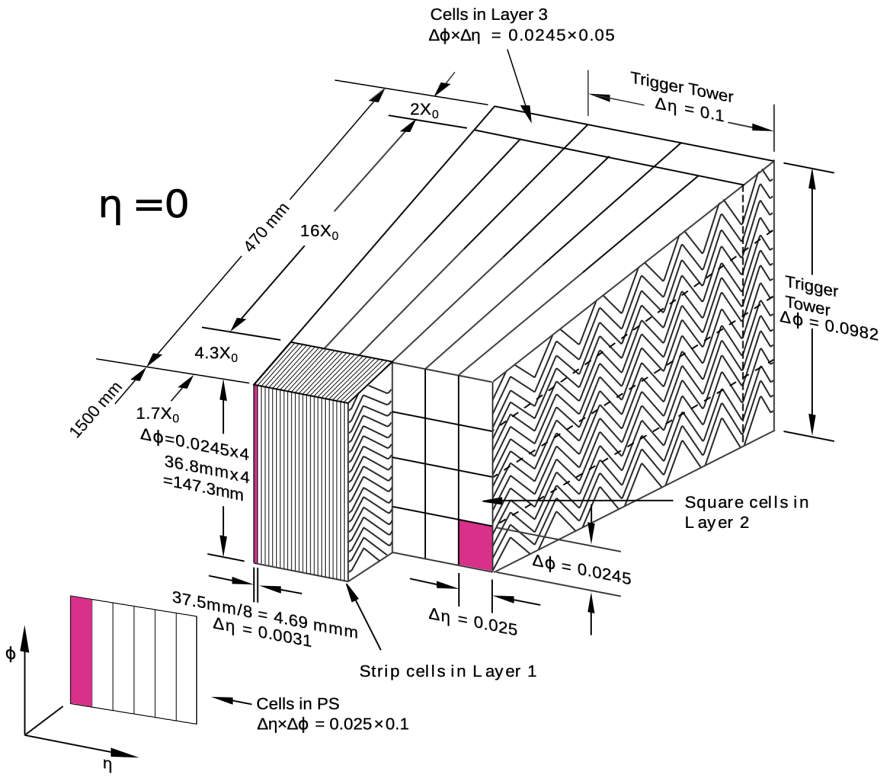

Figure 3.7: A cross-sectional diagram of the EM calorimeter in the ATLAS detector.

The EM calorimeter is designed with high spatial and energy resolution. The barrel part of the EM calorimeter is made up of two half-barrels where each half is divided into 16 equal sectors in the ϕ direction and contains a total of 1024 accordion-shaped absorbers interleaved with readout electrodes running parallel in the axial direction and stacked azimuthally. Each module has three layers of cells in the radial direction with a total thickness of $22X_0 - 30X_0$ between $0 < |\eta| < 0.8$ and of $24X_0 - 33X_0$ between $0.8 < |\eta| < 1.3$ where X_0 is one radiation length. The angular resolutions of the barrel region of the calorimeter are $\Delta\eta = 0.003 - 0.075$ and $\Delta\phi = 0.025 - 0.1$.

The end-cap of EM calorimeter is made up of eight wedge-shaped modules and contains 256 absorbers in the inner wheel and 768 absorbers interleaved with readout electrodes in the outer wheel running parallel in the radial direction and stacked azimuthally. Each wedge has a total thickness of $24X_0 - 38X_0$ between $1.475 < |\eta| < 2.5$ for the outer wheel and of $26X_0 - 36X_0$ between $2.5 < |\eta| < 3.2$ for the inner wheel. The angular resolutions of the end-caps of the calorimeter are $\Delta\eta = 0.003 - 0.1$ and $\Delta\phi = 0.025 - 0.1$. The energy resolution of the entire EM calorimeter is $\Delta E/E = 0.10/\sqrt{E} \pm 0.007$. For a 50 GeV photon typical of this search, the resolution is approximately 1 GeV.

Hadronic calorimeter The HCal is placed after the EM calorimeter to measure the energy of penetrating hadrons and hadronic jets. Different types of absorbing material and active medium are used to stop these heavier hadronic particles through inelastic nuclear interactions and to sample their energy depending on the η region.

The HCal is composed of three parts: a central barrel tile calorimeter with two extended barrels, the LAr Hadronic End-cap Calorimeter (HEC), and the LAr Forward Calorimeter (FCal) as shown in Figure 3.6 [40]. This calorimeter has a pseudorapidity coverage of $|\eta| < 1.7$ for the entire barrel system, of $1.5 < |\eta| < 3.2$ for the HEC, and of $3.1 < |\eta| < 4.9$ for the FCal. The central and extended barrel part of

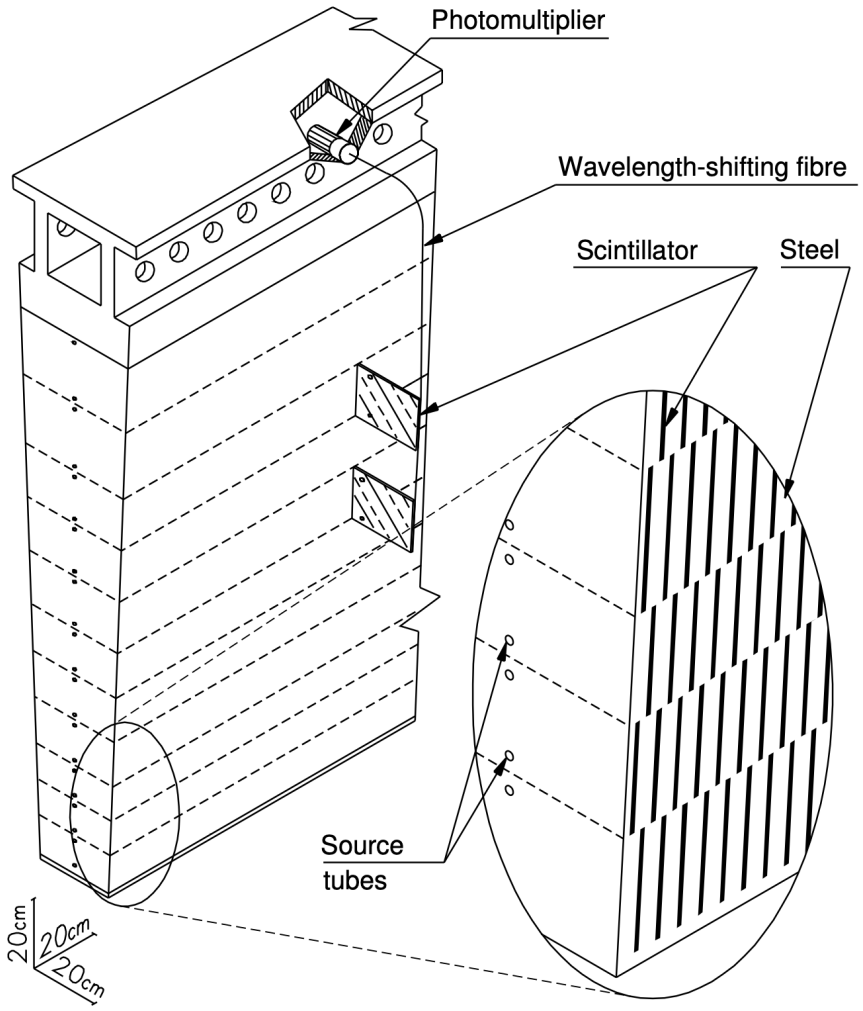

Figure 3.8: A cross-sectional diagram of the hadronic calorimeter in the ATLAS detector.

the hadronic calorimeter is divided into 64 wedges and is composed of steel as the absorbing material with plastic scintillating tiles for the active material as shown in Figure 3.8. The signals collected by the scintillating tiles travel to their respective photomultiplier tube (PMT) at the outer surface of the barrel where it is further processed by readout electronics. Each wedge is radially segmented into three layers with a total thickness of approximately 7.4λ where λ is one nuclear interaction length. The angular resolutions of the barrel region of the calorimeter are $\Delta\eta = \Delta\phi = 0.1$.

Each side of the HEC is made up of two independent wheels each with 32 wedge-shaped modules composed of copper plates stacked longitudinally as the absorbing material and LAr gaps interleaved between each plate to serve as the active medium. The inner wheels are composed of 24 copper plates each 25 mm thick, and the outer wheels are composed of 16 plates each 50 mm thick. The angular resolution of the HEC is $\Delta\eta = \Delta\phi = 0.1 - 0.2$.

The FCal sits at the axial center of the HEC. This part of the hadronic calorimeter not only provides additional pseudorapidity coverage for the hadronic calorimeter, but it also reduces the background radiation levels in the forward regions of the muon spectrometer. Each side is longitudinally split into three modules: one EM module (FCal1) made with copper plates and two hadronic modules (FCal2 and FCal3) made with tungsten plates. Each module consists of a metal matrix with longitudinal channels for concentric tubes and electrode rods. LAr fills the gaps in the channels and serves as the active medium. The spatial resolutions of the FCal are $\Delta x = 0.75 - 5.4\,\text{cm}$ and $\Delta y = 0.65 - 4.7\,\text{cm}$ depending on the FCal module.

The two calorimeter systems provide good containment of EM and hadronic showers and prevents these types of particles from reaching the muon system. The fine granularity of the EM calorimeter allows for precision measurements of electrons and photons while the thickness of the hadronic calorimeters ensures sufficient hadronic jet reconstruction crucial for BSM particle searches.

3.2.5 Muon Spectrometer

To detect and measure muons in the central and forward regions of the ATLAS detector, the muon spectrometer consists of a central barrel composed of Resistive Plate Chamber (RPC) and Monitored Drift Tube (MDT) modules and end-cap detectors composed of Thin Gap Chamber (TGC), Cathode Strip Chamber (CSC), and MDT modules as shown in Figure 3.9. Similar to the function of the inner detector,

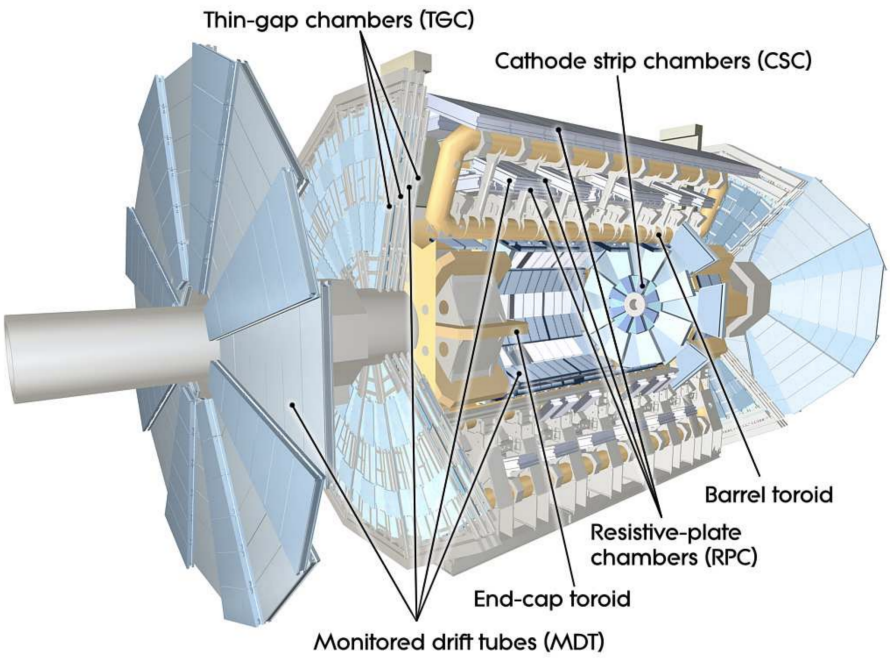

Figure 3.9: A cut-away view of the entire muon system in the ATLAS detector.

this system detects the curved tracks of high-energy muons through the magnetic field and measures their momentum. Muons do not play a role in the scalar search in the diphoton decay channel. Additional information on the muon spectrometer is presented in Appendix 10, including information on my contributions to the muon spectrometer upgrade.

3.2.6 Trigger System

Due to both the high frequency of proton collisions and the number of simultaneous collisions at each bunch crossing provided by the LHC, recording all of the data processed by the ATLAS detector electronics is an impossible task. In order to reduce the actual data recorded to a manageable level, a trigger system is used to flag the most interesting events and read out only these measurements. This system makes rapid decisions in real time. The ATLAS detector trigger system consists of the Level-1 (L1) trigger, Level-2 (L2) trigger, and event filter where the latter two

form the High Level Trigger (HLT) [40]. Together with the data acquisition (DAQ) system, the trigger system aims to select only events of interest to be recorded into permanent storage.

The L1 trigger uses information from the RPC and TGC systems of the muon spectrometer to find hadronically decaying high-p_{T} muons. It also uses all of the information from the calorimeter sub-systems to find EM clusters, $E_{\mathrm{T}}^{\mathrm{miss}}$, and large total E_{T} typically associated with hadronically decaying electrons, photons, jets, and τ-leptons. The maximum acceptance rate for the L1 trigger to record an interaction is 75 - 100 kHz. This frequency limit allows a decision to be made within 2.5 µs after a bunch-crossing has occurred.

The L2 trigger is seeded by regions-of-interest in the η and ϕ direction identified by the L1 trigger as regions possibly containing trigger objects within a given event. By using only information on coordinates, energy, and signature types, this trigger limits the amount of data transferred from the detector readout and reduces the event rate below 3.5 kHz with an average event processing time of approximately 40 ms. The event filter then uses offline analysis procedures to reduce the event rate further to approximately 200 Hz with an average event processing time on the order of 4 s for subsequent offline analysis. The HLT algorithms uses the full granularity and precision of the calorimeters, muon spectrometer, and inner tracker to refine trigger selections through improved energy threshold cuts and enhanced particle identification.

3.2.7 Forward Detectors

Two smaller sets of detectors supplement the main ATLAS energy and track detector systems described previously and are placed further away from the interaction point (IP) along the beamline. These systems seek to provide absolute and relative luminosity information by covering the very forward regions on either side of the

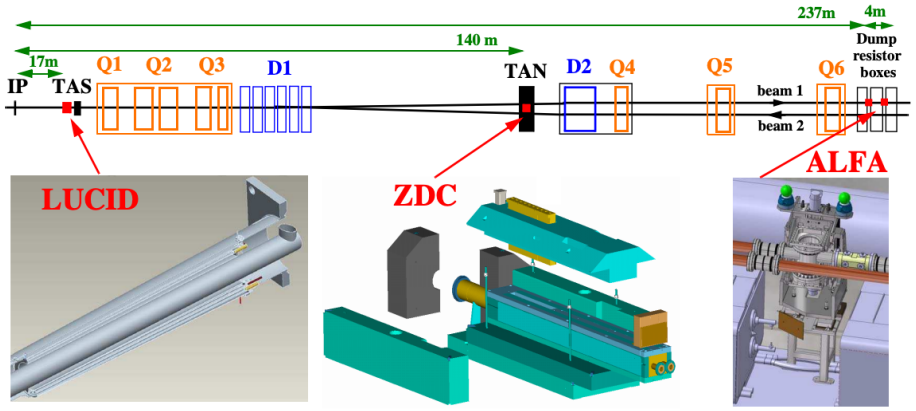

Figure 3.10: The placement of the three main forward detectors (LUCID, ZDC, and ALFA) along the beamline on either side of the IP. The locations of the LHC dipole and quadrupole magnets along with the ATLAS TAS and TAN collimators are also shown for positional reference.

detector as shown in Figure 3.10.

LUCID The first luminosity system is the the LUminosity measurement using Cerenkov Integrating Detector (LUCID) system located 17 m from the IP. It is placed near the Target Absorber Secondary (TAS) collimator which protects the LHC quadrupole magnets from radiation due to collisions at the IP. The LUCID system consists of twenty aluminum Cerenkov tubes that surround the beam-pipe and point towards the IP to detect pp scattering in the forward direction. At the LHC design luminosity, bunch-crossings will usually result in multiple pp interactions, and the number of interactions per bunch-crossing can be used to determine the luminosity. LUCID is based on the principle that the number of interactions in a bunch-crossing is proportional to the number of particles detected. Thus, not only can the signal amplitude from the PMT in each Cerenkov tube be used to distinguish the number of particles per tube, but the fast timing response of the electronics can also provides unambiguous measurements of individual bunch-crossings. As a relative luminosity detector, the LUCID system can assist in the measurement of the integrated luminosity as well as provide online monitoring of the instantaneous luminosity and beam

conditions.

ALFA The second luminosity system is the Absolute Luminosity For ATLAS (ALFA) detector located approximately 240 m from the IP. The ALFA detector measures scattering angles smaller than the nominal beam divergence to extract the luminosity of the proton beam by using the optical theorem to relate the elastic scattering amplitude in the forward direction to the total cross section. Two pairs of Roman pots with scintillating-fiber trackers are installed 4 m apart along the beamline with one of each pair placed above and the other placed below the beam-pipe as shown in Figure 3.11. Each Roman pot consists of ten double-sided modules each with 64 square-cross-section fibers of 0.5 mm width arranged in a curved stereo geometry on each side of each module. The overlapping trimmed-square region of the fibers forms the effective area of the detector which has the ability to approach the beam within 1 mm. The scintillating fibers are each connected to a PMT which amplifies and processes the signals before they are sent to the central trigger processor. The ALFA detector is able to achieve a spatial resolution of 25 µm, and together with the LUCID system the luminosity can be measured with $< 5\%$ uncertainty.

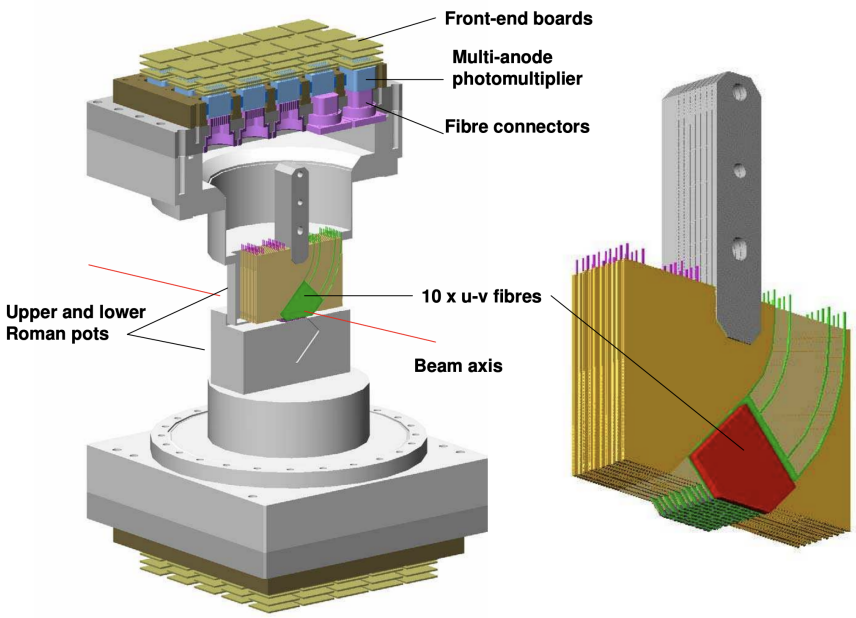

Figure 3.11: The pair of Roman pots with each of the electronic components (left) and the scintillating-fiber stack in each Roman pot (right).

CHAPTER IV

Photon Reconstruction and Identification

The pp collisions at relatively high luminosity in the LHC produce many electrically charged and neutral particles that stream through the ATLAS detector. The trajectories and energies of these particles can be inferred from their interactions in the tracking detectors and the EM shower and hadronic jet energy and shape measurements in the calorimeters. These measurements allow for a complete recreation of the outcome of a collision event with high efficiency.

Among this medley of particles, the most important one for the study of the diphoton decay of a scalar particle is obviously the photon. The next particles in importance are the electrons and positrons: the signal of a primary photon from a Higgs decay is often its conversion into these two charged particles through e^+e^- pair production. The reconstruction of electrons is critical in reconstructing photons since the photons convert via pair production a third of the time before entering the tracking detector. Furthermore, the photon-like characteristics of an electron in its deposited energy and associated tracks can often lead to its incorrect identification as a photon during the object reconstruction process. The photons and photon-like objects resulting from hadronic interactions, such as the diphoton decay of π^0, also pose as SM background in the scalar resonance search.

The reconstruction process of photon and electron objects starts with the energy

information in the EM and hadronic calorimeters to form energy clusters (also known as topoclusters) and is described in Section 4.1.1. The tracking of electrons is performed using particle momentum and location information from the inner detector and is described in Section 4.1.2. The topoclusters are then matched to appropriate particle tracks if possible as described in Section 4.1.3. Conversion vertices are constructed afterwards and matched with track-matched topoclusters for photon candidate conversion classification as described in Section 4.1.4. Finally, the topoclusters are grouped into particle objects and classified based on their shower shape characteristics, tracks, and conversion vertices as described in Sections 4.1.5 and 4.1.6.

The process in which some hadronic jets are misidentified as photon objects is briefly described in Section 4.2. The construction of pp collision primary vertices using track reconstruction information from both unconverted and converted photons is described last in Section 4.3.

4.1 Electron and Photon Reconstruction

Electron and photon objects are each reconstructed through a similar process in the ATLAS detector. Both types of objects use shower shape information from the energy deposited in calorimeter cells and track information from the silicon tracking detectors.

4.1.1 Topocluster Reconstruction

Photon showers represented by "topoclusters" are reconstructed from calorimeter information by a dynamical and topological calorimeter cell-based approach [11]. The "4-2-0" topocluster reconstruction algorithm (named after the energy significance thresholds for each of the three steps) starts with forming three-dimensional "protoclusters" using the cell energy information from the EM and hadronic calorimeters described in Section 3.2.4 [13]. The cell energy significance metric $\varsigma_{\text{cell}}^{\text{EM}}$ is used to measure the energy in a calorimeter cell with respect to its noise threshold:

$$\varsigma_{\text{cell}}^{\text{EM}} = \frac{E_{\text{cell}}^{\text{EM}}}{\sigma_{\text{noise, cell}}^{\text{EM}}} \tag{4.1}$$

where $E_{\text{cell}}^{\text{EM}}$ is the energy in an EM calorimeter cell deposited by EM showers and $\sigma_{\text{noise, cell}}^{\text{EM}}$ is the expected cell noise which is composed of the known electronic noise and the estimated noise for a given pile-up condition.

The protocluster formation process begins with EM calorimeter cells that have an energy significance $\varsigma_{\text{cell}}^{\text{EM}} \geq 4$. Each significant cell subsequently collects neighboring cells with $\varsigma_{\text{cell}}^{\text{EM}} \geq 2$ and associates them with the protocluster of the original cell. This process continues recursively for each protocluster with the newly collected neighboring cells. At the end of the collection process, a padding consisting of the nearest neighboring cells is added for each protocluster regardless of the energy deposited in those neighboring cells. The maxima for each protocluster are identified as cells

with $E_{\text{cell}}^{\text{EM}} > 500$ MeV with lower energy neighboring cells and are used to split the protocluster into multiple clusters [69]. Henceforth, the resulting protoclusters of the formation process are known as topoclusters.

Since the z-direction magnetic field in the inner detector spreads the EM showers in the ϕ direction, no size restriction in the ϕ direction is imposed on each topocluster. However, to limit the effects of pileup when topoclusters are combined in the next step, each cluster is limited in size to a maximum width of 0.075 and 0.125 in the η direction for the barrel and endcap calorimeters, respectively.

4.1.2 Track Reconstruction

The charged particle trajectories (also known as tracks) in the ATLAS inner detectors are used in the process of reconstructing electron objects as well as distinguishing potential electrons from hadronic background at the LHC [43]. These tracks are constructed by using the measured particle positions at multiple points (also known as hits) in the silicon detectors, namely the pixel detector and the SCT. These measurements are first spatially grouped by matching hits that have energy deposits above a certain threshold and share common edges or corners. The groups are then given measurement values (also known as space-points) that reflect their position in the ATLAS coordinate system. Preliminary track seeds are formed with groups of three space-points, first from those found in the SCT, then from those found in the pixel detectors, and finally from those which cross multiple detector layers. These track seeds are further processed such that bad quality track candidates are rejected if they fail certain momentum, geometry, and hit criteria.

As part of the inner detector, the TRT is used as an extension for track reconstruction process. When hits are recorded in the TRT, tracks reconstructed in the silicon detectors can be extended to hit locations in the TRT to increase the efficiency of electron identification [49]. Alternatively, the TRT can be used in an outside-in

approach where track reconstruction begins with the hits in the TRT and are matched inwards to hits from the SCT. This process forms additional tracks that boosts reconstruction efficiency for particles that do not decay in the silicon trackers and for low p_{T} electrons with high energy loss in the TRT.

4.1.3 Track Matching

The reconstructed topoclusters in the calorimeters are matched to the reconstructed tracks in the inner detector to form electron candidates. A standard track pattern reconstruction process is performed for all of the viable topoclusters and tracks with a pion hypothesis first. If a track seed from the silicon trackers fails the pattern recognition for each topocluster, a modified pattern reconstruction process based on a Kalman filter formalism [59] is performed with an electron hypothesis, allowing for energy losses in the electron track due to bremsstrahlung. Successfully matched track candidates are fit with a global χ^2 fitter [50] with a pion hypothesis first and with an electron hypothesis second. Tracks are considered loosely matched to a topocluster if the extrapolation of the track to the second layer of the EM calorimeter is near the cluster in ϕ and η where the latter coordinate constraint is used only if hits in the silicon detectors exist. Loosely matched tracks with silicon hits are refitted with a Gaussian Sum Filter for improved track parameters that better model electron bremsstrahlung [41].

At least one matched track is needed for a cluster to form an electron. If an electron has multiple matched tracks, then the tracks are sorted by those with pixel detector hits first, those with SCT hits but no pixel detector next, and those with only TRT hits last with better ΔR matching in $\eta - \phi$ preferred in each category; the first track in this ranked list is assigned to the topocluster to create an electron candidate.

4.1.4 Conversion Vertex Reconstruction

Topocluster candidates in the calorimeters with $p_{\mathrm{T}} > 500\,\mathrm{MeV}$ that are not matched to a track are classified as unconverted photons while all topocluster candidates with an associated track are initially classified as electrons [43]. As mentioned in the description of the EM calorimeter in Section 3.2.4, a photon may convert into an e^+e^- pair in the presence of matter and are classified as either a single-track or double-track converted photon. The former conversion type generally has no hits in the innermost layers of the inner detector while the latter has two tracks that form a vertex consistent with coming from a massless particle.

The search for a photon conversion vertex is performed at $R \leq 0.8\,\mathrm{m}$ within the inner detector using loosely matched tracks. If two opposite-sign tracks are found with a zero opening angle at their point of closest approach, the vertex candidate is classified as a two-track conversion. Two dedicated algorithms are implemented together to improve the reconstruction efficiency of late-conversion vertices occurring at $R \geq 0.4\,\mathrm{m}$ and vertices with asymmetric energy distribution between the tracks. The first "back-tracking" part uses calorimeter clusters as track seeds to find tracks that originate deep within the inner detector. The second part identifies "single-track" conversion by looking for a vertex along an electron track, the presence of which classifies the topocluster as a converted photon with a single-track. If multiple conversion vertices are mapped to the same topocluster, then the vertices are sorted by those with a double track and two silicon tracker hits first, those with a double track in general next, and those with only a single track last; the first type of vertex in this ranked list is used to label the vertex.

In the low mass diphoton invariant mass regime of this analysis, about one third of the photons convert through pair production, and more than half of these converted photons have two associated tracks.

4.1.5 Supercluster Reconstruction

Although electrons and photons are identified as two distinct types of objects in the final dataset, they are not fully differentiated yet at the topocluster level and still follow the same reconstruction prescription at this point.

Each topocluster is first tested for its viability as a supercluster seed candidate. The clusters are examined in reverse order of E_{T} which is represented by the EM energy of the cluster. Clusters with a minimum E_{T} of 1 GeV with at least 4 hits in the silicon tracking detectors are tagged as potential electron supercluster seeds, and those with a minimum E_{T} of 1.5 GeV are tagged as potential photon supercluster seeds. The photon supercluster seeds can be further classified as unconverted or converted depending on whether a conversion vertex can be matched. Since the tagging criteria is not mutually exclusive, it is possible for a supercluster to be tagged as both an electron and a photon.

After all the potential supercluster seeds have been identified, the remaining topoclusters are assigned as satellite clusters of a given supercluster seed if they fall within a solid angle window of $\Delta\eta \times \Delta\phi = 0.075 \times 0.125$ (which corresponds to 3×5 calorimeter cells) around the center of energy of the seed. Additional clusters are added to supercluster seeds tagged as electrons if they fall within a solid angle window of $\Delta\eta \times \Delta\phi = 0.125 \times 0.400$ (which corresponds to 5×12 calorimeter cells) around the center of energy of the seed and share the same "best-matched" track with the seed. Similarly, additional clusters are also added to superclusters tagged as converted photons if they share the same "best-matched" track with the seed. Since these satellite clusters are usually caused by secondary EM showers that originate from the same initial electron or photon, the deposited energy and spatial information is combined with that of the assigned seed cluster to form a supercluster. The satellite cluster assignment criteria for electrons and photons is summarized and illustrated in Figure 4.1. The use of tracking info in this step helps to select clusters

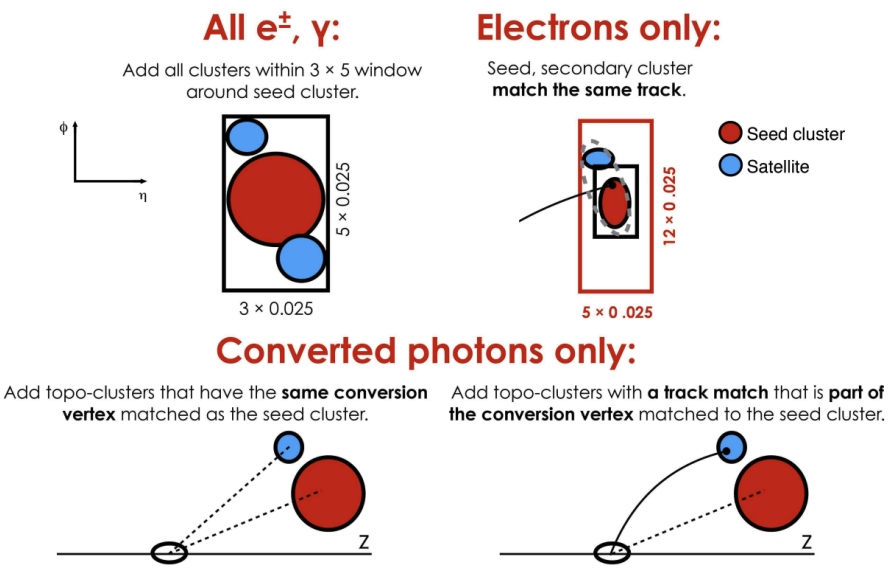

Figure 4.1: A diagram of the superclustering algorithm for electron and photon reconstruction [14]. Seed clusters are shown in red, and satellite clusters are shown in blue.

associated with bremsstrahlung photons and conversion electrons over pileup noise and other unrelated energy clusters.

4.1.6 Identification and Isolation

Additional energy calibrations on the clusters and position corrections on the tracks and conversion vertices are applied before supercluster candidates matched with tracks and/or conversion vertices are identified as photons or electrons. As mentioned earlier, a supercluster is able to produce both an electron and photon object. A classification procedure is used to identify obvious photon objects as superclusters with no tracks and obvious electron objects as superclusters with good tracks and no conversion vertex as shown in Figure 4.2. However, cases where a cluster produces both an electron and a photon object are marked explicitly as an ambiguous electron-photon object which plays a large role in the resonant background of the diphoton search analysis. Shower shape and other discriminating variables also are calculated for electron and photon identification and included in each electron or photon object

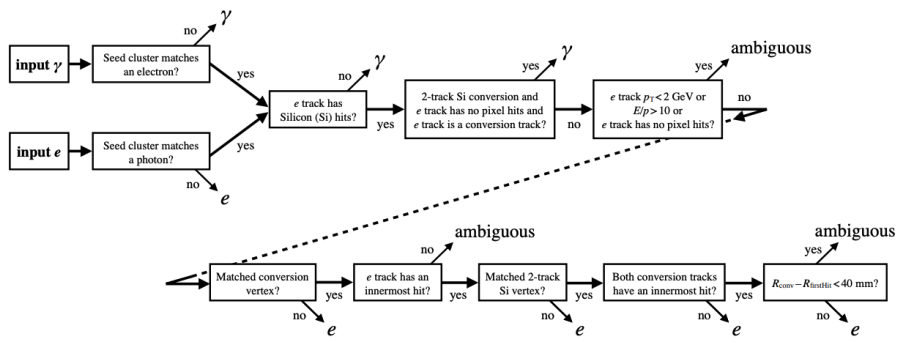

Figure 4.2: A flowchart showing the logic of the ambiguity resolution for a particle object initially reconstructed both as an electron and a photon [14]. An "innermost hit" is a hit in the pixel detector nearest the beamline along the track trajectory, E/p is the ratio of the supercluster energy to the measured momentum of the matched track, R_{conv} is the radial position of the conversion vertex, and R_{firstHit} is the smallest radial position of a hit in the track or tracks that make a conversion vertex.

for further optimization studies. Additionally, the information on total cluster energy and its distribution among the calorimeter cells is also retained for each object and used for isolation energy studies.

4.2 Parton Jets Faking Photons

As described in Section 2.1.2, the outgoing quarks and gluons for the pp collision hadronize into showers of particles measured in the inner detector and calorimeters. These hadronic jets are efficiently reconstructed using various algorithms on the tracking and calorimeter signals associated to each hadronic shower. However, in some cases, fluctuations in the hadronization and hadronic decays to two photons, such as the $\pi^0 \to \gamma\gamma$ process, can produce jets that look like a single isolated photon in the reconstruction process. For this reason, it is important to reconstruct and understand these kinds of jets for the Higgs-like scalar search in the diphoton decay channel.

Hadronic jet reconstruction classifies the final objects by the information available: track jets are reconstructed by solely using tracks, calorimeter jets by solely using calorimeter cell energies, and particle flow jets by using both. The track and calorimeter jet reconstruction begins with the same topocluster formation and track fitting process as that for electrons and photons discussed in Sections 4.1.1 and 4.1.2, respectively. Depending on the shower shape restrictions on calorimeter energy cells, tightly clustered hadronic showers can satisfy many if not all of the criteria for EM showers and ultimately be identified as part of a prompt photon coming form the IP. Optimization studies based on reconstruction variables are performed in the analysis to reduce the impact of these hadronic jets in the background as described later in Chapter 6.

4.3 Primary Vertex Reconstruction

Finally, it is important to know the point where the pp collision occurred. The position of the primary interaction vertex where the hard-scatter occurs is determined by grouping reconstructed tracks that are consistent with coming from the same initial position. The initial vertex seed has its x and y positions set to the center of the LHC beam spot in the $x - y$ plane and its initial z coordinate set to the mode of all z coordinates associated with tracks that originate from the beam line [44]. An iterative process then assigns a compatibility weight to each track through successive χ^2 fits to find tracks that are most compatible with the vertex seed. Any tracks that are located within 7σ from the best-fit vertex position are assigned to that vertex seed while all others are treated as incompatible and removed from the fit. This primary vertex reconstruction process repeats with remaining tracks until all tracks have been associated to a vertex or when there are fewer than two tracks left.

After all vertex candidates are reconstructed, the primary vertex is then identified as the vertex with the largest sum of squared p_{T} of all associated tracks. All other vertex candidates are considered to originate from pileup interactions.

The inner tracker assigns transverse momentum p_{T} to each reconstructed track, and the calorimeters measure the transverse energy E_{T} deposited by particle showers and jets. Although these two variables describe very different quantities, the p_{T} of the photons studied in this analysis is expressed as the magnitude of the transverse momentum. Furthermore, these quantities are equivalent for photons since these bosons are massless, Thus, the variables p_{T} and E_{T} will be used interchangeably henceforth.

CHAPTER V

Scalar Resonance Search Strategy

Searches typically look for statistically significant deviations in the experimental data when compared to a predefined model. The search presented in the following chapters is a "resonance search" that looks for anomalous bump-like features on an otherwise smooth background model as illustrated in Figure 5.1. The model is usually defined to describe SM background processes and behaviors such that any deviations could potentially point to BSM physics. If no deviations are observed, the possibility of BSM physics is not completely excluded. Instead, upper limits are set on the production cross section of a hypothetical BSM signal under study based on the signal-to-background sensitivity of the analysis. This sensitivity can be impacted by the statistical and systematic uncertainties in the MC samples used as well as in the signal and background modeling process. The largest contributor to the overall uncertainty usually arises from the slight mismodeling of the data by the background model which can introduce "spurious signal" as described later in Section 7.3.2. Thus, the limits that are set in a resonance search represent the maximum production level possible for a BSM signal such that its presence in the dataset used is overwhelmed by the uncertainty in the analysis.

For this analysis, limits are set on the cross section of a potential new scalar below 125 GeV as a function of the invariant mass of a resonance using the diphoton decay

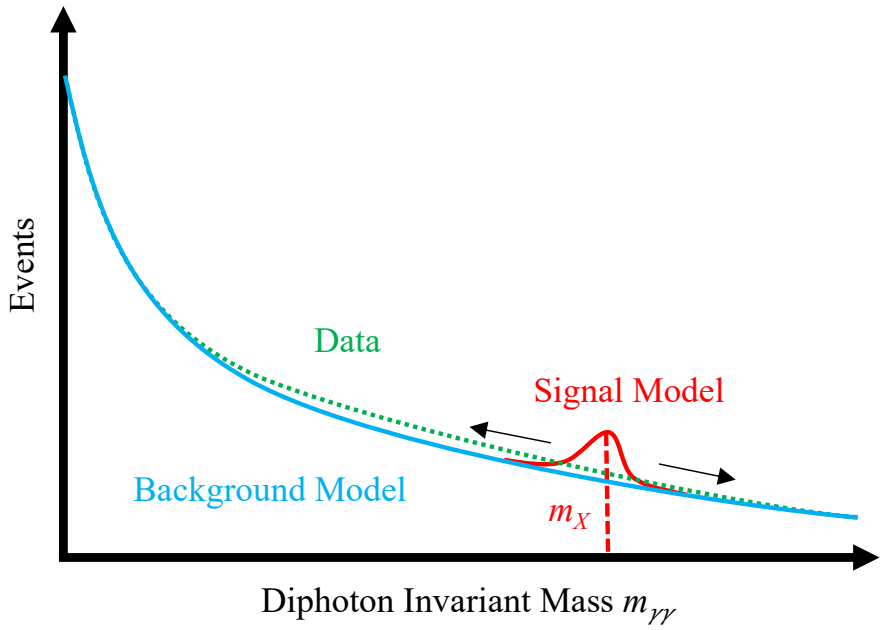

Figure 5.1: The search for a new scalar resonance in the diphoton decay channel. The backgrounds are modeled using both data and MC samples. The "bump-hunt" is performed by fitting the signal shape modeled from simulation along the diphoton invariant mass spectrum.

channel. The diphoton invariant mass $m_{\gamma\gamma}$ is used to compare known SM backgrounds from potential BSM resonances and is defined as

$$m_{\gamma\gamma} = \sqrt{2E_{\mathrm{T}}^{\gamma 1} E_{\mathrm{T}}^{\gamma 2} \left[\cosh\left(\eta_1 - \eta_2\right) - \cos\left(\phi_1 - \phi_2\right)\right]} \tag{5.1}$$

where $E_{\mathrm{T}}^{\gamma 1}$ and $E_{\mathrm{T}}^{\gamma 2}$, η_1 and η_2, and ϕ_1 and ϕ_2 are the transverse energy, pseudorapidity, and azimuthal angle of the leading (γ_1) and subleading (γ_2) photon, respectively. The photons in a reconstructed diphoton event are ordered in decreasing E_{T}.

To search for possible data excesses over the $m_{\gamma\gamma}$ distribution, models for the potential scalar resonance are first hypothesized before building signal and background templates from simulation samples. The two scalar resonance models described in Section 5.1 will be used in this analysis. The outline for the analysis methodology is then presented in Section 5.2.

5.1 Scalar Resonance Models

The analysis presented in this thesis will perform the diphoton resonance search using a model-dependent and a model-independent method. The model-dependent method provides greater signal-to-background sensitivity, but it also makes assumptions on the scalar resonance model that the model-independent method does not. The final analysis selections in Chapter 6 will be applied identically in both methods, but different categorization schemes will be used for each method. The modeling of the signal and background shapes in Chapter 7 and the limits on the cross section for a new Higgs-like scalar in Chapter 8 will be presented separately for each method. The results for each method will be stylistically separated in the format presented below when appropriate.

♦ **Model-Dependent Method** The model-dependent method will use the five dominant SM Higgs production modes — ggH, VBF , ttH, WH, and ZH — in a holistic approach to provide a total cross section limit on a new scalar that closely resembles the SM Higgs boson. Each production mode will be weighted by their respective SM-like cross sections and diphoton branching ratios to form the signal model for this part of the analysis. By including multiple production processes, this method will be sensitive to every type of diphoton decay from scalars produced near rest to those produced with a significant transverse momentum (also known as the boosted regime).

The LHC Higgs Working Group moderates discussions within the LHC community on cross section, branching ratio, and pseudo-observables related to the SM and BSM Higgs bosons. This group provides recommendations on theoretical predictions and methodologies for Higgs boson studies applicable to current and future LHC runs to all LHC experiments. To remain consistent with the other LHC experiments, the recommended cross sections of the five dominant Higgs production modes and

Resonance Mass Point	Production Mode Cross Section [pb]					Branching Ratio
m_X [GeV]	ggH	VBF	ttH	WH	ZH	$X \to \gamma\gamma$
60	155.5	6.924	3.483	11.70	6.183	4.849e-4
70	117.2	6.301	2.113	7.920	4.279	6.871e-4
80	92.40	5.748	1.590	5.538	3.073	9.369e-4
90	75.07	5.258	1.154	3.977	2.261	1.242e-3
100	62.35	4.822	0.9146	2.926	1.704	1.602e-3
110	52.68	4.434	0.6675	2.194	1.309	1.981e-3
120	45.14	4.086	0.5598	1.679	1.024	2.264e-3

Table 5.1: The recommended SM-like Higgs boson cross section and branching ratios values at $\sqrt{s} = 13\,\text{TeV}$ for the ggH, VBF, ttH, WH, and ZH production modes at various mass points m_X provided by the LHC Higgs Working Group [73].

diphoton branching ratio values for a SM-like Higgs boson resembling a light scalar from the 2HDM are used in this analysis and are listed in Table 5.1 [73]. These recommended values correspond to data collected at a center of mass energy of $\sqrt{s} =$ 13 TeV. Henceforth, the light scalar to diphoton decay will be referred to as the $X \to \gamma\gamma$ process.

$\Diamond$ **Model-Independent Method** To facilitate comparisons with other BSM models that predict new scalar particles, a model-independent method is also performed in this resonance search. Fiducial cross section limits are provided by only considering the expected ATLAS detector response to the diphoton decay of a new scalar particle. The fiducial phase space is characterized by the acceptance of diphoton events by the final analysis selections at truth level computed using the MC generated signal samples used in this analysis. Thus, model-independent results can be used to reinterpret the cross section limits on new scalars when building custom BSM models.

The signal model used in the model-independent analysis will be composed of only the dominant ggH production mode. The fiducial phase space of each Higgs production mode is encoded in its respective correction factor C_X provided in Chapter 7. By using these factors, the fiducial cross section limit presented in the model-

independent method can be scaled to the boosted, non-boosted, or combined regime of a custom scalar resonance model.

5.2 Outline of Analysis Methodology

The resonance search analysis begins with a description of the MC generated samples for the signal and background processes along with the LHC datasets and the trigger used to process events online, all of which are presented in Chapter 6. This chapter will then present the final analysis selections and categorization methods applied on diphoton events for both the signal and background samples. Chapter 7 will detail the modeling methods used for representing the signal and background shapes in the model-dependent and model-independent methods. Finally, Chapter 8 will summarize the results of using the expected signal and background models in the model-dependent and model-independent methods to search for a resonance in the experimental data. Each step of the analysis methodology is listed in Table 5.2 with its usage in the two scalar resonance models. The role of the MC samples and LHC datasets at each step is also illustrated in this table.

Methodology Step	Model Dependent Categories	Model Independent Categories	MC Driven	Data Driven
Diphoton Event Selection (Sections 6.3.1 – 6.3.4, 6.3.6)	Same selections		✓	
Photon Conversion Categorization (Section 6.3.5)	Same categorization		✓	
Diphoton BDT Classification (Section 6.3.7)	Used	Unused	✓	
Signal Modeling (Section 7.1)	Separate	Separate	✓	
A_X and C_X Factors (Section 7.2)	Separate	Separate	✓	
$\gamma\gamma$ Background Modeling (Section 7.3.1.2)	Separate	Separate	✓	
$\gamma j + jj$ Background Modeling (Section 7.3.1.3)	Separate	Separate	✓	✓
Non-resonant Background Modeling (Section 7.3.2)	Separate	Separate	✓	✓
Resonant Background Modeling (Section 7.3.3)	Same model per conversion category; separate normalization per BDT category for model-dependent		✓	✓
Results (Sections 8.3 – 8.4)	Separate	Separate	✓	✓

Table 5.2: A list of steps in the resonance search analysis methodology. The usage of how each step is used in each category for the model-dependent and model-independent methods is briefly summarized. The role of the MC samples and LHC datasets is also shown for each step.

CHAPTER VI

Generation, Selection, and Categorization of Diphoton Events

This analysis uses the data collected by the ATLAS particle detector during the LHC Run 2 together with simulated signal and background samples to perform the resonance search. The MC events are generated using various types of particle generators and detector simulators to describe the signal and background templates as detailed in Section 6.1. The data is recorded using unprescaled triggers with at least two photons and fulfilling quality criteria during the nominal operation of both the ATLAS detector and the LHC as described in Section 6.2. The selection of diphoton events uses various cuts on reconstructed variables, categorization schemes, and multivariate analysis (MVA) techniques to increase signal-to-background sensitivity of the search as described in Section 6.3.

6.1 Monte Carlo Samples

The MC simulated events used in this analysis are produced by running a variety of MC event generators to produce truth events at the particle level. The events are then passed through a simulated version of the ATLAS detector to emulate the expected interactions between the truth particles and the detector material. After this detector simulation, the events are reconstructed using the same analysis techniques used to reconstruct the LHC collision data as described in Chapter 4. The effects from pileup are included in these event and are modeled using additional inelastic pp collisions generated with PYTHIA8 [94] using the A14 parameter tune [8].

Each MC sample is reconstructed using conditions that account for the changing pile-up and trigger conditions of the 2015 – 2016, 2017 and 2018 data-taking periods and are labeled as mc16a, mc16d, and mc16e, respectively.

6.1.1 New Scalar Resonance Signal Samples

The Higgs-like scalar signal resonance is simulated in pp collisions events at $\sqrt{s} =$ 13 TeV by using Higgs boson MC generators where the resonance mass m_X is set to values less than 125 GeV. The dominant SM Higgs production modes are used, and the generated bosons are then forced to decay into two photons. The MC samples are produced for different mass hypotheses in the range 40 – 120 GeV. The resonance is assumed to be very narrow, so the narrow width approximation (NWA) [23] is used for all of the generated signal samples with the resonance width of the scalar set to $\Gamma_X = 4$ MeV.

The MC samples for the ggH production mode are generated at next-to-leading order (NLO) in perturbative QCD (pQCD) in the NWA using POWHEGBOX2 [82] [58] [3] interfaced with PYTHIA8.186 for parton showering and hadronization using the AZNLO set of tuned parameters. These PowhegPy8 samples will be used as the nominal MC samples for the model-independent method. For the ggH mode, the

interference between the $gg \to X \to \gamma\gamma$ process and the quantum chromodynamics (QCD)-initiated continuum diphoton background associated to the $gg \to \gamma\gamma$ process is estimated to be negligible for narrow width signals considered in this analysis [9]. This interference effect is therefore neglected in the simulation.

MC samples are also produced for the subdominant production modes VBF, ttH, WH, and ZH. The VBF Higgs-like events are simulated with the same Powheg and Pythia setup as the alternative ggH samples described above. The associated production modes are simulated at leading order (LO) in pQCD using PYTHIA8 for both the matrix element calculation and the subsequent parton showering. These samples were produced with the NNPDF23 LO PDF set [18] using the A14 tune.

The details of each Higgs-like signal resonance MC sample are given in Table 6.1. The $m_X = 40$ GeV mass points are not used in the global signal modeling fit described in Section 7.1 because the shapes of these resonant points is significantly biased by the diphoton trigger kinematic requirements described in Section 6.2.

Production Mode	MC Generator	Mass Points m_X [GeV]	N_{events} ($\times 10^3$)		
			mc16a	mc16d	mc16e
ggH	Powheg+Pythia8	40, 60, 80, 100, 120	30	40	70
VBF	Powheg+Pythia8	40, 60, 80, 100, 120	30	40	70
WH	Pythia8	40, 60, 80, 100, 120	30	40	70
ZH	Pythia8	40, 60, 80, 100, 120	30	40	70
ttH	Pythia8	40, 60, 80, 100, 120	30	40	70

Table 6.1: The signal samples of the five Higgs production modes with the largest SM-like cross sections considered in this analysis. The available simulated mass points and event statistics for each of the three MC campaign is listed for each production mode. All signals are generated using the NWA such that $\Gamma_X = 4\,\text{MeV}$.

6.1.2 QCD Continuum Background Samples

As described later in Section 7.3.1, the main background in this search comes from the irreducible prompt diphoton production in the diphoton background continuum.

Mass Range	Cross Section	Filter	N_{events} ($\times 10^6$)		
$m_{\gamma\gamma}$ [GeV]	σ [pb]	Efficiency	mc16a	mc16d	mc16e
50 – 90	139.04	1.	99.5	121.1	162.3
90 – 175	51.822	1.	137.7	166.6	222.9

Table 6.2: Prompt diphoton background samples generated with the AFII fast detector simulation. The total events given here are the number of events generated and reconstructed at AOD level. The filter efficiency measures the fraction of events from the generator-level sample that are present in the final simulated sample.

The simulation of these events uses the SHERPA2.2.4 [61] [27] event generator with the associated default tuning for the generated events. Matrix elements are calculated with up to one additional parton at NLO and with two or three partons at LO in pQCD and merged with the Sherpa parton-shower simulation [92] using the ME+PS@NLO prescription [62] [63] [36] [64]. The NNPDF3.0 next-to-next-to-leading order (NNLO) PDF set [19] is used in conjunction with a dedicated parton-shower tune in the SHERPA2.2.4 generator.

To simulate the detector response for the very large MC samples required to precisely model the diphoton background, the ATLFAST-II (AFII) fast detector simulation [5] is used in which the full simulation of the ATLAS calorimeter is replaced with a parametrization [6] of the calorimeter response. The sample generation is sliced in ranges of diphoton invariant mass to ensure sufficient statistics across the $m_{\gamma\gamma}$ spectrum. The available statistics per slice are shown in Table 6.2.

6.1.3 $Z \to ee$ Resonance Background Samples

The MC samples of $Z \to ee$ decays are used to study the background arising from electrons faking photons described in Section 7.3.3. The $Z \to ee$ decays were generated with POWHEGBOX2 using the CT10 PDF set in the matrix element and interfaced to the PYTHIA8.186 parton shower model using the AZNLO set of tuned parameters with the CTEQ6L1 PDF set. Sliced samples generated with SHERPA2.2.1

are also used for computing systematic uncertainties. The slices cover the region of $m_{ee} > 40$ GeV and are sliced in $\max(H_{\mathrm{T}}, p_{\mathrm{T}}(V))$ at the parton level, where the boson transverse momentum $p_T(V)$ is worked out from the two parton-level leptons and the parton-level H_{T} is given by the scalar p_{T} sum of all parton-level jets with $p_{\mathrm{T}} > 20$ GeV. For $\max[H_{\mathrm{T}}, p_{\mathrm{T}}(V)] < 500$ GeV, the slices are also filtered according to their b-hadron and c-hadron content at the particle level in order to enhance statistics for phase spaces with associated heavy-flavour jets [10]. Details on the slices and MC statistics for these $Z \to ee$ samples are given in Table 6.3.

6.1.4 Sample Post-Processing

All MC samples are processed through the Higgs working group for $H \to \gamma\gamma$ related analyses (HGam) framework, and the resulting mini xAOD (MxAOD) data structures to be used for the studies presented in this analysis are produced using the `v1.10.25-h026-AmbiguityExtraInfo` tag of `HGamCore` [79]. Weights are applied to correct the simulated samples for data to MC differences by applying scale factors for the photon identification, pile-up, and choice of the diphoton vertex. Additionally, the MC generator weights are applied to account for non-uniform event weights, cross section times branching ratio, and k-factors where applicable.

MC Generator	max(HT,pTV) [GeV]	Cross section σ [pb]	Filter	Filter Efficiency	k-factor	N_{events} ($\times 10^6$)		
						mc16a	mc16d	mc16e
Powheg	–	1901.2	$m_{ee} > 60$ GeV	1	1.026	309.8	386.9	513
Sherpa	0 – 70	1981.0	c-veto, b-veto	0.82143	0.9751	8.0	10.0	13.3
	0 – 70	1981.6	c-filter, b-veto	0.11407	0.9751	5.0	6.2	8.3
	0 – 70	1982.1	b-filter	0.06576	0.9751	8.0	10.0	13.3
	70 – 140	1106.3	c-veto, b-veto	0.69432	0.9751	6.0	7.4	10.0
	70 – 140	110.45	c-filter, b-veto	0.18697	0.9751	2.0	2.5	3.3
	70 – 140	110.43	b-filter	0.11605	0.9751	6.0	7.5	9.9
	140 – 280	40.711	c-veto, b-veto	0.61632	0.9751	5.0	6.3	8.4
	140 – 280	40.683	c-filter, b-veto	0.23302	0.9751	3.0	3.7	5.0
	140 – 280	40.671	b-filter	0.15319	0.9751	12.4	15.7	20.0
	280 – 500	8.6711	c-veto, b-veto	0.56328	0.9751	2.0	2.5	3.4
	280 – 500	8.6597	c-filter, b-veto	0.26640	0.9751	1.0	1.3	1.7
	280 – 500	8.6793	b-filter	0.17638	0.9751	4.0	5.0	6.6
	500 – 1000	1.8096		1	0.9751	3.0	3.7	5.0
	1000 – ∞	0.14875		1	0.9751	1.0	1.3	1.7

Table 6.3: The $Z \to ee$ samples used to study the DY background arising from electrons faking photons. The event totals presented here are the number of events generated and reconstructed at the AOD level. The Sherpa slices cover the region of $m_{ee} > 40\,\text{GeV}$ and are sliced in $\max(H_{\text{T}}, p_{\text{T}}(V))$ at the parton level, where the boson transverse momentum $p_{\text{T}}(V)$ is worked out from the two parton-level leptons and the parton-level H_{T} is given by the scalar p_{T} sum of all parton-level jets with $p_{\text{T}} > 20\,\text{GeV}$. The k-factor, defined as the cross-section ratio $\sigma_{\text{NNLO}}/\sigma_{\text{Generator}}$ for the relevant mass dilepton mass range, is also given here [32].

6.2 Proton-proton Collision Datasets

The data used in this analysis are recorded during the pp collisions of LHC Run 2 in 2015 – 2018 using unprescaled diphoton triggers with the lowest transverse energy E_{T} thresholds that were available in each data-taking period. The L1 and HLT triggers evolved throughout the Run 2 data-taking periods which tightened the energy threshold and isolation requirements for photons to maintain a high efficiency after a four-fold increase both in the LHC peak luminosity and in the number of interactions per beam-crossing [16].

The L1 trigger for photons uses calorimeter information in the central region $|\eta| < 2.5$ to build a L1 seed candidate. A sliding window algorithm uses a window of 4×4 towers (0.1×0.1 in $\eta \times \phi$) longitudinally segmented through both the EM and hadronic calorimeters. The algorithm selects the 2×2 pairing between EM and hadronic towers that has the highest E_{T} as the L1 EM seed. In 2015, each L1 EM seed was required to have a transverse energy of $E_{\mathrm{T}} > 10\,\mathrm{GeV}$. In 2016, the transverse energy threshold was increased to $E_{\mathrm{T}} > 15\,\mathrm{GeV}$ for each L1 EM seed. In the 2017 – 2018 data-taking period, L1 EM seeds with $E_{\mathrm{T}} < 50\,\mathrm{GeV}$ and $E_{\mathrm{iso}} > 2\,\mathrm{GeV}$ had an additional requirement on the EM isolation $E_{\mathrm{iso}} < E_{\mathrm{T}}/8 - 1.8\,\mathrm{GeV}$ where E_{iso} is the transverse energy deposited in the 12 towers surrounding the 2×2 central region towers used for the sliding window algorithm.

The HLT trigger chain for photons uses information based on the L1 EM seeds selected by the L1 trigger. In the 2015 and 2016 data-taking periods, the diphoton trigger used requires each photon to pass a threshold of $E_{\mathrm{T}} > 20\,\mathrm{GeV}$ until the 2016 D3 period, after which the threshold was increased to $E_{\mathrm{T}} > 22\,\mathrm{GeV}$ for each photon until the end of the 2016 data-taking period. In the 2017 – 2018 data-taking period, the threshold is lowered back to $E_{\mathrm{T}} > 20\,\mathrm{GeV}$.

Photon identification (ID) requirements are applied on the two L1 EM seeds. Two different ID working points are defined using rectangular cuts on the shower shape

variables further described in Section 6.3.2:

- `tight`: recommended for use in offline analysis due to its high fake photon rejection and good prompt photon efficiency,
- `loose`: usually used for data-driven background studies due to its low fake rejection and near-unity efficiency.

The `tight` photon ID is used for all data-taking periods in the unprescaled datasets.

Photon isolation requirements as described later in Section 6.3.3 are also considered during the data-taking stage. No photon isolation requirements are applied during the 2015 and 2016 data-taking periods. Photon isolation is applied in the HLT for the lowest unprescaled diphoton triggers during the 2017 – 2018 period. The photon isolation energy represents the residual energy around a photon candidate. It is defined as the sum of the transverse energy of calorimeter clusters located within a cone of fixed radius $\Delta R = \sqrt{(\Delta\eta)^2 + (\Delta\phi)^2}$ around the triggered photon candidate after subtracting the energy of the photon candidate and estimated contributions from pileup interactions. Two different isolation variables `topoetcone20` and `topoetcone40` which use cones of size $\Delta R = 0.2$ and $\Delta R = 0.4$ respectively are used in the two isolation requirements considered:

- `icalotight`: `topoetcone40` $< 0.03 \cdot E_{\mathrm{T}} + 2.45$,
- `icalovloose`: `topoetcone20` $< 0.2 \cdot E_{\mathrm{T}}$.

The `icalovloose` photon isolation is used for the 2017 – 2018 unprescaled datasets. A summary of the different unprescaled L1 and HLT triggers used along with the associated integrated luminosity for each data-taking period is given in Table 6.4.

Data-taking period	L1 Trigger	HLT Trigger	Integrated Luminosity [fb^{-1}]
2015	`2EM10VH`	`2g20_tight`	3.2
2016 to D3	`2EM15VH`	`2g20_tight`	11.5
2016 from D3	`2EM15VH`	`2g22_tight`	21.5
2017 + 2018	`2EM15VHI`	`2g20_tight_icalovloose`	43.6 + 58.5

Table 6.4: The unprescaled diphoton L1 and HLT triggers used per data-taking period with their associated integrated luminosity.

As described later in Section 7.3.1, the data control regions are used to estimate the background composition and model the background shape. This data is recorded during the *pp* collisions of LHC Run 2 in 2015 – 2018 using prescaled diphoton triggers similar to those described above but using `loose` photon ID and no photon isolation criteria instead. The total prescale of the trigger chain varies with the average number of interactions per bunch crossing $\langle\mu\rangle$ and across data-taking periods, ranging from 20 to 60 with the L1 prescale varying from $2.0 - 6.0$ and with the HLT prescale held constant at 10. A summary of the different prescaled L1 and HLT triggers used for each data-taking period along with the recorded integrated luminosity associated to each period is given in Table 6.5.

Data-taking period	L1 Trigger	HLT Trigger	Integrated Luminosity [fb^{-1}]
2015	`2EM10VH`	`2g20_loose`	0.32
2016	`2EM15VH`	`2g20_loose`	3.30
2017	`2EM15VH`	`2g20_loose`	1.56
2018	`2EM15VHI`	`2g20_loose`	1.08

Table 6.5: The prescaled diphoton L1 and HLT triggers used per data-taking period with their associated integrated luminosity.

6.3 Diphoton Event Selection

After the signal and background MC samples are generated and the recorded collision data is processed, event selections and categorization schemes are used to reduce the background contribution in the $m_{\gamma\gamma}$ spectrum and create signal-enriched regions in the resonance search. Many studies are performed using the diphoton event variables to optimize the signal-to-background sensitivity of the analysis.

6.3.1 Vertex Selection

The precise location of the diphoton production vertex in the detector is necessary to achieve a precise measurement of the diphoton invariant mass $m_{\gamma\gamma}$ and a precise computation of track-based quantities such as track isolation. The determination of the vertex is based on the "photon pointing" method where the vertex position along the beam axis is obtained by combining the trajectories of both photon candidates using the longitudinal segmentation of the calorimeter with constraints from the average beam spot position in 3D space [71]. For photons that have converted to e^+e^- pairs before reaching the inner detectors, the position of the conversion vertex is also used if the conversion tracks have hits in the silicon detectors. The diphoton production vertex is selected among all the reconstructed primary vertices using a neural network that is able to find a primary vertex within 0.3 mm of the true one with an efficiency of more than 65%. The four-momenta of each photon is then corrected to point from the chosen diphoton vertex.

6.3.2 Identification Selection

Photon events are selected by imposing requirements on the calorimeter shower-shape variables for each of the two photon candidates. The two photon ID working points, `loose` and `tight`, are defined based on the levels of signal efficiency (also known as acceptance) and background rejection of these cuts as mentioned in Section

6.2. Photon candidates for the final signal region are required to satisfy the `tight` ID criteria while the `loose` ID is used for background estimations in the control regions.

The `loose` ID selection is based on shower shapes in the second layer of the EM calorimeter and on the energy deposited in the hadronic calorimeter. The `tight` ID selection uses additional information from the finely-segmented strip layer of the EM calorimeter. It is separately optimized for photons that remain unconverted and those that are converted to e^+e^- pairs before reaching the inner detector to account for the generally broader lateral shower profile of the latter type of photon [15].

The `tight` ID selection is further optimized in sub-ranges of transverse momentum p_{T} of the photon since its EM shower can be dependent on its energy. Photons with $p_{\mathrm{T}} > 25$ GeV are expected to have a reconstruction and ID efficiency of greater than 80% that reaches a plateau of around $90 - 95\%$ at $40 - 50$ GeV. This p_{T}-dependent selection provides an improved signal efficiency at lower p_{T} ranges. It also provides a similar signal efficiency while improving the fake photon rejection power at higher p_{T} ranges [14].

6.3.3 Isolation Selection

The isolation criteria applied on photon candidates can use information from the inner tracker as well as from the EM calorimeter. A track-based isolation measures the total momentum in tracks contained in a small cone around a photon candidate. On the other hand, a calorimeter-based isolation measures the energy deposited in a similar small cone around a photon candidate

The track-based isolation variables `ptcone20` and `ptcone40` are defined as the scalar sum of the transverse momenta of all tracks with $p_{\mathrm{T}} > 1$ GeV in a cone of size $\Delta R = \sqrt{(\Delta\eta)^2 + (\Delta\phi)^2} = 0.2$ and 0.4, respectively, around each photon candidate. Only tracks originating from the diphoton production vertex as described in Section 6.3.1 are used, and any tracks associated with converted photon candidates after the

conversion vertex are excluded.

The calorimeter-based isolation variables `topoetcone20` and `topoetcone40` are defined as the sum of the transverse energy of all topological clusters with positive energy reconstructed in the EM calorimeter in a cone of size $\Delta R = 0.2$ and 0.4, respectively, around each photon candidate [69]. Similar to the calculation of E_{iso} in Section 6.2, the `topoetcone` energy calculation subtracts the energy from the main calorimeter cluster of the photon, corrects for the leakage of the photon energy into surrounding calorimeter clusters, and uses an event-by-event energy subtraction based on the jet area method to remove energy contributions from the underlying event and pile-up interactions [34] [33].

Three official working points are available and used in this analysis:

- `FixedCutLoose`: designed for SM $H \to \gamma\gamma$ analyses
  - Track Isolation: `ptcone20` $< 0.05 \cdot p_{\text{T}}$
  - Calorimeter Isolation: `topoetcone20` $< 0.065 \cdot E_{\text{T}}$
- `FixedCutTight`: designed for targeting high-E_{T} photons
  - Track Isolation: `ptcone20` $< 0.05 \cdot p_{\text{T}}$
  - Calorimeter Isolation: `topoetcone40` $< 0.022 \cdot E_{\text{T}} + 2.45$ GeV
- `FixedCutTightCaloOnly`: designed for SM precision measurements
  - Track Isolation: None
  - Calorimeter Isolation: `topoetcone40` $< 0.022 \cdot E_{\text{T}} + 2.45$ GeV

Although the calorimeter-based isolation variables work well in the higher E_{T} regime, the correction for the photon energy leakage into the surrounding calorimeter clusters is overestimated in the lower E_{T} regime for events with large pile-up. As a result, the isolation energy is higher and leads to a decrease in efficiency of the working

points listed above. An additional low E_{T} regime correction is parameterized on similar variables used in the original energy leakage correction and is used to recover events that would otherwise be removed. The final isolation variables are adjusted by adding the new correction before being used in the official working points. After the correction, the isolation efficiencies see an overall increase of around 2.5% (absolute) in the $60-90$ GeV mass range. This low E_{T} regime correction method has been used in other diphoton resonance searches in the low $m_{\gamma\gamma}$ range [85] and will also be used in this search.

A comparison of the signal and background efficiencies as well as the signal to background sensitivity $S/\sqrt{B}$ across the official photon isolation working points is shown in Figure 6.1. The number of background and signal events is defined as the number of MC events falling within a window of $m_X \pm 2 \cdot \sigma_{\mathrm{CB},X}$ for each tested signal mass point m_X where $\sigma_{\mathrm{CB},X}$ is the width of the signal sample as described in Section 7.1. The `FixedCutLoose` working point is shown using the isolation variable `topoetcone20` with and without the low E_{T} regime correction. The `FixedCutTight` and `FixedCutTightCaloOnly` working points increase background efficiency as shown in Figure 6.1a and decrease signal efficiency as shown in Figure 6.1b when compared to the `FixedCutLoose` criteria for the ggH production mode. Furthermore, no improvement in sensitivity is seen by choosing the tighter isolation working points as shown in Figure 6.1c. Thus, the `FixedCutLoose` with the low E_{T} regime correction is used as the nominal isolation criteria in this analysis.

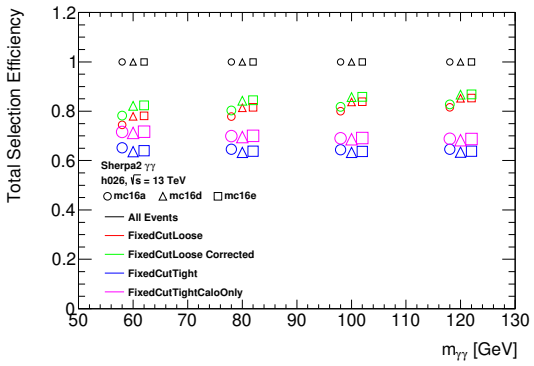

(a) Sherpa2 $\gamma\gamma$ selection efficiencies.

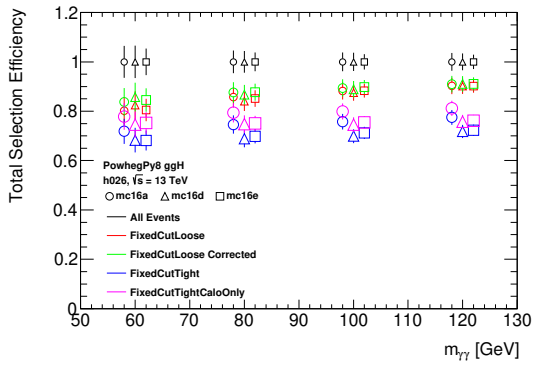

(b) PowhegPy8 ggH selection efficiencies.

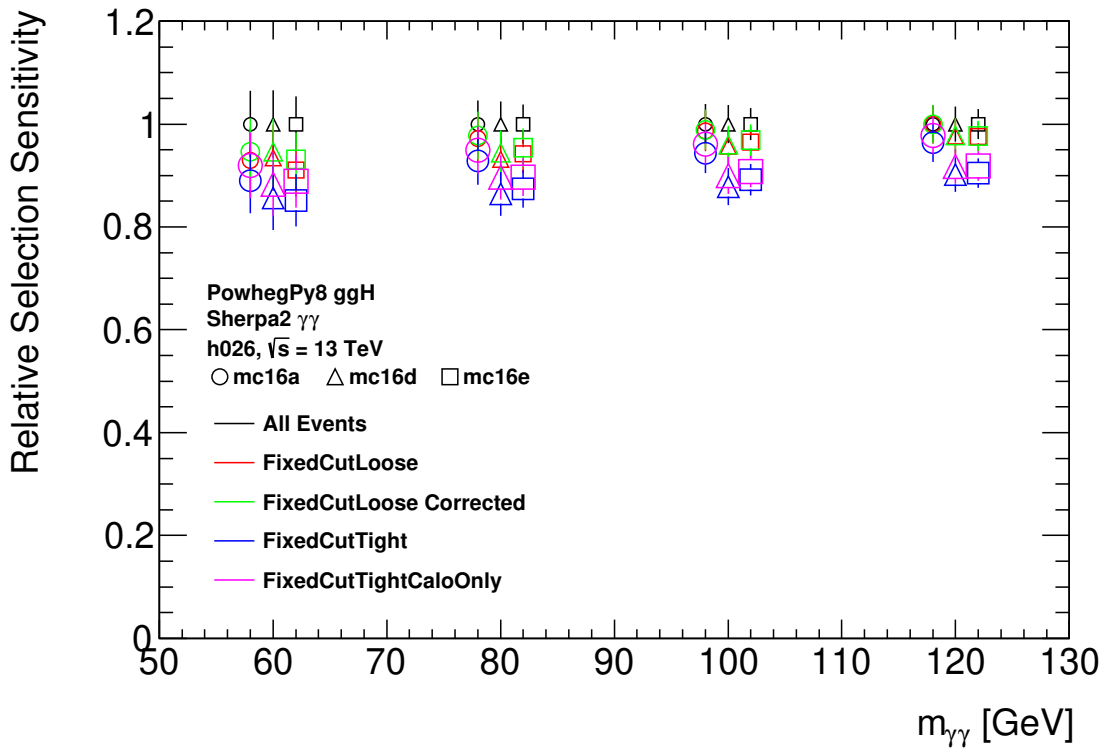

(c) Relative selection sensitivities.

Figure 6.1: The isolation selection efficiencies and the ratios between the signal to background sensitivity $S/\sqrt{B}$ for each MC campaign and each m_X using events in the range $m_X \pm 2 \cdot \sigma_{\mathrm{CB},X}$. The efficiencies compare the use of official photon isolation working points to no photon isolation criteria.

6.3.4 Kinematic Selection

The nominal photon kinematic selection of $E_{\mathrm{T}} > 22$ GeV used in this search is driven by the threshold of the optimal lowest E_{T} unprescaled trigger as described in Section 6.2. This kinematic criteria, which imposes the E_{T} requirement on both photon candidates, creates a "turn-on" effect in the diphoton invariant mass range 40 GeV $< m_{\gamma\gamma} <$ 60 GeV as shown in Figure 6.2 and impacts the lower end of the mass range considered in this analysis. To avoid the necessity of modeling this shape feature, the search is limited to a mass range after 60 GeV where the $m_{\gamma\gamma}$ distribution smoothly decreases. This lower bound allows monotonically decreasing functions to be used for describing the diphoton continuum background shape.

Any function with a smoothly decaying tail, such as an exponential or a power law function, would sufficiently model the smoothly falling background shape. However, the shoulder feature of the "turn-on" effect is still present in the background shape at 60 GeV $< m_{\gamma\gamma} <$ 80 GeV as shown in Figure 6.2 and would require higher order functions to be used in the background modeling. Simply increasing the kinematic cuts on the photon transverse energy will only shift the "turn-on" effect to a higher $m_{\gamma\gamma}$ value. By applying a relative kinematic cut of $E_{\mathrm{T}}/m_{\gamma\gamma} > 22\ \mathrm{GeV}/m_{\mathrm{cusp}}$ such that the transverse energy is scaled by an invariant mass term, the shape of the $m_{\gamma\gamma}$ distribution starts to decrease abruptly at $m_{\gamma\gamma} \approx m_{\mathrm{cusp}}$ and allows a simple lower order function such as an exponential polynomial or Bernstein polynomial to be used for background modeling as described later in Section 7.3.2. The $m_{\gamma\gamma}$ distribution of the diphoton background for various sets of relative kinematic cuts with 30 GeV $< m_{\mathrm{cusp}} <$ 60 GeV is shown in Figure 6.3. Improvement in the signal-to-background sensitivity has also been seen for other similar diphoton searches by cutting on the relative transverse energy of each photon [47] [83].

A comparison of the signal and background efficiencies as well as the signal to background sensitivity $S/\sqrt{B}$ across the various sets of relative kinematic cuts is

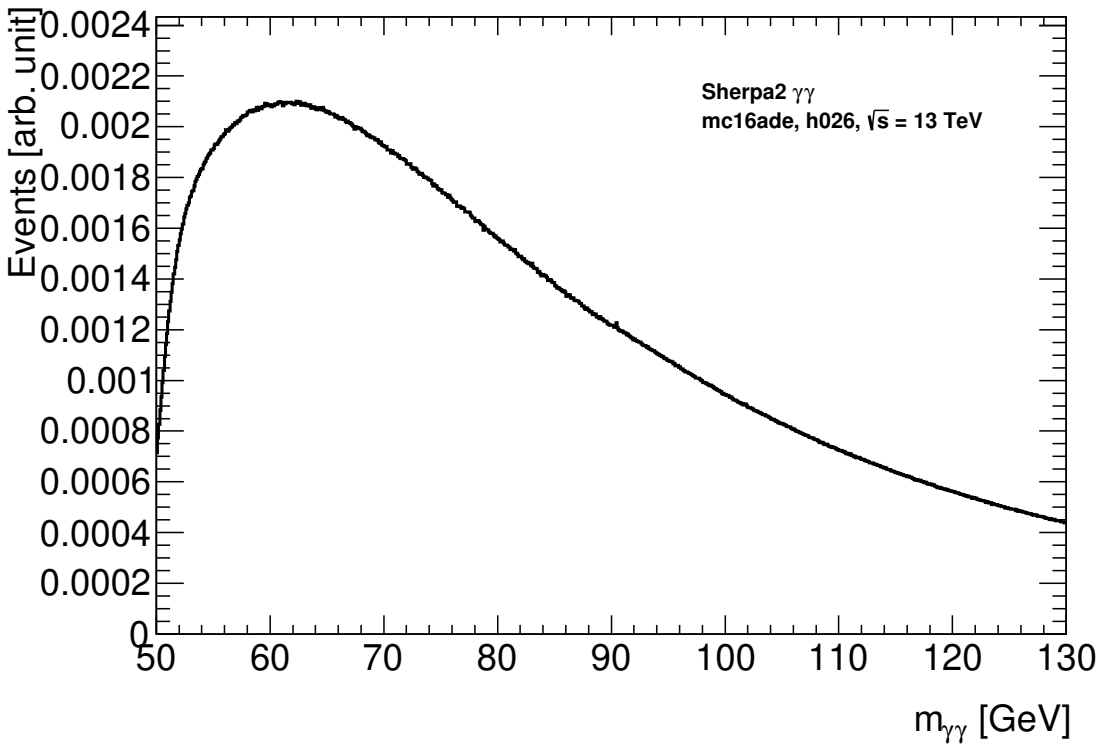

Figure 6.2: The diphoton invariant mass spectrum after applying the trigger and kinematic selection of $E_{\mathrm{T}} > 22\,\mathrm{GeV}$ on each photon which causes the "turn-on" effect in the diphoton invariant mass range $40\,\mathrm{GeV} < m_{\gamma\gamma} < 60\,\mathrm{GeV}$.

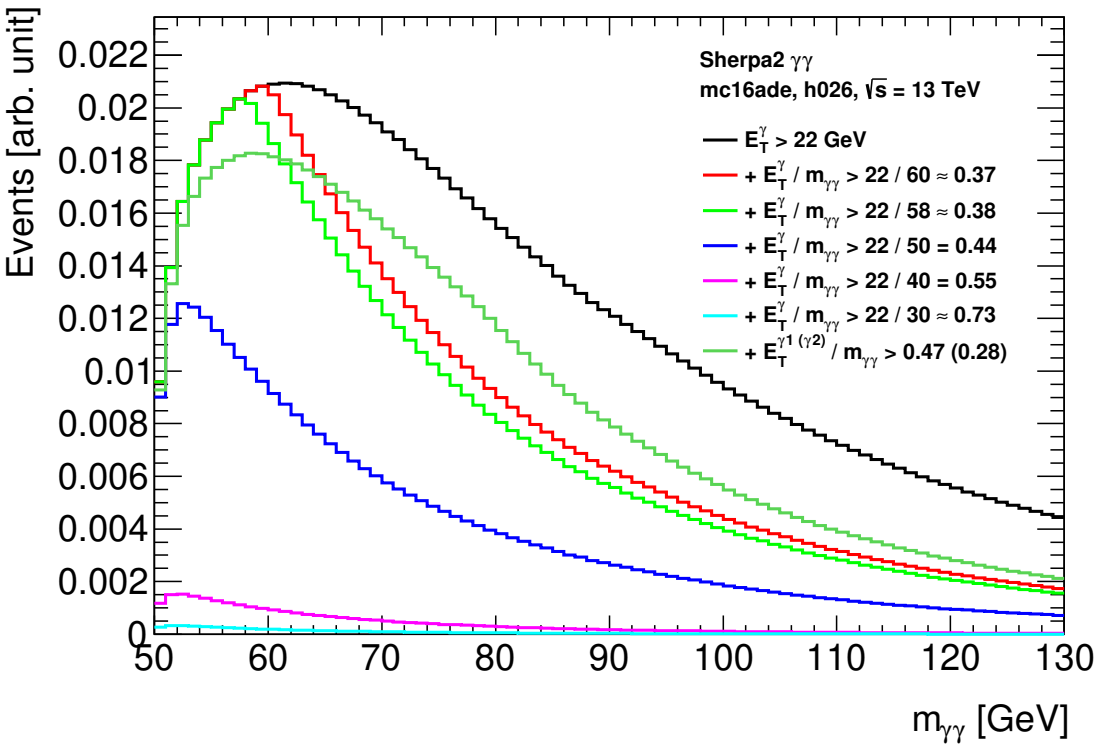

Figure 6.3: The diphoton invariant mass spectrum of the diphoton background continuum with various sets of relative kinematic cuts applied on the photon transverse energies.

shown in Figure 6.4. Similar to the isolation selection study, the number of background and signal events is defined as the number of MC events falling within a window of $m_X \pm 2 \cdot \sigma_{\mathrm{CB},X}$ for each tested signal mass point m_X where $\sigma_{\mathrm{CB},X}$ is the width of the signal sample as described in Section 7.1. The efficiencies are normalized relative to the number of events that pass the nominal photon kinematic selection $E_{\mathrm{T}} > 22$ GeV. The signal efficiency of such cuts is very low for $m_{\mathrm{cusp}} < 40$ GeV at less than 12% for the ggH samples as shown in Figure 6.4b and less than 54% for the Sherpa2 diphoton background as shown in Figure 6.4a. In general, adding stricter relative E_{T} cuts decreases the relative signal sensitivity since the decrease in signal events is not compensated by a large enough decrease in background events. Furthermore, the relative signal sensitivity tends to decrease quickly with higher mass values m_X for strict relative E_{T} cuts as shown in Figure 6.4c.

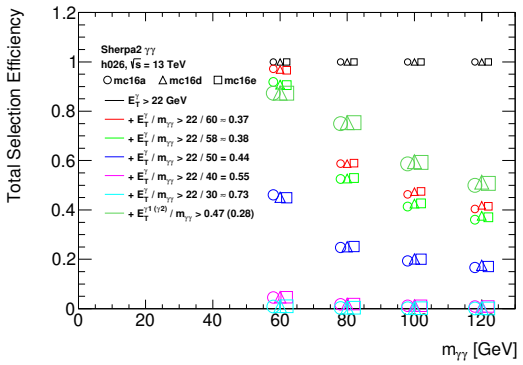

(a) Sherpa2 $\gamma\gamma$ selection efficiencies.

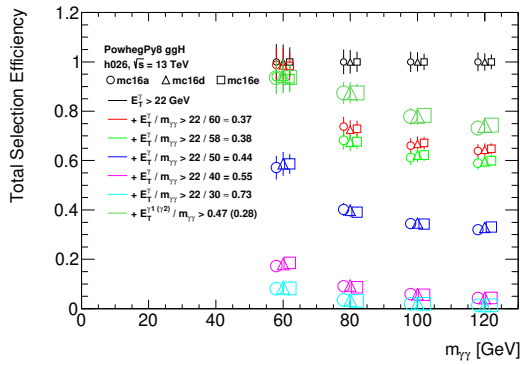

(b) PowhegPy8 ggH selection efficiencies.

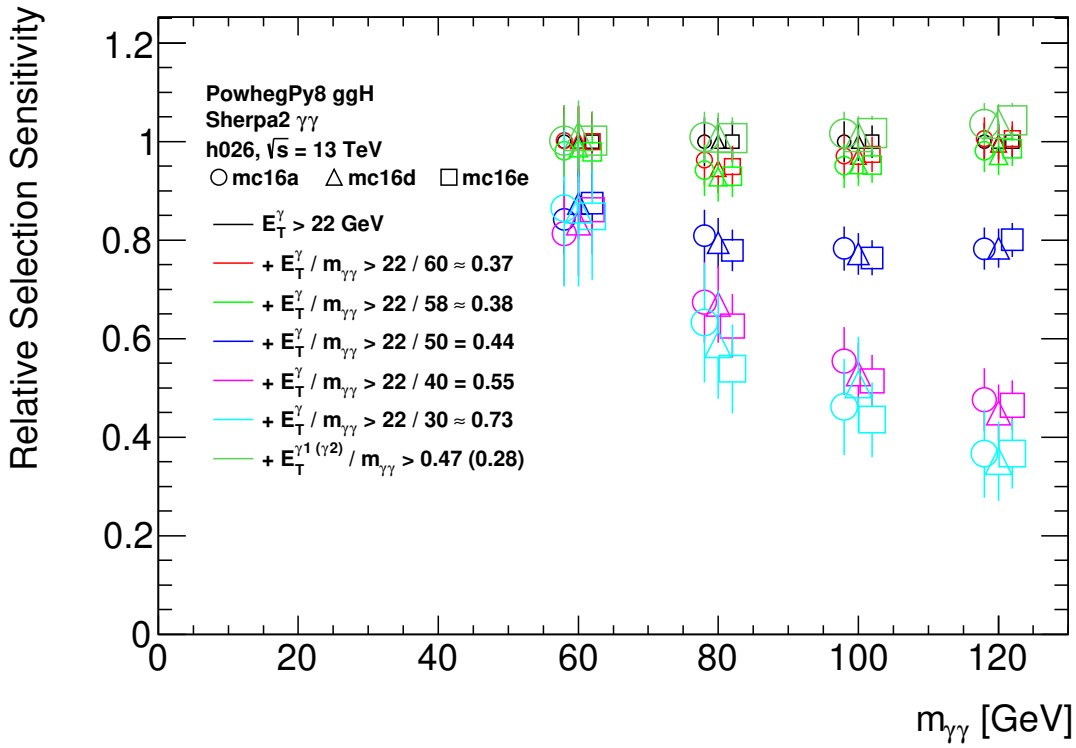

(c) Relative selection sensitivities.

Figure 6.4: The selection efficiencies and the ratios between the signal to background sensitivity $S/\sqrt{B}$ for each MC campaign and each m_X using events in the range $m_X \pm 2 \cdot \sigma_{\mathrm{CB},X}$. The efficiencies compare the use of various sets of relative kinematic cuts applied on the photon E_{T} to the nominal $E_{\mathrm{T}} > 22\,\mathrm{GeV}$ cuts.

Asymmetric kinematic cuts can also be applied instead such that each of the two photons have different kinematic criteria. Despite an improvement in the relative signal sensitivity when asymmetric relative kinematic cuts are used, the shoulder feature from the "turn-on" effect persists as shown in Figure 6.3. Thus, the symmetric $E_{\mathrm{T}}/m_{\gamma\gamma} > 22/58 \approx 0.38$ relative kinematic cuts are chosen together with the nominal $E_{\mathrm{T}} > 22$ GeV cuts to ensure a smooth exponentially decaying background shape for background modeling. The cusp shape at $m_{\gamma\gamma} = 58$ GeV replaces the "turn-on" shape in the low mass range and allows the falling background to be fit with exponential functions starting at $m_{\gamma\gamma} = 60$ GeV. The additional padding 58 GeV $< m_{\gamma\gamma} <$ 60 GeV range is also useful when smoothing the diphoton background continuum using GPR as described in Section 7.3.2.1.

6.3.5 Photon Conversion Categorization

The $Z \to ee$ resonant background is produced through the Drell-Yan (DY) process and contains a large number of electron objects that are misidentified as photon objects — a process referred to as electrons faking photons — during the reconstruction process described in Section 4.1. Since this resonance background at $m_{\gamma\gamma} \approx 90$ GeV lies within the mass range of this search, many step are taken to reduce its contribution to the expected background model. While a small fraction of the $Z \to ee$ electrons are reconstructed as unconverted photons, most of these fake photons are expected to be reconstructed as converted photons whereas only approximately 30% of the real photons from the expected signal and diphoton background processes are expected to be reconstructed as converted photons. With this discrepancy in conversion status tendency between the fake and real diphoton processes, diphoton events can be separated using the conversion status of each photon to make signal-enriched and signal-depleted categories. The signal-enriched categories present a low background statistics region where signal events are retained at high efficiency. On the

other hand, the large presence of background events in the signal-depleted categories provides a validation region for the background models. Thus, the combined use of the two types of categories can boost the signal-to-background sensitivity of the analysis as a whole.

Since the $Z \to ee$ resonant background level depends on the conversion status of the leading γ_1 and subleading γ_2 photons, the following track-based categories as described in Section 4.1.4 for photon conversion status are considered:

- Unconverted (U): unconverted photon
- Converted (C): converted photon
  - 1-track: single-track converted photon
    - Single SCT: one track only with SCT hits
    - Single TRT: one track only with TRT hits only (no SCT hits)
  - 2-track: double-track converted photon
    - Double SCT: two tracks with SCT hits
    - Double TRT: two tracks with TRT hits only (no SCT hits)
    - Double SCT/TRT: one track with SCT hits, and one with TRT hits only (no SCT hits)

Using these individual photon conversion status labels, different photon conversion categorization schemes of the diphoton events are considered based on the conversion status of the leading and subleading photons:

- 4-categories: each photon can be unconverted or converted
- 9-categories: each photon can be unconverted, single-track converted, or double-track converted

- 36-categories: each photon can be unconverted or any of the 5 types of single-track and double-track converted

The overall signal-to-background sensitivity gain is used to study the impact of using different photon conversion categorization schemes. The signal significance or sensitivity Z using the $X \to \gamma\gamma$ process as the signal and the $Z \to ee$ process as the background is defined as

$$Z = \frac{N_{X\to\gamma\gamma}}{\sqrt{N_{Z\to ee}}}, \tag{6.1}$$

where N_i is defined as the number of MC events falling within a window of $m_X \pm 2 \cdot \sigma_{\mathrm{CB},X}$, $\sigma_{\mathrm{CB},X}$ is the width of the signal sample as described in Section 7.1, and $m_X = 90$ GeV. The significance for a category i can then be written as

$$Z_i = \frac{f_i^{X\to\gamma\gamma} \cdot N_{X\to\gamma\gamma}}{\sqrt{f_i^{Z\to ee} \cdot N_{Z\to ee}}}, \tag{6.2}$$

where f_i is the fraction of $\gamma\gamma$ events in category i for a given production process. The combined significance for using a categorization scheme with N categories can then be written as

$$Z_{N \text{ categories}} = \sqrt{\sum_i Z_i^2} = Z_{\text{no categories}} \sqrt{\sum_i \left(\frac{f_i^{X\to\gamma\gamma}}{\sqrt{f_i^{Z\to ee}}} \right)^2}. \tag{6.3}$$

A figure of merit (FoM) value can then be defined as

$$\text{FoM} = \sqrt{\sum_i \left(\frac{f_i^{X\to\gamma\gamma}}{\sqrt{f_i^{Z\to ee}}} \right)^2}, \tag{6.4}$$

which represents the improvement of using a categorization scheme with N categories with respect to not using a photon conversion categorization scheme. The event fractions are derived after applying the trigger, photon isolation, and photon ID selection along with the relative kinematic cut of $E_{\mathrm{T}}/m_{\gamma\gamma} > 22/58$.

The FoM for the 4, 9, and 36-category schemes are 1.80, 1.87, and 1.90 respectively. While there is a small gain in sensitivity from using a larger number of conversion categories, separating the samples into such precise categories leads to some categories having a very low number of events. The category with the fewest events in the 9 category scheme contains only 44.2 (1.6% of the total) $X \to \gamma\gamma$ signal events and 3620.2 (1.3% of the total) $Z \to ee$ background events. More than half of the categories in the 36 category scheme contains fewer than 10 $X \to \gamma\gamma$ signal events and 2000 $Z \to ee$ background events. Additionally, the small gain in sensitivity from using a large number of categories is further reduced after applying the ambiguity BDT categorization described in Section 6.3.6: the FoM for each of the three schemes becomes 2.03, 2.03, and 2.07, respectively, after applying the ambiguity BDT criteria. Thus, the most simple non-trivial categorization scheme for the γ_1/γ_2 photon conversion status is selected:

- unconverted-unconverted (UU),
- unconverted-converted (UC),
- converted-unconverted (CU),
- converted-converted (CC).

This conversion-based categorization will be used in both the model-dependent and model-independent method of the diphoton resonance search.

The different values of $f_i^{X\to\gamma\gamma}/\sqrt{f_i^{Z\to ee}}$ for the nominal categorization scheme is given in Table 6.6. Since signal samples with a resonance mass of $m_X = 90$ GeV were not generated for this analysis, an approximation for this missing mass point is made by taking the average between the number of signal events found for $m_X = 80$ GeV and 100 GeV. This estimate is used to compare the signal fractions to the $Z \to ee$ background fractions at $m_Z \approx 90$ GeV. The fraction of photons in a given conversion

status between the leading or subleading photon are very comparable, motivating the merging of categories where the conversion flavor of the leading and subleading photons can be exchanged. As a result, the UC category will be defined to describe diphoton events that fall in either the UC or CU conversion category. However, the modeling of the resonant $Z \to ee$ background in Section 7.3.3 will be performed separately for the UC and CU categories.

$f_i^{Z\to ee}$ (%)	*Subleading* γ	
	Unconverted	Converted
Leading γ		
Unconverted	9.1	16.8
Converted	21.8	52.3
$f_i^{X\to\gamma\gamma}$ (%)	*Subleading* γ	
	Unconverted	Converted
Leading γ		
Unconverted	50.6	19.8
Converted	20.7	8.9
$f_i^{X\to\gamma\gamma}/\sqrt{f_i^{Z\to ee}}$	*Subleading* γ	
	Unconverted	Converted
Leading γ		
Unconverted	1.68	0.48
Converted	0.44	0.12

Table 6.6: The percentage of events containing photons reconstructed as unconverted or converted in simulated $Z \to ee$ and $X \to \gamma\gamma$ samples and the relative significance per photon conversion category $f_i^{X\to\gamma\gamma}/\sqrt{f_i^{Z\to ee}}$ for all three MC campaigns combined. An average event count is taken between the signal samples with $m_X = 80\,\text{GeV}$ and $100\,\text{GeV}$ to approximate the expected event count for a signal sample at $m_X = 90\,\text{GeV}$. The FoM for this 4-category scheme is 1.804.

6.3.6 Elimination of Ambiguous Electron Fakes

As described in Section 4.1.6, energy superclusters that are reconstructed in the calorimeter can be classified as ambiguous electron/photon objects. In resonance searches that utilize photons, these ambiguous objects are all retained and treated

as photons. This inclusive identification leads to a large contamination of electrons appearing as photons where the electrons originate from the DY process as shown in Table 6.7. After categorizing the diphoton events by photon conversion status, the ambiguous events from both the signal and background are predominantly found in categories containing at least one converted photon as detailed in Table 6.7. To reduce a large component of resonant background and enhance the signal-to-background sensitivity in the conversion categories, a study is performed to better classify the ambiguous objects and remove the electron faking photon events by using a multivariate classifier [100].

Production Mode	Fraction of Ambiguous Events			
	Inclusive	UU	UC	CC
Sherpa2 $\gamma\gamma$	0.24	0.13	0.30	0.49
PowhegPy8 ggH	0.24	0.13	0.30	0.49
PowhegPy8 $Z \to ee$	0.71	0.34	0.63	0.89

Table 6.7: The fraction of events containing ambiguous photons in each photon conversion category in simulated Sherpa2 $\gamma\gamma$, PowhegPy8 ggH, and PowhegPy8 $Z \to ee$ samples.

The overall presence of the $Z \to ee$ resonant background after photon conversion categorization is shown in Figure 6.5. The resonant background is superimposed on top of the diphoton background continuum which contains both the irreducible $\gamma\gamma$ component and the reducible $\gamma j + jj$ component derived from the nominal control region of the data described in Section 7.3.1.3. This $Z \to ee$ background significantly impacts the signal sensitivity in the region around the Z boson mass $m_Z \approx 90$ GeV as shown in the expected limit plot from a previous ATLAS diphoton resonance search in Figure 6.6 [55].

To reduce this resonant background and its impact on the signal sensitivity, a multivariate classifier is used to better classify these ambiguous objects. A BDT is developed and trained using `LightGBM` [66] on single photon and single electron simulated

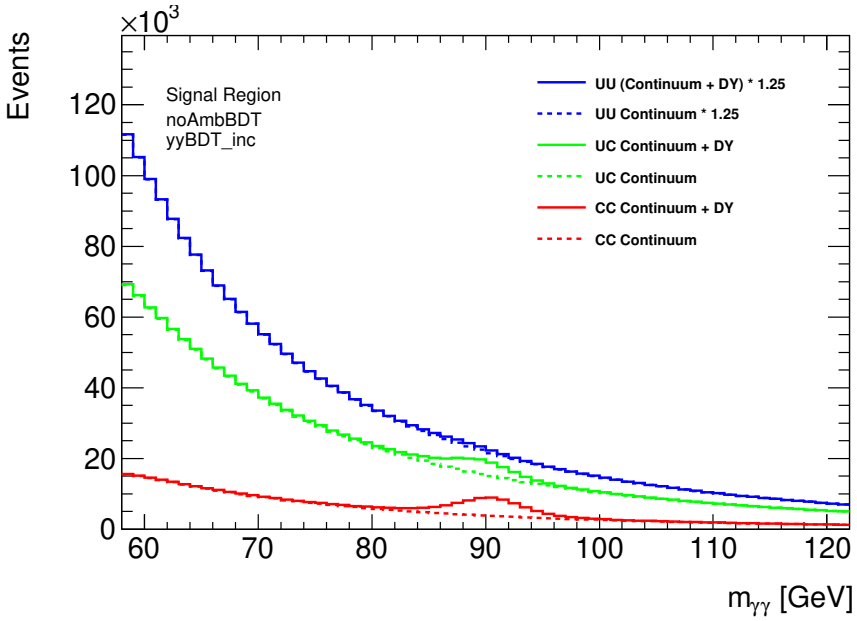

Figure 6.5: The predicted diphoton invariant mass distribution separated by photon conversion categories. The effects of the continuum background using the MC Sherpa $\gamma\gamma$ signal region with the data $\gamma j + jj$ nominal control region as described in Section 7.3.1.3 and the fake photon background from $Z \rightarrow ee$ decays are shown in each distribution. A scale factor of 1.25 is applied to the UU category histograms to separate them visually from those for the UC category.

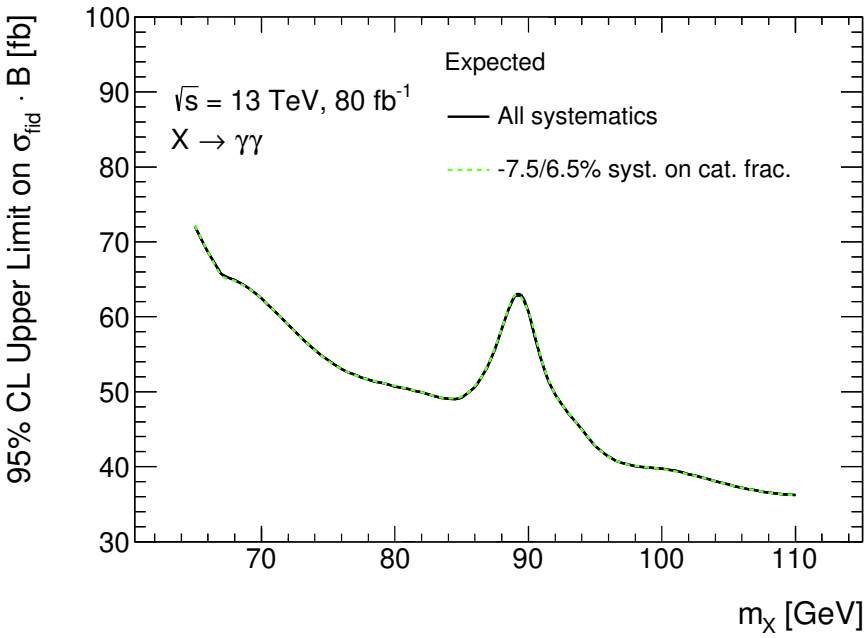

Figure 6.6: The expected limit on the diphoton invariant mass distribution in the low-mass regime from a previous ATLAS diphoton resonance search [55]. The limit in the region around the Z boson worsens due to the impact of the background from DY electrons faking photons.

MC samples. The gradient BDT uses electron track and photon conversion variables during training and evaluation to label ambiguous candidates as more electron-like or more photon-like. The BDT can then assign a score $\xi_{\gamma 1}, \xi_{\gamma 2}$ in the interval $[0, 1]$ for the leading and subleading photon candidate, respectively, in a diphoton event. A score closer to 0 represents an electron-like object, and a score closer to 1 represents a photon-like object.

The 2D distributions of the leading and subleading photon ambiguity BDT score for the PowhegPy8 ggH at $m_X = 100$ GeV, PowhegPy8 $Z \to ee$, and Sherpa2 $\gamma\gamma$ samples are shown in Figure 6.7 for each photon conversion category. The signal sample with a resonance mass of $m_X = 100$ GeV was chosen to approximate the BDT score distribution for the ggH production mode at $m_X = 90$ GeV. This estimate is used to compare the BDT score distribution of the signal to that of the $Z \to ee$ background at $m_Z \approx 90$ GeV. The distributions show that the majority of real

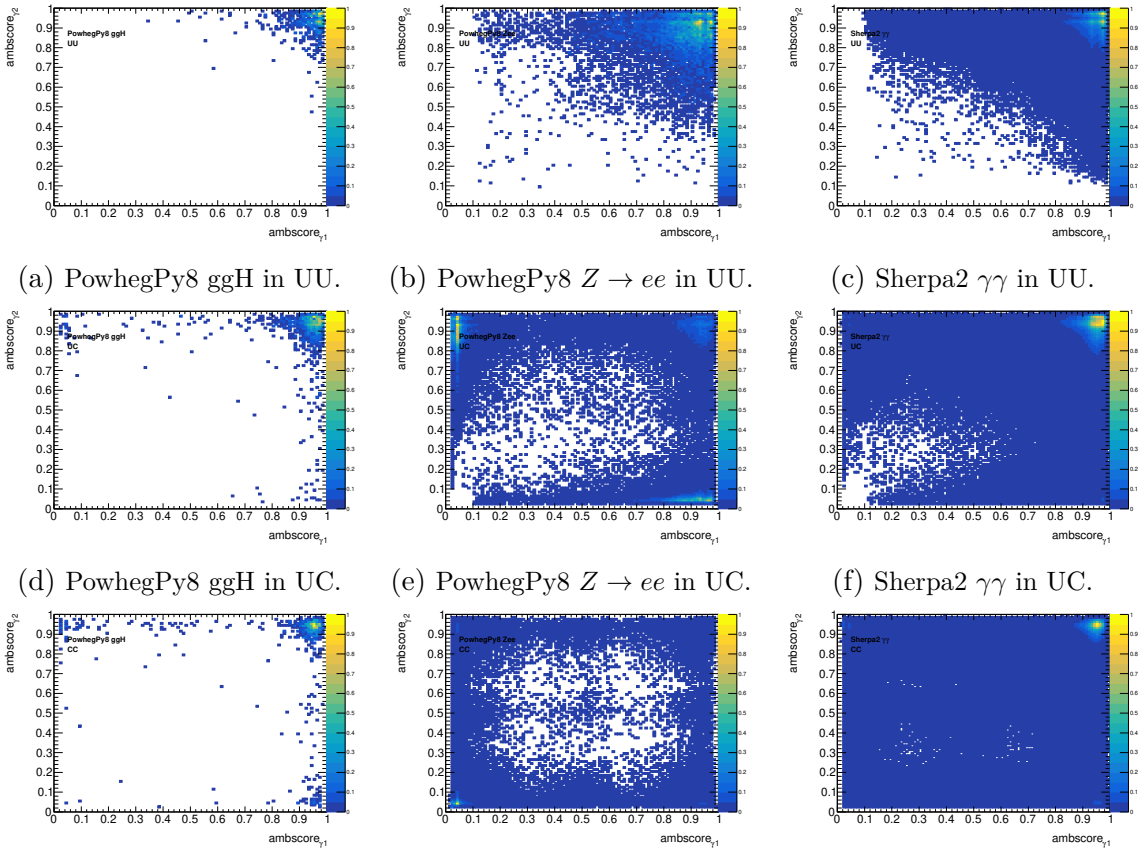

(a) PowhegPy8 ggH in UU. (b) PowhegPy8 $Z \to ee$ in UU. (c) Sherpa2 $\gamma\gamma$ in UU.

(d) PowhegPy8 ggH in UC. (e) PowhegPy8 $Z \to ee$ in UC. (f) Sherpa2 $\gamma\gamma$ in UC.

(g) PowhegPy8 ggH in CC. (h) PowhegPy8 $Z \to ee$ in CC. (i) Sherpa2 $\gamma\gamma$ in CC.

Figure 6.7: The 2D distribution of photon ambiguity BDT scores for the leading and subleading photon candidates in the PowhegPy8 ggH at $m_X = 100\,\text{GeV}$, the PowhegPy8 $Z \to ee$, and the Sherpa2 $\gamma\gamma$ sample for each photon conversion category.

diphoton events are found where both photon candidates have high ambiguity BDT scores while the fake diphoton events tend to be found where at least one of the scores is low.

The minimum value between the two BDT scores `minBDTscore` is used as the discriminant to distinguish the ambiguous events. The score distribution of each of the three samples for the `minBDTscore` discriminant is shown in Figure 6.8 for each photon conversion category. These distributions have peaks near a score of 1 since both distributions contain non-ambiguous photon candidates.

The passing criteria used to remove ambiguous events with electron-like objects

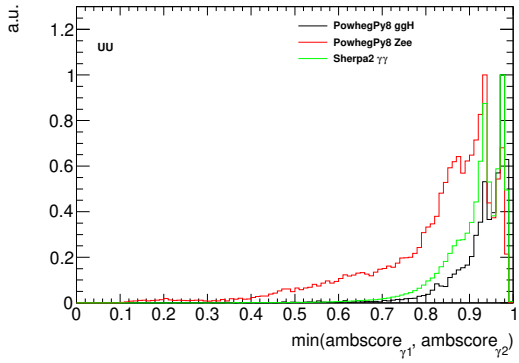

(a) Score distribution in UU.

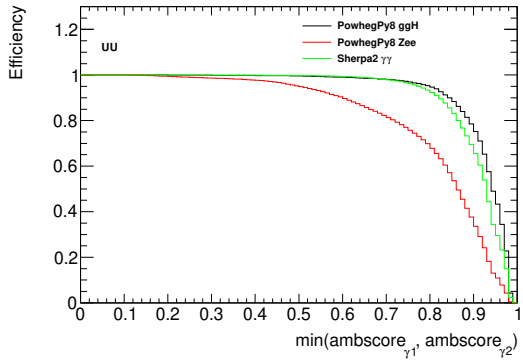

(b) 1 - cumulative distribution in UU.

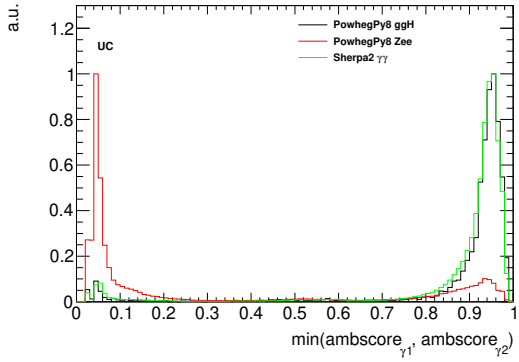

(c) Score distribution in UC.

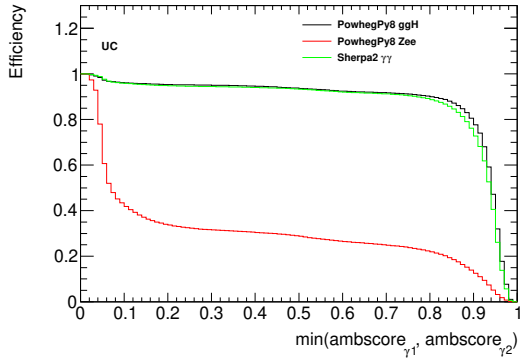

(d) 1 - cumulative distribution in UC.

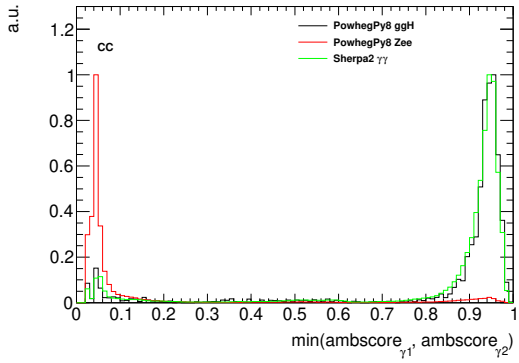

(e) Score distribution in CC.

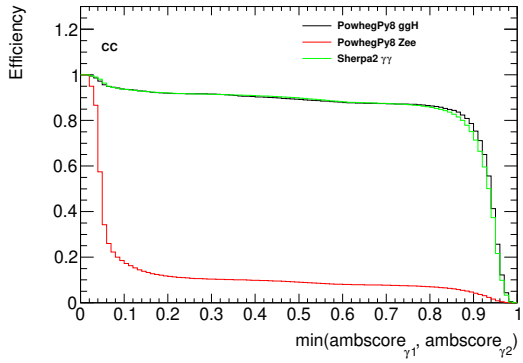

(f) 1 - cumulative distribution in CC.

Figure 6.8: The score distribution and complementary cumulative distribution of the photon ambiguity BDT score $\xi_{\texttt{minBDTscore}}$ for the PowhegPy8 ggH at $m_X = 100\,\text{GeV}$, PowhegPy8 $Z \to ee$, and Sherpa $\gamma\gamma$ samples for each photon conversion category.

is chosen by studying the efficiency of the event-level scores:

$$\epsilon_{\texttt{minBDTscore}} = \frac{N_{\texttt{minBDTscore}}}{N_{\text{selection}}} \tag{6.5}$$

where $N_{\text{selection}}$ is the number of events after applying the trigger, photon ID, and kinematic selections and $N_{\texttt{minBDTscore}}$ is the number of events after applying the ambiguity BDT selection along with all the other selections. The ambiguity BDT selection is applied such that any event with an event-level score $\xi_{\texttt{minBDTscore}}$ greater than or equal to a chosen value $\Xi_{\texttt{minBDTscore}}$ passes the ambiguity BDT criteria. The efficiency as a complementary cumulative function of $\Xi_{\texttt{minBDTscore}}$ for each of the three samples is shown in Figure 6.8 for each photon conversion category.

This discriminant is found to provide the best improvement in signal-to-background sensitivity of approximately 22.1% by setting a criteria of $\Xi_{\texttt{minBDTscore}} = 0.26$. Since the relative improvement when using `minBDTscore` is stable down to a value of 0.2, a criteria of $\Xi_{\texttt{minBDTscore}} = 0.2$ is chosen as the ambiguity BDT selection in order to maintain a high efficiency for real diphoton events from both the $X \to \gamma\gamma$ signal resonance and diphoton background continuum. The ambiguity BDT criteria selects true photon events with an efficiency of 100%, 97%, and 93% for the UU, UC, and CC categories, respectively. This selection significantly reduces the $Z \to ee$ background in the UC and CC photon conversion categories by 65% and 90% respectively while having minimal impact in the UU category. The distribution of background events passing and failing the ambiguity BDT selection is shown in Figure 6.9.

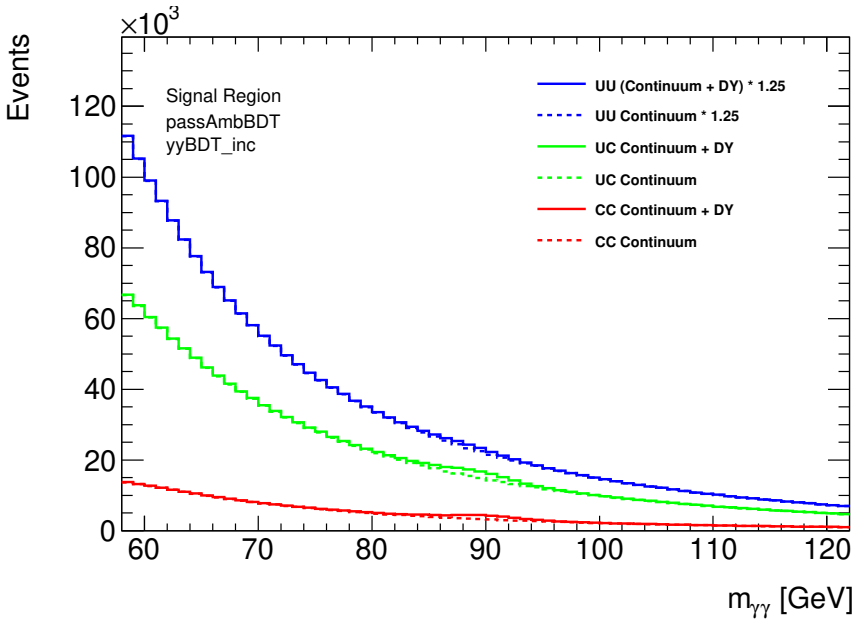

(a) Distribution for events passing ambiguiity BDT selection.

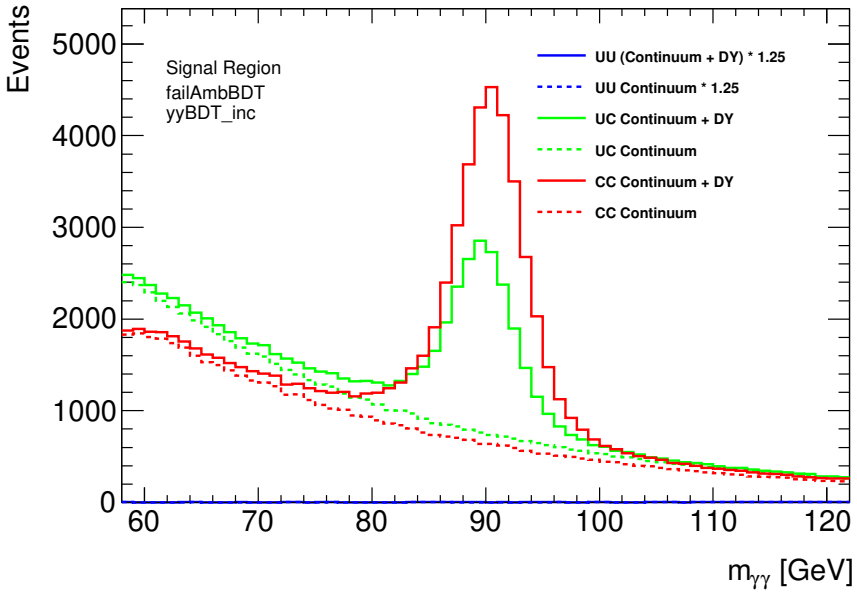

(b) Distribution for events failing ambiguiity BDT selection.

Figure 6.9: The predicted diphoton invariant mass distribution for events that pass and fail the ambiguiity BDT selection criteria separated by photon conversion categories. The effects of the continuum background using the MC Sherpa $\gamma\gamma$ signal region with the data $\gamma j + jj$ nominal control region as described in Section 7.3.1.3 and the fake photon background from $Z \to ee$ decays are shown in each distribution. A scale factor of 1.25 is applied to the UU category histograms to separate them visually from those for the UC category.

6.3.7 Classification of Diphoton Events

At $m_{\gamma\gamma}$ regions away from the resonant $Z \to ee$ background, the diphoton background continuum is dominated by non-resonant QCD diphoton events as described in Section 7.3.1.2. Similar to the strategy of using photon conversion categories, diphoton events can be separated using the kinematic information of each photon to make signal-enriched and signal-depleted classes which can increase the signal to background sensitivity of the analysis as a whole.

A second BDT is designed to categorize the diphoton events in this analysis by using the ROOT multivariate analysis (TMVA) toolkit [65] within the general purpose high energy physics data analysis framework Rapid Object-Oriented Technology (ROOT) [30] developed at CERN. The Sherpa2 $\gamma\gamma$ samples are used to represent the diphoton background, and all signal resonance production modes ggH, VBF, ttH, VH are used to represent the diphoton signal for training the diphoton BDT.

The kinematic variables used to train the BDT are chosen with both physical, statistical, and modeling motivations. Since the signal samples are generated at discrete resonance mass points of $m_X = 60$, 80, 100, and 120 GeV, variables that are correlated with $m_{\gamma\gamma}$, such as $E_{\mathrm{T}}^{\gamma 1}$ and $E_{\mathrm{T}}^{\gamma 2}$, are engineered to reduce their correlation with the diphoton invariant mass as shown in Table 6.8. The background samples are also restricted to the mass range 58 GeV $< m_{\gamma\gamma} <$ 130 GeV to prevent the diphoton BDT from learning trends in mass ranges where signal samples are not available.

Correlation with $m_{\gamma\gamma}$				
Sample Type	$p_{\mathrm{T}}^{\gamma 1}$	$p_{\mathrm{T}}^{\gamma 1}/m_{\gamma\gamma}$	$p_{\mathrm{T}}^{\gamma 2}$	$p_{\mathrm{T}}^{\gamma 2}/m_{\gamma\gamma}$
Signal	0.06	0.05	0.03	0.07
Background	0.38	0.11	0.44	0.19

Table 6.8: The correlation matrix between the diphoton invariant mass $m_{\gamma\gamma}$ and variables highly correlated with it in the signal and background samples used for training the diphoton BDT.

Photon ID variables and the $m_{\gamma\gamma}$ resolution are found to be useful in separating the diphoton continuum from resonant diphoton signal. However, these variables cause significant shape distortions in the background shape which are problematic when attempting to model the background with simple low order functions. As a result, the photon ID variables are replaced with the ambiguity BDT scores of the leading and sub-leading photons, and the resolution variable is omitted completely.

Eight total variables are selected to train the diphoton BDT:

- The ambiguity BDT scores $\xi_{\gamma 1}, \xi_{\gamma 2}$ of the leading and subleading photons
- The `minBDTscore` $= \min(\xi_{\gamma 1}, \xi_{\gamma 2})$ discriminant
- The cosine of the difference in azimuthal angle $\Delta\phi$ between the leading and subleading photons
- The pseudo-rapidities $\eta_{\gamma 1}, \eta_{\gamma 2}$ of the leading and subleading photons
- The relative E_{T} of the leading and subleading photons

The ambiguity BDT scores provide higher-level information on photon ID, the azimuthal separation helps distinguish between boosted and back-to-back events, and the pseudo-rapidity helps distinguish between central and forward events. The distributions of the training variables for both signal and background samples are shown in Figure 6.10.

The diphoton BDT consists of 300 trees each with a maximum depth of 2 nodes. Events with negative weighting are ignored during training. All other parameters of the diphoton BDT are set to their default values according to the TMVA toolkit [65]. To avoid overfitting the model to the MC samples and to allow for a general and robust classifier, two disjoint and randomized subsets of ~ 8 total million events taken from each resonance mass point of each signal production mode and from the Sherpa $\gamma\gamma$ background are used during the training and validation of the diphoton

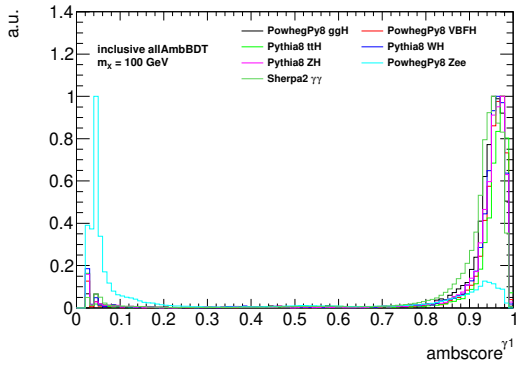

(a) Distribution of $\xi_{\gamma 1}$.

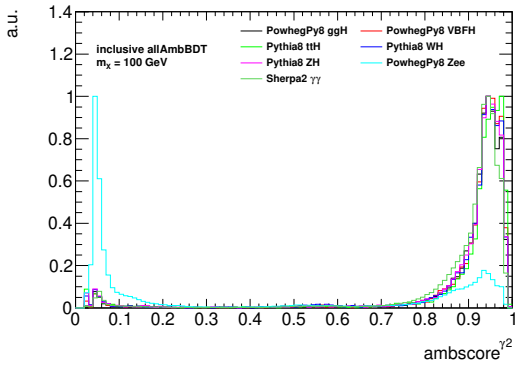

(b) Distribution of $\xi_{\gamma 2}$.

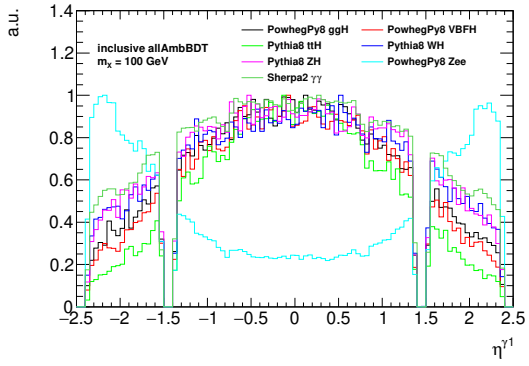

(c) Distribution of $\eta_{\gamma 1}$.

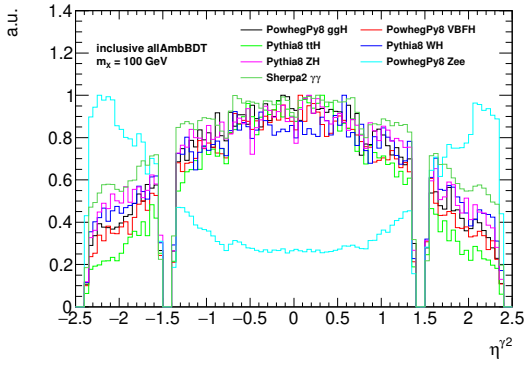

(d) Distribution of $\eta_{\gamma 2}$.

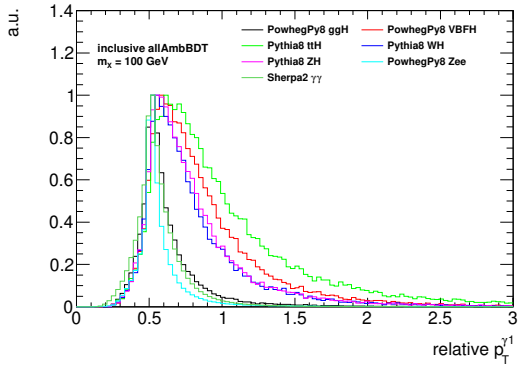

(e) Distribution of $p_{\mathrm{T}}^{\gamma 1}/m_{\gamma\gamma}$.

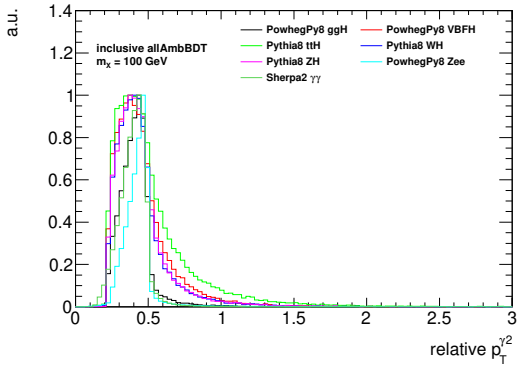

(f) Distribution of $p_{\mathrm{T}}^{\gamma 2}/m_{\gamma\gamma}$.

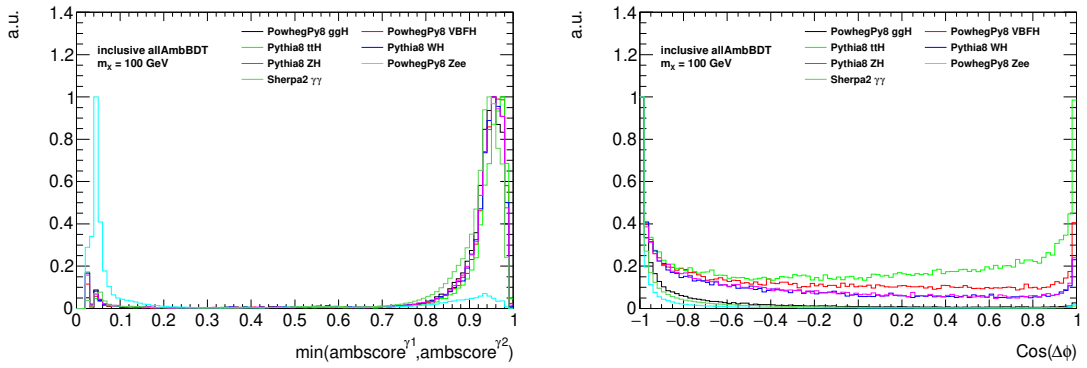

(g) Distribution of $\min(\xi_{\gamma 1}, \xi_{\gamma 2})$.

(h) Distribution of $\cos(\Delta\phi)$.

Figure 6.10: The distribution of diphoton BDT training variables for each signal production mode at $m_X = 100\,\text{GeV}$, the Sherpa2 $\gamma\gamma$ background, and the PowhegPy8 $Z \to ee$ background. The distribution for each sample is normalized separately for shape comparison.

BDT. The trigger, photon isolation, photon ID selections, and nominal kinematic cuts at $E_{\text{T}} > 22$ GeV are applied to each subset. No e/γ ambiguity criteria nor relative E_{T} cuts are applied to the subsets. The training weights of the signal and background class events are normalized to be effectively equivalent and prevent any bias from dataset imbalance. The correlation between variables used in the training of the diphoton BDT for the signal and background samples are listed in Table 6.9.

The BDT assigns a score ζ in the interval $[-1, 1]$ for the diphoton event such that a score closer to -1 represents a background-like event and a score closer to 1 represents a signal-like event. The distributions of diphoton BDT scores from the trained BDT for the signal and background training and testing sets are shown in Figure 6.11. The training and testing sets for signal and background events have similar distributions as determined by a Kolmogorov–Smirnov (KS) test with scores of 0.408 and 0.605, respectively. The importance of a given variable used during training to split decision tree nodes is weighted by the signal-to-background separation gain squared and by the number of events in the node for using the given variable. These importance values are normalized based on its frequency of usage to split a decision tree node and given in Table 6.10.

Correlation Between Diphoton BDT Training Variables								
Signal	$\xi_{\gamma 1}$	$\xi_{\gamma 2}$	$\min(\xi_{\gamma 1}, \xi_{\gamma 2})$	$p_{\mathrm{T}}^{\gamma 1}/m_{\gamma\gamma}$	$p_{\mathrm{T}}^{\gamma 2}/m_{\gamma\gamma}$	$\eta_{\gamma 1}$	$\eta_{\gamma 2}$	$\cos(\Delta\phi)$
$\xi_{\gamma 1}$	1.00	-	0.73	0.01	-	0.01	-	-
$\xi_{\gamma 2}$	-	1.00	0.67	-	-	-	-	-
$\min(\xi_{\gamma 1}, \xi_{\gamma 2})$	0.73	0.67	1.00	0.01	-	-	-	-
$p_{\mathrm{T}}^{\gamma 1}/m_{\gamma\gamma}$	0.01	-	0.01	1.00	0.54	-	-	0.59
$p_{\mathrm{T}}^{\gamma 2}/m_{\gamma\gamma}$	-	-	-	0.54	1.00	-	-	0.54
$\eta_{\gamma 1}$	0.01	-	-	-	-	1.00	0.66	-
$\eta_{\gamma 2}$	-	-	-	-	-	0.66	1.00	-
$\cos(\Delta\phi)$	-	-	-	0.59	0.54	-	-	1.00
Background	$\xi_{\gamma 1}$	$\xi_{\gamma 2}$	$\min(\xi_{\gamma 1}, \xi_{\gamma 2})$	$p_{\mathrm{T}}^{\gamma 1}/m_{\gamma\gamma}$	$p_{\mathrm{T}}^{\gamma 2}/m_{\gamma\gamma}$	$\eta_{\gamma 1}$	$\eta_{\gamma 2}$	$\cos(\Delta\phi)$
$\xi_{\gamma 1}$	1.00	-	0.73	-	-	-	-	-
$\xi_{\gamma 2}$	-	1.00	0.67	-	-	-	-	-
$\min(\xi_{\gamma 1}, \xi_{\gamma 2})$	0.73	0.67	1.00	-	-	-	-	-
$p_{\mathrm{T}}^{\gamma 1}/m_{\gamma\gamma}$	-	-	-	1.00	0.17	-	-	0.43
$p_{\mathrm{T}}^{\gamma 2}/m_{\gamma\gamma}$	-	-	-	0.17	1.00	-	-	0.20
$\eta_{\gamma 1}$	-	-	-	-	-	1.00	0.58	-
$\eta_{\gamma 2}$	-	-	-	-	-	0.58	1.00	-
$\cos(\Delta\phi)$	-	-	-	0.43	0.20	-	-	1.00

Table 6.9: The correlation matrix between variables in the signal and background samples used for training the diphoton BDT. Dashed entries (-) indicate negligible to no correlation between corresponding variables.

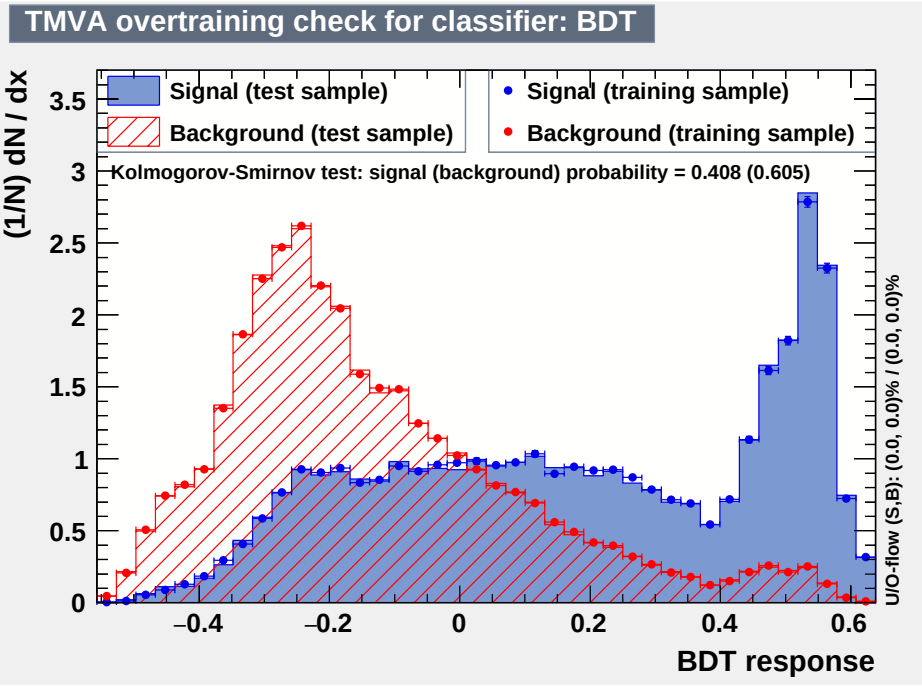

Figure 6.11: The distributions of diphoton BDT scores for the training and validation subsets.

Diphoton BDT Training Variable	Normalized Importance
$\cos(\Delta\phi)$	0.297
$p_{\mathrm{T}}^{\gamma 1}/m_{\gamma\gamma}$	0.196
$p_{\mathrm{T}}^{\gamma 2}/m_{\gamma\gamma}$	0.130
$\eta^{\gamma 1}$	0.113
$\eta^{\gamma 2}$	0.106
$\min(\xi_{\gamma 1}, \xi_{\gamma 2})$	0.056
$\xi_{\gamma 1}$	0.053
$\xi_{\gamma 2}$	0.049

Table 6.10: The normalized importance values for each variable based on its frequency of usage to split a decision tree node. The variable importance is weighted by the signal to background separation gain squared and by the number of events in the node of a given variable.

The normalized diphoton BDT score distribution of all production modes, Sherpa $\gamma\gamma$ background, the nominal data control region as described in Section 7.3.1.3, and the $Z \to ee$ DY background are shown in Figure 6.12.

The nominal data control region described in Section 7.3.1.3 is used to estimate the response of the diphoton BDT on the γj background. Both the diphoton BDT score distribution and the importance value for $\cos(\Delta\phi)$ indicate that the trained BDT places a large emphasis on distinguishing between events where the trajectories of the two photons are in the same direction in the detector (also known as boosted) and those where the trajectories are back-to-back. Production modes such as VBF and ttH usually produce highly boosted Higgs bosons while most of the photon pairs produced in the non-resonant background processes are back-to-back. The ggH production mode usually produces Higgs bosons close to rest as indicated by its background-like distribution of the diphoton BDT score. The distribution for the diphoton BDT score of an SM-like cross-section weighted signal sample and each background sample is shown separately in Figure 6.12. The fraction of events with a diphoton BDT score above a value ζ is shown in Figure 6.13. The relative signal sensitivity for each production mode with respect to the combined background is calculated as a function

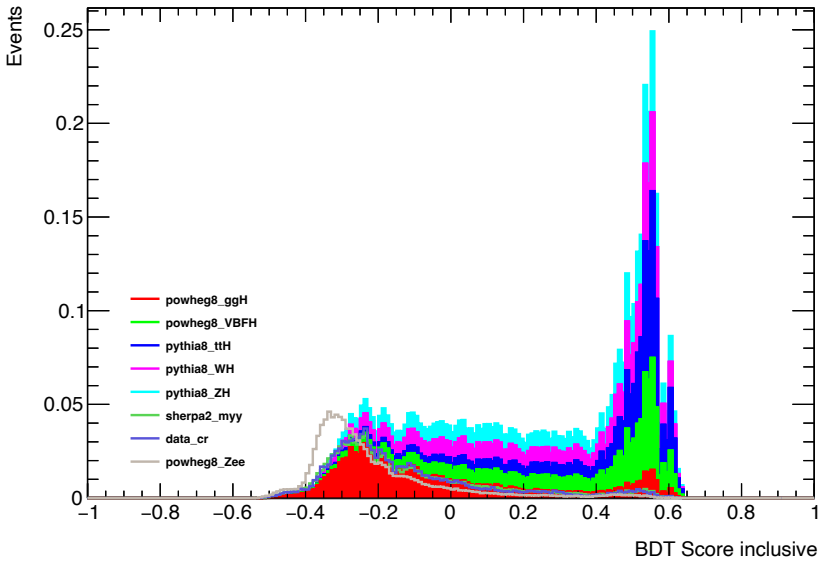

Figure 6.12: The distribution of the diphoton BDT event-level scores for each signal production mode at all four mass points $m_X = 60, 80, 100, 120\,\text{GeV}$, the Sherpa2 $\gamma\gamma$ background, the nominal data control region, and the PowhegPy8 $Z \to ee$ background. The production modes in the cut efficiency is both luminosity weighted and SM-like cross-section weighted while the backgrounds are separately normalized to unity.

of ζ and is shown in Figure 6.14.

The diphoton events will be separated into multiple classes based on their diphoton BDT score. The 3-class classification scheme is studied to determine the effect on overall signal sensitivity by using two diphoton BDT score values ζ_1, ζ_2 to define the boundaries of the three classes of events. The most optimal bounds that maximizes the gain in signal sensitivity are found to create classes with very low background statistics which can lead to significant shape changes in the lower $m_{\gamma\gamma}$ range near 80 GeV. To avoid the need to use complex functions for modeling the background shape, a constraint is applied to the optimization process such that each of the three classes must contain at least 20% of the total diphoton background events.

Similar to photon conversion categorization described in Section 6.3.5, the gain in signal sensitivity from using the diphoton BDT classification can be quantified by

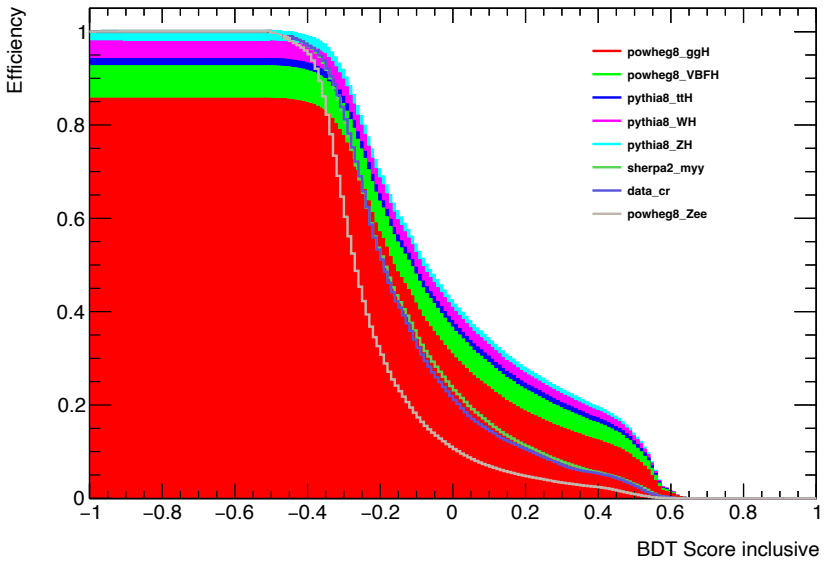

Figure 6.13: The cumulative distribution of the diphoton BDT event-level scores using the score as the lower bound for each signal production mode at all four mass points $m_X = 60, 80, 100, 120\,\text{GeV}$, the Sherpa2 $\gamma\gamma$ background, the nominal data control region, and the PowhegPy8 $Z \to ee$ background. The production modes in the cut efficiency is both luminosity weighted and SM-like cross-section weighted while the backgrounds are separately normalized to unity.

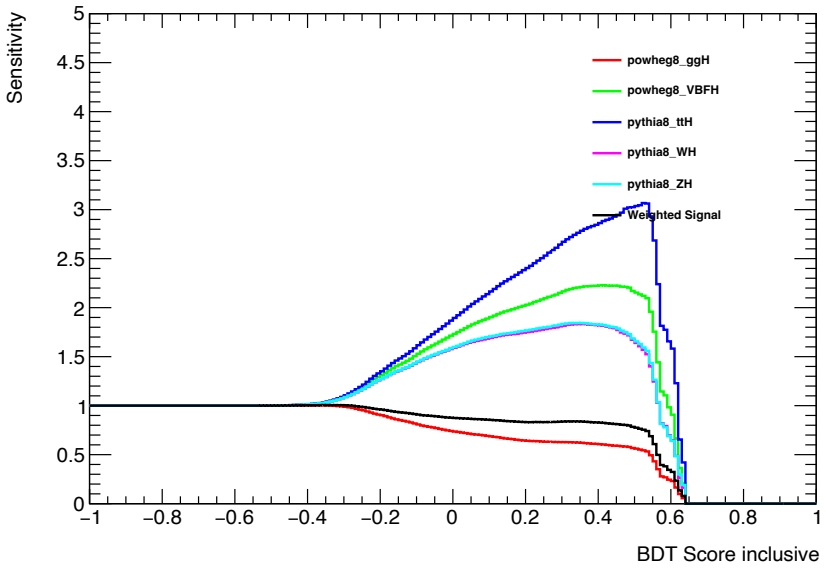

Figure 6.14: The relative signal sensitivity for each production mode after applying the diphoton BDT score criteria relative to no criteria applied.

measuring the signal significance or sensitivity Z with the $X \to \gamma\gamma$ process as the signal and the dominant diphoton background $pp \to \gamma\gamma$ predicted by the Sherpa $\gamma\gamma$ sample defined as

$$Z = \frac{N_{X\to\gamma\gamma}}{\sqrt{N_{pp\to\gamma\gamma}}} \tag{6.6}$$

where N_j is defined as the number of MC events falling within a window of $m_X \pm 2 \cdot \sigma_{\mathrm{CB},X}$, $\sigma_{\mathrm{CB},X}$ is the width of the signal sample as described in Section 7.1, and $m_X = 60, 80, 100, 120$ GeV. The significance per class j can be written as

$$Z_j = \frac{f_j^{X\to\gamma\gamma} \cdot N_{X\to\gamma\gamma}}{\sqrt{f_j^{pp\to\gamma\gamma} \cdot N_{pp\to\gamma\gamma}}}, \tag{6.7}$$

where f_j is the fraction of $\gamma\gamma$ events in each diphoton class, measured both with the $X \to \gamma\gamma$ and non-resonant $pp \to \gamma\gamma$ Sherpa2 $\gamma\gamma$ MC samples. The combined significance can then be written as

$$Z_{N \text{ classes}} = \sqrt{\sum_j Z_j^2} = Z_{\text{no classes}} \sqrt{\sum_j \left(\frac{f_j^{X\to\gamma\gamma}}{\sqrt{f_j^{pp\to\gamma\gamma}}} \right)^2}. \tag{6.8}$$

A FoM value similar to Equation 6.4 can then be written as

$$\text{FoM} = \sqrt{\sum_j \left(\frac{f_j^{X\to\gamma\gamma}}{\sqrt{f_j^{pp\to\gamma\gamma}}} \right)^2}, \tag{6.9}$$

which can be interpreted as the improvement with respect to not using a diphoton BDT classification scheme. The event fractions are derived after applying the trigger, photon isolation, photon ID selection, and nominal kinematic cuts at $E_{\mathrm{T}} > 22$ but without any ambiguity BDT score criteria or relative E_{T} cuts. This calculation of the significance does not take into account the fake diphoton background arising from resonant $Z \to ee$ or reducible $\gamma j + jj$ backgrounds since the former is localized to the

Diphoton BDT Class	SM-like Higgs boson ($m_X = 90$ GeV)						Bkg. ($m_{\gamma\gamma} = 90$ GeV)	
	Total Events	Fraction within Class					$\gamma\gamma$ [GeV^{-1}]	DY [GeV^{-1}]
		ggH	VBF	ttH	WH	ZH		
1	506.28	0.970	0.008	0.002	0.012	0.007	12269.76	1589.41
2	746.12	0.937	0.019	0.005	0.024	0.014	10313.97	566.00
3	1055.34	0.710	0.126	0.048	0.074	0.043	5627.81	203.05
Total	2307.74	84.0	6.6	2.4	4.4	2.6	28211.54	2358.46

Table 6.11: The fractions of events for each production mode estimated at $m_X = 90\,\text{GeV}$ and the number of background events per GeV at $m_{\gamma\gamma} = 90\,\text{GeV}$ for each diphoton BDT class.

diphoton invariant mass range near $m_{\gamma\gamma} = 90$ GeV and the latter contributes much less to the diphoton background continuum as described in Section 7.3.1.3.

The optimal splitting of the 3-class scheme is found at scores of $Z_1^{3\text{ class scheme}} = -0.23$ and $Z_2^{3\text{ class scheme}} = 0.01$ to give a FoM of 1.20. The fraction of each signal production mode in each class is given in Table 6.11. The number of background events from $pp \to \gamma\gamma$ diphoton background and from the resonant $Z \to ee$ background is defined as the 1 GeV average of events in the 89 GeV $< m_{\gamma\gamma} <$ 91 GeV range and is also given in the table.

To further increase the signal sensitivity, the diphoton BDT classification can be convoluted with the photon conversion categorization to create a total of 9 diphoton categories:

- unconverted-unconverted diphoton BDT class 1 (UU1),
- unconverted-unconverted diphoton BDT class 2 (UU2),
- unconverted-unconverted diphoton BDT class 3 (UU3),
- unconverted-converted diphoton BDT class 1 (UC1),
- unconverted-converted diphoton BDT class 2 (UC2),
- unconverted-converted diphoton BDT class 3 (UC3),

$\frac{f_j^{X\to\gamma\gamma}}{\sqrt{f_j^{pp\to\gamma\gamma}}}$	*Diphoton BDT*		
	Class 1	Class 2	Class 3
Photon Conversion			
UU	0.344	0.530	1.019
UC	0.314	0.536	1.028
CC	0.355	0.495	1.036

Table 6.12: Relative sensitivities for each of the 9 categories using both photon conversion categorization and diphoton BDT classification.

- converted-converted diphoton BDT class 1 (CC1),
- converted-converted diphoton BDT class 2 (CC2),
- converted-converted diphoton BDT class 3 (CC3).

The relative sensitivities of each category with respect to using no classification or categorization is given in Table 6.12. The FoM for using this convolution scheme is 2.080. Henceforth, the 9 categories resulting from the convolution of photon conversion categorization and diphoton classification will be referred to as the model-dependent categories. The model-independent method will only utilize the photon conversion categorization scheme and will not use the diphoton BDT The three photon conversion categories used for the model-independent method will be referred to as the model-independent categories.

6.3.8 Selection Efficiency

The final event selections used in this analysis are summarized in Table 6.13. The total and relative selection efficiency in the PowhegPy8 ggH production mode is summarized in Figure 6.15. The main efficiency loss comes from the trigger selection due to its 20 GeV or 22 GeV online E_{T} cuts on the photon candidates as listed in Table 6.4. The preselection criteria which requires two `loose` ID photon candidates each with $E_{\mathrm{T}} > 22$ GeV also has a relative efficiency increasing from 60% to 85% with

Selection	Definition
Trigger	Event must pass triggers detailed in Section 6.2
Preselection	Photons must pass `loose` ID AND $E_{\mathrm{T}} > 22$ GeV AND $\lvert\eta\rvert < 2.37$ with crack region veto
Identification	Photons must pass `tight` ID
Isolation	Photons must pass low-E_{T} corrected `FixedCutLoose`
Relative Kinematic	Photons must have $E_{\mathrm{T}}/m_{\gamma\gamma} > 22/58$
Ambiguity BDT	Event must have `minBDTscore` > 0.2
Photon Conversion	**Category Definitions**
UU Category	Event must have unconverted γ_1, unconverted γ_2
UC Category	Event must have unconverted γ_1, converted γ_2 OR converted γ_1, unconverted γ_2
CC Category	Event must have converted γ_1, converted γ_2
Diphoton BDT	**Class Definitions**
Class 1	Diphoton BDT score must be $-1.00 < \zeta < -0.23$
Class 2	Diphoton BDT score must be $-0.23 < \zeta < 0.01$
Class 3	Diphoton BDT score must be $0.01 < \zeta < 1.00$

Table 6.13: Summary of the final analysis selections and categorization.

increasing E_{T}. The offline `tight` ID efficiency is on the order of 90%, flat with the invariant mass since a `tight` ID cut is already applied at the online trigger level. The overall signal efficiency decreases from 17% / 14% / 15% for $m_X = 60$ GeV to 23% / 22% / 22% for $m_X = 120$ GeV for mc16a, mc16d, and mc16e corresponding to the 2015 – 2016, 2017, and 2018 data-taking periods, respectively. The differences across the years come from the increasing pile-up where the trigger efficiency degrades at higher pile-up. The number of background and signal events is defined as the number of MC events falling within a window of $m_X \pm 2 \cdot \sigma_{\mathrm{CB},X}$ for each tested signal mass point m_X where $\sigma_{\mathrm{CB},X}$ is the width of the signal sample as described in Section 7.1.

The number of events passing all selection cuts in the data samples is summarized in Table 6.14. The total number of selected events across the 2015 – 2016, 2017, and 2018 data-taking periods sums to 5543611. Since an isolation trigger is used in 2017,

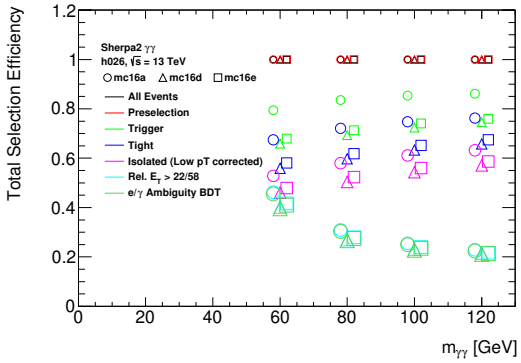

(a) Total efficiencies for Sherpa2 $\gamma\gamma$.

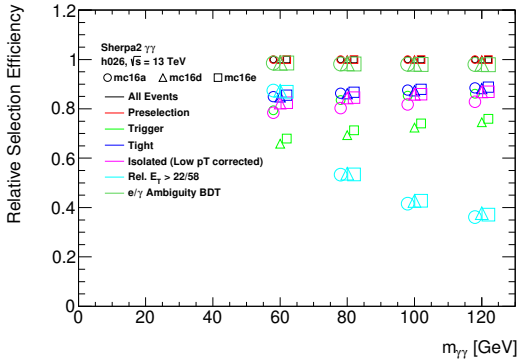

(b) Relative efficiencies for Sherpa2 $\gamma\gamma$.

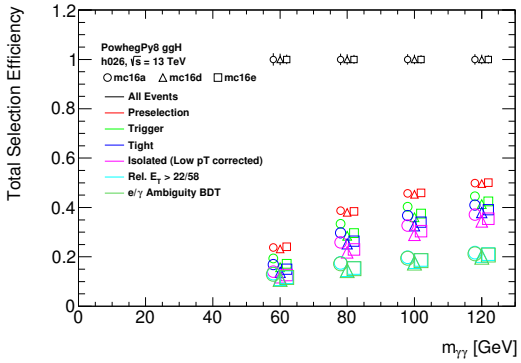

(c) Total efficiencies for PowhegPy8 ggH.

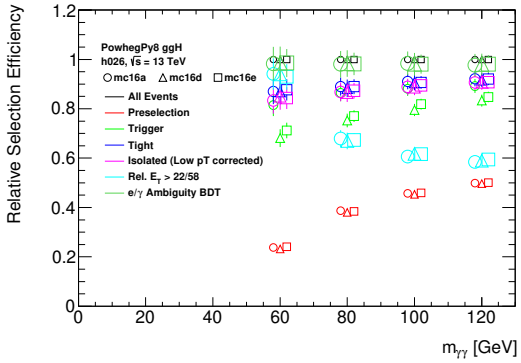

(d) Relative efficiencies for PowhegPy8 ggH.

Figure 6.15: The total and relative selection efficiencies for each MC campaign and each m_X using events in the range $m_X \pm 2 \cdot \sigma_{\mathrm{CB},X}$ using the final analysis selections. The total selection efficiencies are calculated with sequential application of the final analysis selections. The relative selection efficiencies are calculated by comparing each analysis selection to the previous selection.

Analysis	Data-taking Period			
Selection	2015	2016	2017	2018
Total	3614495	36410576	21857452	28374145
Trigger	1206429	11455420	7954795	10457493
Preselection	1206429	11455420	7954795	10457493
Fixed p_{T}	1206429	11455420	7954793	10457489
Tight	701648	6452191	5303032	7636329
Isolated	289210	2658993	3285481	4642846
Pass e/γ Ambiguity	230421	2095705	2568774	3642428
Relative $E_{\mathrm{T}} > 22/58$	149995	1366862	1665836	2360918
Fraction in each Photon Conversion Category				
UU	53.1%	55.9%	51.0%	50.2%
UC	38.9%	37.2%	40.4%	40.8%
CC	8.1%	6.8%	8.7%	9.0%

Table 6.14: Event cutflow using the final analysis selections measured in data for 2015, 2016, 2017, and 2018. Fractions of events for each photon conversion category is also given below the analyis selection cutflow.

the number of selected events at the preselection level in 2017 is lower compared to 2016 despite the comparable luminosity between the two years. However, the number of events are comparable after the full set of selection cuts are applied.

CHAPTER VII

Signal and Background Modeling

After applying the final analysis selections and categorizing the diphoton events into signal-dominated and background-dominated regions (also known as signal and control regions, respectively), the MC samples and data control regions are used to construct and test the signal model and background models for the analysis. The MC samples for each Higgs production mode are used to construct the analytical scalar resonance model as described in Section 7.1. The MC samples for the diphoton background continuum and the resonant $Z \to ee$ background are used to construct the non-resonant and resonant background models, respectively, as described in Section 7.3.

7.1 Signal Modeling

From the perspective of the underlying physics, the line-shape of a signal in the diphoton invariant mass $m_{\gamma\gamma}$ spectrum seen by the ATLAS detector is a convolution of the true line-shape of the resonance with a function that mimics the experimental resolution effects. Since the width of the generated MC signal resonance samples are on the order of 4 MeV/100 GeV = 0.004% (using $m_X = 100$ GeV as an example), the intrinsic width of the resonant signals can be neglected such that the signal model is characterized by the resolution function centered around a given resonance mass m_X.

7.1.1 Signal Shape

The narrow-width signal line-shape is approximated using a double-sided Crystal Ball (DSCB) function [84] [60] [95] that takes into account the asymmetric and non-Gaussian low and high mass tails. The DSCB function is defined as

$$f_X(m_{\gamma\gamma}; \mu_{\mathrm{CB}}, \sigma_{\mathrm{CB}}, \alpha_{\mathrm{low}}, \alpha_{\mathrm{high}}, n_{\mathrm{low}}, n_{\mathrm{high}}) = N \cdot \begin{cases} e^{-t^2/2} \\ \quad \text{if } -\alpha_{\mathrm{low}} \leq t \leq \alpha_{\mathrm{high}}, \\ \dfrac{e^{-0.5\alpha_{\mathrm{low}}^2}}{\left[\frac{\alpha_{\mathrm{low}}}{n_{\mathrm{low}}}\left(\frac{n_{\mathrm{low}}}{\alpha_{\mathrm{low}}} - \alpha_{\mathrm{low}} - t\right)\right]^{n_{\mathrm{low}}}} \\ \quad \text{if } t < -\alpha_{\mathrm{low}}, \\ \dfrac{e^{-0.5\alpha_{\mathrm{high}}^2}}{\left[\frac{\alpha_{\mathrm{high}}}{n_{\mathrm{high}}}\left(\frac{n_{\mathrm{high}}}{\alpha_{\mathrm{high}}} - \alpha_{\mathrm{high}} + t\right)\right]^{n_{\mathrm{high}}}} \\ \quad \text{if } t > \alpha_{\mathrm{high}}, \end{cases} \tag{7.1}$$

where $t = (m_{\gamma\gamma} - \mu_{\mathrm{CB}})/\sigma_{\mathrm{CB}}$, N is a normalization parameter, μ_{CB} is the peak of the Gaussian distribution, σ_{CB} is the width of the Gaussian part of the function, α_{low} and α_{high} are the points where the Gaussian becomes a power law on the low and high

mass side, and n_{low} and n_{high} are the exponents of this power law, respectively. The final functional form of the signal model fit takes the following form for each category:

$$f_X(m_{\gamma\gamma} \mid m_X) = f_{\text{DSCB}}(m_{\gamma\gamma} \mid \mu_{\text{CB}}(m_X), \sigma_{\text{CB}}(m_X), \alpha_{\text{low}}(m_X), \alpha_{\text{high}}(m_X), n_{\text{low}}(m_X), n_{\text{high}}(m_X)) \tag{7.2}$$

The six parameters of the DSCB function are correlated and mass dependent. For the studies here, the values of n_{low} and n_{high} are kept fixed at 19.7 and 16.9, respectively, to improve fit stability. First-order polynomial functions are chosen to describe the other four parameters — $\Delta m_X = m_X - \mu_{\text{CB}}$, α_{low}, α_{high}, and σ_{CB} — as a function of the resonance mass m_X:

$$\Delta m_X = a + b \cdot m_X, \tag{7.3}$$

$$\sigma_{\text{CB}} = c + d \cdot m_X, \tag{7.4}$$

$$\alpha_{\text{low}} = e + f \cdot m_X, \tag{7.5}$$

$$\alpha_{\text{high}} = g + h \cdot m_X. \tag{7.6}$$

The signal model is derived using the MC samples detailed in Table 6.1 with only the masses between 60 – 120 GeV considered in the fit. The signal shape is fit in the mass range 50 GeV $< m_{\gamma\gamma} <$ 130 GeV.

♦ **Model-Dependent Method** To simulate a SM-like signal shape, all the production modes — ggH, VBF, ttH, WH, and ZH — are combined into a merged sample and used for the nominal signal model fits. The MC signal samples from the different production modes are weighted according to the SM-like Higgs cross-sections recommended by the LHC Higgs cross-section working group for center-of-mass energies of 13 TeV [73]. After this production mode weighting, the merged signal templates for each m_X are then normalized to the same number of events before being used in a

global m_X-parameterized DSCB fit.

All three MC campaigns (mc16a, mc16d, and mc16e) are used and weighted according to the relative luminosity of the 2015 – 2016, 2017, and 2018 data-taking periods, respectively. The input signal samples are then split into the model-dependent categories.

The coefficients of the signal parameterization as a function of m_X are obtained from a simultaneous likelihood fit to the signal samples at various resonance masses. The global fit over the input signal datasets is performed as an unbinned fit. The output of the fits for each model-dependent category is compared to its respective input dataset and shown in Figure 7.1. The parameterizations of Δm_X, σ_{CB}, α_{low}, and α_{high} are extracted from the global fits for each model-dependent category and shown in Figures 7.2, 7.3, 7.4, and 7.5, respectively. Good agreement between the input signal models and the fitted functions are seen in all model-dependent categories. The parameterizations obtained from the multiple mass point fits for the model-dependent categories are given in Table 7.1.

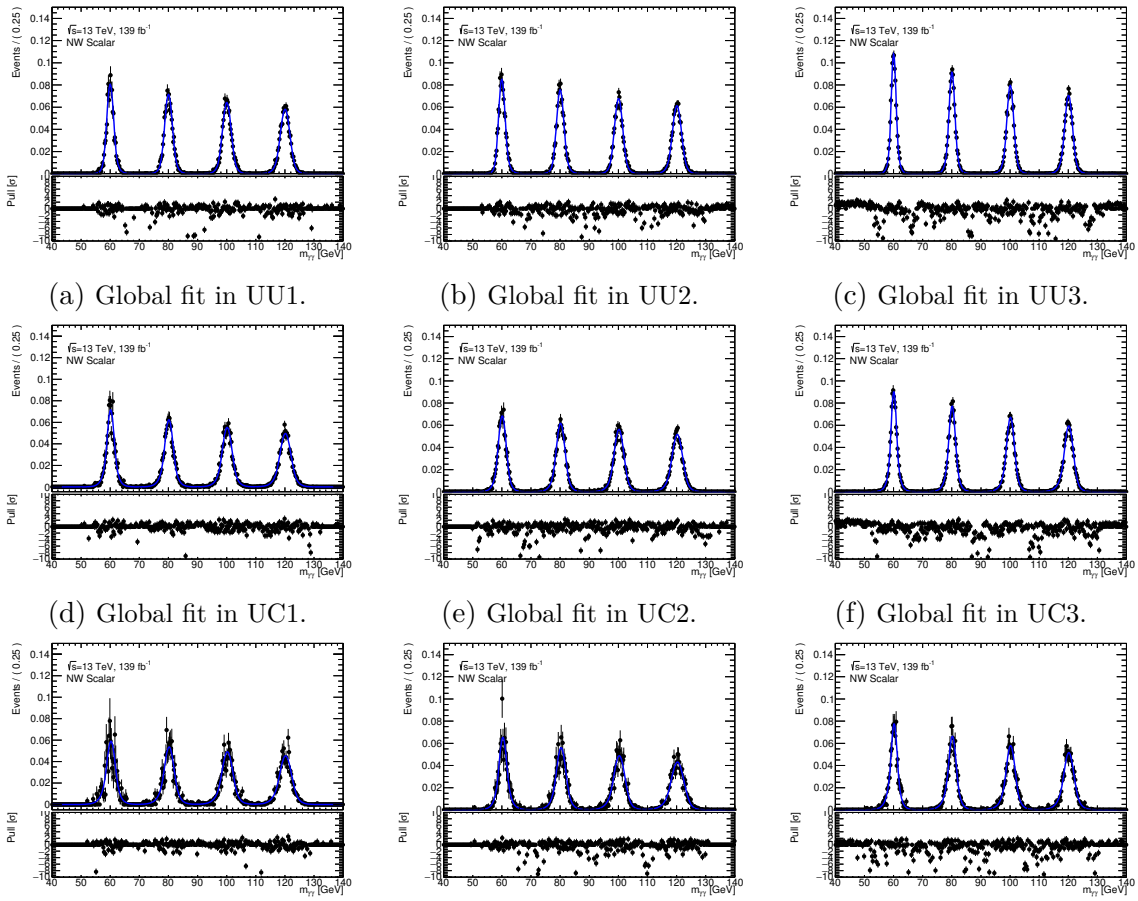

(a) Global fit in UU1. (b) Global fit in UU2. (c) Global fit in UU3.

(d) Global fit in UC1. (e) Global fit in UC2. (f) Global fit in UC3.

(g) Global fit in CC1. (h) Global fit in CC2. (i) Global fit in CC3.

Figure 7.1: The global mass-parameterized fit to the $m_{\gamma\gamma}$ distributions of the merged NWA signals weighted by SM-like Higgs cross-sections using a DSCB function in each model-dependent category. The bottom panels show the pulls of the fit.

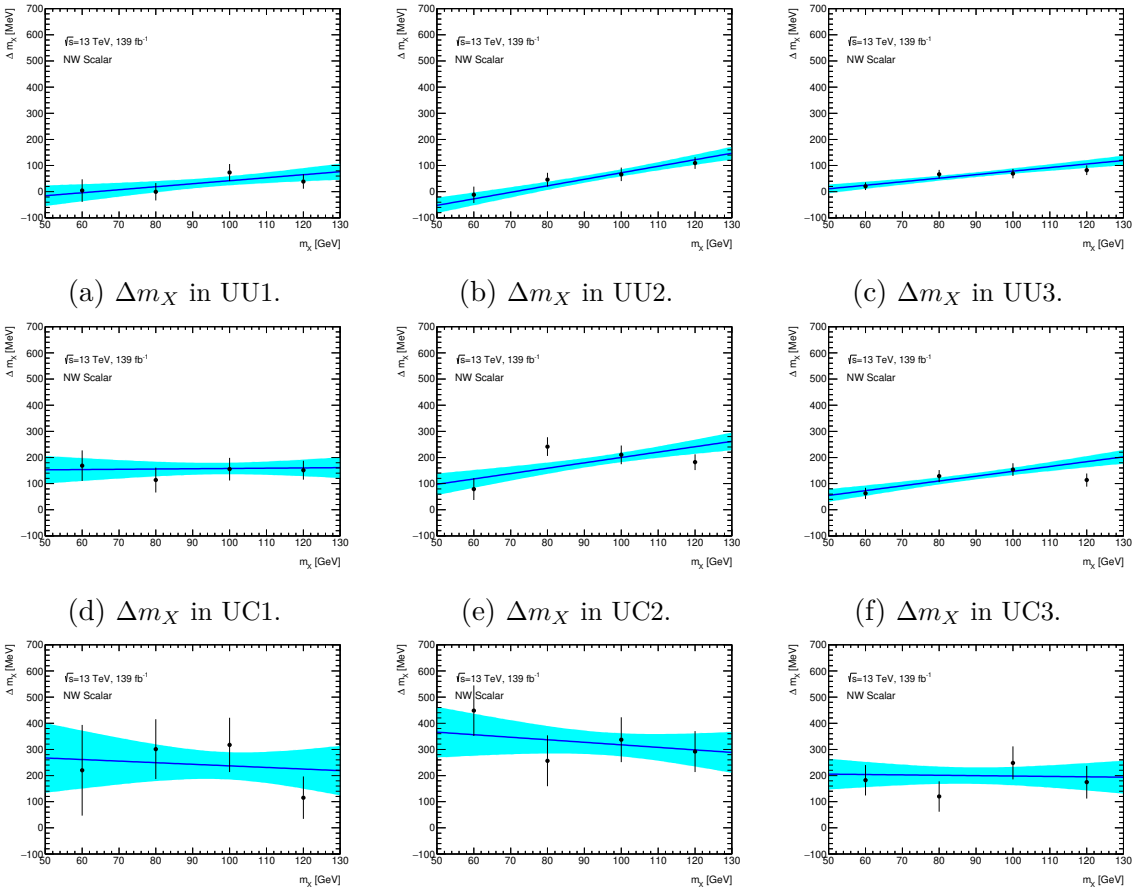

(a) Δm_X in UU1. (b) Δm_X in UU2. (c) Δm_X in UU3.

(d) Δm_X in UC1. (e) Δm_X in UC2. (f) Δm_X in UC3.

(g) Δm_X in CC1. (h) Δm_X in CC2. (i) Δm_X in CC3.

Figure 7.2: The mass-parameterized linear fit to the Δm_X parameter of the merged NWA signals weighted by SM-like Higgs cross-sections in each model-dependent category. The blue shaded bands indicate the possible range of parameters based on the error of the likelihood fit. The points are the values and associated errors derived from single mass point DSCB fits.

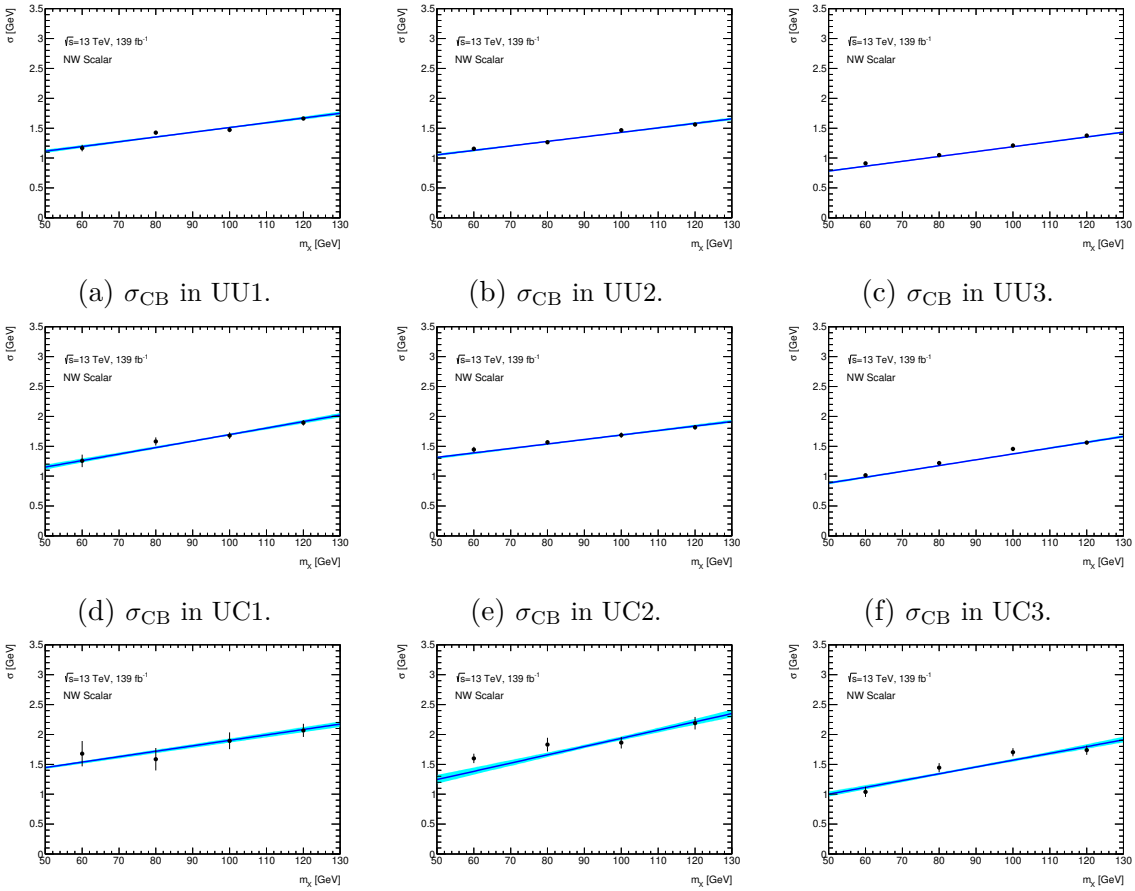

(a) σ_{CB} in UU1. (b) σ_{CB} in UU2. (c) σ_{CB} in UU3.

(d) σ_{CB} in UC1. (e) σ_{CB} in UC2. (f) σ_{CB} in UC3.

(g) σ_{CB} in CC1. (h) σ_{CB} in CC2. (i) σ_{CB} in CC3.

Figure 7.3: The mass-parameterized linear fit to the σ_{CB} parameter of the merged NWA signals weighted by SM-like Higgs cross-sections in each model-dependent category. The blue shaded bands indicate the possible range of parameters based on the error of the likelihood fit. The points are the values and associated errors derived from single mass point DSCB fits.

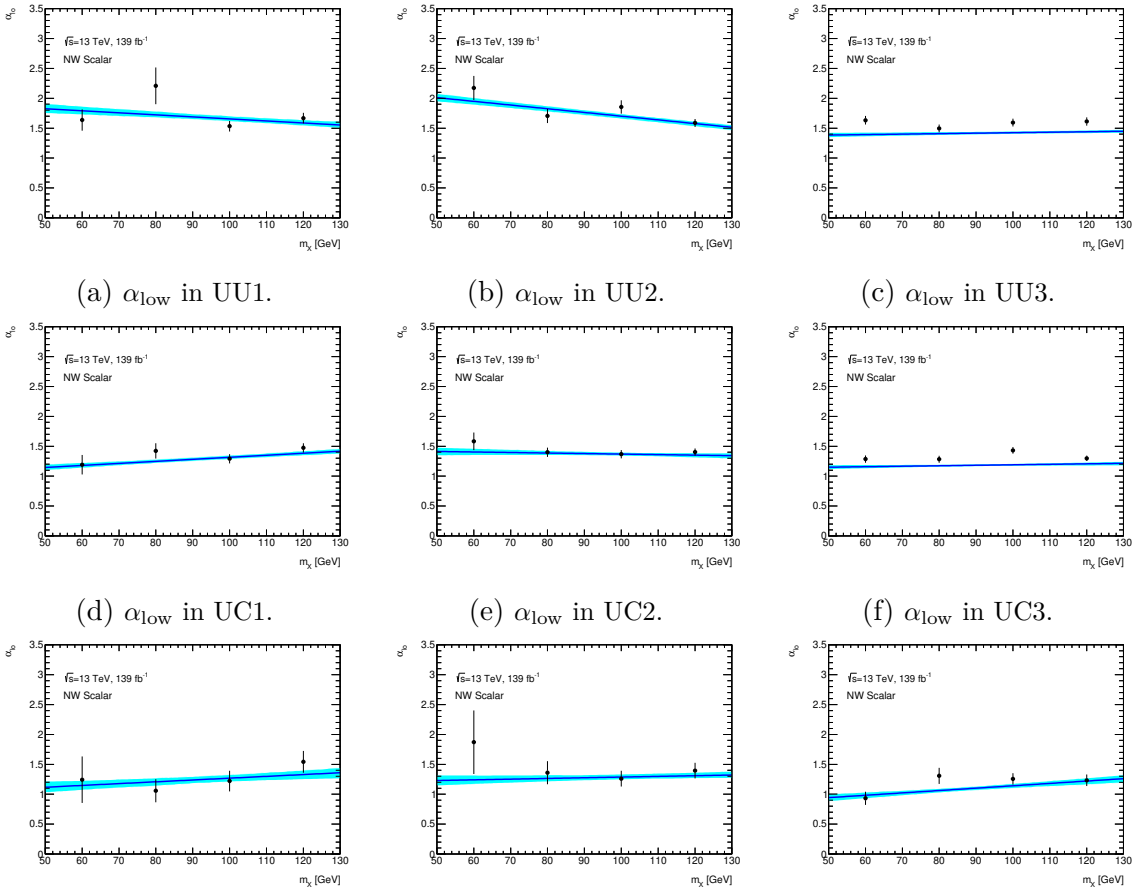

(a) α_{low} in UU1. (b) α_{low} in UU2. (c) α_{low} in UU3.

(d) α_{low} in UC1. (e) α_{low} in UC2. (f) α_{low} in UC3.

(g) α_{low} in CC1. (h) α_{low} in CC2. (i) α_{low} in CC3.

Figure 7.4: The mass-parameterized linear fit to the α_{low} parameter of the merged NWA signals weighted by SM-like Higgs cross-sections in each model-dependent category. The blue shaded bands indicate the possible range of parameters based on the error of the likelihood fit. The points are the values and associated errors derived from single mass point DSCB fits.

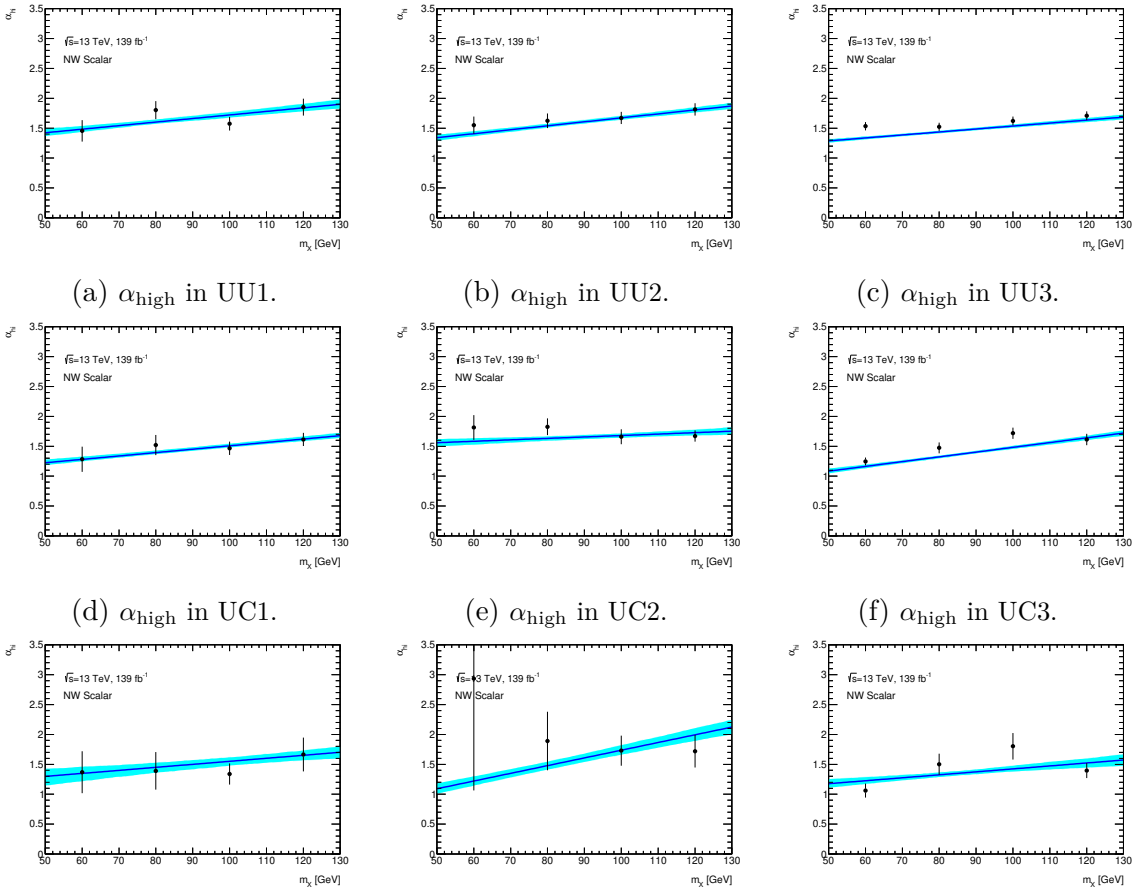

(a) α_{high} in UU1. (b) α_{high} in UU2. (c) α_{high} in UU3.

(d) α_{high} in UC1. (e) α_{high} in UC2. (f) α_{high} in UC3.

(g) α_{high} in CC1. (h) α_{high} in CC2. (i) α_{high} in CC3.

Figure 7.5: The mass-parameterized linear fit to the α_{high} parameter of the merged NWA signals weighted by SM-like Higgs cross-sections in each model-dependent category. The blue shaded bands indicate the possible range of parameters based on the error of the likelihood fit. The points are the values and associated errors derived from single mass point DSCB fits.

Parameter	Parameterization	Coefficient	UU1	UU2	UU3
Δm_X	$a + b \cdot m_X$	a [GeV]	-0.0729	-0.1769	-0.0565
		b	1.0011	1.0024	1.0013
σ_{CB}	$c + d \cdot m_X$	c [GeV]	0.7191	0.6765	0.3756
		d	0.0079	0.0075	0.0081
α_{low}	$e + f \cdot m_X$	e	1.9970	2.3209	1.3449
		f	-0.0034	-0.0061	0.0007
α_{high}	$g + h \cdot m_X$	g	1.1263	1.0099	1.0385
		h	0.0059	0.0066	0.0049
n_{low}	constant	-	19.7	19.7	19.7
n_{high}		-	16.9	16.9	16.9
			UC1	UC2	UC3
Δm_X	$a + b \cdot m_X$	a [GeV]	0.1474	-0.0051	-0.0373
		b	1.0001	1.0020	1.0018
σ_{CB}	$c + d \cdot m_X$	c [GeV]	0.6088	0.9407	0.3983
		d	0.0108	0.0074	0.0097
α_{low}	$e + f \cdot m_X$	e	0.9742	1.4571	1.1095
		f	0.0034	-0.0008	0.0008
α_{high}	$g + h \cdot m_X$	g	0.9410	1.4392	0.6858
		h	0.0056	0.0024	0.0079
n_{low}	constant	-	19.7	19.7	19.7
n_{high}		-	16.9	16.9	16.9
			CC1	CC2	CC3
Δm_X	$a + b \cdot m_X$	a [GeV]	0.2976	0.4142	0.2127
		b	0.9993	0.9990	0.9998
σ_{CB}	$c + d \cdot m_X$	c [GeV]	0.9921	0.5553	0.4332
		d	0.0090	0.0137	0.0113
α_{low}	$e + f \cdot m_X$	e	0.9655	1.1720	0.7447
		f	0.0030	0.0011	0.0039
α_{high}	$g + h \cdot m_X$	g	1.0458	0.4472	0.9285
		h	0.0050	0.0128	0.0049
n_{low}	constant	-	19.7	19.7	19.7
n_{high}		-	16.9	16.9	16.9

Table 7.1: The m_X-parameterizations of the DSCB function parameters describing the signal shape for each model-dependent category. In these fits, n_{high} and n_{low} are set to fixed values.

◊ **Model-Independent Method** Only the ggH production mode is used for the nominal signal model fits in the model-independent method. All three MC campaigns (mc16a, mc16d, and mc16e) are used and weighted according to the relative luminosity of the 2015 – 2016, 2017, and 2018 data-taking periods, respectively. The input signal samples are then split into the model-independent categories.

The coefficients of the signal parameterization as a function of m_X are obtained from a simultaneous likelihood fit to the signal samples at various resonance masses. The output of the fits for each model-independent category is compared to its respective input dataset and shown in Figure 7.6. The parameterizations of Δm_X, σ_{CB}, α_{low}, and α_{high} are extracted from the global fits for each model-independent category and shown in Figure 7.7. Good agreement between the input signal models and the fitted functions are seen in all model-independent categories as well. The parameterizations obtained from the multiple mass point fits for the model-independent categories are given in Table 7.2.

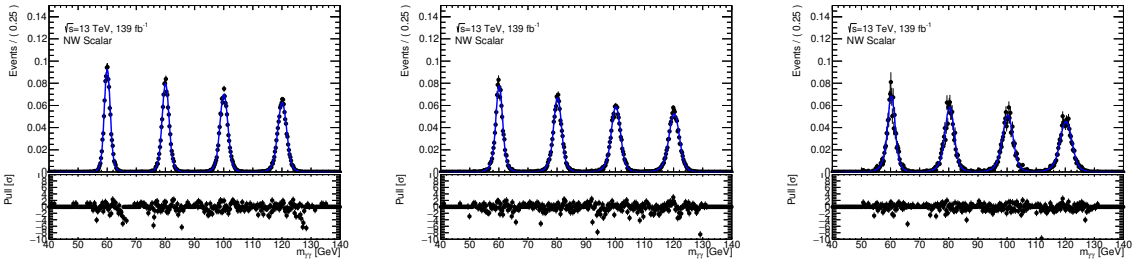

(a) Global fit in UU. (b) Global fit in UC. (c) Global fit in CC.

Figure 7.6: The global mass-parameterized fit to the $m_{\gamma\gamma}$ distributions of the merged NWA signals weighted by SM-like Higgs cross-sections using a DSCB function in each model-dependent category. The bottom panels show the pulls of the fit.

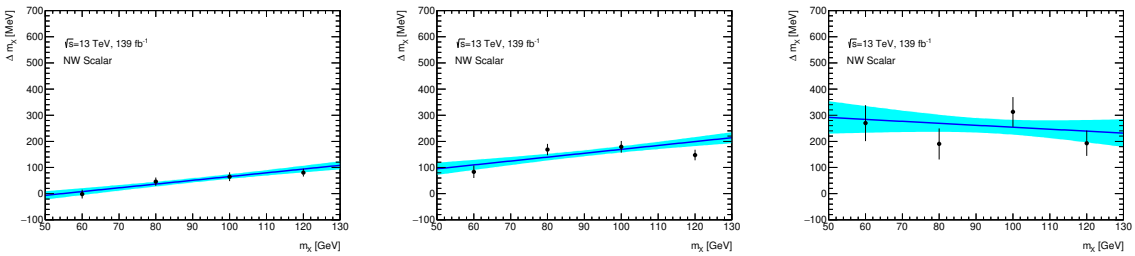

(a) Δm_X in UU. (b) Δm_X in UC. (c) Δm_X in CC.

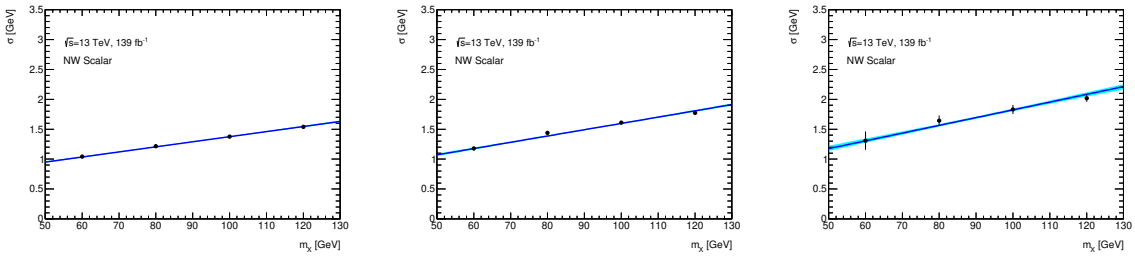

(d) σ_{CB} in UU. (e) σ_{CB} in UC. (f) σ_{CB} in CC.

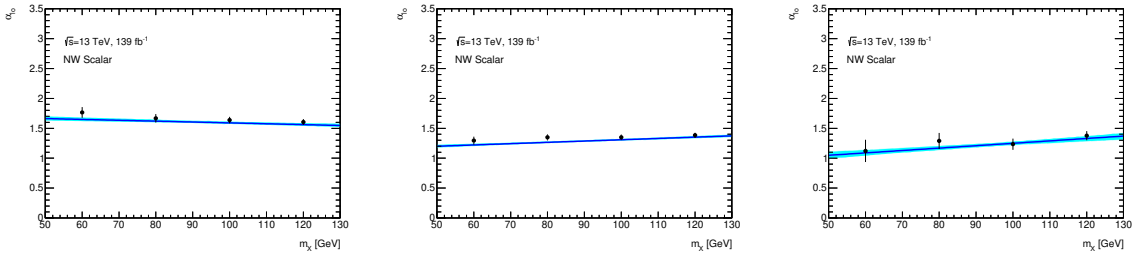

(g) α_{low} in UU. (h) α_{low} in UC. (i) α_{low} in CC.

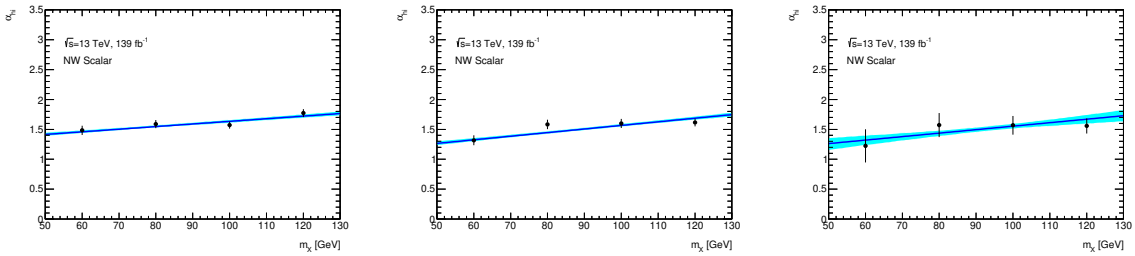

(j) α_{high} in UU. (k) α_{high} in UC. (l) α_{high} in CC.

Figure 7.7: The mass-parameterized linear fit to the Δm_X, σ_{CB}, α_{low}, and α_{high} parameters of the ggH signal in each model-independent category. The blue shaded bands indicate the possible range of parameters based on the error of the likelihood fit. The points are the values and associated errors derived from single mass point DSCB fits.

Parameter	Parameterization	Coefficient	UU	UC	CC
Δm_X	$a + b \cdot m_X$	a [GeV]	-0.0782	0.0207	0.3288
		b	1.0014	1.0014	0.9992
σ_{CB}	$c + d \cdot m_X$	c [GeV]	0.5260	0.5454	0.5275
		d	0.0084	0.0105	0.0129
α_{low}	$e + f \cdot m_X$	e	1.7358	1.0911	0.8478
		f	-0.0014	0.0021	0.0040
α_{high}	$g + h \cdot m_X$	g	1.1965	0.9640	0.9707
		h	0.0043	0.0060	0.0058
n_{low}	constant	-	19.7	19.7	19.7
n_{high}		-	16.9	16.9	16.9

Table 7.2: The m_X-parameterizations of the DSCB function parameters describing the signal shape for each model-independent category. In these fits, n_{high} and n_{low} are set to fixed values.

7.1.2 Signal Shape Uncertainties

The uncertainties on the deviation of the mean Δm_X and width σ_{CB} of the signal shape are computed by producing alternative signal MC templates where the photon energy scale and resolution are varied. These templates are then fit in a setup where the Δm_X and σ_{CB} terms are allowed to float while the other DSCB model parameters are fixed to their nominal values.

♦ **Model-Dependent Method** The values of the mean and width from the fits performed on the up and down variations for each model-dependent category are given in Tables 7.3, 7.4, and 7.5. These values are then used to derive uncertainties on each parameter, which are computed as the relative difference between the new values and the nominal signal model parameters found in Table 7.1. The signal samples generated with the energy scale and resolution systematic variations included do not have the information needed to perform the low E_{T} photon isolation correction as described in Section 6.3.3. As a result, the nominal signal model parameters used to derive the uncertainties use all of the final analysis selection listed in Table 6.13

except the E_{T} photon isolation correction. The uncertainties are shown in Figures 7.8, 7.9, and 7.10 as a function of m_X in the range 65 – 110 GeV. The uncertainty on Δm_X varies between 0.2% and 0.5%, and the uncertainty on the width σ_{CB} varies between 2% and 13%, depending on the category of the signal process.

Parameter	Parameterization	Coefficient	UU1	UU2	UU3
Nominal without Low E_{T} Isolation Correction					
Δm_X	$a + b \cdot m_X$	a [GeV]	-0.0765	-0.1686	-0.0568
		b	1.0011	1.0023	1.0013
σ_{CB}	$c + d \cdot m_X$	c [GeV]	0.7360	0.6786	0.3670
		d	0.0077	0.0075	0.0082
Energy scale up					
Δm_X	$a + b \cdot m_X$	a [GeV]	-0.1857	-0.2702	-0.1601
		b	1.0067	1.0072	1.0070
Energy scale down					
Δm_X	$a + b \cdot m_X$	a [GeV]	0.0252	-0.0307	0.0648
		b	0.9956	0.9970	0.9954
Energy resolution up					
σ_{CB}	$c + d \cdot m_X$	c [GeV]	0.7289	0.6293	0.3569
		d	0.0090	0.0091	0.0098
Energy resolution down					
σ_{CB}	$c + d \cdot m_X$	c [GeV]	0.7398	0.7200	0.3991
		d	0.0068	0.0063	0.0068

Table 7.3: Parameterizations of the DSCB function describing the signal shape that result from the global fit to signal templates where the photon energy scale and resolutions are varied up and down. The parameters are derived in each UU model-dependent category.

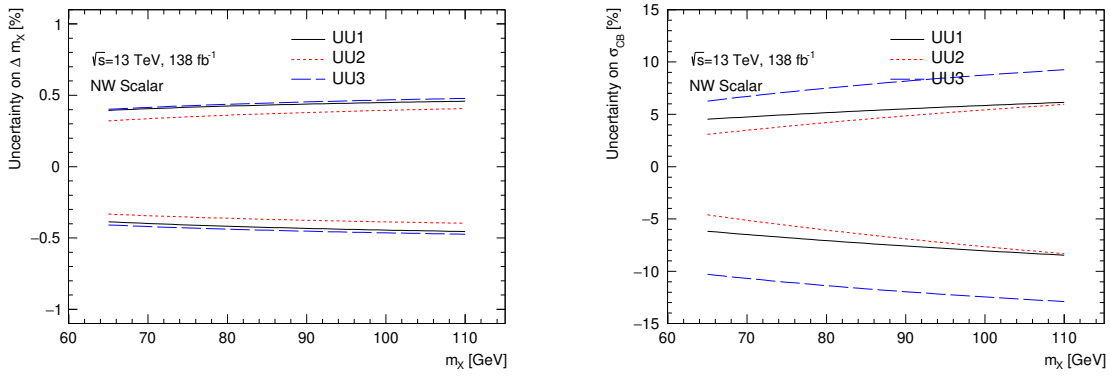

(a) Photon energy scale in UU.

(b) Photon energy resolution in UU.

Figure 7.8: Systematic uncertainties associated with the photon energy scale and photon energy resolution as a function of m_X, computed for each UU model-dependent category.

Parameter	Parameterization	Coefficient	UC1	UC2	UC3
Nominal without Low E_{T} Isolation Correction					
Δm_X	$a + b \cdot m_X$	a [GeV]	0.1501	-0.0103	-0.0357
		b	1.0000	1.0020	1.0018
σ_{CB}	$c + d \cdot m_X$	c [GeV]	0.5632	0.9324	0.3833
		d	0.0111	0.0075	0.0098
Energy scale up					
Δm_X	$a + b \cdot m_X$	a [GeV]	0.2220	-0.0110	-0.0695
		b	1.0030	1.0056	1.0064
Energy scale down					
Δm_X	$a + b \cdot m_X$	a [GeV]	0.1345	-0.0123	0.0184
		b	0.9963	0.9984	0.9970
Energy resolution up					
σ_{CB}	$c + d \cdot m_X$	c [GeV]	0.5077	0.9465	0.4027
		d	0.0129	0.0084	0.0112
Energy resolution down					
σ_{CB}	$c + d \cdot m_X$	c [GeV]	0.5509	0.9263	0.3668
		d	0.0102	0.0066	0.0085

Table 7.4: Parameterizations of the DSCB function describing the signal shape that result from the global fit to signal templates where the photon energy scale and resolutions are varied up and down. The parameters are derived in each UC model-dependent category.

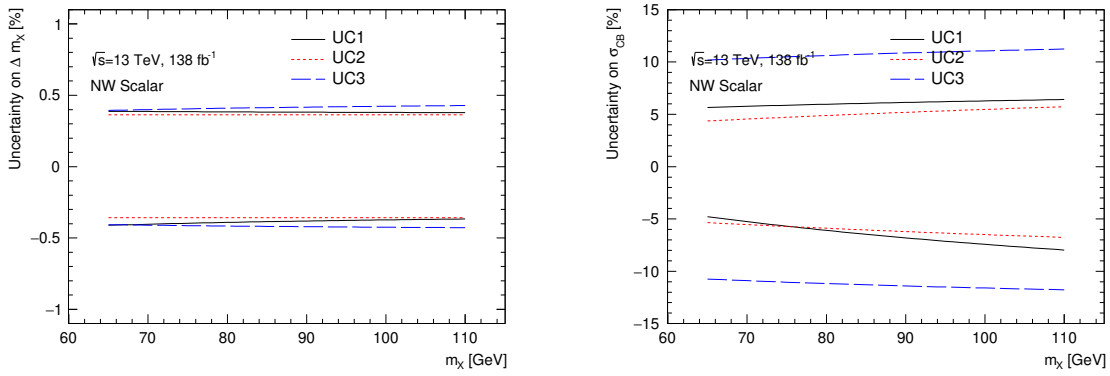

(a) Photon energy scale in UC.

(b) Photon energy resolution in UC.

Figure 7.9: Systematic uncertainties associated with the photon energy scale and photon energy resolution as a function of m_X, computed for each UC model-dependent category.

Parameter	Parameterization	Coefficient	CC1	CC2	CC3
Nominal without Low E_{T} Isolation Correction					
Δm_X	$a + b \cdot m_X$	a [GeV]	0.3556	0.4746	0.2152
		b	0.9987	0.9984	0.9998
σ_{CB}	$c + d \cdot m_X$	c [GeV]	0.9900	0.4997	0.4359
		d	0.0093	0.0142	0.0110
Energy scale up					
Δm_X	$a + b \cdot m_X$	a [GeV]	0.4375	0.7190	0.2068
		b	1.0004	0.9984	1.0031
Energy scale down					
Δm_X	$a + b \cdot m_X$	a [GeV]	0.2023	0.3410	0.1580
		b	0.9976	0.9971	0.9971
Energy resolution up					
σ_{CB}	$c + d \cdot m_X$	c [GeV]	0.9996	0.4864	0.4538
		d	0.0104	0.0154	0.0126
Energy resolution down					
σ_{CB}	$c + d \cdot m_X$	c [GeV]	0.9975	0.6053	0.3938
		d	0.0080	0.0120	0.0096

Table 7.5: Parameterizations of the DSCB function describing the signal shape that result from the global fit to signal templates where the photon energy scale and resolutions are varied up and down. The parameters are derived in each CC model-dependent category.

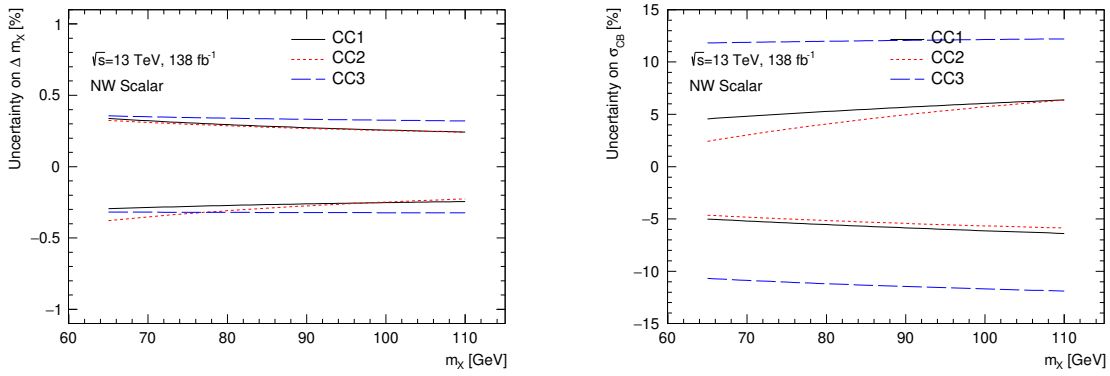

(a) Photon energy scale in CC.

(b) Photon energy resolution in CC.

Figure 7.10: Systematic uncertainties associated with the photon energy scale and photon energy resolution as a function of m_X, computed for each CC model-dependent category.

◊ **Model-Independent Method** The values of the mean and width from the fits performed on the up and down variations for each model-independent category are given in Table 7.6. These values are then used to derive uncertainties on each parameter, which are computed as the relative difference between the new values and the nominal signal model parameters found in Table 7.2. The uncertainties are shown in Figure 7.11 as a function of m_X in the range 65 – 110 GeV. The uncertainty on Δm_X varies between 0.2% and 0.5%, and the uncertainty on the width σ_{CB} varies between 3% and 9%, depending on category of the signal process.

Parameter	Parameterization	Coefficient	UU	UC	CC
Nominal without Low E_{T} Isolation Correction					
Δm_X	$a + b \cdot m_X$	a [GeV]	-0.0747	0.0185	0.3374
		b	1.0014	1.0015	0.9992
σ_{CB}	$c + d \cdot m_X$	c [GeV]	0.526	0.5104	0.5243
		d	0.0085	0.0108	0.0129
Energy scale up					
Δm_X	$a + b \cdot m_X$	a [GeV]	-0.1818	0.0114	0.4459
		b	1.0067	1.0054	1.0007
Energy scale down					
Δm_X	$a + b \cdot m_X$	a [GeV]	0.0348	0.0317	0.2221
		b	0.996	0.9975	0.9976
Energy resolution up					
σ_{CB}	$c + d \cdot m_X$	c [GeV]	0.4822	0.5237	0.5614
		d	0.0102	0.012	0.0138
Energy resolution down					
σ_{CB}	$c + d \cdot m_X$	c [GeV]	0.5457	0.5034	0.6115
		d	0.0074	0.0096	0.0107

Table 7.6: Parameterizations of the DSCB function describing the signal shape that result from the global fit to signal templates where the photon energy scale and resolutions are varied up and down. The parameters are derived in each model-independent category.

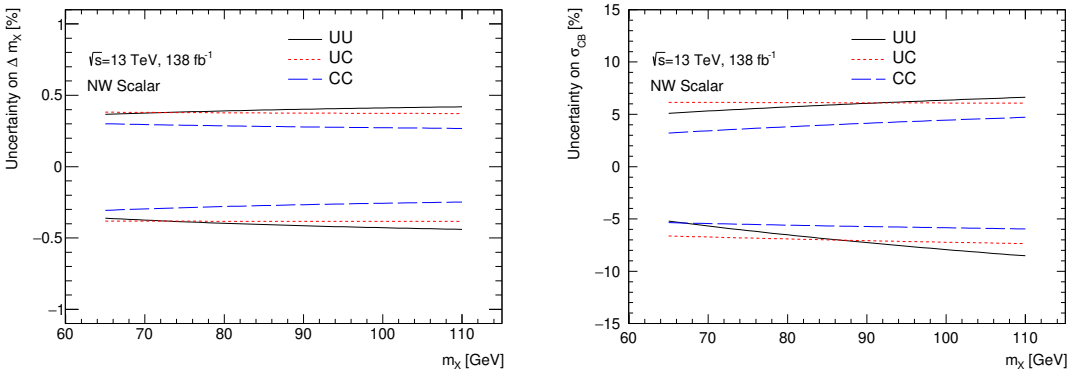

(a) Photon energy scale.

(b) Photon energy resolution.

Figure 7.11: Systematic uncertainties associated with the photon energy scale and photon energy resolution as a function of m_X, computed for each model-independent category.

7.2 Fiducial Volume and Correction Factors

As mentioned in Chapter 5, the aim of this analysis is to provide both a model-dependent and model-independent result on the search for a Higgs-like scalar. In the absense of an excess, the analysis aims to place an expected limit on the cross-section of a Higgs-like scalar that could exist given the uncertainty constraints of the measurement.

The fiducial event count of a new scalar resonance is used explicitly in the model-independent method to produce an expected fiducial cross section limit:

$$N_{\text{fiducial}} = \sigma_X \cdot L_{\text{int}} \cdot C_X \tag{7.7}$$

where σ_X is production cross section of the new resonance at mass m_X, L_{int} is the integrated luminosity of the dataset, and C_X is the correction factor described in Section 7.2.1. This fiducial event count is used implicitly in the model-dependent method with the fiducial acceptance factor A_X described in Section 7.2.2 to calculate the event count after applying the final analysis sections described in Section 6.3.8. The selection event count is then used to produce an expected total cross section limit:

$$N_{\text{selection}} = \sigma_X \cdot L_{\text{int}} \cdot C_X \cdot A_X. \tag{7.8}$$

7.2.1 Fiducial Volume Definition

The fiducial cross-section extraction is used to correct for the number of fitted signal events in the data due to detector effects such as reconstruction, identification, and selection efficiencies. The correction factor is defined as

$$C_X = \frac{N_{\text{selection}}}{N_{\text{fiducial}}} \tag{7.9}$$

where $N_{\text{selection}}$ is the number of reconstructed signal events passing all the analysis cuts and N_{fiducial} is the number of signal events generated within the fiducial volume. To provide a model-independent limit, the fiducial volume must be chosen such that the correction factor does not depend on the final state. As a result, all events containing two reconstructed photons must have similar identification and reconstruction efficiencies independent from the production mode. The correction factor for a model-dependent process is then calculated by weighting each production mode with its corresponding SM-like scalar cross section.

The definition of the fiducial volume is optimized using signal MC samples for the ggH, VBF, ttH, WH, and ZH production modes in order to cover a large variety of possible final states. The kinematic cuts applied on the truth photon variables to define the fiducial volume are the same as the ones used at the reconstruction level. Both photons are required to be within $|\eta| < 2.37$, excluding the transition region between the barrel and the end-cap calorimeters set as $1.37 < |\eta| < 1.52$. The transverse energies for the leading and sub-leading photons are required to be larger than 22 GeV and the relative E_{T} for each of the two photons are also required to be larger than 22/58.

The acceptance cuts applied on E_{T} and η are not enough to define a model-independent fiducial volume. Photons reconstructed in events where the resonance is produced in association with many high E_{T} jets, such as ttH, WH, and ZH events, have a larger calorimeter isolation energy and hence a lower isolation selection efficiency. To reduce this effect, the particle isolation cuts applied on the truth photon variables to help define the fiducial volume are changed slightly from those used at the reconstruction level. Adding an offset of 1 GeV to the truth photon isolation criteria as shown in Figures 7.12a and 7.12b is found to increase the selection efficiency and acceptance of the fiducial volume for the ggH production mode. Similar increases in efficiency are found for the other production modes as well. The 2-D distribution of

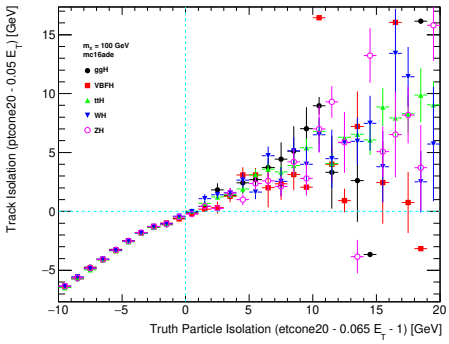

(a) Profile distribution of track isolation.

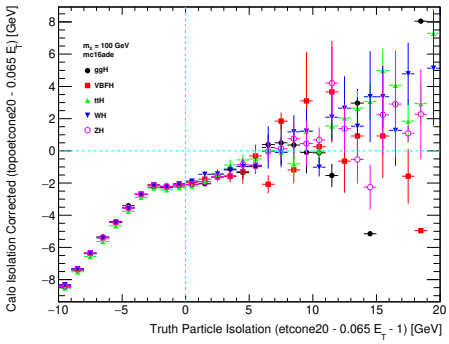

(b) Profile distribution of calorimeter isolation.

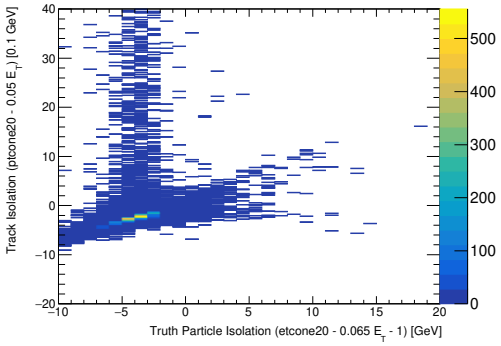

(c) 2D distribution of track isolation.

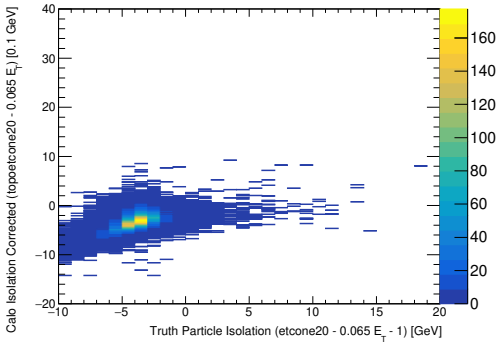

(d) 2D distribution of calorimeter isolation.

Figure 7.12: Profile distributions of (a) track and (b) calorimeter isolation with respect to truth isolation for a resonance at $m_X = 100\,\text{GeV}$. 2D distributions of (c) track and (d) calorimeter isolation with respect to truth isolation for ggH resonance at $m_X = 100\,\text{GeV}$. Dotted cyan line indicates the truth and reconstruction isolation cuts where the bottom left quadrant passes selection cuts.

the truth and reconstruction variables also indicate minimal bias in the reconstruction efficiency by shifting the truth isolation criteria as shown in Figures 7.12c and 7.12d. Applying this particle isolation cut on top of the kinematic cuts reduces the dependency of the C_X factor on the final state.

7.2.2 C_X and A_X Factors

The C_X factors computed after applying the particle isolation with the kinematic cuts for the inclusive category is shown in Figure 7.13. The parameterized fits on the merged production mode as well as the upper envelope of the C_X factor are also

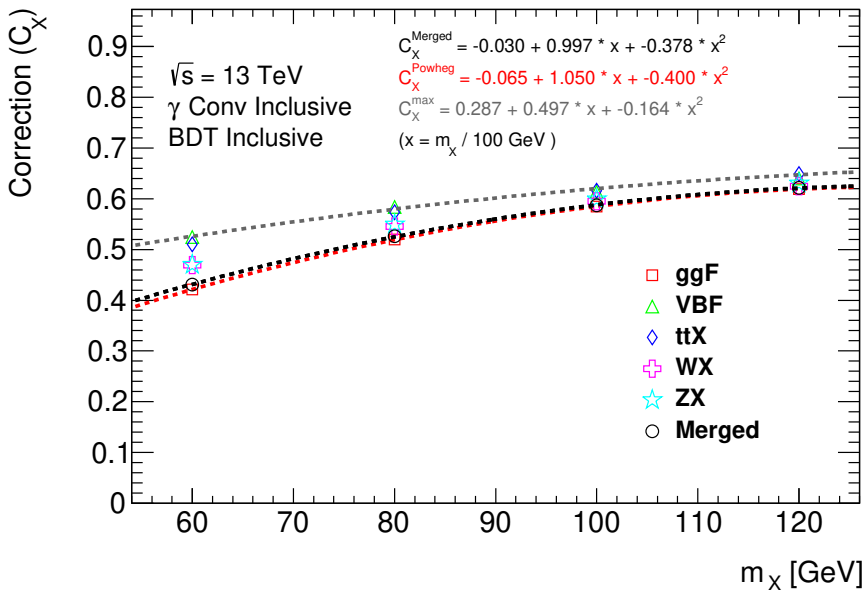

Figure 7.13: The inclusive category correction factor (C_X) comparing the number of events passing the full set of selection cuts with the number of events passing the fiducial volume criteria for each mass point and each production mode.

shown. For the merged production mode, the C_X factor is found to be approximately 0.43 at 60 GeV and 0.62 at 120 GeV. The comparison of the C_X factor for each production mode to that of the merged production mode is shown in Figure 7.14 for the inclusive category. The factors for each production mode per mass point is shown independently for a model-independent analysis as well as jointly for a SM-like model-dependent process. The statistical uncertainty on these factors are on the order of 10^{-6}.

The fiducial acceptance factor is used to correct the total number of events that lie within the fiducial volume defined above. The acceptance factor is defined as

$$A_X = \frac{N_{\text{fiducial}}}{N_{\text{total}}} \tag{7.10}$$

where $N_{\text{total}} = \sigma_X \cdot L_{\text{int}}$ is the total number of signal events expected to be produced using the given signal resonance model. The fiducial acceptance as a function of m_X using the fiducial volume is shown in Figure 7.15. This acceptance factor is provided

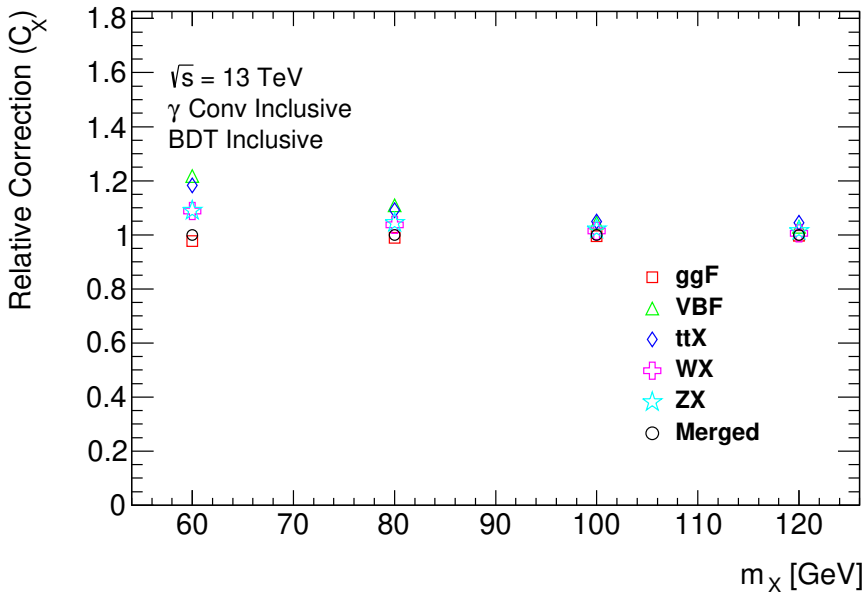

Figure 7.14: The inclusive category correction factor (C_X) relative to the value for the merged production mode.

for the truth-level reinterpretation of the results of this analysis. The factor for the merged process can be modeled using a second order polynomial function:

$$A_X^{\text{Merged}} = 0.220 + 0.136 \cdot \left(\frac{m_X}{100\ \text{GeV}}\right) - 0.028 \cdot \left(\frac{m_X}{100\ \text{GeV}}\right)^2. \tag{7.11}$$

For the merged production mode, the A_X factor is found to be approximately 0.29 at 60 GeV and 0.34 at 120 GeV.

The product of the A_X and C_X factors, equivalent to the selection efficiency, for the merged production mode for the inclusive category is shown in Figure 7.16.

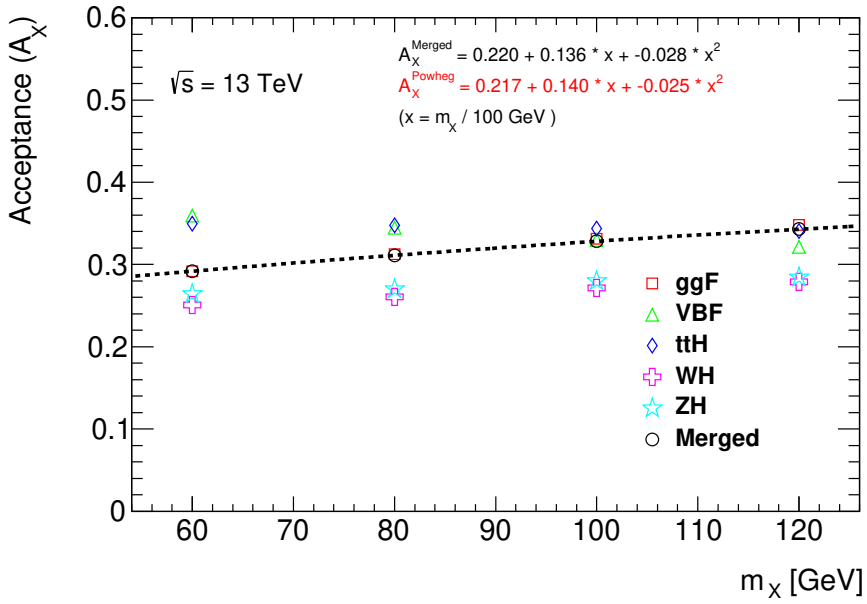

Figure 7.15: The acceptance factor (A_X) comparing the number of events passing the fiducial volume criteria with the total number of events for each mass point and each production mode.

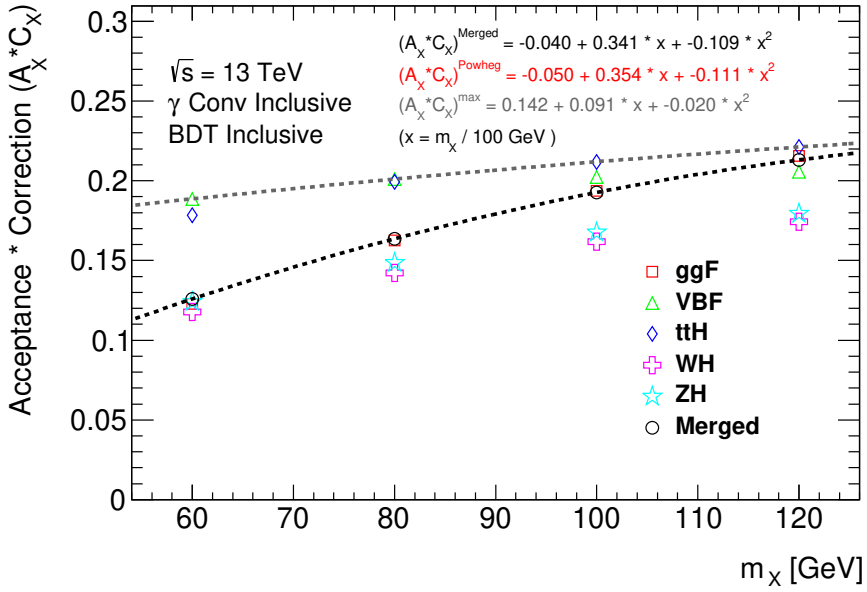

Figure 7.16: The inclusive category acceptance factor (A_X) times correction factor (C_X) comparing the number of events passing the full set of selection cuts with the total number of events for each mass point and each production mode.

7.2.3 Systematic Variations on the C_X Factors

The largest sources of systematic uncertainty on the C_X factor arises from the difference in signal production modes and from the impact of systematic variation on the experimental parameters. The production mode uncertainty will be used in the model-independent analysis of the diphoton resonance search. The experimental systematic uncertainties will be derived for each model-dependent and model-independent category.

7.2.3.1 Production Mode Variation

The uncertainties on the C_X factors due to the production modes are computed using the envelope containing all of the various production modes (ggH, VBF, ttH, WH, ZH) as illustrated in Figure 7.13. The ggH and VBF production modes are used as the lower and upper bounds of the envelope respectively. The difference between these two modes is mainly due to the photon isolation since the VBF production mode has a busier interaction point environment. Since the isolation variable is sensitive to pile-up, the uncertainty is also dependent on pile-up.

The uncertainty is symmetrized around the merged production mode and is taken as the ratio between the upper envelope and the merged production mode shown in Figure 7.13:

$$\text{variation} = \frac{0.287 + 0.497 \cdot \left(\frac{m_{\gamma\gamma}}{100\ \text{GeV}}\right) - 0.164 \cdot \left(\frac{m_{\gamma\gamma}}{100\ \text{GeV}}\right)^2}{-0.030 + 0.997 \cdot \left(\frac{m_{\gamma\gamma}}{100\ \text{GeV}}\right) - 0.378 \cdot \left(\frac{m_{\gamma\gamma}}{100\ \text{GeV}}\right)^2} - 1. \tag{7.12}$$

This uncertainty due to production modes decreases from 21.8% at 60 GeV to 4.0% at 120 GeV as shown in Figure 7.13. This uncertainty is only used in the case of a model-independent limit.

7.2.3.2 Experimental Parameter Variations

The experimental parameters varied for the signal templates are the trigger scale factor, the pile-up reweighting, the photon ID efficiency, the photon isolation efficiency, the photon energy resolution, and the photon energy scale. The impact of these systematic variations is computed by recomputing the C_X factors with signal templates where the up and down variations of the experimental parameters have been applied and comparing the systematically varied values to the nominal value. The signal template used here is the merged production mode.

♦ **Model-Dependent Method** The variation is calculated for each model-dependent category, and an envelope is taken over the diphoton BDT categories for each photon conversion category. The effect on the C_X factor associated with varying the experimental parameters are shown in Figure 7.17. An additional uncertainty on the C_X factor is derived to account for the systematic uncertainties on the corrected isolation. This uncertainty is derived by taking the difference between signal efficiencies when the data-driven shifts are applied to the calorimeter isolation and when these corrections are not applied. This additional uncertainty on the photon isolation is also shown in Figure 7.17 and is symmetrized for the up and down variations.

The parameterization of the experimental systematic uncertainties for each photon conversion category is taken as the envelope over the diphoton BDT categories and is given in Table 7.7.

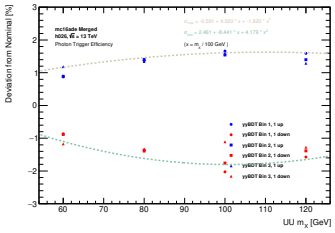

(a) Photon trigger scale factor in UU.

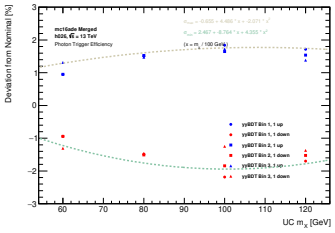

(b) Photon trigger scale factor in UC.

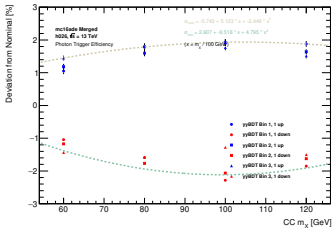

(c) Photon trigger scale factor in CC.

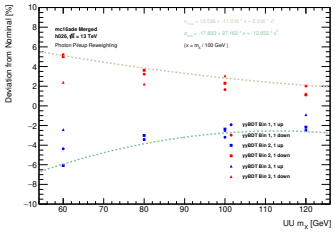

(d) Pileup reweighting in UU.

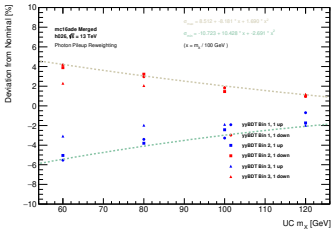

(e) Pileup reweighting in UC.

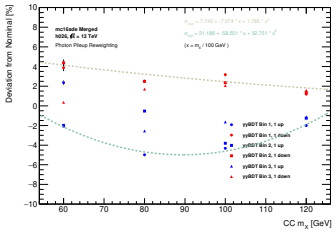

(f) Pileup reweighting in CC.

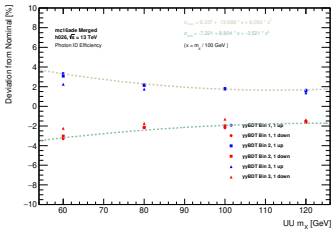

(g) Photon ID efficiency in UU.

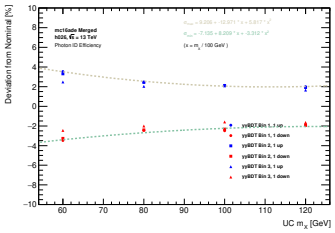

(h) Photon ID efficiency in UC.

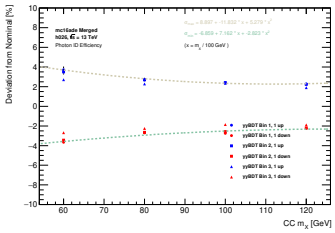

(i) Photon ID efficiency in CC.

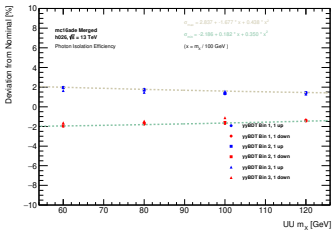

(j) Photon isolation efficiency in UU.

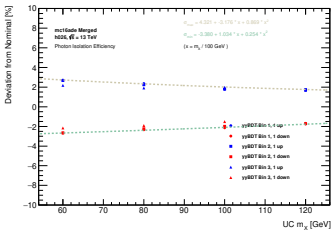

(k) Photon isolation efficiency in UC.

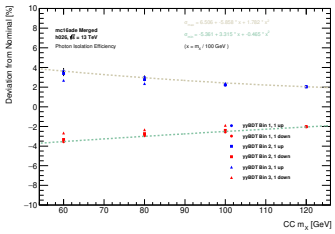

(l) Photon isolation efficiency in CC.

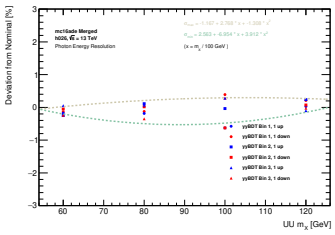

(m) Photon energy resolution in UU.

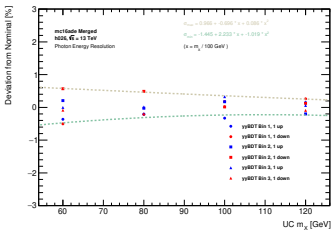

(n) Photon energy resolution in UC.

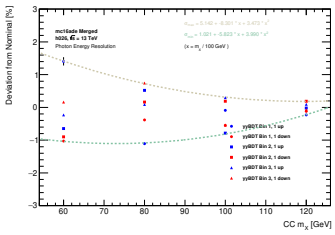

(o) Photon energy resolution in CC.

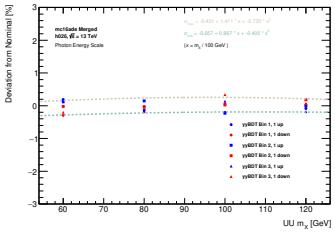

(p) Photon energy scale in UU.

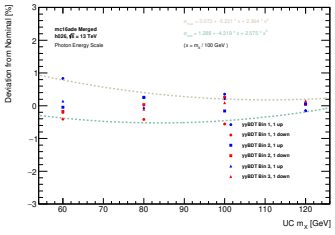

(q) Photon energy scale in UC.

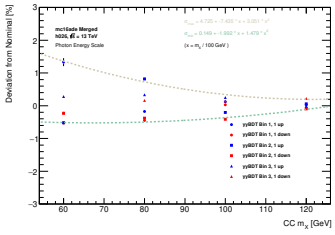

(r) Photon energy scale in CC.

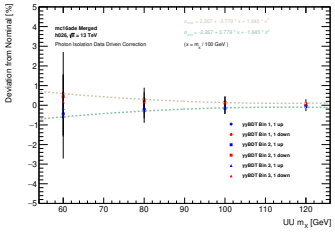

(s) DD Isolation correction in UU.

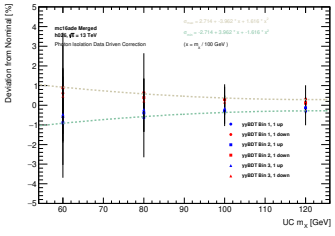

(t) DD Isolation correction in UC.

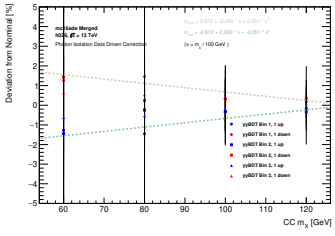

(u) DD Isolation correction in CC.

Figure 7.17: Experimental uncertainties on the C_X factor associated with the trigger scale factor, the pile-up reweighting, the photon identification efficiency, the photon isolation efficiency, the photon energy resolution, the photon energy scale, and the data-driven (DD) photon isolation correction for the model-dependent method.

Experimental Systematic			$f(m_X/100\text{ GeV})$, $139.5\,\text{fb}^{-1}$
Trigger	UU	up	- 0.0059 + 0.0401 *x - 0.0182 *x*x
		down	0.0246 - 0.0844 *x + 0.0417 *x*x
	UC	up	- 0.0065 + 0.0448 *x - 0.0207 *x*x
		down	0.0246 - 0.0876 *x + 0.0435 *x*x
	CC	up	- 0.0074 + 0.0512 *x - 0.0244 *x*x
		down	0.0260 - 0.0951 *x + 0.0479 *x*x
Pileup Reweighting	UU	up	0.1053 - 0.1101 *x + 0.0331 *x*x
		down	- 0.1789 + 0.2716 *x - 0.1203 *x*x
	UC	up	0.0851 - 0.0818 *x + 0.0168 *x*x
		down	- 0.1072 + 0.1042 *x - 0.0269 *x*x
	CC	up	0.0774 - 0.0707 *x + 0.0178 *x*x
		down	0.2118 - 0.5855 *x + 0.3275 *x*x
ID	UU	up	0.0933 - 0.1368 *x + 0.0609 *x*x
		down	- 0.0722 + 0.0880 *x - 0.0352 *x*x
	UC	up	0.0920 - 0.1297 *x + 0.0581 *x*x
		down	- 0.0713 + 0.0820 *x - 0.0331 *x*x
	CC	up	0.0889 - 0.1183 *x + 0.0527 *x*x
		down	- 0.0685 + 0.0716 *x - 0.0282 *x*x
Isolation	UU	up	0.0283 - 0.0167 *x + 0.0043 *x*x
		down	- 0.0218 + 0.0018 *x + 0.0034 *x*x
	UC	up	0.0432 - 0.0317 *x + 0.0086 *x*x
		down	- 0.0338 + 0.0103 *x + 0.0025 *x*x
	CC	up	0.0650 - 0.0585 *x + 0.0178 *x*x
		down	- 0.0536 + 0.0331 *x - 0.0046 *x*x
Energy Scale	UU	up	- 0.0042 + 0.0141 *x - 0.0073 *x*x
		down	- 0.0065 + 0.0086 *x - 0.0039 *x*x
	UC	up	0.0307 - 0.0523 *x + 0.0236 *x*x
		down	0.0128 - 0.0431 *x + 0.0257 *x*x
	CC	up	0.0472 - 0.0743 *x + 0.0305 *x*x
		down	0.0014 - 0.0199 *x + 0.0147 *x*x
Energy Resolution	UU	up	- 0.0116 + 0.0276 *x - 0.0130 *x*x
		down	0.0256 - 0.0695 *x + 0.0391 *x*x
	UC	up	0.0096 - 0.0069 *x + 0.0008 *x*x
		down	- 0.0144 + 0.0223 *x - 0.0101 *x*x
	CC	up	0.0514 - 0.0830 *x + 0.0347 *x*x
		down	0.0102 - 0.0582 *x + 0.0399 *x*x
Data-driven Isolation	UU	up	0.0226 - 0.0377 *x + 0.0164 *x*x
		down	- 0.0226 + 0.0377 *x - 0.0164 *x*x
	UC	up	0.0271 - 0.0396 *x + 0.0161 *x*x
		down	- 0.0271 + 0.0396 *x - 0.0161 *x*x
	CC	up	0.0291 - 0.0228 *x + 0.0005 *x*x
		down	- 0.0291 + 0.0228 *x - 0.0005 *x*x

Table 7.7: Parametrization of the experimental uncertainties on the C_X factor as function of m_X in each photon conversion categories and expressed for the luminosity of the data. The parameterization for each photon conversion category is taken as the envelope over the diphoton BDT categories.

◊ **Model-Independent Method** The variation is calculated for each model-independent category, and the effect on the C_X factor associated with varying the experimental parameters are shown in Figure 7.18. An additional uncertainty on the C_X factor is derived to account for the systematic uncertainties on the corrected isolation. This uncertainty is derived by taking the difference between signal efficiencies when the data-driven shifts are applied to the calorimeter isolation and when these corrections are not applied. This additional uncertainty on the photon isolation is also shown in Figure 7.18 and is symmetrized for the up and down variations.

The parameterization of the experimental systematic uncertainties for each photon conversion category is given in Table 7.8.

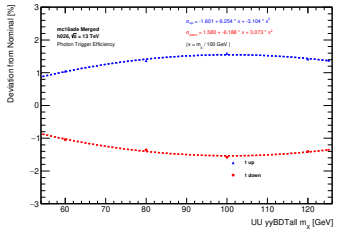

(a) Photon trigger scale factor in UU.

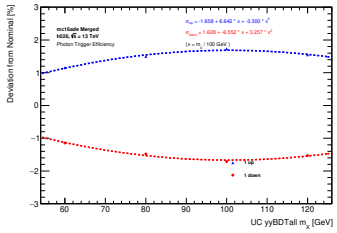

(b) Photon trigger scale factor in UC.

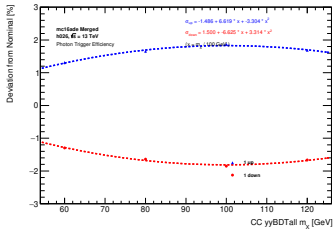

(c) Photon trigger scale factor in CC.

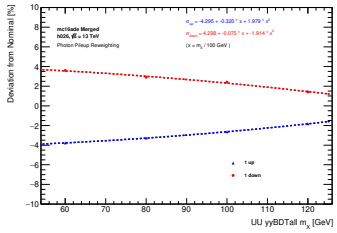

(d) Pileup reweighting in UU.

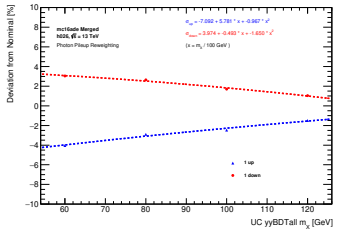

(e) Pileup reweighting in UC.

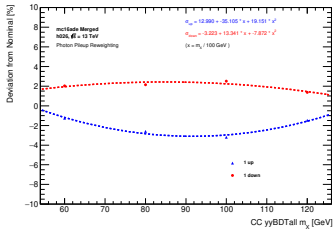

(f) Pileup reweighting in CC.

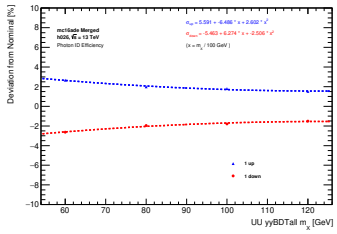

(g) Photon ID efficiency in UU.

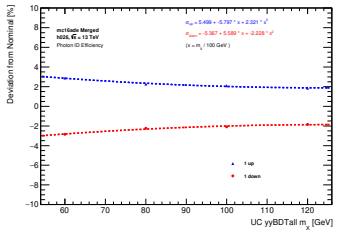

(h) Photon ID efficiency in UC.

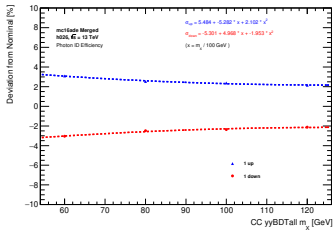

(i) Photon ID efficiency in CC.

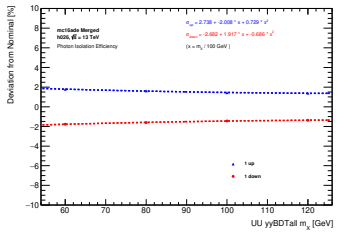

(j) Photon isolation efficiency in UU.

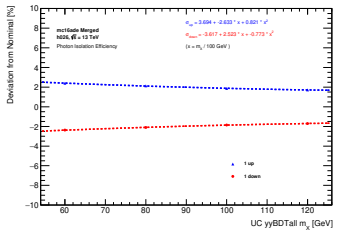

(k) Photon isolation efficiency in UC.

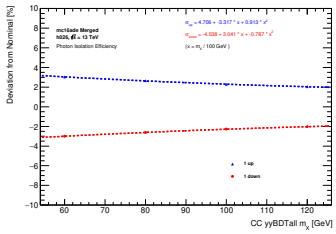

(l) Photon isolation efficiency in CC.

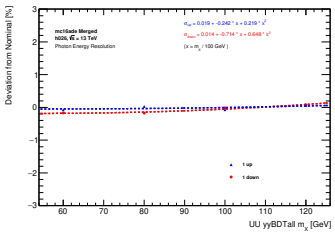

(m) Photon energy resolution in UU.

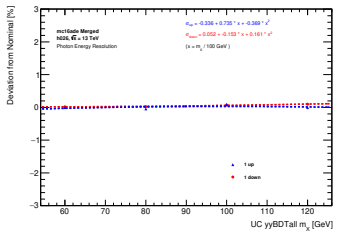

(n) Photon energy resolution in UC.

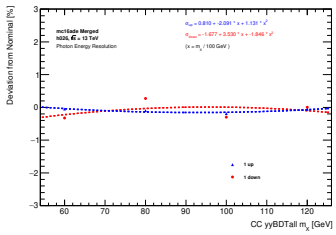

(o) Photon energy resolution in CC.

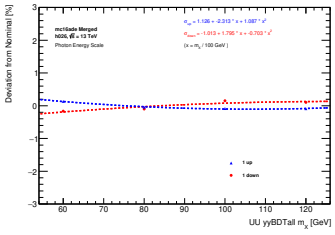

(p) Photon energy scale in UU.

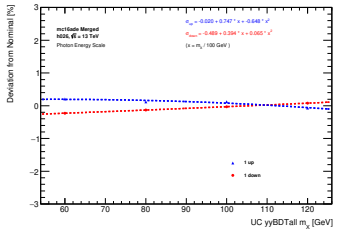

(q) Photon energy scale in UC.

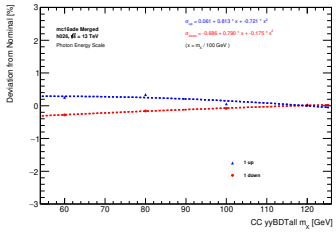

(r) Photon energy scale in CC.

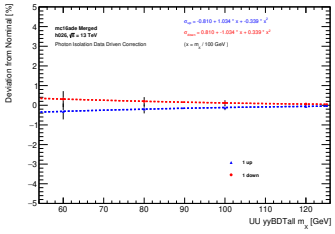

(s) DD Isolation correction in UU.

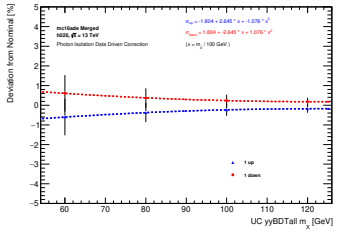

(t) DD Isolation correction in UC.

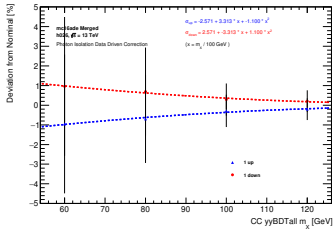

(u) DD Isolation correction in CC.

Figure 7.18: Experimental uncertainties on the C_X factor associated with the trigger scale factor, the pile-up reweighting, the photon identification efficiency, the photon isolation efficiency, the photon energy resolution, the photon energy scale, and the data-driven (DD) photon isolation correction for the model-independent method.

Experimental Systematic			$f(m_X/100\ \text{GeV}), 139.5\,\text{fb}^{-1}$
Trigger	UU	up	- 0.0160 + 0.0625 *x - 0.0310 *x*x
		down	0.0158 - 0.0618 *x + 0.0307 *x*x
	UC	up	- 0.0165 + 0.0664 *x - 0.0329 *x*x
		down	0.0162 - 0.0655 *x + 0.0325 *x*x
	CC	up	- 0.0148 + 0.0661 *x - 0.0330 *x*x
		down	0.0149 - 0.0662 *x + 0.0331 *x*x
Pileup Reweighting	UU	up	- 0.0429 - 0.0032 *x + 0.0197 *x*x
		down	0.0429 - 0.0007 *x - 0.0191 *x*x
	UC	up	- 0.0709 + 0.0578 *x - 0.0096 *x*x
		down	0.0397 - 0.0049 *x - 0.0165 *x*x
	CC	up	0.1299 - 0.3510 *x + 0.1915 *x*x
		down	- 0.0322 + 0.1334 *x - 0.0787 *x*x
ID	UU	up	0.0559 - 0.0648 *x + 0.0260 *x*x
		down	- 0.0546 + 0.0627 *x - 0.0250 *x*x
	UC	up	0.0549 - 0.0579 *x + 0.0232 *x*x
		down	- 0.0536 + 0.0558 *x - 0.0222 *x*x
	CC	up	0.0548 - 0.0528 *x + 0.0210 *x*x
		down	- 0.0530 + 0.0496 *x - 0.0195 *x*x
Isolation	UU	up	0.0273 - 0.0200 *x + 0.0072 *x*x
		down	- 0.0268 + 0.0191 *x - 0.0068 *x*x
	UC	up	0.0369 - 0.0263 *x + 0.0082 *x*x
		down	- 0.0361 + 0.0252 *x - 0.0077 *x*x
	CC	up	0.0470 - 0.0331 *x + 0.0091 *x*x
		down	- 0.0453 + 0.0304 *x - 0.0078 *x*x
Energy Scale	UU	up	0.0112 - 0.0231 *x + 0.0108 *x*x
		down	- 0.0101 + 0.0179 *x - 0.0070 *x*x
	UC	up	- 0.0001 + 0.0074 *x - 0.0064 *x*x
		down	- 0.0048 + 0.0039 *x + 0.0006 *x*x
	CC	up	0.0006 + 0.0081 *x - 0.0072 *x*x
		down	- 0.0068 + 0.0078 *x - 0.0017 *x*x
Energy Resolution	UU	up	0.0001 - 0.0024 *x + 0.0021 *x*x
		down	0.0001 - 0.0071 *x + 0.0064 *x*x
	UC	up	- 0.0033 + 0.0073 *x - 0.0036 *x*x
		down	0.0005 - 0.0015 *x + 0.0016 *x*x
	CC	up	0.0080 - 0.0209 *x + 0.0113 *x*x
		down	- 0.0167 + 0.0353 *x - 0.0184 *x*x
Data-driven Isolation	UU	up	- 0.0081 + 0.0103 *x - 0.0033 *x*x
		down	0.0081 - 0.0103 *x + 0.0033 *x*x
	UC	up	- 0.0180 + 0.0264 *x - 0.0107 *x*x
		down	0.0180 - 0.0264 *x + 0.0107 *x*x
	CC	up	- 0.0257 + 0.0331 *x - 0.0110 *x*x
		down	0.0257 - 0.0331 *x + 0.0110 *x*x

Table 7.8: Parametrization of the experimental uncertainties on the C_X factor as function of m_X in each photon conversion categories and expressed for the luminosity of the data.

7.3 Background Modeling

The main sources of background for this analysis can be divided into three components:

- The non-resonant background coming from the QCD production of photon pairs ($\gamma\gamma$), referred to as the "irreducible background,"
- The non-resonant background coming from the QCD production of photon+jet pairs (γj) and jet pairs (jj), where the jets are misidentified as photons, referred to as the "reducible background,"
- The resonant $Z \to ee$ background coming from the DY process, where the two electrons are misidentified as photons, referred to as the "electron background."

The non-resonant background components $\gamma\gamma$, γj, and jj all have smoothly falling mass spectra but with different slopes, and the models are discussed in Section 7.3.1. After each non-resonant background components is modeled, they are combined into a full non-resonant background template as described in Section 7.3.2. The resonant background from $Z \to ee$ events requires a detailed understanding of electron to photon fake rates. The modeling of this background component is further described in Section 7.3.3.

7.3.1 Non-resonant Background Components

A representative template of the non-resonant background is constructed first from MC samples and data. The irreducible $\gamma\gamma$ component is taken from the two high-statistics MC samples generated for $50 < m_{\gamma\gamma} < 175$ GeV. The reducible component is taken from data-driven control regions due to the limited MC statistics available for this component of the non-resonant background. The two components of the non-resonant background are then added together according to the fractions which are measured in data using the 2x2D sideband method described in Section 7.3.1.1.

7.3.1.1 Non-resonant Background Composition

To measure the relative fraction of the $\gamma\gamma$, γj, and jj components in the low mass $m_{\gamma\gamma}$ spectrum, the 2x2D sideband decomposition method [35] is used. In order to use this method, two requirements on the signal region selection are loosened:

- the isolation criteria on the two photon candidates are removed
- the photon identification for the two photon candidates are relaxed when compared to the Tight photon ID as shown in Table 7.9

This new sample of two photon candidates passing relaxed selections is referred to as LoosePrime-LoosePrime (L′L′). The observed event count (also known as yield) $W_{\mathrm{tot}}^{\mathrm{L'L'}}$ is the sum of the diphoton signal yield $W_{\gamma\gamma}^{\mathrm{L'L'}}$ and the background yields split into the various reducible components $W_{\gamma\mathrm{j}}^{\mathrm{L'L'}}$, $W_{\mathrm{j}\gamma}^{\mathrm{L'L'}}$ and $W_{\mathrm{jj}}^{\mathrm{L'L'}}$. The total sum is then described as

$$W_{\mathrm{tot}}^{\mathrm{L'L'}} = W_{\gamma\gamma}^{\mathrm{L'L'}} + W_{\gamma\mathrm{j}}^{\mathrm{L'L'}} + W_{\mathrm{j}\gamma}^{\mathrm{L'L'}} + W_{\mathrm{jj}}^{\mathrm{L'L'}}. \tag{7.13}$$

The exact definition of each L′ region are detailed in Table 7.9. The L′4 photon ID is chosen as the nominal criteria since it is similar to the photon ID criteria of the signal region and minimizes the contamination from true diphoton events as described in Section 7.3.1.3. The L′4 region also provides a reasonable amount of statistics after applying all the corresponding selections.

This sample is then divided into 16 orthogonal sub-samples defined by whether each of the two photons in a diphoton event passes or fails the Tight photon ID criteria and passes or fails the photon isolation criteria. The sub-sample with the Tight-Isolated-Tight-Isolated criteria (TITI) is defined as the signal region. The other 15 regions are defined as control regions for calculating the background composition. In each of these 16 sub-samples, the observed yield can be expressed as

ID name	Cuts
Loose	R_{had1}, R_{had}, R_{η}, $w_{\eta 2}$
Tight	Loose + R_{ϕ}, w_{s3}, F_{side}, ΔE, E_{ratio}, $w_{s1,\text{tot}}$
LoosePrime-2	Tight – w_{s3}, F_{side}
LoosePrime-3	Tight – w_{s3}, F_{side}, ΔE
LoosePrime-4	Tight – w_{s3}, F_{side}, ΔE, $w_{s1,tot}$
LoosePrime-5	Tight – w_{s3}, F_{side}, ΔE, E_{ratio}, $w_{s1,tot}$

Table 7.9: The variables used to determine the definitions of the Loose, Tight [45], and LoosePrime photon ID selections.

a function of the signal and background yields in the whole L′4-L′4 sample, the ID and isolation efficiencies for prompt photon candidates passing the L′4 selection, and the correlations between the isolation distributions of the two fake photons in dijet events. The efficiencies are assumed to be identical for leading photons in the $\gamma\gamma$ and γj components, and identical for the subleading photons in the $\gamma\gamma$ and $j\gamma$ events. By inverting the system and using the ID and isolation efficiencies of the signal, it is possible to obtain the signal and background yields from the observed yields in the signal region and each control region. Using this inverted setup, it is also possible to determine the ID and isolation fake rates and the correlations between the fake rates. As an example, the equation that relates the observed yield in the signal region to the various unknown quantities is given by:

$$\begin{aligned} N_{\text{TITI}} = & W_{\gamma\gamma}^{\text{L}'\text{L}'} \epsilon_{I1}\epsilon_{T1}\epsilon_{I2}\epsilon_{T2} \\ & + W_{\gamma\text{j}}^{\text{L}'\text{L}'} \epsilon_{I1}\epsilon_{T1} f_{I2} f_{T2} \\ & + W_{\text{j}\gamma}^{\text{L}'\text{L}'} f_{I1} f_{T1} \epsilon_{I2}\epsilon_{T2} \\ & + W_{\text{jj}}^{\text{L}'\text{L}'} f'_{I1} f'_{T1} f'_{I2} f'_{T2} \xi_{Ijj}\ \xi_{Tjj} \xi_{TIjj}, \end{aligned} \tag{7.14}$$

where

- ϵ_{I1} and ϵ_{I2} are the efficiencies of the FixedCutLoose isolation criteria with respect to no isolation criteria for the leading and subleading photons, respectively, determined from the diphoton MC simulation;

- ϵ_{T1} and ϵ_{T2} are the Tight identification efficiencies with respect to the L′4 ID for the leading and subleading photons, respectively, also determined from the diphoton MC simulation;

- f_{I1} and f_{I2} are the isolation fake rates for γj and $j\gamma$ events, determined directly from fits to the data;

- f_{T1} and f_{T2} are the Tight identification fake rates for γj and $j\gamma$ events, determined directly from fits to the data;

- f'_{I1} and f'_{I2} are the isolation fake rates for jj events, determined directly from fits to the data;

- f'_{T1} and f'_{T2} are the Tight identification fake rates for jj events, determined either directly from fits to the data or forced to be equal to f_{T1} and f_{T2} as described below;

- ξ_{Ijj}, ξ_{Tjj}, and ξ_{TIjj} are the isolation and identification correlation factors between the jets in jj events, the first of the three is determined directly from fits to the data while the other two are set to a value of 1.

In Equation 7.14, the correlation between the isolation and the identification efficiencies for the $\gamma\gamma$ and γj is neglected. In this system of 16 equations, 6 of the 19 unknowns quantities are fixed: the four efficiencies ϵ_{I1}, ϵ_{I2}, ϵ_{T1} and ϵ_{T2} are fixed to the expectation from the Sherpa2 $\gamma\gamma$ MC simulation, and the two correlations ξ_{Tjj} and ξ_{TIjj} between the ID and the isolation of the dijet events are both fixed to one. The systematic uncertainty coming from this choice has been evaluated previously

[83] and found to be negligible compared to the other sources of systematic uncertainty. The remaining 13 unknowns — the four yields $W_{\gamma\gamma}^{\mathrm{L'L'}}$, $W_{\gamma\mathrm{j}}^{\mathrm{L'L'}}$, $W_{\mathrm{j}\gamma}^{\mathrm{L'L'}}$, $W_{\mathrm{jj}}^{\mathrm{L'L'}}$, the eight fake rates f_{I1}, f_{I2}, f_{T1}, f_{T2}, f'_{I1}, f'_{I2}, f'_{T1}, f'_{T2}, and the correlation ξ_{Ijj} — are determined from the data using a minimization procedure.

♦ **Model-Dependent Method** The isolation and ID efficiencies are determined using the Sherpa2 $\gamma\gamma$ MC samples. The efficiencies are given for each model-dependent category in Table 7.10. The fractions of the $\gamma\gamma$, γj and jj background components over the [60, 120] GeV mass range obtained using the 2x2D sideband decomposition are shown in Table 7.11 for each model-dependent category.

Since the 2x2D sideband decomposition method relies on L′4 candidates, the decomposition is performed only on events with photon candidates that pass the prescaled `2g20_loose` HLT described in Section 6.2. This prescaled trigger only gives approximately 5% of the total data statistics in the signal region to be used for this background composition determination. The results of the decomposition as a function of diphoton mass are shown in Figure 7.19. The overall fractions of the $\gamma\gamma$, γj, and jj components are shown in Figure 7.20. The diphoton purity slightly increases with the mass and depends on the diphoton BDT categorization as expected. The purity is highest in the most signal-enriched UU3 category and the lowest in the most signal-depleted CC1 category.

Category		Isolation		Identification
UU1	ϵ_{I1}	0.9199 ± 0.0001	ϵ_{T1}	0.9259 ± 0.0001
	ϵ_{I2}	0.8827 ± 0.0002	ϵ_{T2}	0.9229 ± 0.0001
UC1	ϵ_{I1}	0.8932 ± 0.0002	ϵ_{T1}	0.9398 ± 0.0001
	ϵ_{I2}	0.8519 ± 0.0002	ϵ_{T2}	0.9348 ± 0.0001
CC1	ϵ_{I1}	0.8699 ± 0.0004	ϵ_{T1}	0.9548 ± 0.0002
	ϵ_{I2}	0.8204 ± 0.0004	ϵ_{T2}	0.9487 ± 0.0002
UU2	ϵ_{I1}	0.9237 ± 0.0001	ϵ_{T1}	0.9263 ± 0.0001
	ϵ_{I2}	0.8771 ± 0.0002	ϵ_{T2}	0.9199 ± 0.0001
UC2	ϵ_{I1}	0.9003 ± 0.0002	ϵ_{T1}	0.9402 ± 0.0001
	ϵ_{I2}	0.8446 ± 0.0002	ϵ_{T2}	0.9302 ± 0.0001
CC2	ϵ_{I1}	0.8783 ± 0.0004	ϵ_{T1}	0.9546 ± 0.0003
	ϵ_{I2}	0.8143 ± 0.0005	ϵ_{T2}	0.9423 ± 0.0003
UU3	ϵ_{I1}	0.9288 ± 0.0002	ϵ_{T1}	0.9330 ± 0.0002
	ϵ_{I2}	0.8888 ± 0.0002	ϵ_{T2}	0.9213 ± 0.0002
UC3	ϵ_{I1}	0.9109 ± 0.0002	ϵ_{T1}	0.9467 ± 0.0002
	ϵ_{I2}	0.8589 ± 0.0002	ϵ_{T2}	0.9327 ± 0.0002
CC3	ϵ_{I1}	0.8930 ± 0.0005	ϵ_{T1}	0.9619 ± 0.0003
	ϵ_{I2}	0.8307 ± 0.0005	ϵ_{T2}	0.9454 ± 0.0003

Table 7.10: The photon isolation and ID efficiencies for true photons from Sherpa2 $\gamma\gamma$ samples in the [60, 120] GeV mass range for each model-dependent category. The efficiencies are determined with respect to the leading and subleading photon candidates of true diphoton events that pass the full event selection except the photon isolation and having the ID criteria replaced with L′4 ID requirements. The uncertainty on these efficiencies comes from the MC statistical uncertainty.

Category	Component	Fraction
UU1	$\gamma\gamma$	$0.724 \pm 0.007^{+0.007}_{-0.019}$
	γj	$0.157 \pm 0.005^{+0.010}_{-0.003}$
	$j\gamma$	$0.044 \pm 0.003^{+0.010}_{-0.000}$
	jj	$0.075 \pm 0.002^{+0.000}_{-0.006}$
UC1	$\gamma\gamma$	$0.687 \pm 0.007^{+0.026}_{-0.033}$
	γj	$0.176 \pm 0.005^{+0.012}_{-0.012}$
	$j\gamma$	$0.061 \pm 0.004^{+0.015}_{-0.004}$
	jj	$0.076 \pm 0.002^{+0.005}_{-0.009}$
CC1	$\gamma\gamma$	$0.618 \pm 0.018^{+0.033}_{-0.006}$
	γj	$0.216 \pm 0.012^{+0.000}_{-0.024}$
	$j\gamma$	$0.085 \pm 0.009^{+0.000}_{-0.012}$
	jj	$0.081 \pm 0.004^{+0.028}_{-0.013}$
UU2	$\gamma\gamma$	$0.749 \pm 0.006^{+0.007}_{-0.013}$
	γj	$0.153 \pm 0.005^{+0.011}_{-0.006}$
	$j\gamma$	$0.049 \pm 0.003^{+0.006}_{-0.000}$
	jj	$0.048 \pm 0.002^{+0.000}_{-0.005}$
UC2	$\gamma\gamma$	$0.699 \pm 0.008^{+0.025}_{-0.040}$
	γj	$0.171 \pm 0.005^{+0.015}_{-0.013}$
	$j\gamma$	$0.078 \pm 0.004^{+0.021}_{-0.006}$
	jj	$0.051 \pm 0.002^{+0.004}_{-0.006}$
CC2	$\gamma\gamma$	$0.659 \pm 0.017^{+0.034}_{-0.034}$
	γj	$0.190 \pm 0.011^{+0.019}_{-0.018}$
	$j\gamma$	$0.083 \pm 0.008^{+0.011}_{-0.006}$
	jj	$0.068 \pm 0.004^{+0.004}_{-0.011}$
UU3	$\gamma\gamma$	$0.800 \pm 0.007^{+0.005}_{-0.007}$
	γj	$0.110 \pm 0.005^{+0.002}_{-0.007}$
	$j\gamma$	$0.069 \pm 0.004^{+0.007}_{-0.000}$
	jj	$0.021 \pm 0.001^{+0.000}_{-0.003}$
UC3	$\gamma\gamma$	$0.744 \pm 0.009^{+0.019}_{-0.027}$
	γj	$0.127 \pm 0.005^{+0.016}_{-0.012}$
	$j\gamma$	$0.101 \pm 0.005^{+0.002}_{-0.004}$
	jj	$0.028 \pm 0.002^{+0.009}_{-0.003}$
CC3	$\gamma\gamma$	$0.672 \pm 0.023^{+0.035}_{-0.046}$
	γj	$0.158 \pm 0.014^{+0.015}_{-0.021}$
	$j\gamma$	$0.129 \pm 0.012^{+0.018}_{-0.008}$
	jj	$0.042 \pm 0.004^{+0.013}_{-0.006}$

Table 7.11: The $\gamma\gamma$, γj, and jj fractions in the [60, 120] GeV mass range, obtained using the 2x2D sideband method for each model-dependent category. The first error term reflects the statistical uncertainty, and the second error term reflects the systematic uncertainties derived from the L′ variations.

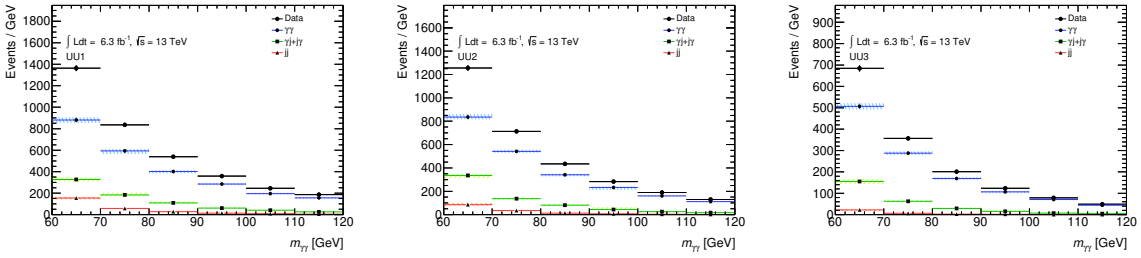

(a) Yields in UU1. (b) Yields in UU2. (c) Yields in UU3.

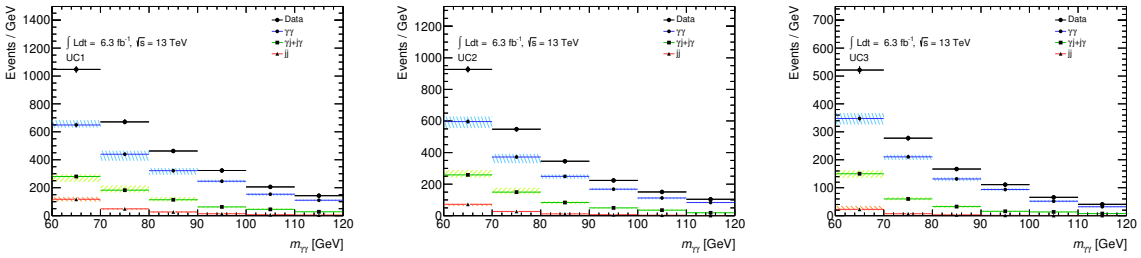

(d) Yields in UC1. (e) Yields in UC2. (f) Yields in UC3.

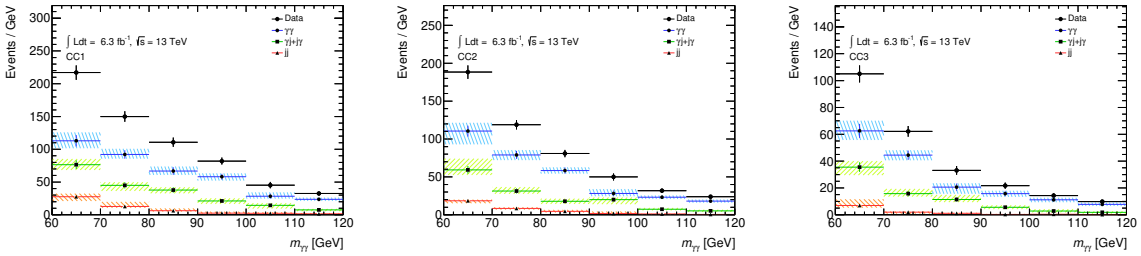

(g) Yields in CC1. (h) Yields in CC2. (i) Yields in CC3.

Figure 7.19: The $\gamma\gamma$, γj, and jj component yields for each model-dependent category determined by the 2x2D sideband method as a function of the diphoton mass.

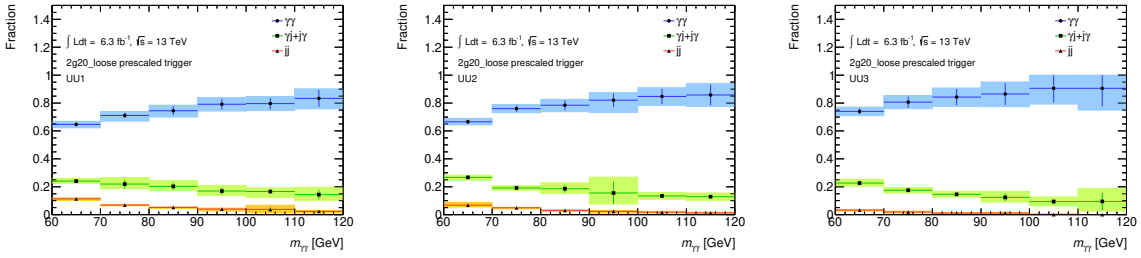

(a) Fractions in UU1.

(b) Fractions in UU2.

(c) Fractions in UU3.

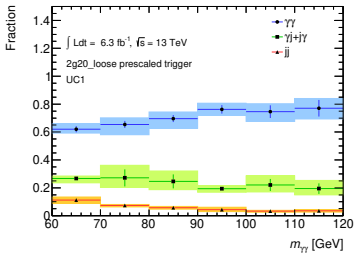

(d) Fractions in UC1.

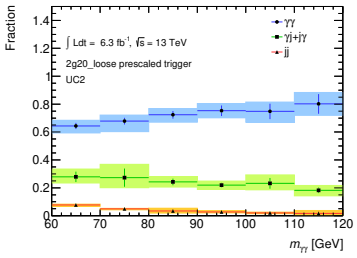

(e) Fractions in UC2.

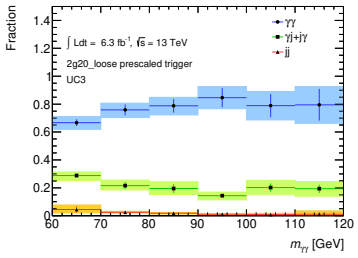

(f) Fractions in UC3.

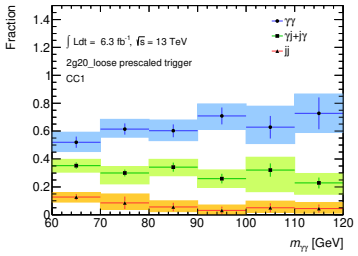

(g) Fractions in CC1.

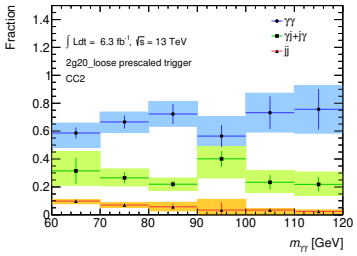

(h) Fractions in CC2.

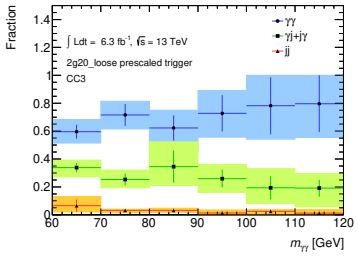

(i) Fractions in CC3.

Figure 7.20: The $\gamma\gamma$, γj, and jj component fractions for each model-dependent category determined by the 2x2D sideband method as a function of the diphoton mass.

◊ **Model-Independent Method** The isolation and ID efficiencies are given for each model-independent category in Table 7.12. The fractions of the $\gamma\gamma$, γj and jj background components over the [60, 120] GeV mass range obtained using the 2x2D sideband decomposition are shown in Table 7.13 for each model-independent category.

The results of the decomposition as a function of diphoton mass are shown in Figure 7.21. The overall fractions of the $\gamma\gamma$, γj, and jj components are shown in Figure 7.22. The diphoton purity slightly increases with the mass as expected.

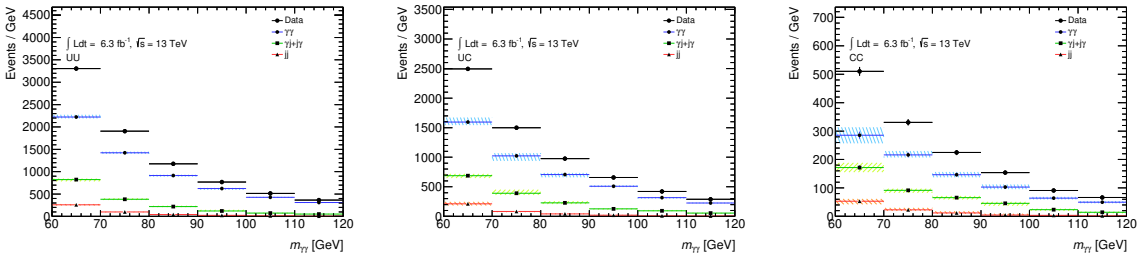

(a) Yields in UU. (b) Yields in UC. (c) Yields in CC.

Figure 7.21: The $\gamma\gamma$, γj, and jj component yields for each model-independent category determined by the 2x2D sideband method as a function of the diphoton mass.

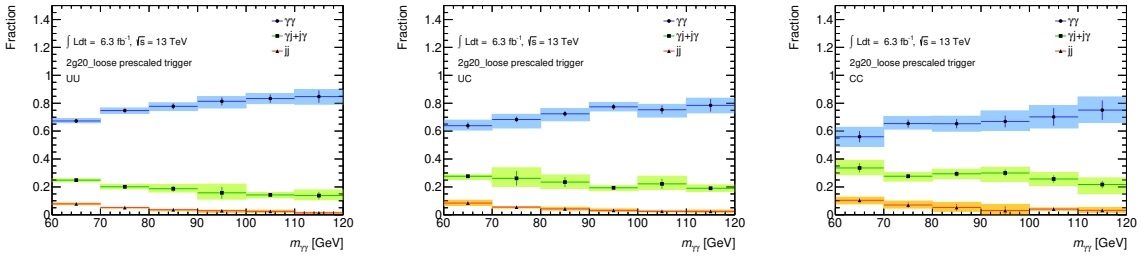

(a) Fractions in UU. (b) Fractions in UC. (c) Fractions in CC.

Figure 7.22: The $\gamma\gamma$, γj, and jj component fractions for each model-independent category determined by the 2x2D sideband method as a function of the diphoton mass.

Category	Isolation		Identification	
UU	ϵ_{I1}	0.9233 ± 0.0001	ϵ_{T1}	0.9276 ± 0.0001
	ϵ_{I2}	0.8819 ± 0.0001	ϵ_{T2}	0.9214 ± 0.0001
UC	ϵ_{I1}	0.8996 ± 0.0001	ϵ_{T1}	0.9415 ± 0.0001
	ϵ_{I2}	0.8508 ± 0.0001	ϵ_{T2}	0.9327 ± 0.0001
CC	ϵ_{I1}	0.8777 ± 0.0002	ϵ_{T1}	0.9562 ± 0.0001
	ϵ_{I2}	0.8203 ± 0.0003	ϵ_{T2}	0.9457 ± 0.0002

Table 7.12: The photon isolation and ID efficiencies for true photons from Sherpa2 $\gamma\gamma$ samples in the [60, 120] GeV mass range for each model-dependent category. The efficiencies are determined with respect to the leading and subleading photon candidates of true diphoton events that pass the full event selection except the photon isolation and having the ID criteria replaced with L′4 ID requirements. The uncertainty on these efficiencies comes from the MC statistical uncertainty.

Category	Component	Fraction
UU	$\gamma\gamma$	$0.748 \pm 0.004^{+0.007}_{-0.012}$
	γj	$0.147 \pm 0.003^{+0.009}_{-0.005}$
	$j\gamma$	$0.052 \pm 0.002^{+0.007}_{-0.000}$
	jj	$0.054 \pm 0.001^{+0.000}_{-0.005}$
UC	$\gamma\gamma$	$0.703 \pm 0.005^{+0.024}_{-0.033}$
	γj	$0.164 \pm 0.003^{+0.014}_{-0.012}$
	$j\gamma$	$0.075 \pm 0.002^{+0.013}_{-0.005}$
	jj	$0.058 \pm 0.001^{+0.006}_{-0.007}$
CC	$\gamma\gamma$	$0.643 \pm 0.011^{+0.035}_{-0.025}$
	γj	$0.195 \pm 0.007^{+0.001}_{-0.019}$
	$j\gamma$	$0.092 \pm 0.005^{+0.007}_{-0.004}$
	jj	$0.070 \pm 0.002^{+0.017}_{-0.011}$

Table 7.13: The $\gamma\gamma$, γj, and jj fractions in the [60, 120] GeV mass range, obtained using the 2x2D sideband method for each model-dependent category. The first error term reflects the statistical uncertainty, and the second error term reflects the systematic uncertainties derived from the L′ variations.

7.3.1.2 Irreducible Background Shape

The irreducible part of the QCD background is described using the high-statistics Sherpa2 $\gamma\gamma$ sample. Since the irreducible background is composed of two mass slices, the relative normalization between the two does not produce the most smooth transition at the 90 GeV stitching point where the two mass slices meet. Although the difference is smaller than the 1% statistical uncertainty on the cross-section, the spurious signal method that characterizes the difference between the constructed background model and the data as described later in Section 7.3.2.2 is still sensitive to this small discontinuity in shape.

To correct for this difference, a maximum likelihood fit using a fifth order polynomial function is performed on the distribution where the $90 - 175$ GeV slice is weighted with a stitching factor before being added to the non-weighted $50 - 90$ GeV slice. Despite having much higher statistics than the data, the MC sample can experience fluctuations in the $m_{\gamma\gamma}$ shape due to the event weights which are the product of the MC generator, z-vertex, pileup, diphoton trigger scale factor, and photon ID and isolation scale factor weights. The distribution of the weight values is used with respect to the truth invariant mass instead of the reconstructed invariant mass to reduce fluctuations further.

The MC generator, pileup weights, and diphoton trigger scale factor weights have clear dependence on the truth invariant mass as shown in Figures 7.23a, 7.23c, and 7.23d and thus must be applied when determining the stitching factor for the two mass slices. However, the z-vertex and photon ID and isolation scale factor shown in Figures 7.23b and 7.23e have a much smaller trend compared to the variation in the weights themselves as well as the variations of the template presented in Section 7.3.1.3 and thus will not be applied when performing the maximum likelihood fit to mitigate fluctuations. Additionally, a cut of 3 is applied to the absolute value of the used composite weight, a product of the MC generator, pileup weights, and diphoton

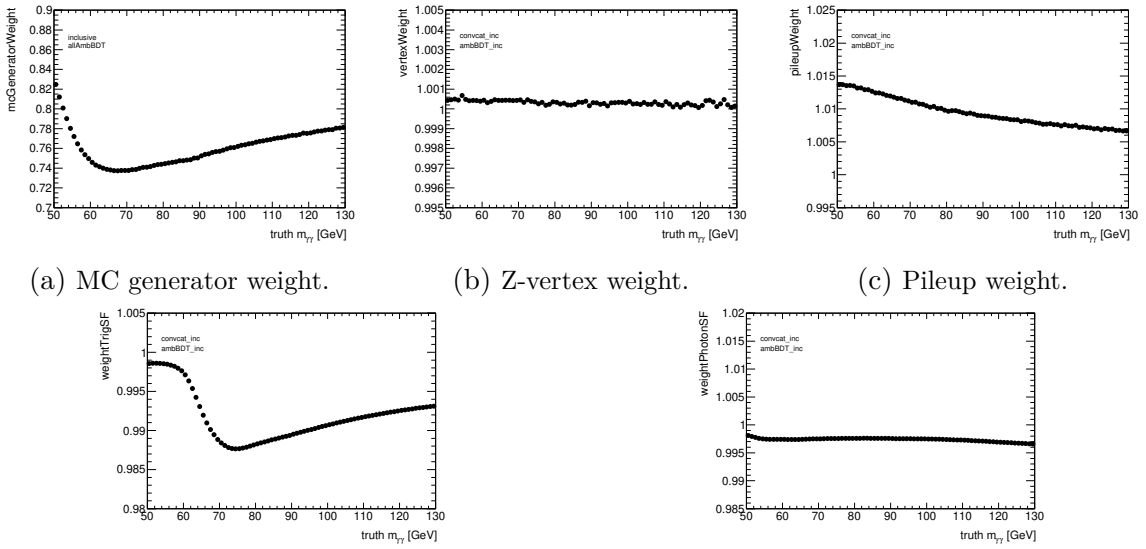

(a) MC generator weight. (b) Z-vertex weight. (c) Pileup weight.

(d) Diphoton trigger scale factor weight. (e) Photon ID and isolation scale factor weight.

Figure 7.23: Components of the event weight shown as a distribution with respect to the truth invariant mass for the Sherpa2 $\gamma\gamma$ samples in the fully inclusive category. The two mass slices are combined with no stitch weighting applied and is composed of all three MC campaigns (mc16a, mc16d, and mc16e).

trigger scale factor weights, with minimal impact on the the overall shape to limit the statistical variations associated with this composite weight.

♦ **Model-Dependent Method** This stitching factor on the weighted slice is tested using values between 0.95 and 1.05 in 0.001 steps for each model-dependent category in each MC campaign. The best value for each case is listed in Table 7.14 along with the associated χ^2 value and probability. A comparison between the irreducible background with and without weighting on the slices in the UU3 category is shown in Figure 7.24 as an example.

MC Campaign	Category	Stitching Factor	χ^2/ndf	p-value
mc16a	UU1	1.037	$21.286/24 = 0.887$	0.622
	UU2	1.024	$31.227/24 = 1.301$	0.147
	UU3	1.030	$27.520/24 = 1.147$	0.281
	UC1	1.027	$26.554/24 = 1.106$	0.326
	UC2	1.038	$18.669/24 = 0.778$	0.769
	UC3	1.027	$25.393/24 = 1.058$	0.385
	CC1	1.029	$20.753/24 = 0.865$	0.653
	CC2	1.028	$31.240/24 = 1.302$	0.147
	CC3	1.022	$20.885/24 = 0.870$	0.646
mc16d	UU1	0.991	$17.356/24 = 0.723$	0.833
	UU2	0.998	$20.531/24 = 0.855$	0.666
	UU3	0.983	$19.454/24 = 0.811$	0.727
	UC1	0.995	$29.069/24 = 1.211$	0.218
	UC2	0.998	$20.601/24 = 0.858$	0.662
	UC3	0.978	$25.439/24 = 1.060$	0.382
	CC1	0.991	$19.746/24 = 0.823$	0.711
	CC2	0.990	$23.109/24 = 0.963$	0.513
	CC3	0.983	$26.143/24 = 1.089$	0.346
mc16e	UU1	0.994	$31.386/24 = 1.308$	0.143
	UU2	0.995	$40.244/24 = 1.677$	0.020
	UU3	0.988	$18.650/24 = 0.777$	0.770
	UC1	0.993	$20.494/24 = 0.854$	0.668
	UC2	0.994	$22.711/24 = 0.946$	0.537
	UC3	0.983	$24.721/24 = 1.030$	0.421
	CC1	0.993	$31.004/24 = 1.292$	0.154
	CC2	0.994	$35.411/24 = 1.475$	0.063
	CC3	1.009	$15.680/24 = 0.653$	0.899

Table 7.14: Stitching factors applied as an overall weight to the Sherpa2 $\gamma\gamma$ $90 - 175$ GeV slice before being combined with the $50 - 90$ GeV slice to reduce the transition discontinuity at 90 GeV. The factor is found using a maximum likelihood fit using a fifth order polynomial for each model-dependent category in each of the three MC campaigns.

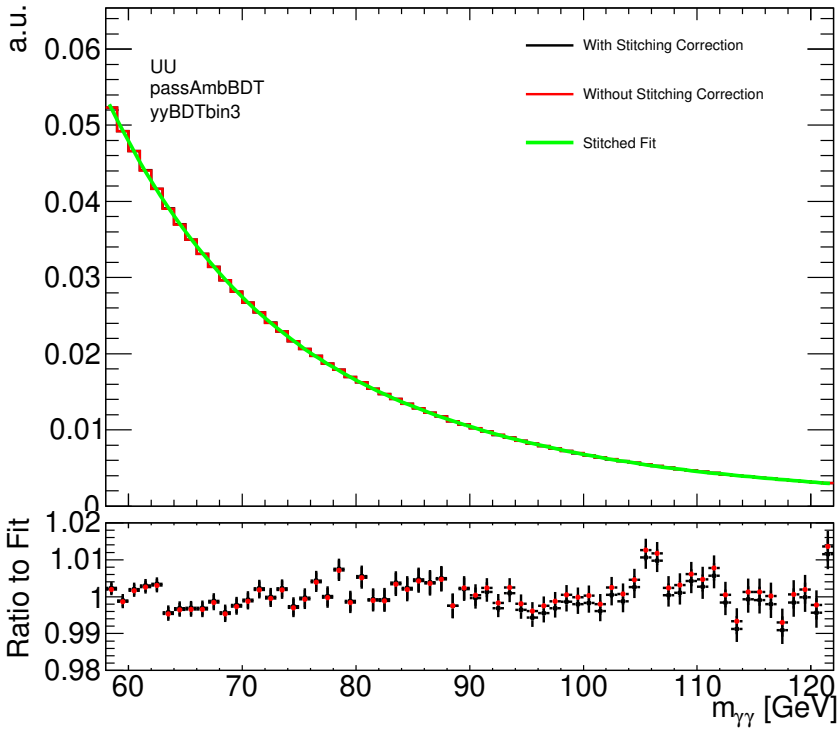

Figure 7.24: The irreducible background with (red) and without (black) weighting on the slices for the UU3 category. The ratio to the fit (green) on the weighted shape is shown for comparison.

◊ **Model-Independent Method** This stitching factor on the weighted slice is tested using values between 0.95 and 1.05 in 0.001 steps for each model-independent category in each MC campaign as well. The best value for each case is listed in Table 7.15 along with the associated χ^2 value and probability. A comparison between the irreducible background with and without weighting on the slices in the UU category is shown in Figure 7.25.

MC Campaign	Category	Stitching Factor	χ^2/ndf	p-value
mc16a	UU	1.031	$26.474/24 = 1.103$	0.330
	UC	1.031	$18.336/24 = 0.764$	0.786
	CC	1.027	$25.053/24 = 1.044$	0.403
mc16d	UU	0.992	$18.237/24 = 0.760$	0.791
	UC	0.992	$24.230/24 = 1.010$	0.449
	CC	0.990	$21.351/24 = 0.890$	0.618
mc16e	UU	0.993	$36.183/24 = 1.508$	0.053
	UC	0.991	$13.755/24 = 0.573$	0.952
	CC	0.997	$26.721/24 = 1.113$	0.318

Table 7.15: Stitching factors applied as an overall weight to the Sherpa2 $\gamma\gamma$ $90-175$ GeV slice before being combined with the $50-90$ GeV slice to reduce the transition discontinuity at 90 GeV. The factor is found using a maximum likelihood fit using a fifth order polynomial for each model-independent category in each of the three MC campaigns.

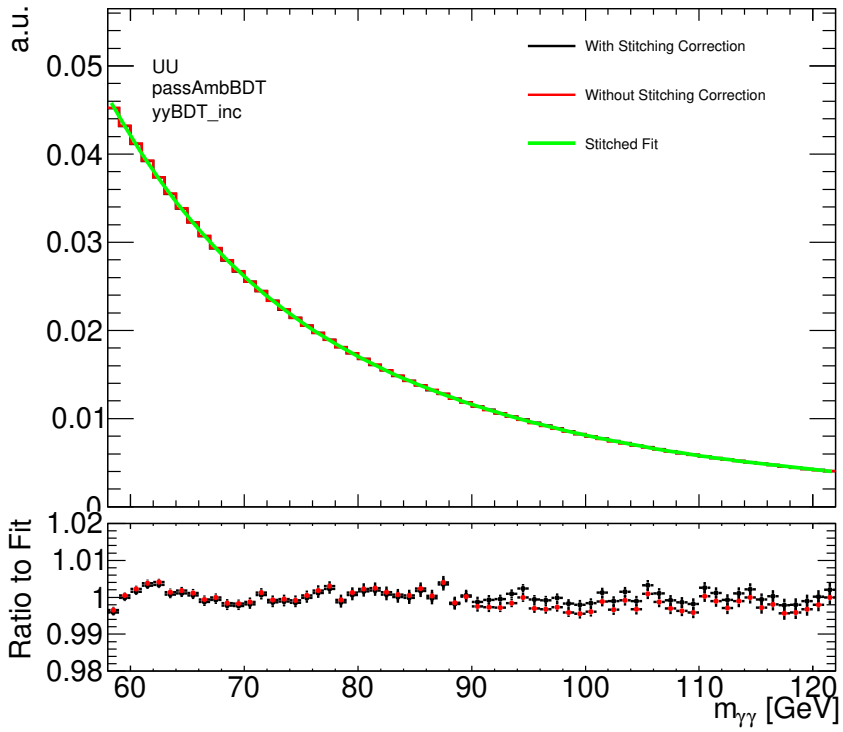

Figure 7.25: The irreducible background with (red) and without (black) weighting on the slices for the UU category. The ratio to the fit (green) on the weighted shape is shown for comparison.

7.3.1.3 Reducible Background Shape

In principle, the 2x2D decomposition method could be used to estimate the shape of the reducible background component arising from the jet fake background (γj + jj) if the results of the decomposition were provided in a fine $m_{\gamma\gamma}$ binning. However, this approach would effectively use the dataset itself as the template to create the background model. The granularity required for such an estimation would allow for a new resonance to be seen prematurely over the background template expectation before the full background model is constructed. A second shortcoming arises from the already limited statistics seen in the 2x2D decomposition binning, making the 2x2D method susceptible to statistical fluctuations for fine $m_{\gamma\gamma}$ binning.

A simpler approach is used to estimate the reducible background component, focusing mainly on the shape of the γj component given its dominating size relative to the jj component of the reducible background. The contribution of jj events is expected to be insignificant as shown in Section 7.3.1.1. The effect of the jj shape on the reducible background shape is therefore neglected, and only its effect on the normalization of the reducible background is taken into account when scaling the reducible background template shape. This assumption has been demonstrated to be valid in the other similar diphoton resonance searches [85] [55] [1] where the reducible background compositions are similar to those of this analysis.

Although control regions are used to estimate the shape of the reducible component of the non-resonant background, prompt diphoton events can still leak from the signal region into nearby control regions. Furthermore, this true $\gamma\gamma$ leakage can become a large contribution in some control regions since the modified loose ID criteria set by some L$'$ definitions can still reject a significant amount of jets faking photons. The diphoton contamination in these regions can be effectively estimated by the MC samples and is removed via subtraction of the MC estimated contribution from the data control region.

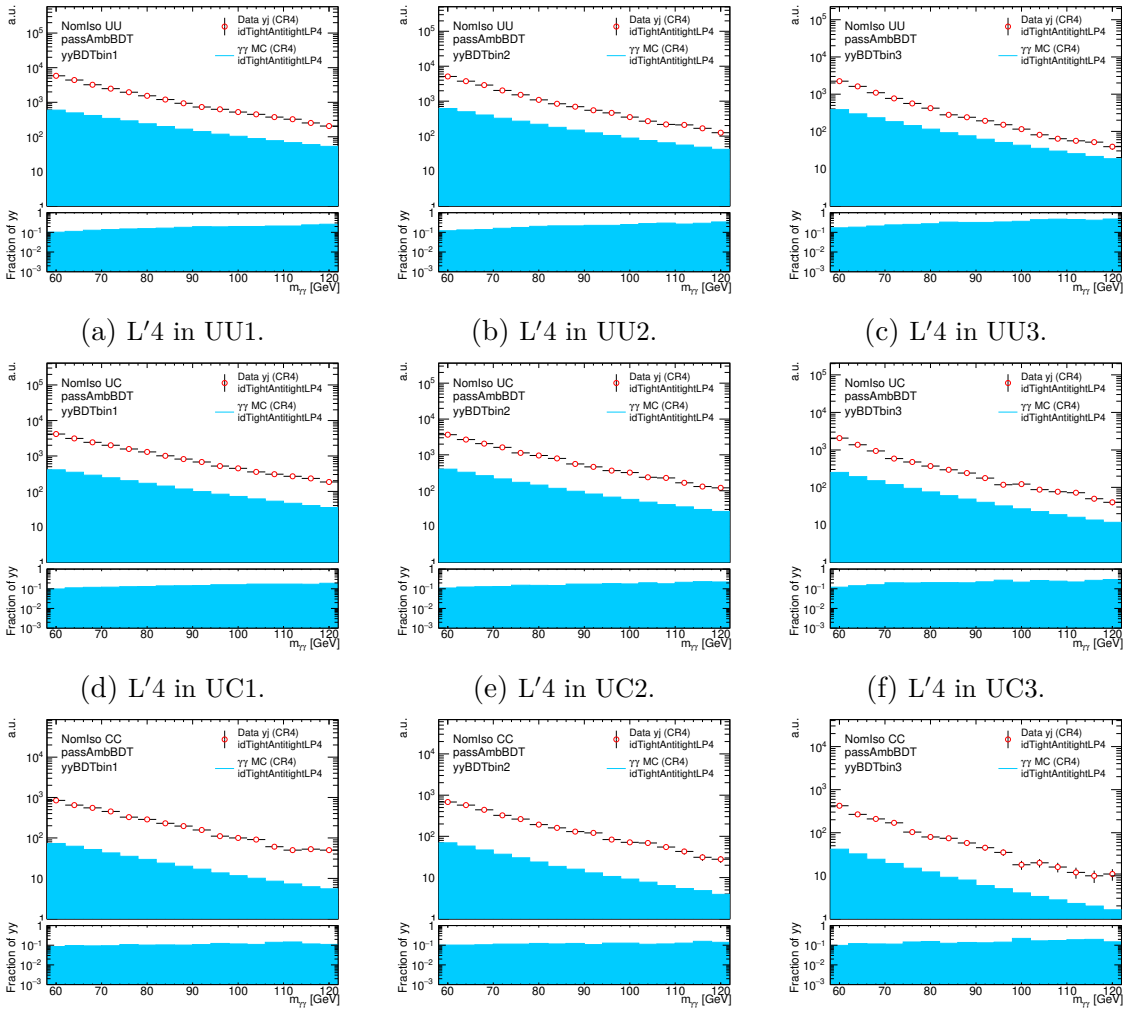

(a) L′4 in UU1. (b) L′4 in UU2. (c) L′4 in UU3.

(d) L′4 in UC1. (e) L′4 in UC2. (f) L′4 in UC3.

(g) L′4 in CC1. (h) L′4 in CC2. (i) L′4 in CC3.

Figure 7.26: Reducible background shapes from data in L′4 shown with the expected contribution for prompt diphoton events from Sherpa2 $\gamma\gamma$ MC simulation in L′4 for each model-dependent category.

♦ **Model-Dependent Method** To illustrate the true $\gamma\gamma$ contamination in the model-dependent categories, Figure 7.26 shows the data in the L'4 control region together with the expected contributions from prompt diphoton events as predicted by MC simulation. To better estimate the shape of the reducible component, the $\gamma\gamma$ contribution is subtracted from the data control region bin-by-bin in 4 GeV wide bins using the expected $\gamma\gamma$ leakage from MC simulation.

Since the $\gamma\gamma$ contamination strongly affects the shape estimation of the reducible

component, the L′ definition is varied to observe the dependence on the different sets of selections. The diphoton mass distribution for each L′ variation is obtained from the data with the $\gamma\gamma$ leakage subtracted and shown in Figure 7.27 for each model-dependent category. Since the L′5 control region requires the loosest photon candidate ID of all L′ variations, this region gives the highest statistics and purity in γj events. However, the fake photons in this region might not be representative of the reducible background in the signal region. On the other hand, since the L′2 control region requires the tightest photon candidate ID, this region is expected to contain a large contamination of true diphoton events leaking from the signal to the control region due to inefficiencies in the tight identification requirements. To maintain sufficient purity in γj events while balancing the identification requirements, the L′4 control region (referred to as CR4) is used as the nominal control region. This control region is defined as the region where both photons pass the isolation selections and where one photon passes the Tight identification while the other photon passes the LoosePrime-4 identification but fails the Tight identification. This control region uses data from the `2g20_loose` HLT and has the advantage of being close to the signal region. The $\gamma\gamma$ contamination can be high depending on the category and is on average approximately 30% of the reducible background template. The other L′ variations are used to determine a systematic uncertainty on the reducible background shape.

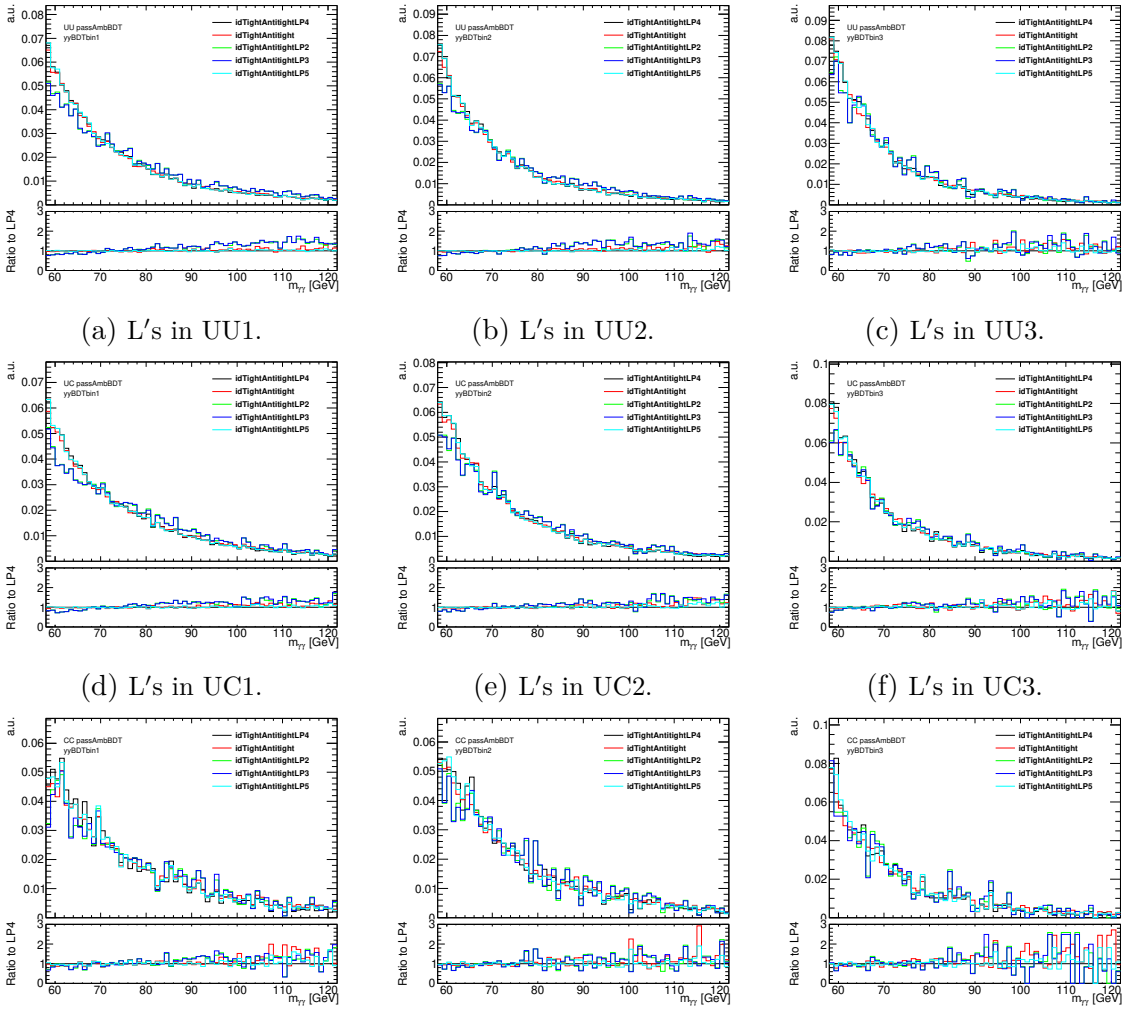

(a) L′s in UU1. (b) L′s in UU2. (c) L′s in UU3.

(d) L′s in UC1. (e) L′s in UC2. (f) L′s in UC3.

(g) L′s in CC1. (h) L′s in CC2. (i) L′s in CC3.

Figure 7.27: Reducible background shapes obtained from the data in the different L′ variations for each model-dependent category. All distributions are normalized to unity to compare shapes with the nominal control region (L′4). The Tight-Antitight control region, which has no additional L′ requirement, is also shown in red for comparison but is not used in this analysis. The bottom panel shows the ratio comparing each control region to L′4.

◊ **Model-Independent Method** The real $\gamma\gamma$ contamination of prompt diphoton events as predicted by MC simulation into the L′4 data control region for the model-independent categories is shown in Figure 7.28. The $\gamma\gamma$ contribution is subtracted from the data control region bin-by-bin in 4 GeV wide bins using the expected $\gamma\gamma$ leakage from MC simulation. The L′ definition is also varied for the model-independent categories to observe the dependence on the different sets of selections. The diphoton mass distribution for each L′ variation is obtained from the data with the $\gamma\gamma$ leakage subtracted and shown in Figure 7.29.

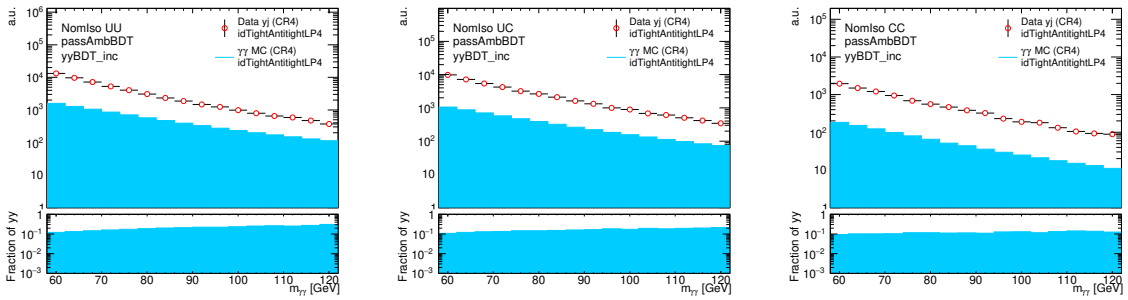

(a) L′4 in UU. (b) L′4 in UC. (c) L′4 in CC.

Figure 7.28: Reducible background shapes from data in L′4 shown with the expected contribution for prompt diphoton events from Sherpa2 $\gamma\gamma$ MC simulation in L′4 for each model-independent category.

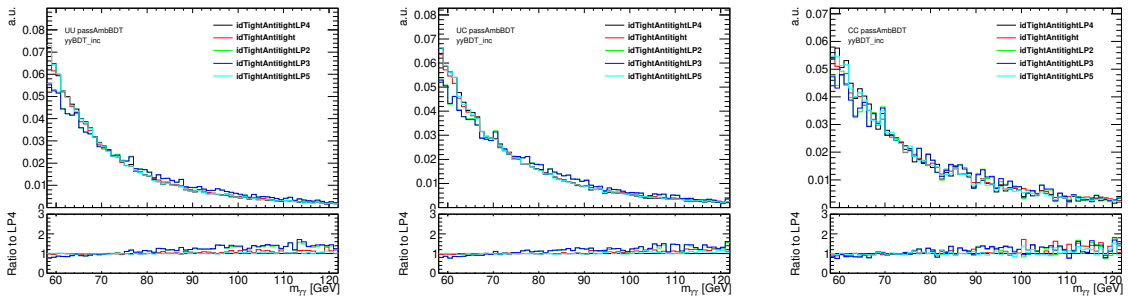

(a) L′s in UU. (b) L′s in UC. (c) L′s in CC.

Figure 7.29: Reducible background shapes obtained from the data in the different L′ variations for each model-independent category. All distributions are normalized to unity to compare shapes with the nominal control region (L′4). The Tight-Antitight control region, which has no additional L′ requirement, is also shown in red for comparison but is not used in this analysis. The bottom panel shows the ratio comparing each control region to L′4.

7.3.2 Full Background Continuum Shape

The full background template is constructed by using the high-statistics MC $\gamma\gamma$ component and the L′4 data control region reducible background component. Each component is scaled to their relative contribution according to the measured fractions integrated across the range 62 GeV $< m_{\gamma\gamma} <$ 120 GeV in the signal region estimated from the 2x2D decomposition method. To retain the smoothness of the $\gamma\gamma$ component in the full template, a smooth version of the γj component is created by a simple reweighting applied on the $\gamma\gamma$ component.

♦ **Model-Dependent Method** The scaled $\gamma\gamma$ and γj components are added and the sum is divided by the $\gamma\gamma$ component to obtain a ratio fit with a simple exponential function as shown in Figure 7.30. The fitted function is used to construct the smooth full $\gamma\gamma + \gamma j$ component by reweighting the $\gamma\gamma$ MC component.

The reducible background consisting of the γj and jj components can be further decomposed by taking the component fractions derived from the 2x2D method. The expected number of events for the $\gamma\gamma$, γj, and jj components based on the total event count of the data signal region is listed in Table 7.16. The full QCD diphoton background continuum with each component is shown in Figure 7.31.

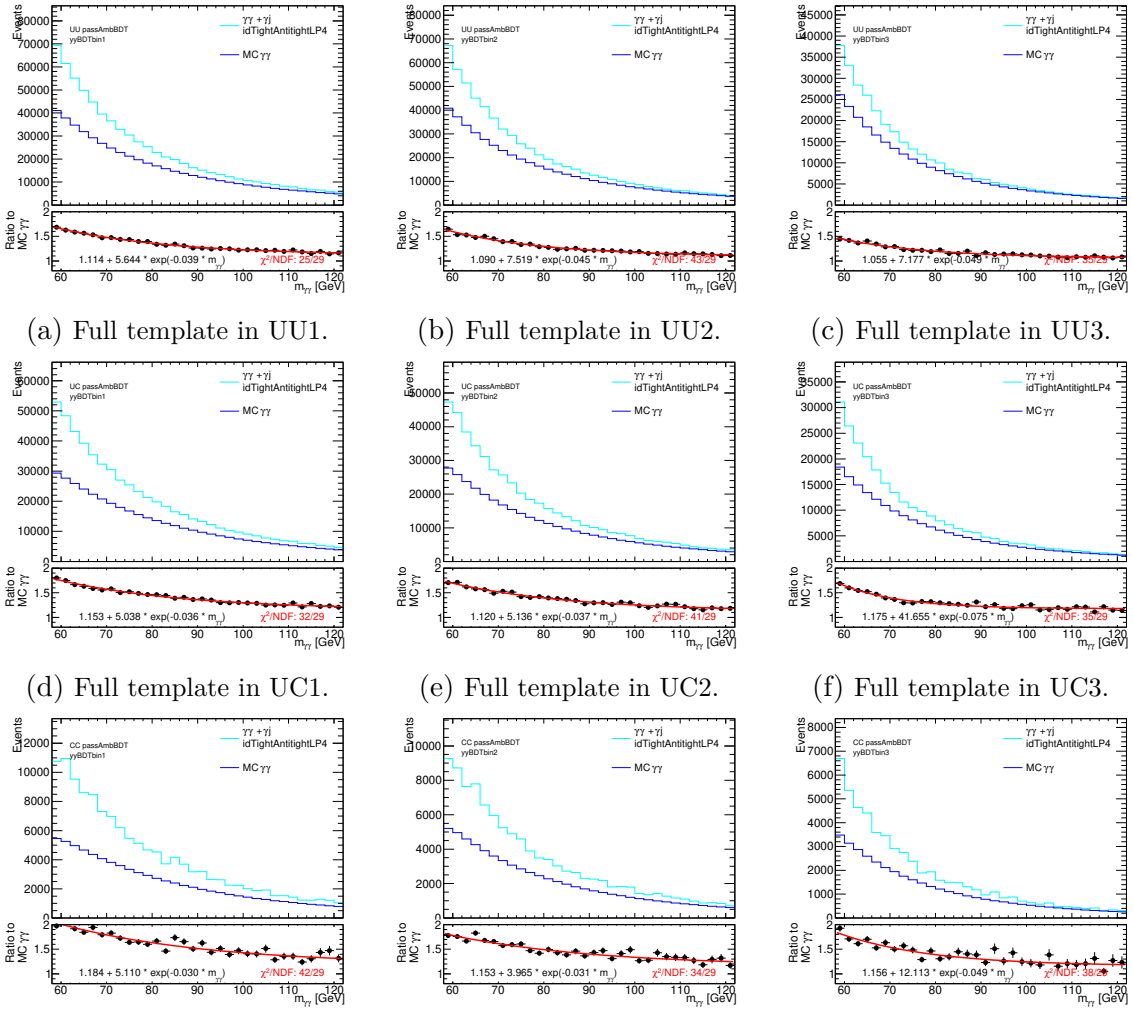

(a) Full template in UU1. (b) Full template in UU2. (c) Full template in UU3.

(d) Full template in UC1. (e) Full template in UC2. (f) Full template in UC3.

(g) Full template in CC1. (h) Full template in CC2. (i) Full template in CC3.

Figure 7.30: Full background template constructed from MC signal region $\gamma\gamma$ component and the L′4 data control region reducible γj component for each model-dependent category. The contributions of the $\gamma\gamma$ component are separately shown in dark blue to emphasize its contribution to the full template shown in light blue. The bottom panel shows the ratio between the full template and the $\gamma\gamma$ component.

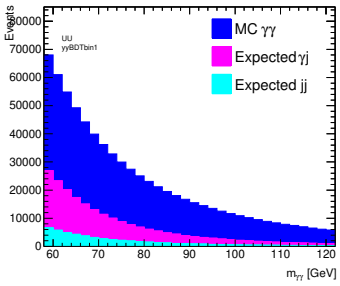

(a) Template stack in UU1.

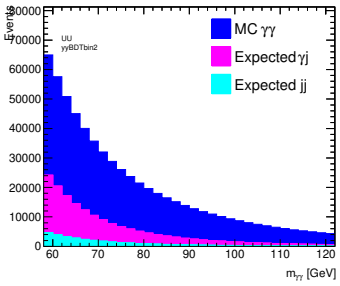

(b) Template stack in UU2.

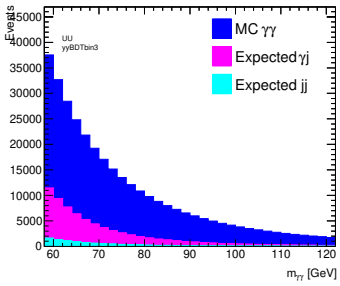

(c) Template stack in UU3.

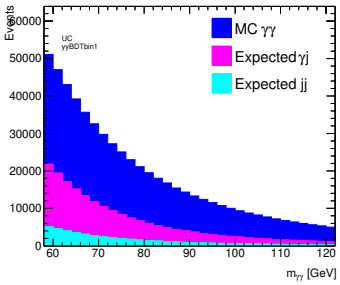

(d) Template stack in UC1.

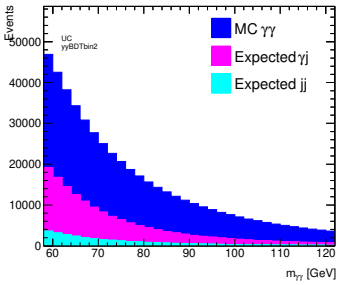

(e) Template stack in UC2.

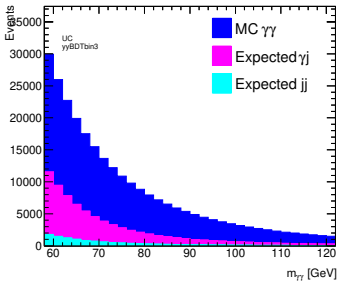

(f) Template stack in UC3.

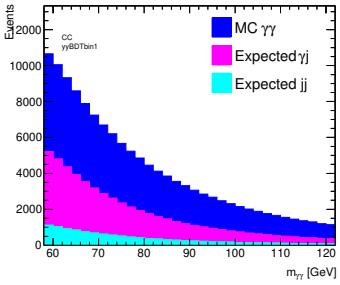

(g) Template stack in CC1.

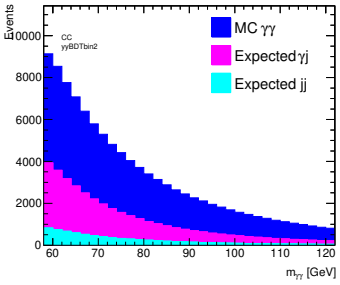

(h) Template stack in CC2.

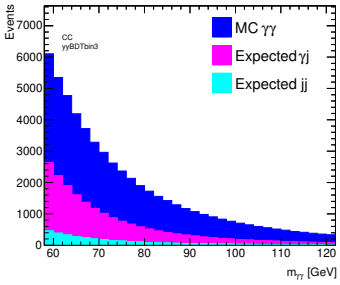

(i) Template stack in CC3.

Figure 7.31: Full background template of the $\gamma\gamma$, γj, and jj component for each model-dependent category.

Diphoton BDT	Photon Conversion	QCD Background Component $\gamma\gamma$	γj	jj
Bin 1	UU	423746	124037	40357
	UC	331118	118863	35958
	CC	64521	33610	9217
Bin 2	UU	379797	102841	24437
	UC	279785	96895	22205
	CC	55632	23029	6037
Bin 3	UU	205134	42662	6897
	UC	153411	45750	8395
	CC	30061	11808	2479

Table 7.16: The expected number of events for each of the diphoton background continuum components for each model-dependent category in the diphoton invariant mass range $62\,\text{GeV} < m_{\gamma\gamma} < 120\,\text{GeV}$.

$\Diamond$ **Model-Independent Method** The scaled $\gamma\gamma$ and γj components are added and the sum is divided by the $\gamma\gamma$ component to obtain a ratio fit with a simple exponential function as shown in Figure 7.32. The fitted function is used to construct the smooth full $\gamma\gamma + \gamma j$ component by reweighting the $\gamma\gamma$ MC component. The expected number of events for the $\gamma\gamma$, γj, and jj components based on the total event count of the data signal region is listed in Table 7.17. The full QCD diphoton background continuum with each component is shown in Figure 7.33.

Photon Conversion	QCD Background Component $\gamma\gamma$	γj	jj
UU	1008677	269540	71691
UC	764314	261508	66558
CC	150214	68447	17733

Table 7.17: The expected number of events for each of the diphoton background continuum components for each model-independent category in the diphoton invariant mass range $62\,\text{GeV} < m_{\gamma\gamma} < 120\,\text{GeV}$.

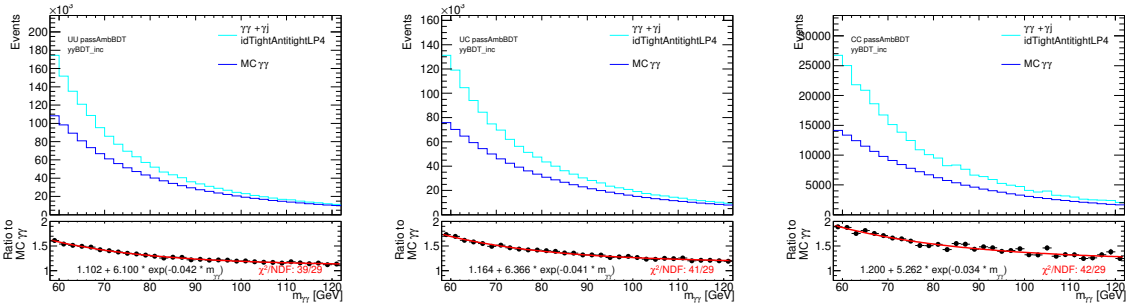

(a) Full template in UU1. (b) Full template in UC. (c) Full template in CC.

Figure 7.32: Full background template constructed from MC signal region $\gamma\gamma$ component and the L′4 data control region reducible γj component for each model-independent category. The contributions of the $\gamma\gamma$ component are separately shown in dark blue to emphasize its contribution to the full template shown in light blue. The bottom panel shows the ratio between the full template and the $\gamma\gamma$ component.

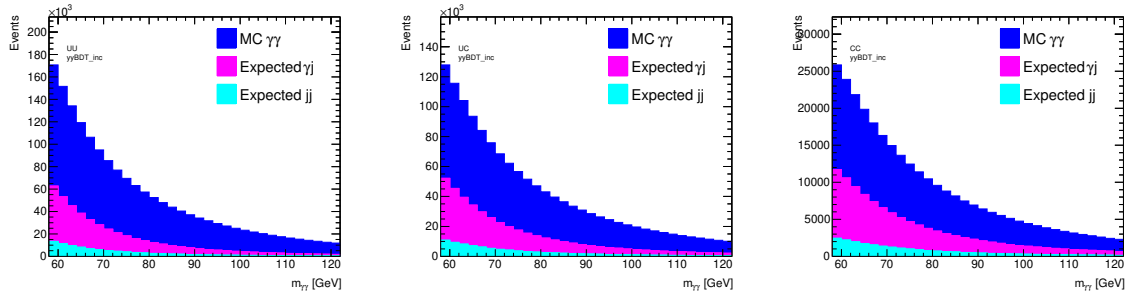

(a) Template stack in UU. (b) Template stack in UC. (c) Template stack in CC.

Figure 7.33: Full background template of the $\gamma\gamma$, γj, and jj component for each model-independent category.

7.3.2.1 Smoothing Background Templates using GPR

Although the irreducible background template shape is derived from the high-statistics Sherpa2 $\gamma\gamma$ MC samples, statistical fluctuations are still present throughout its $m_{\gamma\gamma}$ spectrum. These fluctuations are found to introduce potential signal yield bias when the signal-free full background continuum template is fit with a smoothly falling analytical function and a signal model. Gaussian Process Regression (GPR) is used to smooth the background template in the full diphoton invariant mass range between [60, 120] GeV [85]. This technique smooths binned data by exploiting the correlation between each pair of bins, constraining the content of a given bin by the content of the surrounding bins.

A Gaussian Process (GP) is defined as a set of random processes where all finite subsets of these processes follow a multivariate normal distribution. The multivariate distribution used here is described by two quantities: the mean and the covariance.

The posterior mean of the GP fit to a histogram can be interpreted as the smooth, underlying shape of the histogram, and a prior mean may be provided to help stabilize the GP fit. If a prior is not provided, the prior mean is assumed to be a flat line at the mean value of the input data. For this analysis, the prior mean function is defined as an exponential function which is used to model the full $m_{\gamma\gamma}$ range. The parameters of this functional form are determined by fitting the function to the unsmoothed $\gamma\gamma$ template histogram. Although using a rough estimate of the mean helps ensure the GP fit converges properly, it has been observed in previous diphoton resonance search analyses [85] that the exact shape of this mean does not significantly impact the posterior mean.

In the context of fitting a GP to a histogram, the diagonal elements of the covariance matrix define the uncertainty on the content of each bin. The off-diagonal elements define the correlation between the contents of different bins. These off-diagonal elements are defined by a function (known as the kernel function) whose

parameters are referred to as "hyper-parameters" of the GP fit. This analysis uses the Gibbs kernel function defined as:

$$K(x, x') = e^{\frac{-(x-x')^2}{2l(x)}} \tag{7.15}$$

where the length scale $l(x) = b_\lambda x + \lambda$ is allowed to vary linearly and the two hyper-parameters λ, b_λ denote the length scale and the length scale slope, respectively.

When performing a GP fit to a histogram, bins which are close together in x compared to the length scale are highly correlated while bins which are further apart in $m_{\gamma\gamma}$ compared to the length scale are effectively uncorrelated. The length scale is therefore chosen to be larger than the bin width to prevent all of the histogram bins from being considered uncorrelated. On the other hand, the length scale cannot be set to a large value compared to the size of real features in the histogram An excessive length scale will lead to an "oversmoothed" posterior mean (smoothed output template), and real shape features in the histogram will become suppressed. Smoothing using a GP in this analysis is motivated since features the size of a bin width in the template are expected to only reflect bin-by-bin statistical fluctuations. Any true physical features are expected to be significantly wider than a bin width.

The hyper-parameters of the GP kernel are determined by maximizing the log marginal likelihood function [86]:

$$\mathcal{L} = -\frac{1}{2} y^\intercal [K + \sigma^2 I]^{-1} y - \frac{1}{2} \log |K + \sigma^2 I| - \frac{n}{2} \log(2\pi) \tag{7.16}$$

where $K + \sigma^2 I$ denotes the correlation matrix, $\sigma^2 I$ denotes the uncertainties on the input data points, and y denotes the bin contents of the input histogram data. The first term of the log marginal likelihood is represents an "accuracy" term, and the second term represents a "complexity" penalty. The last term is a normalizing constant factor.

The irreducible background templates are binned in 0.2 GeV wide bins before GPR smoothing is applied on the mass range 58 GeV $< m_{\gamma\gamma} <$ 122 GeV. After the GP has been fit to the original irreducible background template histogram, a "smoothed" irreducible background template is constructed by taking the prediction of the posterior mean at each bin center as the new bin content. This smoothed template ideally lacks the problematic bin-by-bin statistical fluctuations of the original template, while retaining the true physical shape features of the template. The full background continuum template is then constructed by using the $\gamma\gamma + \gamma j$ fits described in Section 7.3.2.

7.3.2.2 Spurious Signal Estimation

The non-resonant background continuum contribution to the diphoton $m_{\gamma\gamma}$ distribution is based on a fit using a smooth functional form. The parameter values of the functional form and the background yield are determined simultaneously with a signal-plus-background model fit. The $m_{\gamma\gamma}$ distribution is fit with analytical functions in the range 62–120 GeV, and the search range for the signal is 66–110 GeV. The spurious signal test is used to check that the functional form is flexible enough to accommodate different physics-motivated underlying background distributions from MC simulations and to measure the bias that may arise from using an incorrect functional form to fit the background template. The potential bias due to the choice of the functional form is estimated by the yield of fitted signal models (known as "spurious signal") on these background distributions. The spurious signal in each category is considered as a systematic uncertainty.

In order to choose a functional form to model the non-resonant background and validate the background model against systematic shape variations, an estimate of the spurious signal is made by using a method employed in similar diphoton resonance searches [83]. First, a fit is performed to the non-resonant background-only template

for each category using a candidate background function and the signal model from Section 7.1 in a signal-plus-background fit for a given resonance mass hypothesis m_X. The signal yield is extracted from the fit and treated as the spurious signal $N_{\mathrm{SS}}(m_X)$. The spurious signal is evaluated in steps of 1 GeV in the range $m_{\gamma\gamma} \in [66, 110]$ GeV. The spurious signal across the full mass range is parameterized by a functional form fit. The resulting function is then used as a systematic uncertainty associated with the background modeling.

In order to minimize the effect of fit bias on the final result, a given background function must pass the spurious signal test. The criteria is set such that a function passes the test if it does not generate a spurious signal $N_{\mathrm{SS}}^{\mathrm{max}}(m_X)$ larger than a certain fraction of the expected statistical uncertainty on the signal yield $\delta S(m_X)$. This analysis requires that the number of spurious signal events relative to uncertainty on the signal yield $N_{\mathrm{SS}}/\delta S$ (referred to as the relative spurious signal) must be considerably lower than 1. This criteria prevents the uncertainty on the result from being dominated by the systematic uncertainty of the fit. However, δS becomes quite small when the spurious signal method is used on a dataset with a large integrated luminosity. To maintain a low relative spurious signal, large MC datasets are needed to ensure that the statistical fluctuations in the template remain significantly lower than any fluctuations in the data. The GPR smoothing technique described in Section 7.3.2.1 also helps to minimize the fluctuations in the template significantly.

For this analysis, the criterion for the goodness of fit as determined by the χ^2 probability is chosen to be $p > 0.50$ in order for a function to be considered. Furthermore, the criterion for the relative spurious signal is chosen to be $|N_{\mathrm{SS}}|/\delta S < 50\%$ in order for a function to pass the spurious signal test. If several functions fulfill these constraint, the functional form with fewest degrees of freedom is chosen for the non-resonant background continuum modeling. However, the functional form with the lowest relative spurious signal is chosen for the background modeling if none of

the functions fulfill these constraints.

7.3.2.3 Full Background Continuum Functional Fit

Several functions are tested for modeling the non-resonant background continuum in the mass range [60, 120] GeV: exponentials of second, third, and fourth-order polynomials (referred to as ExpPoly2 – ExpPoly4) and Bernstein polynomials of degree 4 through 7 (referred to as Bern4 – Bern7) [76]. The exponential polynomials of order n are given by the form

$$\mathcal{E}\left(m_{\gamma\gamma}, \alpha_{\text{bkg}}\right) = N(\alpha_{\text{bkg}}) \cdot \exp\left(\sum_{i=1}^{n} \alpha_i m_{\gamma\gamma}^i\right) \tag{7.17}$$

where α_i are the nuisance parameters, $N(\alpha_{\text{bkg}})$ normalizes the function, and n runs up to 4 for the different orders of exponential polynomials considered. The Bernstein polynomials of degree n are defined as

$$\mathcal{B}\left(m_{\gamma\gamma}, \alpha_{\text{bkg}}\right) = N(\alpha_{\text{bkg}}) \cdot \sum_{i=1}^{n} \alpha_i x^i (1-x)^{n-i} \cdot \frac{n!}{i!(n-i)!} \tag{7.18}$$

where x is defined as $\frac{m_{\gamma\gamma} - m_{\gamma\gamma}^{\text{min}}}{m_{\gamma\gamma}^{\text{max}} - m_{\gamma\gamma}^{\text{min}}}$ such that the variable is mapped from [0, 1] and $\alpha_0^{\text{bkg}} = 1$.

♦ **Model-Dependent Method** In order to determine the final functional form used in each model-dependent category, the fits are performed on the total background template including the reducible background component. The results of using the full background continuum template for the spurious signal test are shown in Figure 7.34.

The list of functions that are selected by this spurious signal test using the full smoothed $\gamma\gamma + \gamma j$ background template are listed in Table 7.18, along with the maximum value of the spurious signal in terms of events and the uncertainty relative to the statistical uncertainty. The values of the relative uncertainty range from approx-

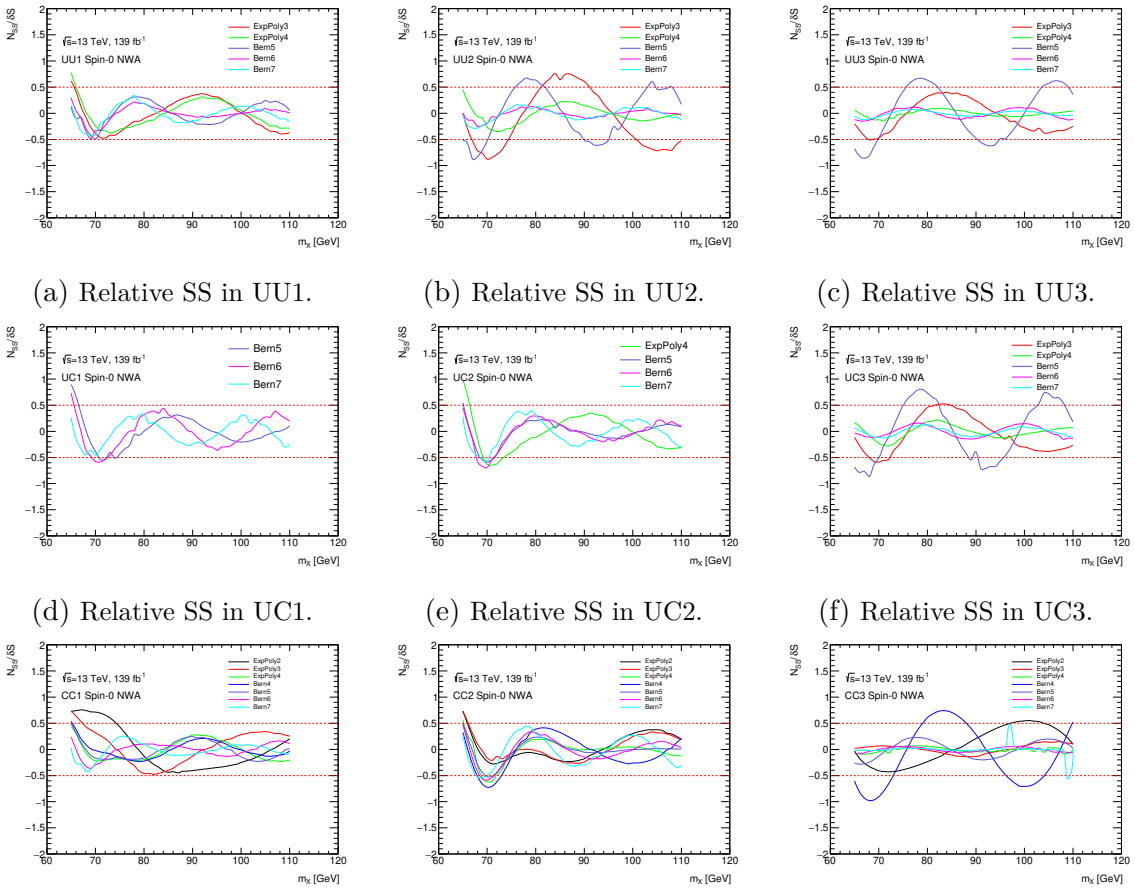

(a) Relative SS in UU1. (b) Relative SS in UU2. (c) Relative SS in UU3.

(d) Relative SS in UC1. (e) Relative SS in UC2. (f) Relative SS in UC3.

(g) Relative SS in CC1. (h) Relative SS in CC2. (i) Relative SS in CC3.

Figure 7.34: Relative spurious signal (SS) systematic estimated on the smoothed full background continuum templates obtained for each model-dependent category. The dashed lines are used for illustrating the 50% background uncertainty. Functions that have a relative spurious signal greater than 100% have been excluded for plotting purposes.

Category	Function	$\lvert S/\delta S\rvert$[%]	N_{SS}	Order
UU1	ExpPoly4	19.7	81.3	4
UC1	ExpPoly3	29.7	125	3
CC1	ExpPoly3	27.6	47.1	3
UU2	ExpPoly4	-17	-48.1	4
UC2	ExpPoly3	-27.3	-85.1	3
CC2	ExpPoly3	25.6	34.2	3
UU3	ExpPoly4	-13.6	-28.9	4
UC3	ExpPoly4	-25.7	-52.7	4
CC3	ExpPoly3	14.4	-9.19	3

Table 7.18: The output of the spurious signal test run on the smoothed templates built from Sherpa $\gamma\gamma$ and the γj reweighting. The information per analysis category indicates the fit function chosen, the size of the spurious signal in event count, the size of the spurious signal divided by the background statistical uncertainty, the 2σ error on the size of the spurious signal divided by the background uncertainty, and number of free parameters in the fit function.

imately 15% for the CC3 category up to approximately 57% for the UC2 category.

The final spurious signal systematic uncertainty is parameterized as a function of the diphoton mass to accurately model its effect on the signal-plus-background fits per category. This parameterization is derived in terms of the absolute number of spurious signal events, which is shown in Figure 7.35 for the chosen fit functions for each model-dependent category. The final parameterization of the spurious signal is obtained by identifying local maxima in the $|N_{SS}|$ distributions and fitting these maxima with a functional form. The parameterized functions extracted from these fits are then used in the limit setting to describe the background modeling uncertainty. The functional parameterizations of the number of spurious signal events as a function of m_X for each model-dependent category are given in Table 7.19.

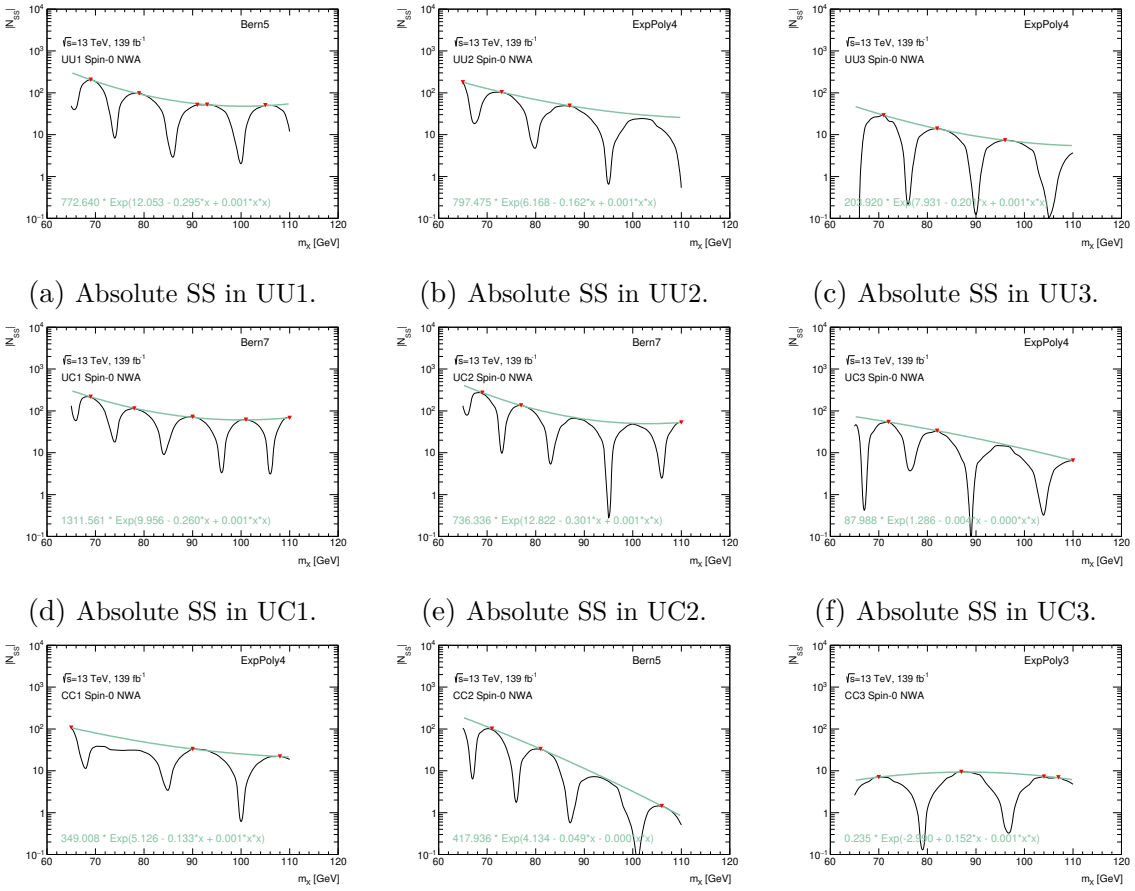

(a) Absolute SS in UU1. (b) Absolute SS in UU2. (c) Absolute SS in UU3.

(d) Absolute SS in UC1. (e) Absolute SS in UC2. (f) Absolute SS in UC3.

(g) Absolute SS in CC1. (h) Absolute SS in CC2. (i) Absolute SS in CC3.

Figure 7.35: Absolute number of spurious signal events as a function of m_X estimated on the smoothed $\gamma\gamma + \gamma j$ templates obtained for each model-dependent category for the chosen fit function.

Category	$N_{\mathrm{SS}}(m_X[\text{ GeV}])$, $139.5\,\mathrm{fb}^{-1}$								
UU1	671.899	* Exp(	4.856	- 0.138	*x	0.000	*x*x)		
UC1	173.893	* Exp(	0.942	0.003	*x -	0.000	*x*x)		
CC1	324.373	* Exp(	6.929	- 0.164	*x	0.000	*x*x)		
UU2	61.287	* Exp(	0.718	- 0.003	*x -	0.000	*x*x)		
UC2	692.316	* Exp(	7.697	- 0.204	*x	0.000	*x*x)		
CC2	75.947	* Exp(	0.527	- 0.002	*x -	0.000	*x*x)		
UU3	0.210	* Exp(	4.380	- 0.113	*x	0.000	*x*x)		
UC3	95.229	* Exp(	1.884	- 0.031	*x -	0.000	*x*x)		
CC3	363.752	* Exp(-	3.512	0.165	*x -	0.000	*x*x)		

Table 7.19: Parameterization of the spurious signal in this search, N_{SS}, as function of m_X, obtained for the background modeling for each model-dependent category and expressed for the luminosity of the data.

The spurious signal is also estimated on the smoothed template for each of the shape variations described in Section 7.3.1.3. The spurious signal systematic for the nominal background model is obtained from the envelope of the maximum spurious signal observed of all background template variations. The observed envelope is parameterized as a function of the diphoton invariant mass in order to accurately model its effect in the signal-plus-background fits when performing the statistical analysis. The envelopes for each model-dependent category are shown in Figure 7.36. The parameterizations are given in Table 7.20.

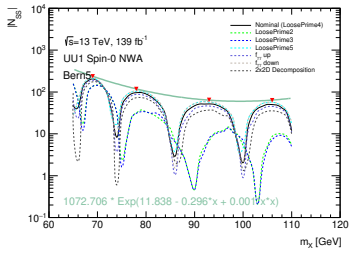

(a) Absolute SS variations in UU1.

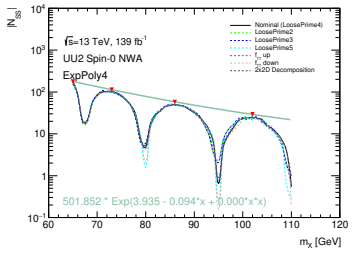

(b) Absolute SS variations in UU2.

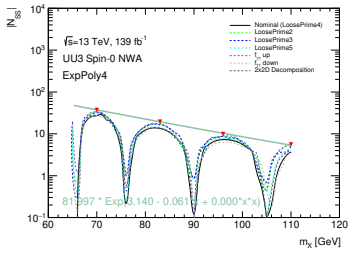

(c) Absolute SS variations in UU3.

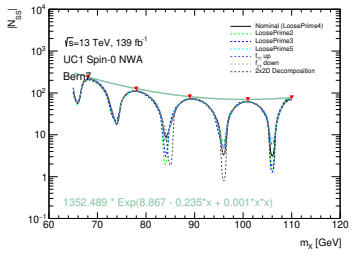

(d) Absolute SS variations in UC1.

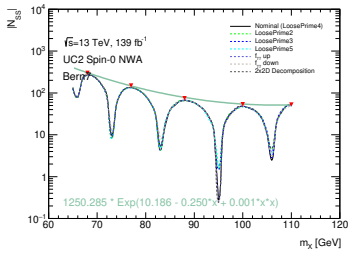

(e) Absolute SS variations in UC2.

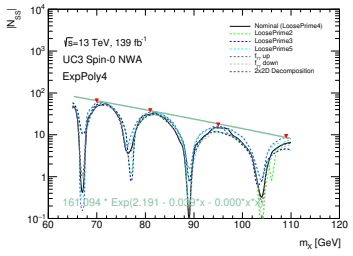

(f) Absolute SS variations in UC3.

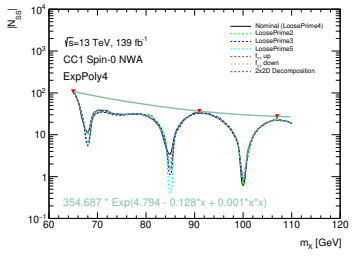

(g) Absolute SS variations in CC1.

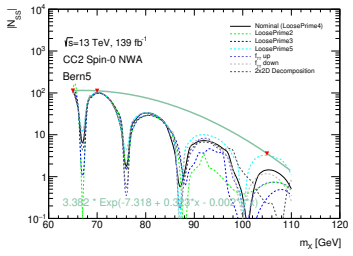

(h) Absolute SS variations in CC2.

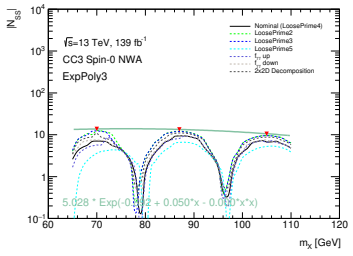

(i) Absolute SS variations in CC3.

Figure 7.36: Absolute number of spurious signal events as a function of m_X estimated on the smoothed $\gamma\gamma + \gamma j$ template variations obtained for each model-dependent category for the chosen fit function.

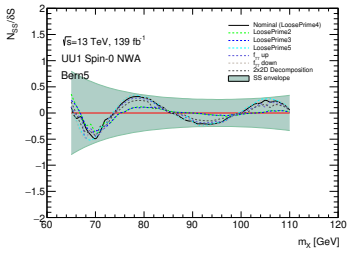

(a) Relative SS variations in UU1.

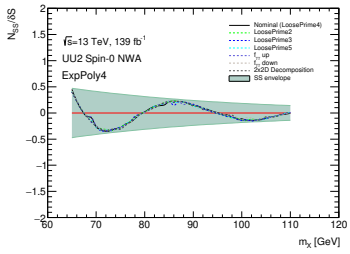

(b) Relative SS variations in UU2.

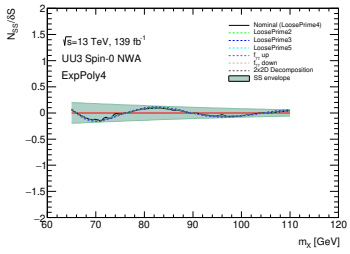

(c) Relative SS variations in UU3.

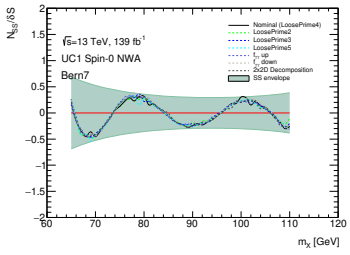

(d) Relative SS variations in UC1.

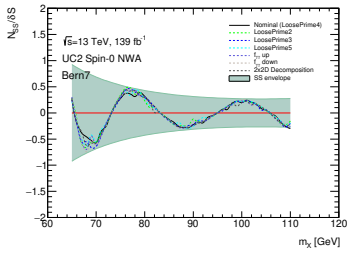

(e) Relative SS variations in UC2.

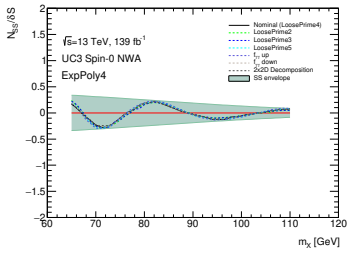

(f) Relative SS variations in UC3.

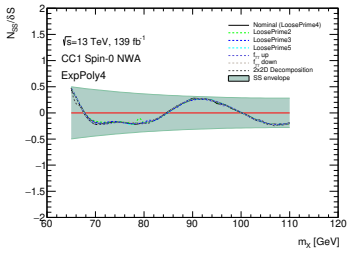

(g) Relative SS variations in CC1.

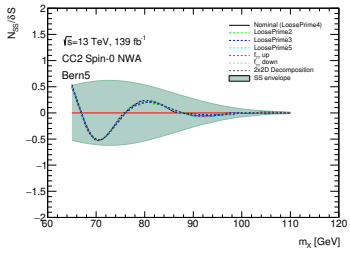

(h) Relative SS variations in CC2.

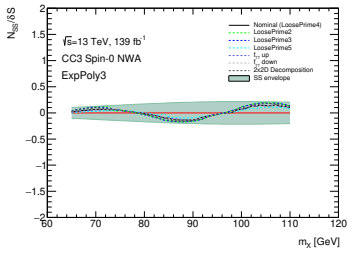

(i) Relative SS variations in CC3.

Figure 7.37: Spurious signal relative to the expected statistical uncertainty in the data obtained from the smoothed template variations for each model-dependent category for the chosen fit function.

Category	$N_{\mathrm{SS}}(m_X[\text{ GeV}])$, $139.5\,\mathrm{fb}^{-1}$					
UU1	911.682 * Exp(	5.281	- 0.152 *x	+ 0.000 *x*x)		
UC1	338.730 * Exp(	3.952	- 0.087 *x	+ 0.000 *x*x)		
CC1	155.565 * Exp(	0.938	- 0.005 *x	- 0.000 *x*x)		
UU2	85.603 * Exp(	0.756	- 0.003 *x	- 0.000 *x*x)		
UC2	800.268 * Exp(	9.131	- 0.237 *x	+ 0.001 *x*x)		
CC2	100.314 * Exp(	0.485	- 0.003 *x	- 0.000 *x*x)		
UU3	277.286 * Exp(	4.982	- 0.119 *x	+ 0.000 *x*x)		
UC3	174.954 * Exp(	3.864	- 0.087 *x	+ 0.000 *x*x)		
CC3	3.482 * Exp(	- 1.253	+ 0.065 *x	- 0.000 *x*x)		

Table 7.20: Parameterization of the spurious signal in this search, N_{SS}, as function of m_X, obtained for the background modeling template variations for each model-dependent category and expressed for the luminosity of the data.

◊ **Model-Independent Model** In order to determine the final functional form used in each model-independent category, the fits are also performed on the these total background template including the reducible background component. The results of using the full background continuum template for the spurious signal test are shown in Figure 7.38.

The list of functions that are selected by this spurious signal test using the full smoothed $\gamma\gamma + \gamma j$ background template are listed in Table 7.21, along with the maximum value of the spurious signal in terms of events and the uncertainty relative to the statistical uncertainty. The values of the relative uncertainty range from approximately 54% for the CC category up to approximately 75% for the UC category.

The final spurious signal systematic uncertainty is parameterized as a function of the diphoton mass to accurately model its effect on the signal-plus-background fits per category. This parameterization is derived in terms of the absolute number of spurious signal events, which is shown in Figure 7.39 for the chosen fit functions for each model-indpendent category. The final parameterization of the spurious signal is obtained by identifying local maxima in the $|N_{SS}|$ distributions and fitting these maxima with a functional form. The parameterized functions extracted from these

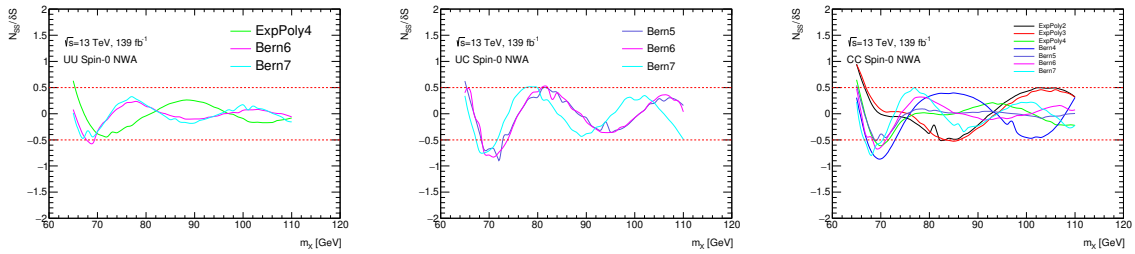

(a) Relative SS in UU. (b) Relative SS in UC. (c) Relative SS in CC.

Figure 7.38: Relative spurious signal (SS) systematic estimated on the smoothed full background continuum templates obtained for each model-independent category. The dashed lines are used for illustrating the 50% background uncertainty. Functions that have a relative spurious signal greater than 100% have been excluded for plotting purposes.

Category	Function	$\lvert S/\delta S\rvert$[%]	N_{SS}	Order	Prob(χ^2) [%]
UU	ExpPoly4	-17.2	-85.7	4	100
UC	Bern6	-42.7	-263	6	100
CC	ExpPoly3	34.7	78	3	100

Table 7.21: The output of the spurious signal test run on the smoothed templates built from Sherpa $\gamma\gamma$ and the γj reweighting. The information per analysis category indicates the fit function chosen, the size of the spurious signal in event count, the size of the spurious signal divided by the background statistical uncertainty, the 2σ error on the size of the spurious signal divided by the background uncertainty, and number of free parameters in the fit function.

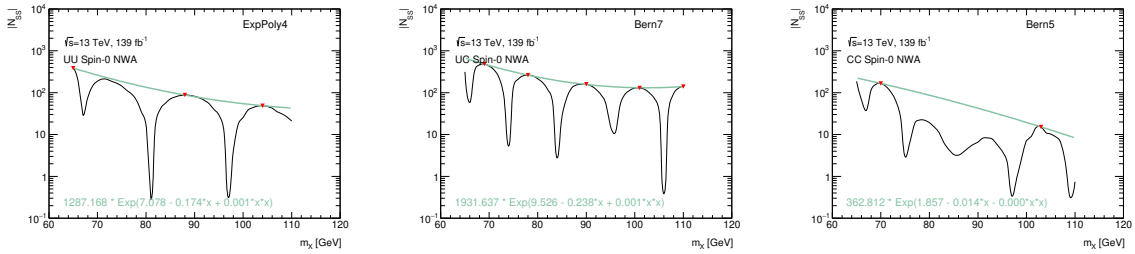

(a) Absolute SS in UU. (b) Absolute SS in UC. (c) Absolute SS in CC.

Figure 7.39: Absolute number of spurious signal events as a function of m_X estimated on the smoothed $\gamma\gamma + \gamma j$ templates obtained for each model-independent category for the chosen fit function.

Category	$N_{\mathrm{SS}}(m_X[\text{ GeV}])$, $139.5\,\mathrm{fb}^{-1}$
UU	`114.084 * Exp( 0.858 - 0.004 *x - 0.000 *x*x)`
UC	`954.111 * Exp( 7.477 - 0.169 *x 0.000 *x*x)`
CC	`64.325 * Exp( - 0.333 0.030 *x - 0.000 *x*x)`

Table 7.22: Parameterization of the spurious signal in this search, N_{SS}, as function of m_X, obtained for the background modeling for each model-independent category and expressed for the luminosity of the data.

fits are then used in the limit setting to describe the background modeling uncertainty. The functional parameterizations of the number of spurious signal events as a function of m_X for each model-independent category are given in Table 7.22.

The spurious signal is also estimated on the smoothed template for each of the shape variations described in Section 7.3.1.3. The spurious signal systematic for the nominal background model is obtained from the envelope of the maximum spurious signal observed of all background template variations. The observed envelope is parameterized as a function of the diphoton invariant mass in order to accurately model its effect in the signal-plus-background fits when performing the statistical analysis. The envelopes for each category are shown in Figure 7.40. The parameterizations are given in Table 7.23.

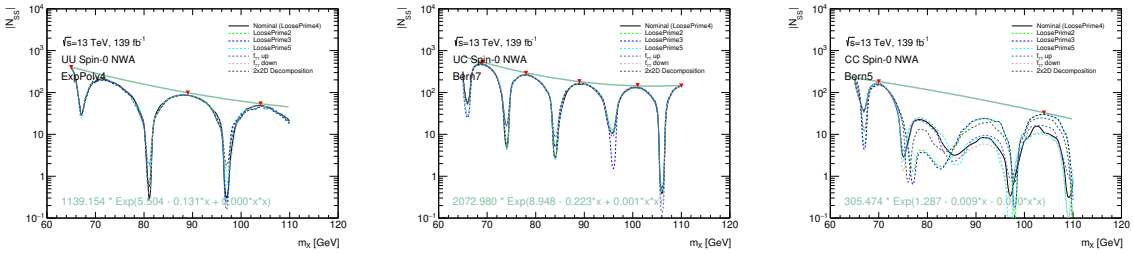

(a) Absolute SS variations in UU.

(b) Absolute SS variations in UC.

(c) Absolute SS variations in CC.

Figure 7.40: Absolute number of spurious signal events as a function of m_X estimated on the smoothed $\gamma\gamma + \gamma j$ template variations obtained for each model-independent category for the chosen fit function.

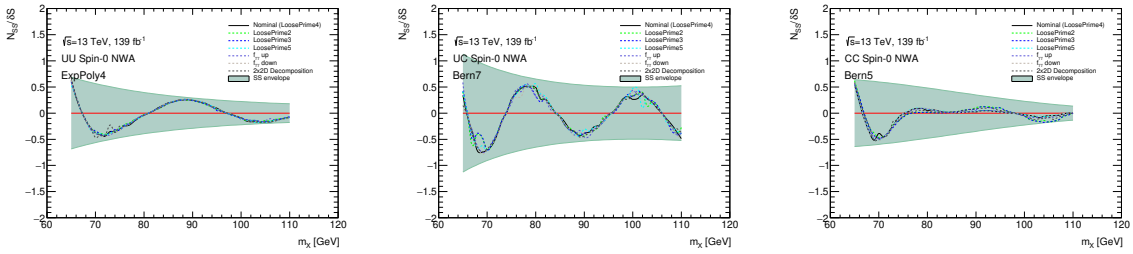

(a) Relative SS variations in UU.

(b) Relative SS variations in UC.

(c) Relative SS variations in CC.

Figure 7.41: Spurious signal relative to the expected statistical uncertainty in the data obtained from the smoothed template variations for each model-independent category for the chosen fit function.

Category	$N_{\mathrm{SS}}(m_X[\text{ GeV}])$, $139.5\,\mathrm{fb}^{-1}$
UU	`456.614 * Exp(  9.869 - 0.242 *x + 0.001 *x*x)`
UC	`0.016 * Exp(- 28.631 + 1.503 *x - 0.018 *x*x) + 0.000 *x*x`
CC	`61.901 * Exp(-  0.194 + 0.031 *x - 0.000 *x*x)`

Table 7.23: Parameterization of the spurious signal in this search, N_{SS}, as function of m_X, obtained for the background modeling template variations for each model-independent category and expressed for the luminosity of the data.

7.3.3 Resonant Background from Drell-Yan Electron Fakes

The second background source considered in this search is the resonant background component that results from the $Z \to ee$ DY process where both electrons are misidentified as photons. This background would appear in the data as a bump at the Z boson mass of $m_Z \approx 90$ GeV. Fake photons from the resonant background mostly originate from electrons that undergo large bremsstrahlung and are misidentified by photon reconstruction and identification algorithms described in Section 4.1. Due to the non-negligible energy loss from bremsstrahlung, the $Z \to ee$ mass distribution is shifted in $m_{\gamma\gamma}$ for events where the electrons are misidentified as photons as seen in Figure 7.42. A precise description of this background is a crucial ingredient for a proper background estimate, especially in the region around $m_{\gamma\gamma} \approx 90$ GeV.

In the following, electrons will be referred to using e, electrons that have been misidentified as photons will be referred to using y, and electrons that have been transformed to look like electrons misidentified as photons will be referred to using e'. To study the DY background shape that contributes to the $m_{\gamma\gamma}$ spectra, the m_{ee} shape for each conversion category is first taken from data and transformed to $m_{e'e'}$ using a correction derived in MC simulation as described in Section 7.3.3.2. Next, the shape is normalized using $e \to y$ fake rates derived from data and MC simulation as described in Section 7.3.3.3. Finally, the resulting $m_{e'e'}$ distributions from data are cross-checked with m_{yy} distributions from MC simulation, the $m_{e'e'}$ distribution is parameterized by a DSCB function, and systematic uncertainties are assigned to the resonant background model as described in Section 7.3.3.4.

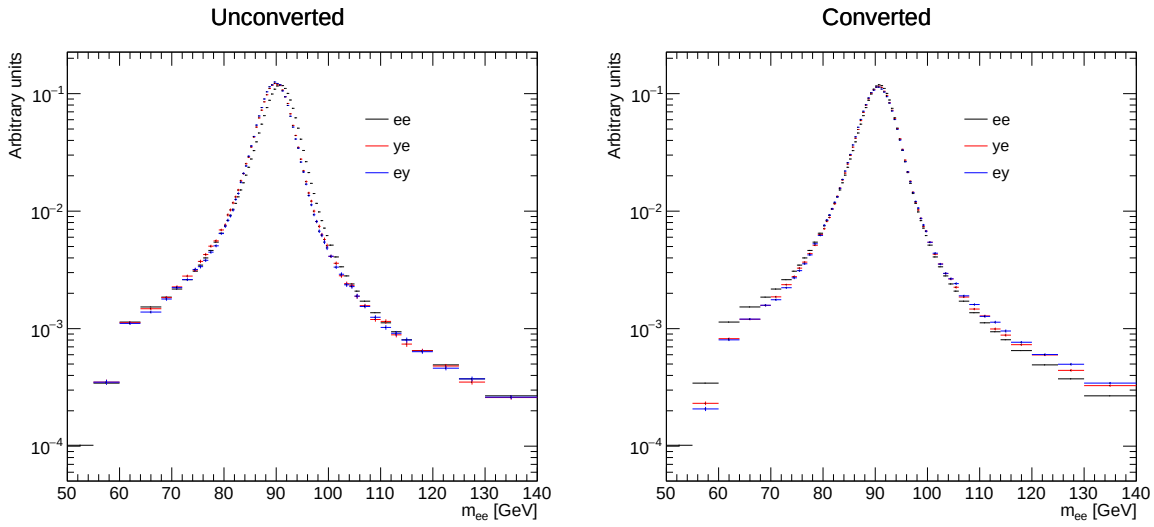

(a) Distribution of unconverted fake photons.

(b) Distribution of converted fake photons.

Figure 7.42: Invariant mass distributions (normalized to unity) of electrons pairs (black), pairs made of a leading truth-matched electron reconstructed as a photon and subleading truth-matched electron reconstructed as an electron (red), and pairs made of a leading truth-matched electron reconstructed as an electron and subleading truth-matched electron reconstructed as a photon (blue). The unconverted (a) and converted (b) photons are obtained through a $Z \to ee$ simulation sample.

7.3.3.1 Electron Selection

The DY background is estimated from dielectron data and MC simulation. Electrons that are reconstructed as electrons are calibrated in the usual way and required to pass the Tight electron identification criteria. The requirements on electron E_{T} and η are the same as those on photons, and no isolation requirement is applied for these studies. Electrons that are reconstructed as photons (y) are calibrated as photons, and required to pass the standard photon analysis selection criteria.

7.3.3.2 Transformation of the dielectron mass spectrum

A Smirnov transformation [96] is used to model the differences between e and y. This is accomplished using the cumulative distribution functions (CDFs) of the unity-normalized invariant mass distributions m_{ee}, m_{ey} and m_{ye} measured in MC simulation of $Z \to ee$ events. To build the CDFs, candidate e and y objects are required to be matched to one of the two truth electrons originating from the Z boson. An example of the resulting CDFs is shown in Figure 7.43.

For a given CDF value, the differences $\delta_1 = m_{ye} - m_{ee}$ and $\delta_2 = m_{ey} - m_{ee}$ are used to transform the dielectron mass distribution on an event-by-event basis. To determine a CDFs value at an arbitrary mass value, a linear interpolation is made between the two nearest bins centers. this transformation accurately reproduces electrons misidentified as unconverted and converted photons as shown in Figures 7.44 and 7.45, respectively.

To obtain the invariant mass distribution where both electrons are misidentified as photons, the corrections derived for leading and subleading transformations at a given invariant mass value are combined:

$$m_{e'e'} = m_{ee} + \delta_1 + \delta_2 = m_{e'e} + m_{ee'} - m_{ee}. \tag{7.19}$$

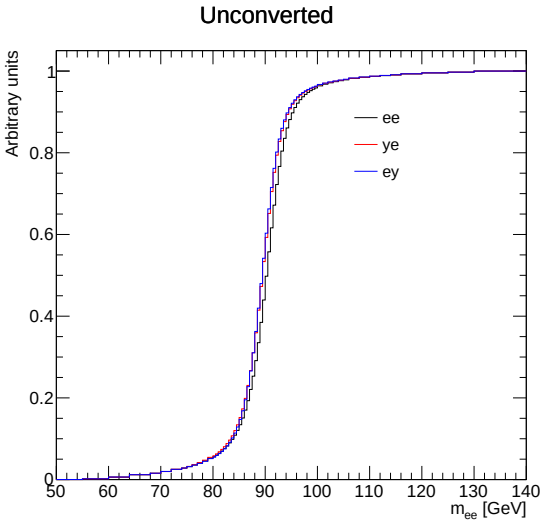

(a) CDF of unconverted fake photons.

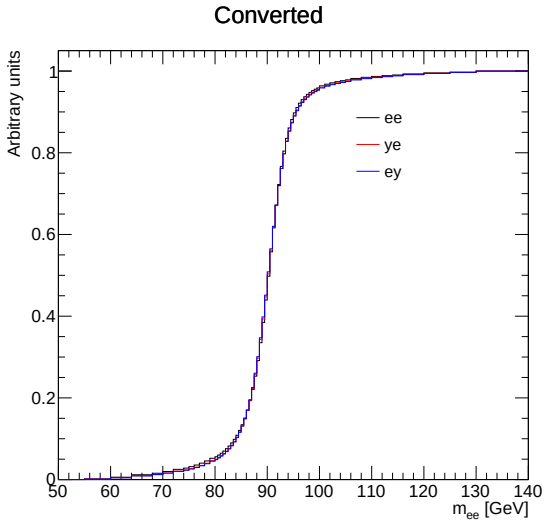

(b) CDF of converted fake photons.

Figure 7.43: Cumulative distribution functions of discrete invariant mass distributions of electrons pairs (black) and electron with fake leading photon (red) or fake subleading photon (blue) pairs in unconverted (a) and converted (b) photon category, obtained on a $Z \to ee$ simulation sample.

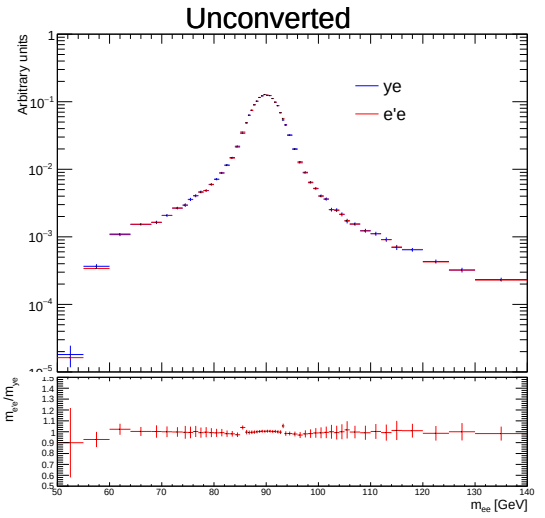

(a) Transformed distribution of unconverted fake leading photons.

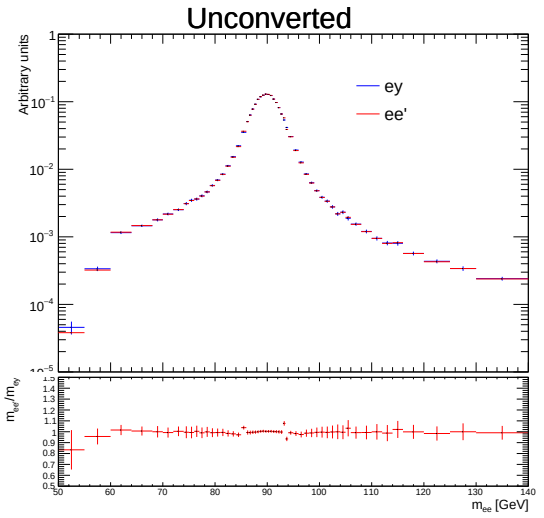

(b) Transformed distribution of unconverted fake subleading photons.

Figure 7.44: Invariant mass distributions (normalized to unity) of electron with fake photon (blue) and transformed electron (red) pairs in leading (a) and subleading (b) cases for unconverted photons, obtained on a $Z \to ee$ simulation sample.

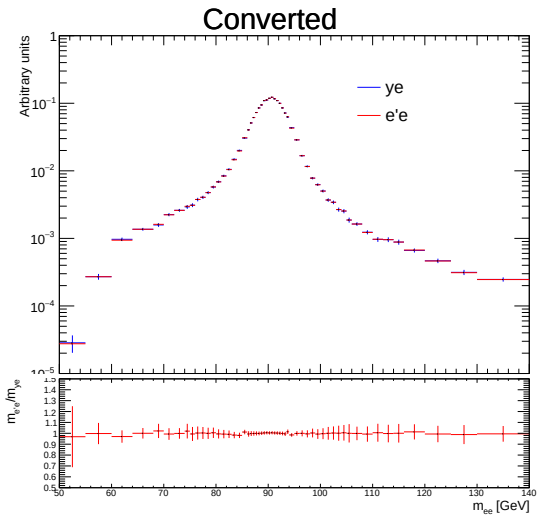

(a) Transformed distribution of converted fake leading photons.

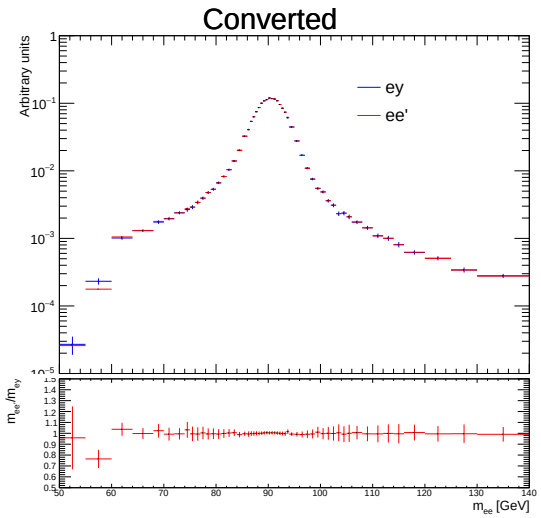

(b) Transformed distribution of converted fake subleading photons.

Figure 7.45: Invariant mass distributions (normalized to unity) of electron with fake photon (blue) and transformed electron (red) pairs in leading (a) and subleading (b) cases for converted photons, obtained on a $Z \to ee$ simulation sample.

This estimation provides an $m_{e'e'}$ transformation without significant statistical fluctuations since there is a large number of ey/ye events compared to yy events. The transformed distribution $m_{e'e'}$ in Figure 7.46 shows good agreement with the m_{yy} mass distributions from $Z \to ee$ MC simulation along with reduced statistical fluctuations. Once the transformations are derived using the $Z \to ee$ MC simulation, they are applied to $Z \to ee$ events in data.

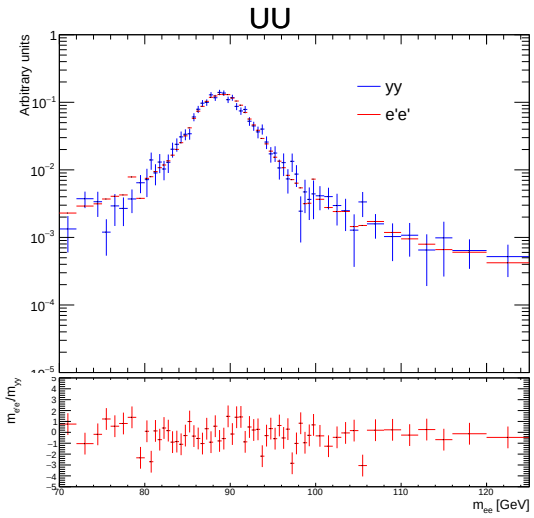

(a) Transformed distribution of fake photons in UU.

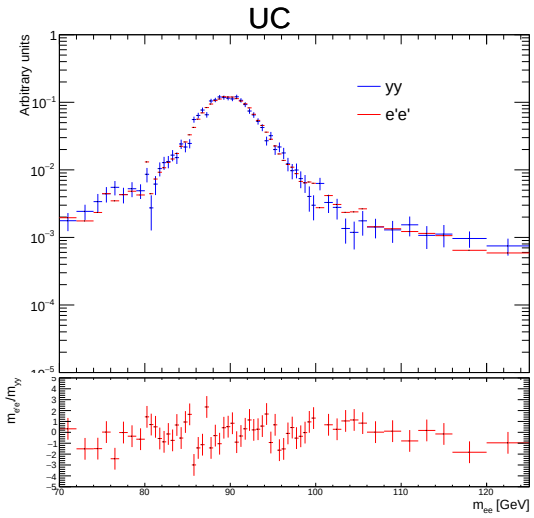

(b) Transformed distribution of fake photons in UC.

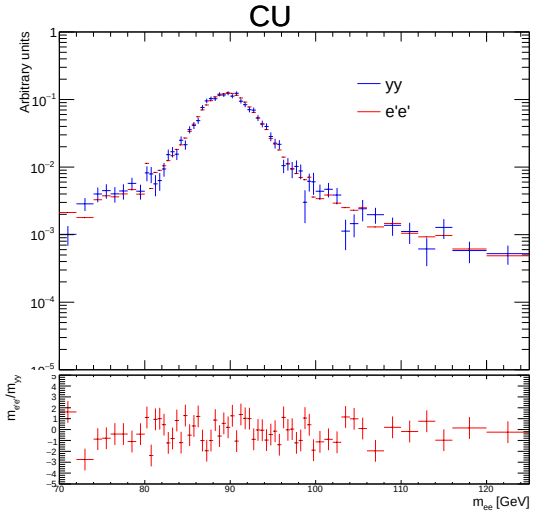

(c) Transformed distribution of fake photons in CU.

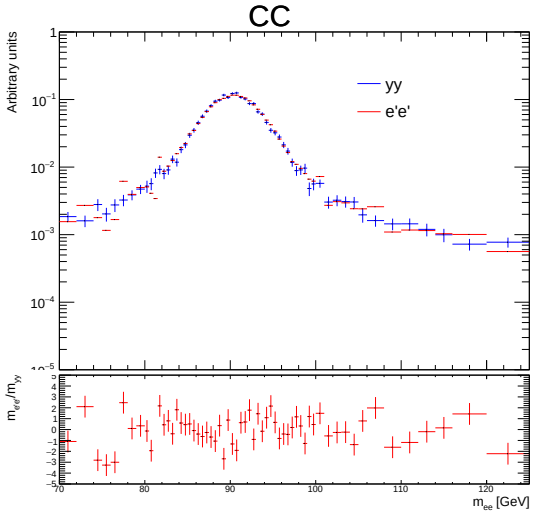

(d) Transformed distribution of fake photons in CC.

Figure 7.46: Invariant mass distributions (normalized to unity) of diphoton pair (blue) and transformed electrons pairs obtained with summed up shifts (red) in the UU (a), UC (b), CU (c) and CC (d) categories, obtained on a $Z \to ee$ simulation sample.

7.3.3.3 Electron to photon fake rates

The $e \to y$ fake rates are measured by using ee and ey/ye events in the dataset. In the ey/ye events, the misidentified photon is required to pass the cut of 0.2 on the electron-photon ambiguity BDT score. The fake rates are derived independently for the leading and subleading candidates and in the two photon conversion categories. The leading (ρ_1) and subleading (ρ_2) fake rates are measured in a window around the Z-peak, defined as 6 times the width of the Gaussian from a fit using a DSCB function of the ey invariant mass distribution. The subtraction of non-resonant background is performed using the results of signal + background fits, where the signal is the combination of a DSCB modeling the Z-peak and a Fermi $\times$ power-law modeling the DY continuum. The diphoton background is described by Fermi $\times$ exponential function.

The mass-dependent fake rates are defined as follows:

$$\rho_1 = N_{ye}/N_{e'e} \tag{7.20}$$

$$\rho_2 = N_{ey}/N_{ee'}, \tag{7.21}$$

where the different N correspond to the number of events in bins of the invariant-mass distributions that are obtained from fits to data, after the subtraction of the non-resonant background. The fits to data are shown in Figure 7.47.

As a closure check on the shapes, the fake rates are also computed in the $Z \to ee$ MC sample. Before applying the kinematic transformations to the electrons, the fake rates are not flat as a function of the mass because of the shift between electrons reconstructed as electrons or as photons as shown in Figure 7.48. After the Smirnov transform is applied, this ratio is flat around the Z-peak as indicated by the constant fit within the Z-mass window in Figure 7.49.

The final values of the fake rates are measured in data and shown in Figure 7.50.

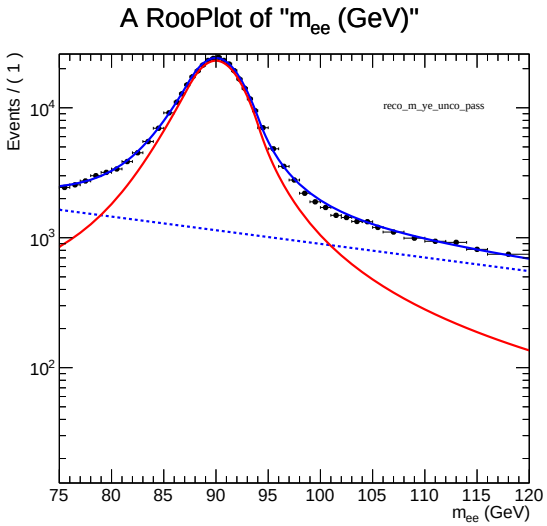

(a) Resonant background fit of unconverted leading fake photon.

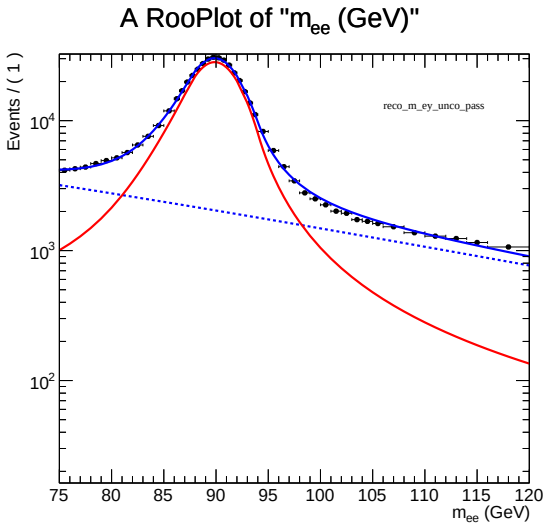

(b) Resonant background fit of unconverted subleading fake photon.

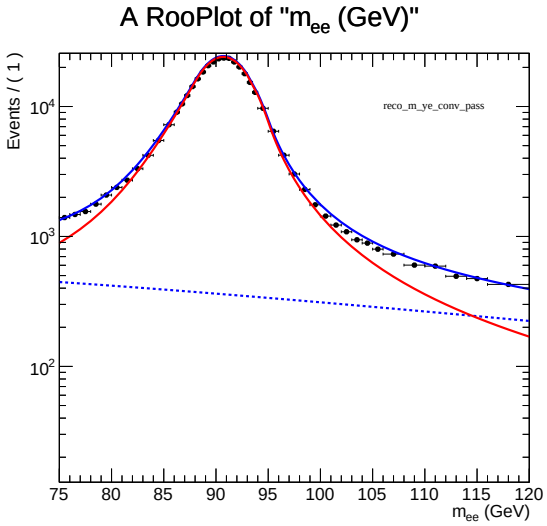

(c) Resonant background fit of converted leading fake photon.

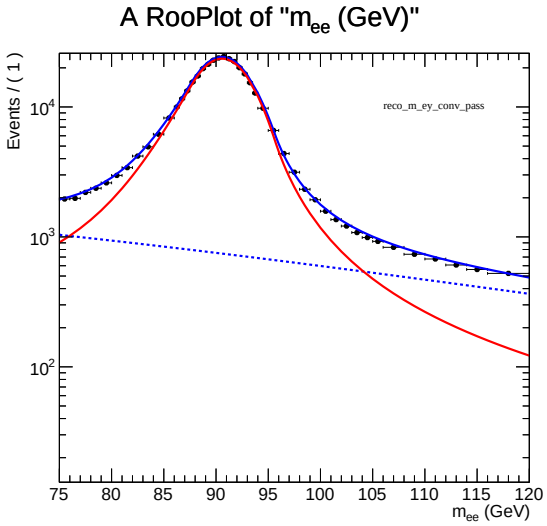

(d) Resonant background fit of converted subleading fake photon.

Figure 7.47: The fit of the resonant and non-resonant backgrounds in the (a) unconverted photon γe spectrum, (b) unconverted photon $e\gamma$ spectrum, (c) the converted photon γe spectrum and the (d) the converted photon $e\gamma$ spectrum from the control region data. The non-resonant background subtraction in these invariant mass distributions is performed before calculation of the leading and subleading fake rates in data.

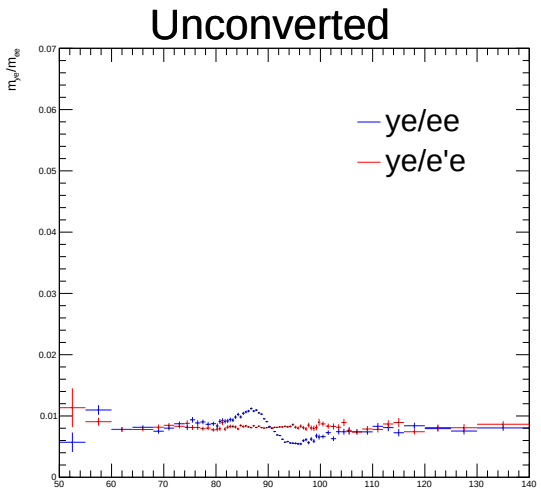

(a) Fake rate in unconverted leading fake photon.

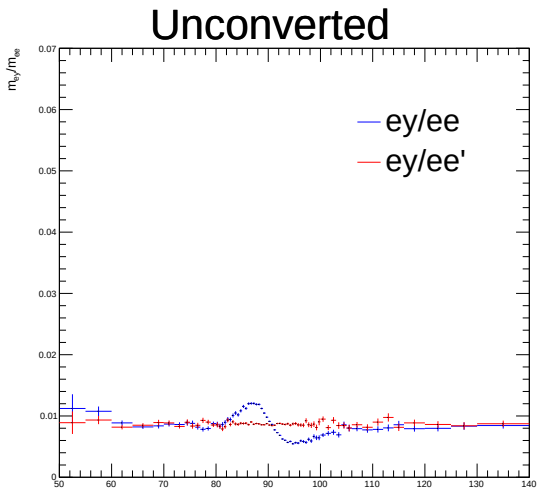

(b) Fake rate in unconverted subleading fake photon.

Figure 7.48: Invariant mass dependence of the leading (a) and subleading (b) unconverted photon fake rates as measured in $Z \to ee$ simulation, before (blue) and after (red) applying the Smirnov transformation.

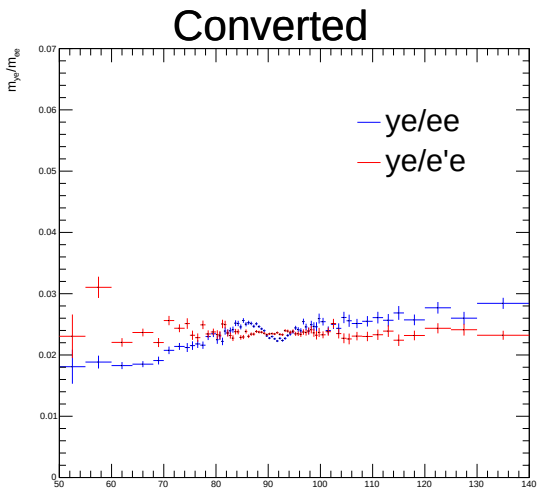

(a) Fake rate in unconverted leading fake photon.

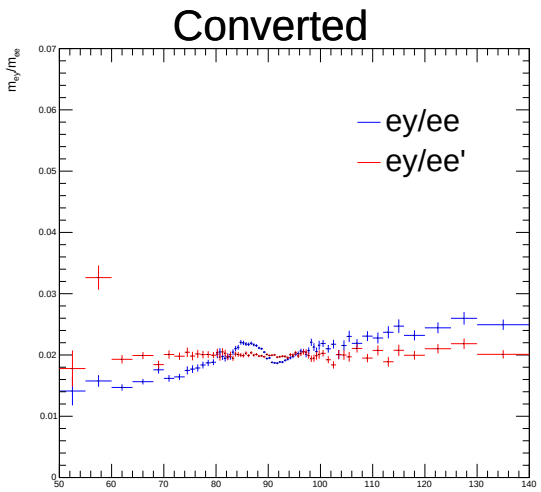

(b) Fake rate in unconverted subleading fake photon.

Figure 7.49: Invariant mass dependence of the leading (a) and subleading (b) converted photon fake rates as measured in $Z \to ee$ simulation, before (blue) and after (red) applying the Smirnov transformation.

The total number of fake diphoton events coming from the Drell-Yan process in a given mass bin is measured as

$$N_{yy,\,c} = \alpha_c \rho_1 \rho_2 N_{e'e'}, \tag{7.22}$$

where $N_{e'e'}$ is the number of $Z \to ee$ events for a given mass bin of the transformed m_{ee} distribution in data and α_c is a correction factor introduced to take into account the reconstruction efficiency differences between single y and pairs of y, as well as to separate the estimated Drell-Yan background in the c categories of the diphoton BDT. This correction factor α_c is evaluated in $Z \to ee$ MC events for each mass bin by rearranging Equation 7.22 such that

$$\alpha_c = \frac{1}{\rho_1^{MC} \rho_2^{MC}} N_{yy,\,c}^{MC} / N_{e'e'}^{MC} \tag{7.23}$$

where the $N_{yy,\,c}^{MC}$ is the number of yy events in a given mass bin that pass into the category c of the diphoton BDT. Because the α factor is meant to account for mass-independent differences in reconstruction, the $m_{e'e'}$ distribution that the $N_{e'e'}$ are obtained from is derived using the $m_{yy,\,c}$ shape normalized to the total number of ee events. As such, the derived α_c factors are also mass independent, as seen in Figure 7.51. The sum of these factors over the BDT categories c is expected to be 1 if the y reconstruction does not depend on the reconstruction of the other candidate. However, the two y are not completely independent as the track-isolation energy needs the information from both y candidates to determine the primary vertex.

Overall, the estimation of the fake diphoton background from Drell-Yan in Equation 7.22 is given by the shape of the transformed m_{ee} distribution from data, the fake rate scale factors of individual misidentified photons ρ_i that are measured in data, and the α scale scale factors from MC that cover the effects of the diphoton selection. The shapes of the $m_{yy,\,c}$ distributions are found to be the same across the

BDT categories in MC as shown in Figure 7.52. Therefore they are taken from the inclusive CDF transformation as described in Section 7.3.3.2.

The final scale factors $f = \alpha_c \rho_1 \rho_2$ are shown in Figure 7.53 where α_c has been derived in MC simulation and the two ρ values are derived from data. Since the α and ρ components are mass independent, the resulting f factors are also mass independent. Thus, the mass-independent scale factors (f_{fit}) are derived for normalizing the $m_{e'e'}$ distributions in each of the four conversion categories (UU, UC, CU, CC) from Section 7.3.3.2 and diphoton BDT categories.

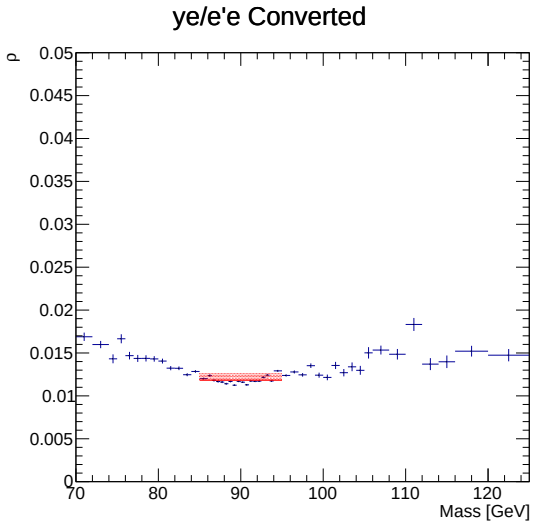

(a) Fake rate in converted leading fake photon.

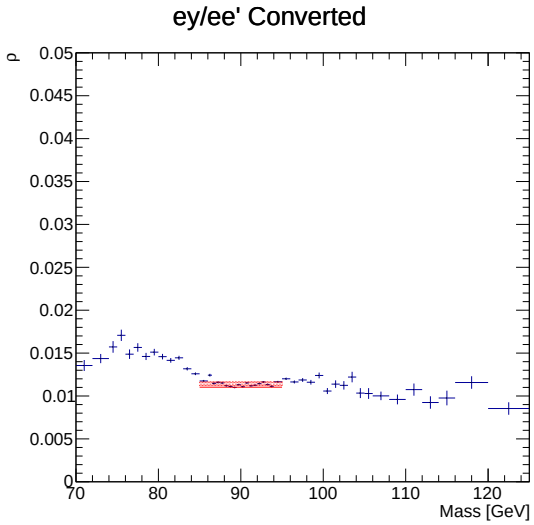

(b) Fake rate in converted subleading fake photon.

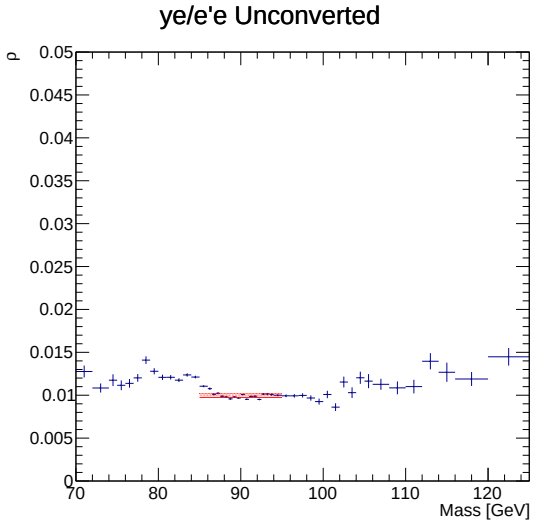

(c) Fake rate in unconverted leading fake photon.

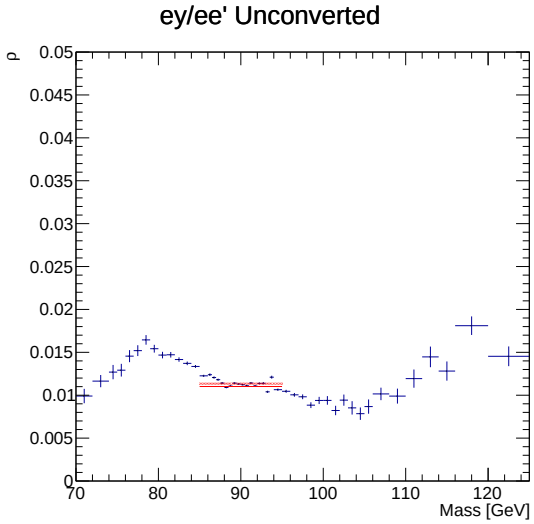

(d) Fake rate in unconverted subleading fake photon.

Figure 7.50: Invariant mass dependence of the leading (left) and subleading (right) converted (top) and unconverted (bottom) photon fake rates, as measured in data. The red lines represent the fit in the mass window.

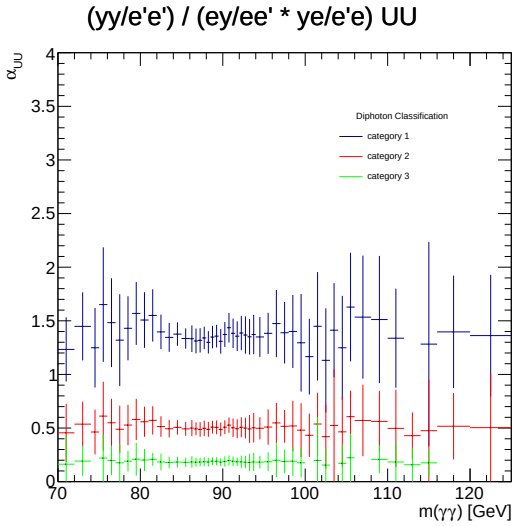

(a) Correlation factor in UU.

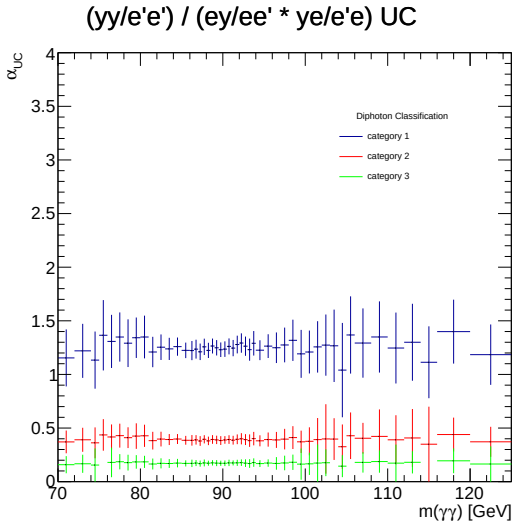

(b) Correlation factor in UC.

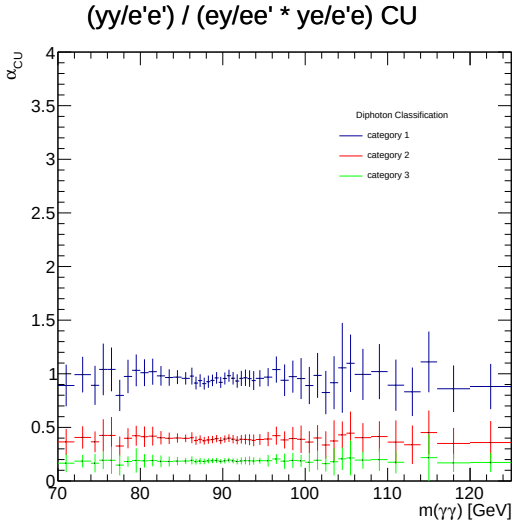

(c) Correlation factor in CU.

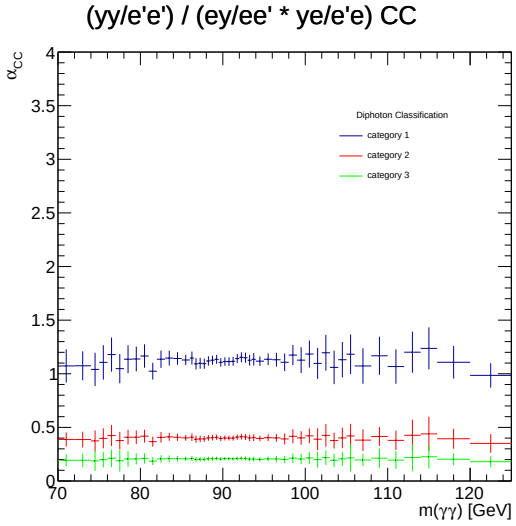

(d) Correlation factor in CC.

Figure 7.51: Invariant mass dependence of correlation factor α in UU (a), UC (b), CU (c) and CC (d) categories, obtained on a $Z \to ee$ simulation sample. The red lines represent the fit in the mass window.

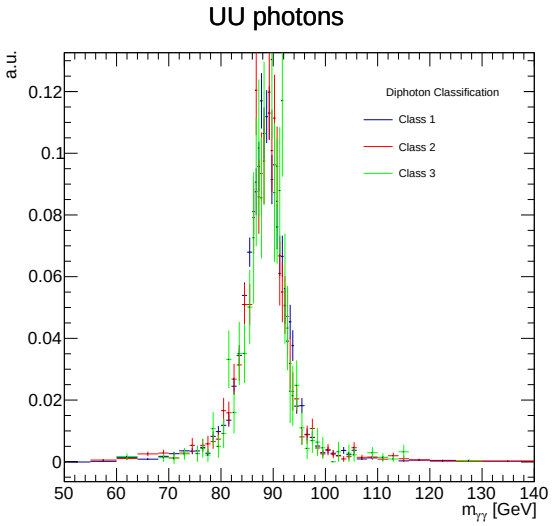

(a) Distribution in UU.

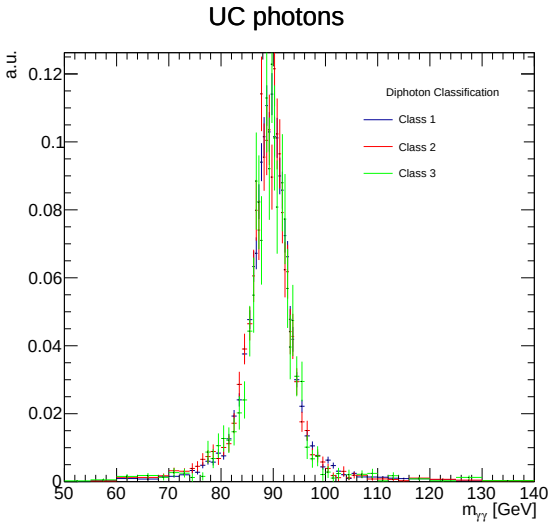

(b) Distribution in UC.

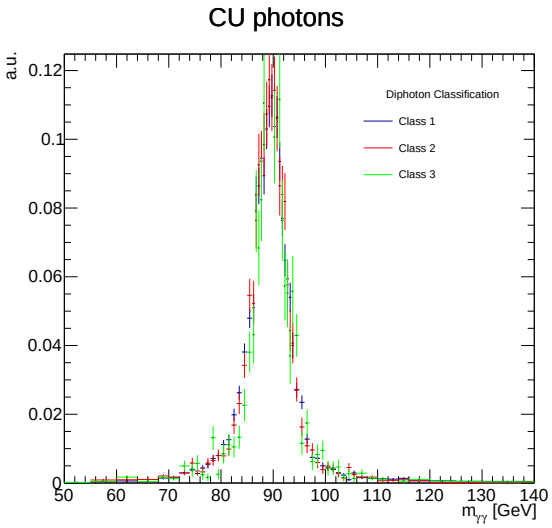

(c) Distribution in CU.

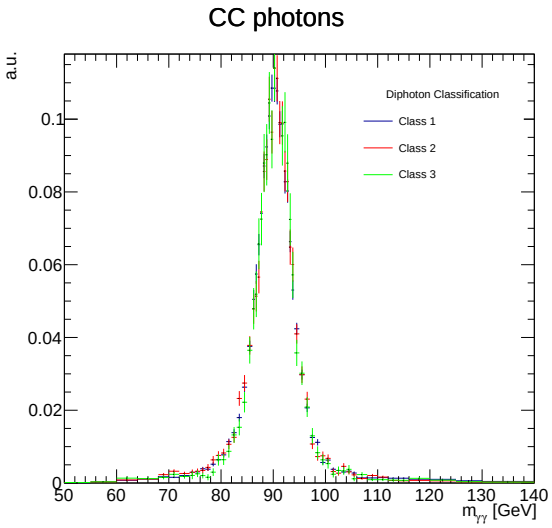

(d) Distribution in CC.

Figure 7.52: Invariant mass distributions per diphoton BDT category in UU (a), UC (b), CU (c) and CC (d) photon conversion categories, integrals are normalized to unity, obtained on a $Z \to ee$ simulation sample.

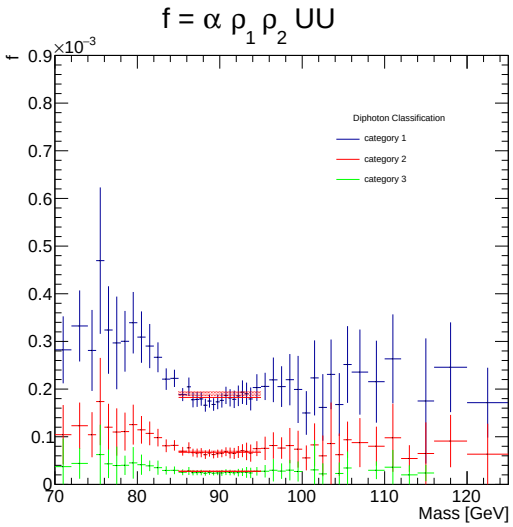

(a) Normalization factor in UU.

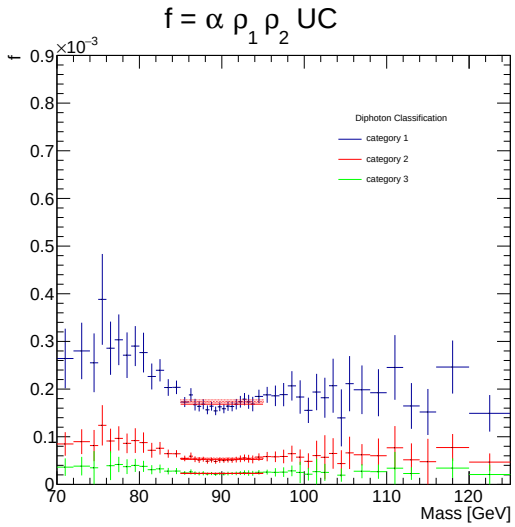

(b) Normalization factor in UC.

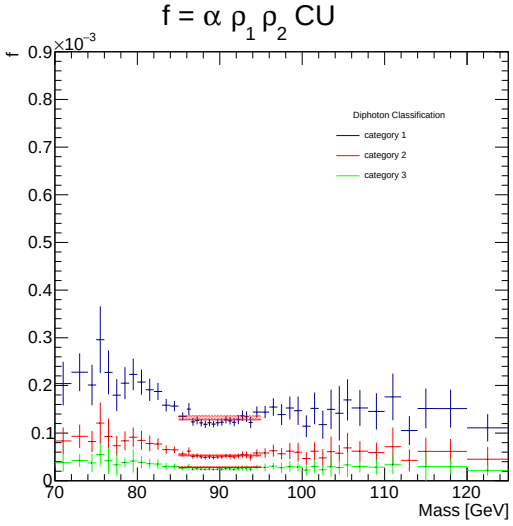

(c) Normalization factor in CU.

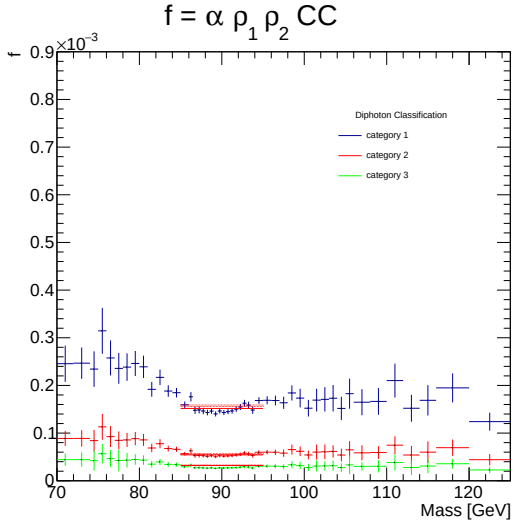

(d) Normalization factor in CC.

Figure 7.53: Invariant mass dependence of normalization factor f in UU (a), UC (b), CU (c) and CC(d) conversion categories, given for each diphoton BDT category, used to obtain expected number of fake photons in data. The red lines represent the fit in the mass window.

7.3.3.4 Final Drell-Yan Background Description and Uncertainties

The final Drell-Yan background templates are extracted using m_{ee} distributions taken from $Z \to ee$ data, corrected to $m_{e'e'}$ using the Smirnov transforms described in Section 7.3.3.2, and finally normalized using the $e \to y$ fake rates discussed in Section 7.3.3.3. As a closure test, this is compared to yy events from $Z \to ee$ simulation for each conversion category, shown in Figure 7.54. The final analysis considers fully unconverted (UU), mixed conversion (UC+CU) and fully converted (CC) categories, where the UC and CU templates are combined with a simple summation. These final three templates are fit with a DSCB function which serves as the DY background description in the statistical analysis for this diphoton resonance search.

Systematic uncertainties are evaluated for each fake rate and for the correction factor α, as well as on the final normalization factor to account for correlations. The systematics uncertainties considered are:

- variations of the mass window,
- the limited statistics of the MC sample,
- the background subtraction,
- statistical uncertainty from the background fit,
- Different MC samples are used to obtain alternate transformation parameters and to evaluate the impact on the fake rates, the factor α and the shape: Sherpa2 and PowhegPy8 with distorted material geometries.

The mass window is varied between 2 and 4 times the measured Z peak width (σ_Z^{fake}) and its center is shifted by $\pm 1\,\sigma$ of the Z peak position (m_Z^{fake}) uncertainty, leading to an uncertainty on the fake rates of the order to 1%. The limited statistics of the MC, the background subtraction and the statistical uncertainty from the fits are all considered with a bootstrap method: the procedure of extraction of the shape

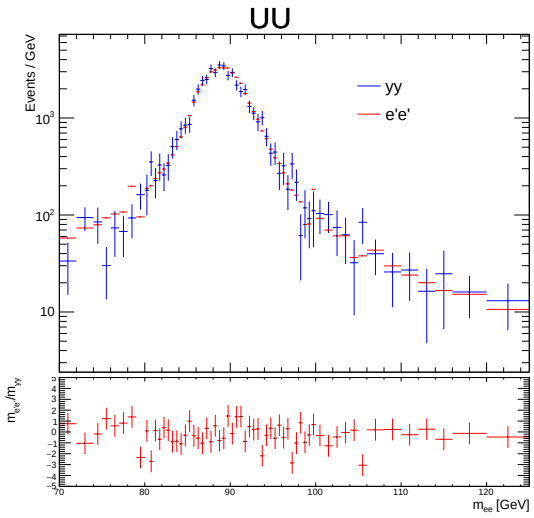

(a) Resonant background template in UU.

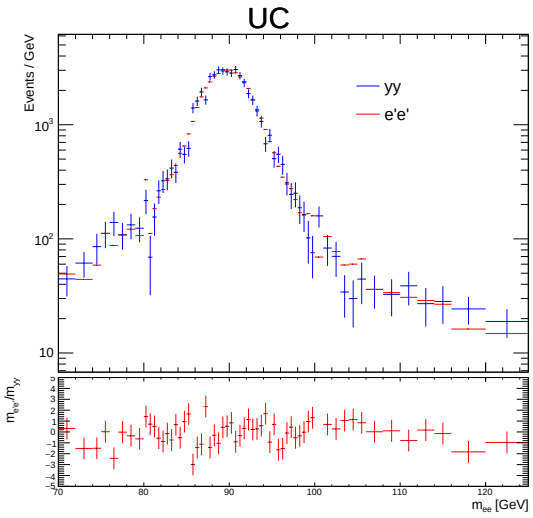

(b) Resonant background template in UC.

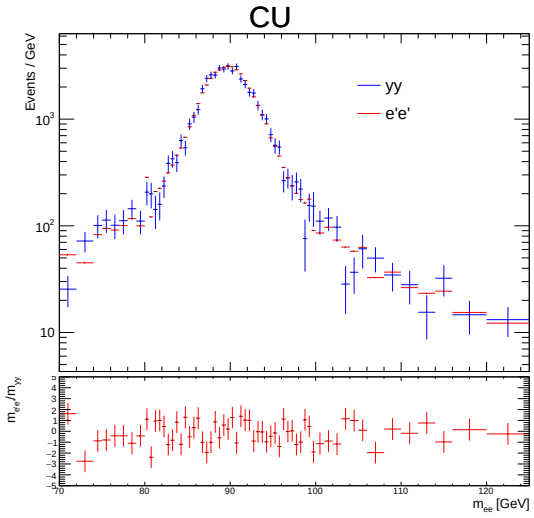

(c) Resonant background template in CU.

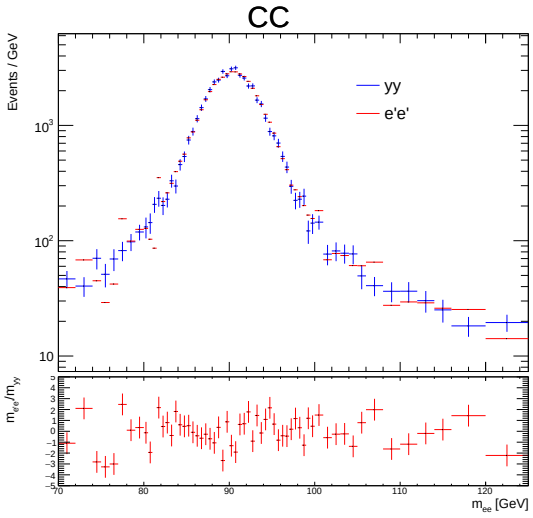

(d) Resonant background template in CC.

Figure 7.54: Drell-Yan invariant mass templates, that are derived from *ee* events in data, (red) and the expected diphoton background component (blue) in the UU (a), UC (b), CU (c) and CC (d) categories, obtained from the $Z \to ee$ simulation sample and normalized to the Run2 luminosity.

on data is repeated 100 times, with the content of each point being taken from a Gaussian around the default value, taking into account the eigenvectors of the covariance matrix. This gives an uncertainty of around 0.01% on the peak position and 0.5% on the width. The analysis on data is also repeated using alternate samples for computing the transformation parameters. Different material variations of the PowhegPy8 MC samples are considered:

- ATLAS-R2-2016-01-00-02 (config A) with ID +5% overall material scaling,
- ATLAS-R2-2016-01-00-03 (config IBL) with +10% IBL material scaling,
- ATLAS-R2-2016-01-00-04 (config PP0) with +25% PP0 material scaling,
- ATLAS-R2-2016-01-00-11 (config N) with +5% X0 LArPS-layer1 end-cap,
- ATLAS-R2-2016-01-00-12 (config E'+L') with +7.5 X0 for SCT/TRT endplate, +5X X0 radial LArbarrel cryostat
- ATLAS-R2-2016-01-00-13 (config F+M+X) with +7.5% X0 for ID endplate, +5% X0 radial PS-Layer1 barrel, Transition distortion.

Unfortunately no sample exists with all variations at the same time with release 21. The statistical precision of these sample is poor (1 million events each) compared to the default sample, so some of the variations are likely of statistical origin. To address this problem, the envelope of the different material variations is used as the systematic uncertainty for the normalization and shape and the CU and UC are considered together for the normalization uncertainty as the separated values are too asymmetric to have a physical meaning. The uncertainty on the normalization goes from 6 to 8.5% while the uncertainty on the peak position and on the width is around 0.1-0.2% and around 1-3% respectively. The line shape of a Sherpa sample is also used, with an impact on the fake rates of 3 to 10%, and an uncertainty on the peak position and on the width of 0.1% maximum and around 0.5-3% respectively. The

Parameter	Category	Central value	Bootstrap	Material
mean m_0	UU	89.35	0.01	0.2% (FMX)
	UC	89.77	0.01	0.1% (FMX)
	CU	89.74	0.01	0.1% (PP0)
	CC	90.29	0.01	0.1% (A)
width σ	UU	2.40	0.01	1.2 (EL)
	UC	2.66	0.03	1.7 (EL)
	CU	2.59	0.02	2.1 (FMX)
	CC	2.83	0.03	2.3 (FMX)

Table 7.24: Absolute (and relative) uncertainties in GeV on the DY shape for each category. The material distortion giving the highest deviation is also shown.

Conversion	Central values ± Stat+window				Material
Category	Inclusive	BDT Bin 1	BDT Bin 2	BDT Bin 3	
UU	6222	4263 ±3.2%	1473 ±3.2%	486 ±3.0%	5.3%
UC	6359	4456 ±2.3%	1348 ±2.0%	555 ±4.0%	8.0%
CU	5851	3833 ±2.8%	1413 ±2.5%	605 ±2.9%	5.6%
CC	7590	5255 ±1.9%	1577 ±1.9%	758 ±1.5%	8.3%

Table 7.25: Absolute (and relative) uncertainties in number of events on the DY normalization for each category. The material distortion giving the highest deviation is also shown.

systematic uncertainties for the template parameters (normalization factor f, peak position m_Z^{fake}) are summarized in Tables 7.24 and 7.25.

The resulting background templates of the expected DY $\gamma\gamma$ contribution, modeled with the double-sided Crystal Ball function, are shown in Figure 7.55. Also shown are the alternate templates arising from the systematic uncertainties on the shape and normalization parameters described in this section.

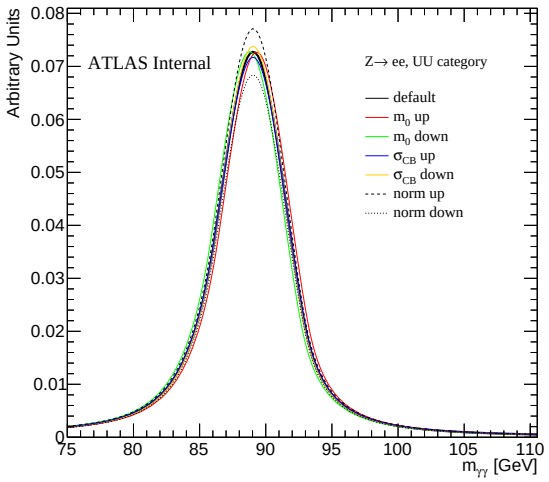

(a) Resonant background template variation in UU.

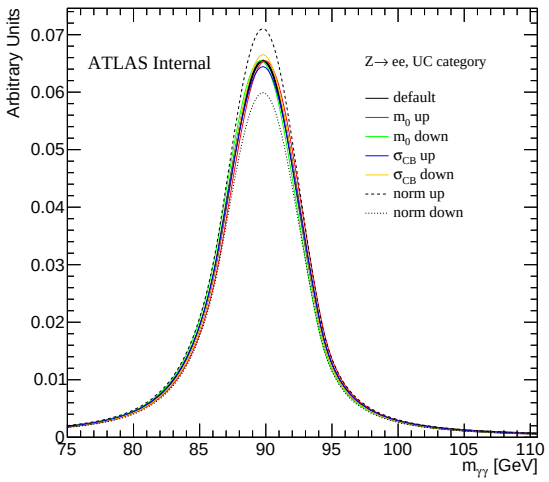

(b) Resonant background template variation in UU.

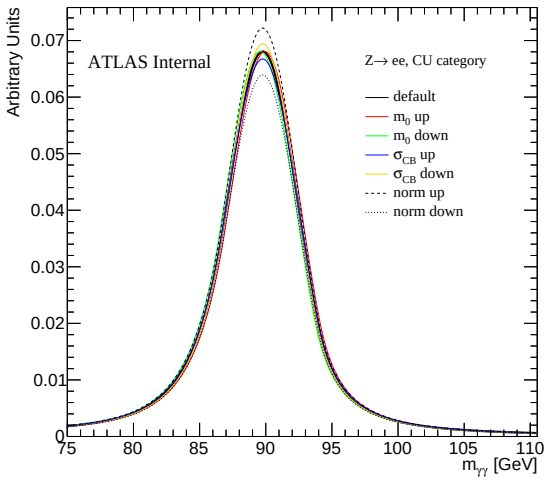

(c) Resonant background template variation in CU.

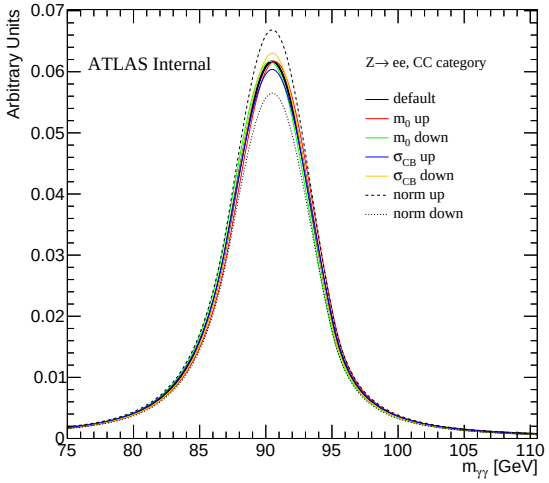

(d) Resonant background template variation in CC.

Figure 7.55: DY invariant mass templates describing the expected diphoton background component in the UU (a), UC (b), CU (c) and CC (d) categories, inclusive across the diphoton BDT categories, with individual systematic variations of the mean, width and normalization. The different sources of uncertainties are added in quadrature.

CHAPTER VIII

Results for Diphoton Decays of Higgs-like Scalars

In this search, the number of signal and background events are estimated with maximum-likelihood fits using a profile likelihood to incorporate the systematic uncertainties from the signal and background modeling described in Chapter 7. The final signal yield in each category is obtained in all of the categories via a simultaneous fit on the $m_{\gamma\gamma}$ data distributions obtained in every category. The resulting yields are then interpreted using the CL_s method [87] to provide upper limits on the production cross section times branching ratio of the $X \to \gamma\gamma$ decay for a hypothetical resonance at a given m_X.

The statistical methods used to perform the maximum-likelihood fit on the data using the expected signal and background models are described in Section 8.1. The uncertainties arising from systematic variations on the signal and background modeling is summarized in Section 8.2. The final background template and the associated event count for each category to be used in the likelihood fit is described in Section 8.3. Finally, the observed limits on the cross section for a scalar resonance in the diphoton invariant mass range of 66 – 110 GeV is presented in Section 8.4.

8.1 Statistical Methods

For this setup, the likelihood is built for each category separately. An optimization procedure is performed to find the best cross section value at each resonance mass point when using a given background model and dataset. The product of these terms is given as

$$\mathcal{L} = \prod_{c=1}^{N_c} e^{-n_c^{\text{total}}} \prod_{i=1}^{n_c^{\text{data}}} \mathcal{L}_{i,c}(m_{\gamma\gamma}(i,c)) \tag{8.1}$$

where N_c is the number of categories, n_c^{data} is the the number of data events in category c, n_c^{total} is the number of events in category c predicted from the background model, and $m_{\gamma\gamma}(i,c)$ is the $m_{\gamma\gamma}$ value for event i in category c. Nuisance parameters denoted as θ are also included in the likelihood function to provide flexibility in the model as permitted by the systematic uncertainty. The likelihood function for an event i in category c with diphoton invariant mass $m_{\gamma\gamma}(i,c)$ is expressed as

$$\begin{aligned}
\mathcal{L}_{i,c}(m_{\gamma\gamma}; \sigma, m_X, N_c^{\text{QCD}}, \mathbf{x}_c, \boldsymbol{\theta}_c) = N_c^{\text{signal}}(\sigma, m_X, \boldsymbol{\theta}_{N_c}^{\text{signal}}) \\
\cdot f_c^{\text{signal}}(m_{\gamma\gamma}, m_X, \mathbf{x}_c^{\text{signal}}, \boldsymbol{\theta}_c^{\text{signal}}) \\
+ N_{\text{UU},c}^{\text{DY}}(\boldsymbol{\theta}_{N_{\text{UU},c}}^{\text{DY}}) \cdot f_{\text{UU}}^{\text{DY}}(m_{\gamma\gamma}, \mathbf{x}_{\text{UU}}^{\text{DY}}, \boldsymbol{\theta}_{\text{UU}}^{\text{DY}}) \\
+ N_{\text{UC},c}^{\text{DY}}(\boldsymbol{\theta}_{N_{\text{UC},c}}^{\text{DY}}) \cdot f_{\text{UC}}^{\text{DY}}(m_{\gamma\gamma}, \mathbf{x}_{\text{UC}}^{\text{DY}}, \boldsymbol{\theta}_{\text{UC}}^{\text{DY}}) \\
+ N_{\text{CU},c}^{\text{DY}}(\boldsymbol{\theta}_{N_{\text{CU},c}}^{\text{DY}}) \cdot f_{\text{CU}}^{\text{DY}}(m_{\gamma\gamma}, \mathbf{x}_{\text{CU}}^{\text{DY}}, \boldsymbol{\theta}_{\text{CU}}^{\text{DY}}) \\
+ N_{\text{CC},c}^{\text{DY}}(\boldsymbol{\theta}_{N_{\text{CC},c}}^{\text{DY}}) \cdot f_{\text{CC}}^{\text{DY}}(m_{\gamma\gamma}, \mathbf{x}_{\text{CC}}^{\text{DY}}, \boldsymbol{\theta}_{\text{CC}}^{\text{DY}}) \\
+ N_c^{\text{QCD}} \cdot f_c^{\text{QCD}}(m_{\gamma\gamma}, \mathbf{x}_c^{\text{QCD}})
\end{aligned} \tag{8.2}$$

where

- σ is the production cross section of the new resonance of mass m_X;
- N_c^{signal} is the number of $X \to \gamma\gamma$ signal events contributing to category c;

- f_c^{signal} is the DSCB line-shape for modeling a scalar resonance in category c;
- $N_{\text{UU},c}^{\text{DY}}$, $N_{\text{UC},c}^{\text{DY}}$, $N_{\text{CU},c}^{\text{DY}}$, and $N_{\text{CC},c}^{\text{DY}}$ are the expected number of $Z \to ee$ resonant background events identified as UU, UC, CU, and CC, respectively, and contributing to category c according to the resonant background modeling;
- $f_{\text{UU}}^{\text{DY}}$, $f_{\text{UC}}^{\text{DY}}$, $f_{\text{CU}}^{\text{DY}}$, $f_{\text{CC}}^{\text{DY}}$ is the DSCB line-shape for modeling the resonant background in the UU, UC, CU, and CC category, respectively;
- N_c^{QCD} is the expected number of QCD diphoton background continuum events contributing to category c according to the non-resonant background modeling;
- f_c^{QCD} is the exponential or Bernstein polynomial for modeling the QCD diphoton background continuum in category c;
- $\mathbf{x}_c = \{\mathbf{x}_c^{\text{signal}}, \mathbf{x}_{\text{UU}}^{\text{DY}}, \mathbf{x}_{\text{UC}}^{\text{DY}}, \mathbf{x}_{\text{CU}}^{\text{DY}}, \mathbf{x}_{\text{CC}}^{\text{DY}}, \mathbf{x}_c^{\text{QCD}}\}$ refers to the collection of parameters used to model the signal and background shapes for category c;
- $\boldsymbol{\theta}_c = \{\boldsymbol{\theta}_{N_c}^{\text{signal}}, \boldsymbol{\theta}_c^{\text{signal}}, \boldsymbol{\theta}_{N_{\text{UU},c}}^{\text{DY}}, \boldsymbol{\theta}_{\text{UU}}^{\text{DY}}, \boldsymbol{\theta}_{N_{\text{UC},c}}^{\text{DY}}, \boldsymbol{\theta}_{\text{UC}}^{\text{DY}}, \boldsymbol{\theta}_{N_{\text{CU},c}}^{\text{DY}}, \boldsymbol{\theta}_{\text{CU}}^{\text{DY}}, \boldsymbol{\theta}_{N_{\text{CC},c}}^{\text{DY}}, \boldsymbol{\theta}_{\text{CC}}^{\text{DY}}\}$ refers to the collection of nuisance parameters used to describe the systematic uncertainties for category c.

The UC and the CU categories for the DY resonant background are described separately due to slightly differing fake rates.

The nuisance parameters are constrained by Gaussian penalty terms and are organized below:

- $\boldsymbol{\theta}_{N_c}^{\text{signal}}$: signal normalization uncertainties arising from the experimental variations and spurious signal described in Sections 7.2.3 and 7.3.2, respectively
  - θ_{lumi}: uncertainty on the integrated luminosity of the data sample
  - θ_{C_X}: uncertainty on the signal yield arising from choice of the signal production mode (only used in the model-independent method)

- θ_{trigger}: uncertainty on the signal yield due to the trigger scale factor variations
- θ_{pileup}: uncertainty on the signal yield coming from the variation of the pileup reweighting scale factor variation
- θ_{ID}, $\theta_{\text{isolation}}$: uncertainties on the signal yield based variations on the photon ID and isolation efficiency
- θ_{scale}, $\theta_{\text{resolution}}$: uncertainty on the signal yield arising from the photon energy scale and resolution variation
- θ_{SS}: spurious signal systematic uncertainty

- $\boldsymbol{\theta}_c^{\text{signal}} = \{\theta_{\text{scale}}, \theta_{\text{resolution}}\}$: signal modeling uncertainties arising from the photon energy scale and resolution variations described in Section 7.1.2

- $\boldsymbol{\theta}^{\text{DY}}_{N_{\text{UU,c}}}, \boldsymbol{\theta}^{\text{DY}}_{N_{\text{UU,c}}}, \boldsymbol{\theta}^{\text{DY}}_{N_{\text{UU,c}}}, \boldsymbol{\theta}^{\text{DY}}_{N_{\text{UU,c}}}$: DY resonant background normalization uncertainties arising from systematic variations described in Section 7.3.3.4
  - $\theta_{\text{statistic}}$: uncertainty arising from the limited statistics in the $Z \to ee$ template (including the systematic effect of mass window variations used to compute the electron fake rate around the Z mass)
  - θ_{material}: uncertainty arising from the systematic effects of the detector material
  - $\theta_{\text{generator}}$: uncertainty arising from differences between the PowhegPy8 and Sherpa2 generators

- $\boldsymbol{\theta}^{\text{DY}}_c, \boldsymbol{\theta}^{\text{DY}}_c, \boldsymbol{\theta}^{\text{DY}}_c, \boldsymbol{\theta}^{\text{DY}}_c$: DY resonant background modeling uncertainties arising from systematic variations described in Section 7.3.3.4
  - $\theta_{\text{BS, peak}}, \theta_{\text{BS, sigma}}, \theta_{\text{BS, ALo}}, \theta_{\text{BS, AHi}}$: uncertainty on the parameters of the DSCB used to model the DY background computed with a bootstrap (BS)

method. These effects are assumed to be uncorrelated between categories and are described as separate nuisance parameters

- $\theta_{\text{material, peak}}, \theta_{\text{material, sigma}}$: uncertainty on the peak position and width of the DY background due to systematic effects of the detector material description. These effects are assumed to be correlated between categories and are described as a single nuisance parameter
- $\theta_{\text{generator, peak}}, \theta_{\text{generator, sigma}}$: uncertainty on the peak position and width of the DY background due to the differences between the PowhegPy8 and Sherpa2 generators. These effects are assumed to be correlated between categories and are described as a single nuisance parameter

The quantity N_c^{signal} represents the number of events for the new hypothetical resonance and is parameterized as

$$N_c^{\text{signal}}(\sigma, m_X, \boldsymbol{\theta}_{N_c}^{\text{signal}}) = \sigma \cdot L_{\text{int}} \cdot C_X(m_X) \cdot A_X(m_X) \cdot f_c \cdot \prod_{\theta_k \in \boldsymbol{\theta}_{N_c}} K_k(\theta_k) \tag{8.3}$$

where L_{int} is the integrated luminosity of the dataset, $C_X(m_X)$ and $A_X(m_X)$ are the correction and acceptance factors for a resonance mass m_X, f_c is the signal fraction for category c, K_k denotes a function characterizing the effect of the kth signal normalization systematic θ_k, and the index k runs over the set of systematic uncertainties affecting N_c^{signal} such that each $K_i(\theta_i)$ implements one of the systematic uncertainties on the number of signal events as listed above.

The function that characterizes the systematic uncertainty is given as

$$K_k(\theta_k) = [r_k(m_X)]^{\theta_k} \tag{8.4}$$

where $r_k(m_X)$ is approximately given by

$$r_k(m_X) = \begin{cases} N_{c,+k}^{\text{signal}}(m_X)/N_{c,0}^{\text{signal}}(m_X) & \text{for} \quad \theta_k > 0 \\ N_{c,0}^{\text{signal}}(m_X)/N_{c,-k}^{\text{signal}}(m_X) & \text{for} \quad \theta_k < 0. \end{cases} \tag{8.5}$$

The nominal $N_{c,0}^{\text{signal}}$ term is defined as the $N_{c,0}^{\text{signal}}$ value with no systematic variations applied. The $N_{c,\pm k}^{\text{signal}}(m_X)$ term is defined as the nominal $N_{c,0}^{\text{signal}}$ value scaled up or down for $+k$ or $-k$, respectively, only by the uncertainty value for the kth systematic as listed in Table 8.1. This expression ensures that the modifications to the signal event yield for $\theta_k = \pm 1$ correspond to the $\pm 1\sigma$ variations used to define the uncertainties. The actual expression for r_k is interpolated smoothly between the cases $\theta_k > 0$ and $\theta_k < 0$ to avoid numerical problems at $\theta_k = 0$. The interpolation is implemented using the `FlexibleInterpVar` method of the `HistFactory` class in the `RooStats` library of ROOT with modifications made to allow mass-dependent values for the uncertainties. Since the signal yield is described as the product of the total number of events and the category fractions, σ_{sig} can be directly extracted from the fit.

The number of resonant background events in a photon conversion category $j \in \{\text{UU}, \text{UC}, \text{CU}, \text{CC}\}$ is defined as

$$N_{j,c}^{\text{DY}} = N_{j,c,0}^{\text{DY}} \cdot \prod_{\theta_k \in \boldsymbol{\theta}_{N_{j,c}}^{\text{DY}}} \exp(\theta_k) \tag{8.6}$$

where $N_{j,c,0}$ is the nominal normalization of the DY resonant background template and $\boldsymbol{\theta}_{N_{j,c}}^{\text{DY}}$ are the systematic uncertainties on the template normalization due to statistical and systematic effects as described above.

8.2 Summary of Systematic Variations

The uncertainties due to systematic variations in the signal and background modeling process described in Section 7 are all included in the likelihood function given by Equation 8.1.

♦ **Model-Dependent Method** The level of uncertainty associated to statistical limitations and each systematic variation for the model-dependent method is summarized in Table 8.1.

Source	Uncertainty	Remarks
Signal yield, C_X factors		
Luminosity	$\pm 0.83\%$	
Trigger	$\pm 1.4 - 2.2\%$	m_X-dependent
Pile-up	$\pm 2.5 - 6.1\%$	m_X-dependent
Photon ID efficiency	$\pm 2.3 - 3.7\%$	m_X-dependent
Photon Isolation efficiency	$\pm 2.0 - 3.6\%$	m_X-dependent
Photon energy resolution	$\pm 0.2 - 1.4\%$	m_X-dependent
Photon energy scale	$\pm 0.2 - 1.4\%$	m_X-dependent
DD Isolation efficiency	$\pm 0.4 - 1.5\%$	m_X-dependent
Signal modeling		
Photon energy scale	$\pm 0.2 - 0.5\%$	m_X and category-dependent
Photon energy resolution	$\pm 2.4 - 13\%$	m_X and category-dependent
Non-resonant Background		
Spurious Signal	$\pm 20 - 50\%$	m_X and category-dependent
DY Background Modeling		
Peak position	$\pm 0.1 - 0.2\%$	category-dependent
Template shape	$\pm 1.2 - 2.3\%$	category-dependent
Normalization	$\pm 6.1 - 9\%$	category-dependent

Table 8.1: Summary of the main sources of systematic uncertainty on the scalar resonance cross section limit for the model-dependent method.

◊ **Model-Independent Method** The level of uncertainty associated to statistical limitations and each systematic variation for the model-independent method is summarized in Table 8.2.

Source	Uncertainty	Remarks
Signal yield, C_X factors		
Luminosity	$\pm 0.83\%$	
Trigger	$\pm 1.4 - 1.9\%$	m_X-dependent
Pile-up	$\pm 1.8 - 3.7\%$	m_X-dependent
Photon ID efficiency	$\pm 2.1 - 3.0\%$	m_X-dependent
Photon Isolation efficiency	$\pm 2.0 - 3.0\%$	m_X-dependent
Photon energy resolution	$\pm 0.2 - 0.3\%$	m_X-dependent
Photon energy scale	$\pm 0.2 - 0.3\%$	m_X-dependent
DD Isolation efficiency	$\pm 0.2 - 1.0\%$	m_X-dependent
Signal modeling		
Photon energy scale	$\pm 0.2 - 0.5\%$	m_X and category-dependent
Photon energy resolution	$\pm 3.2 - 8.5\%$	m_X and category-dependent
Non-resonant Background		
Spurious Signal	$\pm 20 - 50\%$	m_X and category-dependent
DY Background Modeling		
Peak position	$\pm 0.1 - 0.2\%$	category-dependent
Template shape	$\pm 1.2 - 2.3\%$	category-dependent
Normalization	$\pm 6.1 - 9\%$	category-dependent

Table 8.2: Summary of the main sources of systematic uncertainty on the scalar resonance cross section limit for the model-independent method.

8.3 Expected Model and Limits

The expected background models and the event counts for each component will be presented for the model-dependent and model-independent methods separately. The expected limits on the cross section times branching ratio to two photons calculated by using the likelihood method described in Section 8.1 on the background models will also be shown separately for each method. Henceforth, the cross section times branching ratio will be referred to as just the cross section for brevity.

♦ **Model-Dependent Method** The estimated event count and contribution fraction for each background process in the model-dependent method is given in Table 8.3. The $m_{\gamma\gamma}$ distribution from each resonant and non-resonant background on the mass spectrum for each model-dependent category is shown in Figure 8.1.

Diphoton BDT	Photon Conversion	QCD $\gamma\gamma$ Events	%	QCD γj Events	%	QCD jj Events	%	DY $Z \to ee$ Events	%	Total Events
Bin 1	UU	423746	71.5	124037	20.9	40357	6.8	4263	0.7	592403
	UC	331118	67.0	118863	24.1	35958	7.2	8289	1.7	494228
	CC	64521	57.3	33610	29.9	9217	8.2	5255	4.6	112603
Bin 2	UU	379797	74.7	102841	20.2	24437	4.8	1473	0.3	508548
	UC	279785	69.7	96895	24.1	22205	5.5	2761	0.7	401646
	CC	55632	64.5	23029	26.7	6037	7.0	1577	1.8	86275
Bin 3	UU	205134	80.3	42662	16.7	6897	2.7	486	0.2	255179
	UC	153411	73.5	45750	21.9	8395	4.0	1160	0.6	208716
	CC	30061	66.6	11808	26.2	2479	5.5	758	1.7	45106

Table 8.3: The estimated contribution from each resonant and non-resonant background in the $62 - 120\,\text{GeV}$ $m_{\gamma\gamma}$ range for the model-dependent method.

The expected total cross section limits for the Higgs-like resonance are shown in Figure 8.2. The limits represent the total production cross-section times branching ratio to two photons as a function of m_X. Benefiting from larger integrated luminosity, reduced spurious signal systematic uncertainties in signal-enriched categories by using tighter kinematic selections and GPR smoothing, and multi-variate classification techniques to reduce the background, the expected limits presented here are

approximately 2.5 times stronger compared to the previous iteration of the analysis by ATLAS [55] after scaling for luminosity. A comparison of the expected limit to the recent CMS diphoton resonance search result [48] is shown. The projected expected limits of this analysis are comparable to those of CMS at the higher diphoton invariant mass range and competitive near the Z resonance at $m_Z \approx 90$ GeV.

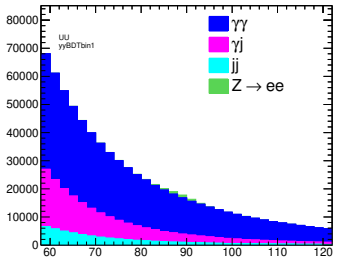

(a) Final template in UU1.

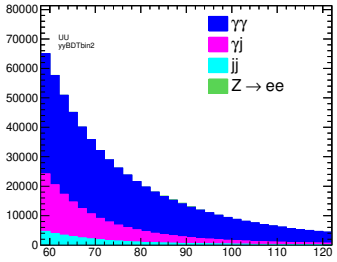

(b) Final template in UU2.

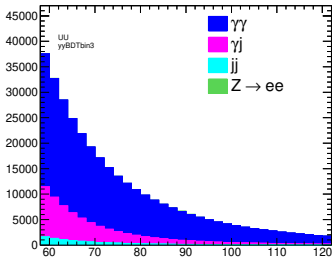

(c) Final template in UU3.

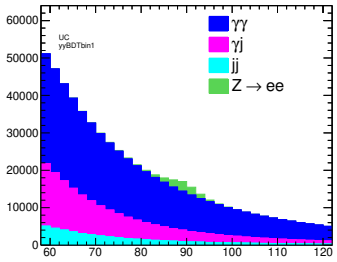

(d) Final template in UC1.

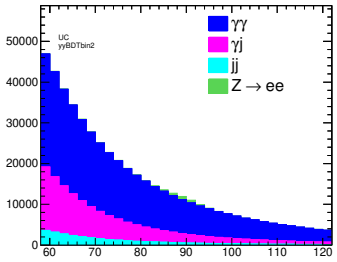

(e) Final template in UC2.

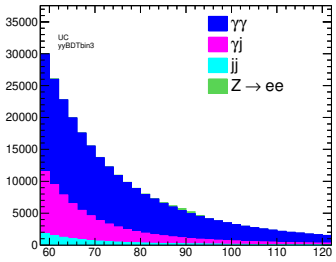

(f) Final template in UC3.

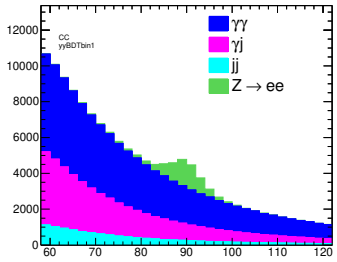

(g) Final template in CC1.

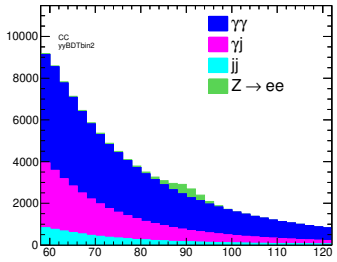

(h) Final template in CC2.

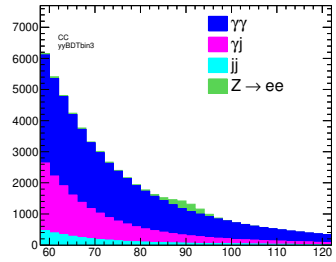

(i) Final template in CC3.

Figure 8.1: The $m_{\gamma\gamma}$ distribution from each resonant and non-resonant background for each model-dependent category. The $\gamma\gamma$ contribution is taken from the Sherpa MC samples, the γj and jj contribution from data-driven control regions, and the $Z \to ee$ contribution from the data-driven template.

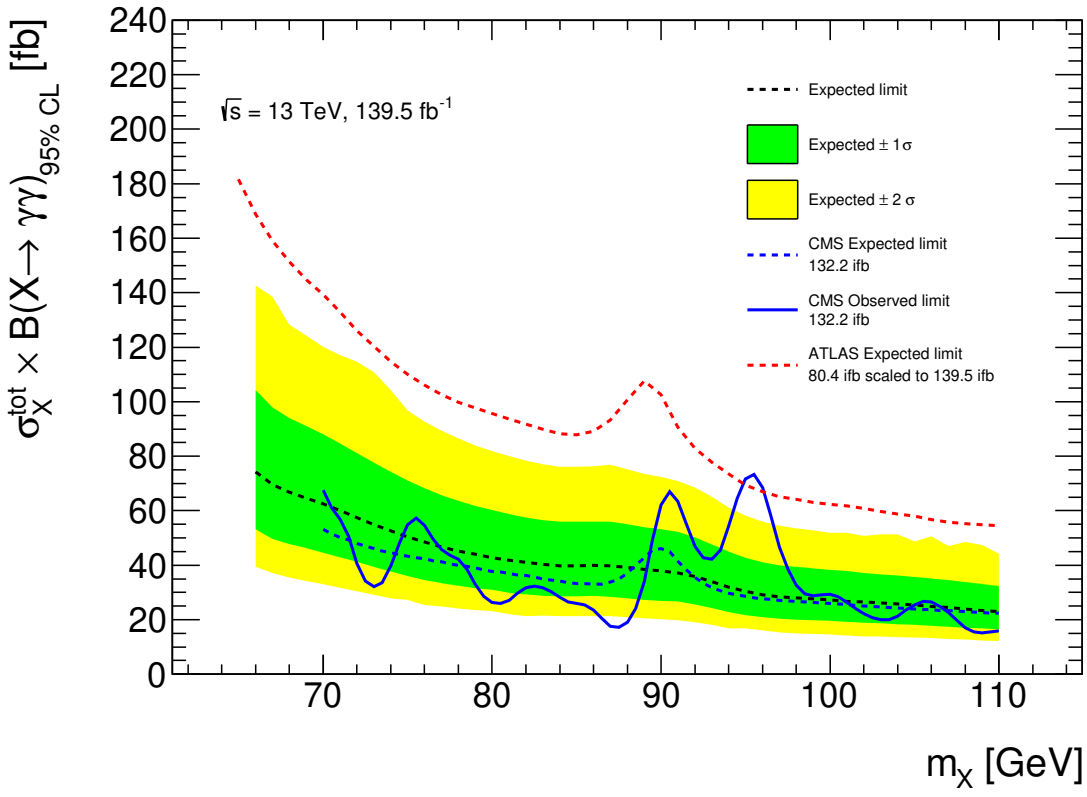

Figure 8.2: Expected limit on the total production cross-section times branching ratio to two photons for a Higgs-like resonance as a function of the resonance mass m_X for the model-dependent method. Central values of the expected and observed limit from the recent CMS analysis [48] and the expected limit from the previous ATLAS analysis [55] using 80.4 fb^{-1} scaled to 139.5 fb^{-1} are shown for comparison. The expected limit here considers all systematic uncertainties and an integrated luminosity of 139.5 fb^{-1}.

◊ **Model-Independent Method** The estimated event count and contribution fraction for each background process in the model-independent method is given in Table 8.4. The $m_{\gamma\gamma}$ distribution from each resonant and non-resonant background on the mass spectrum for each model-dependent category is shown in Figure 8.3.

Conversion	QCD $\gamma\gamma$		QCD γj		QCD jj		DY $Z \to ee$		Total
Category	Events	%	Events	%	Events	%	Events	%	Events
UU	1008677	74.3	269540	19.8	71691	5.2	6222	0.4	1356130
UC	764314	69.1	261508	23.6	66558	6.0	12210	1.1	1104590
CC	150214	61.5	68447	28.0	17733	7.2	7590	3.1	243984

Table 8.4: The estimated contribution from each resonant and non-resonant background in the $62 - 120\,\text{GeV}$ $m_{\gamma\gamma}$ range for the model-independent method.

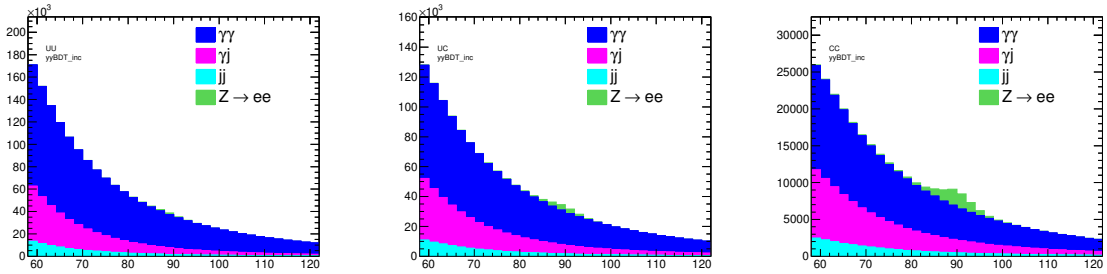

(a) Final template in UU. (b) Final template in UC. (c) Final template in CC.

Figure 8.3: The $m_{\gamma\gamma}$ distribution from each resonant and non-resonant background for each model-independent category. The $\gamma\gamma$ contribution is taken from the Sherpa MC samples, the γj and jj contribution from data-driven control regions, and the $Z \to ee$ contribution from the data-driven template.

The expected fiducial cross section limits for the Higgs-like resonance are shown in Figure 8.4. The limits represent the fiducial production cross-section times branching ratio to two photons as a function of m_X. Similarly, the expected total cross section limits for the Higgs-like resonance are shown in Figure 8.5. A comparison of the expected limit to the recent CMS diphoton resonance search result [48] and to the previous iteration of the analysis by ATLAS [55] after scaling for luminosity is shown. The projected expected limits of this analysis are much more competitive compared to the previous ATLAS search.

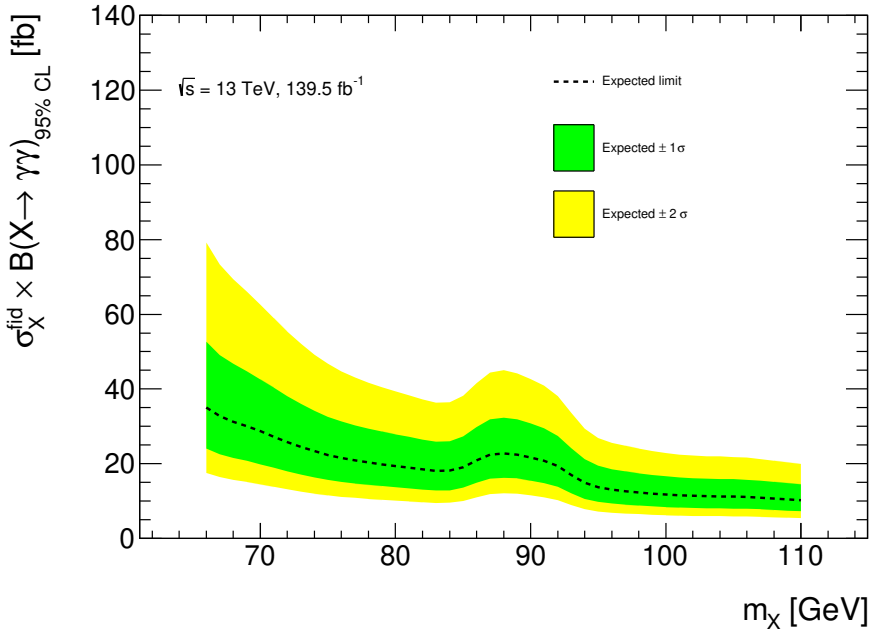

Figure 8.4: Expected limit on the fiducial production cross-section times branching ratio to two photons for a Higgs-like resonance as a function of the resonance mass m_X for the model-independent method. The expected limit here considers all systematic uncertainties and an integrated luminosity of 139.5 fb^{-1}.

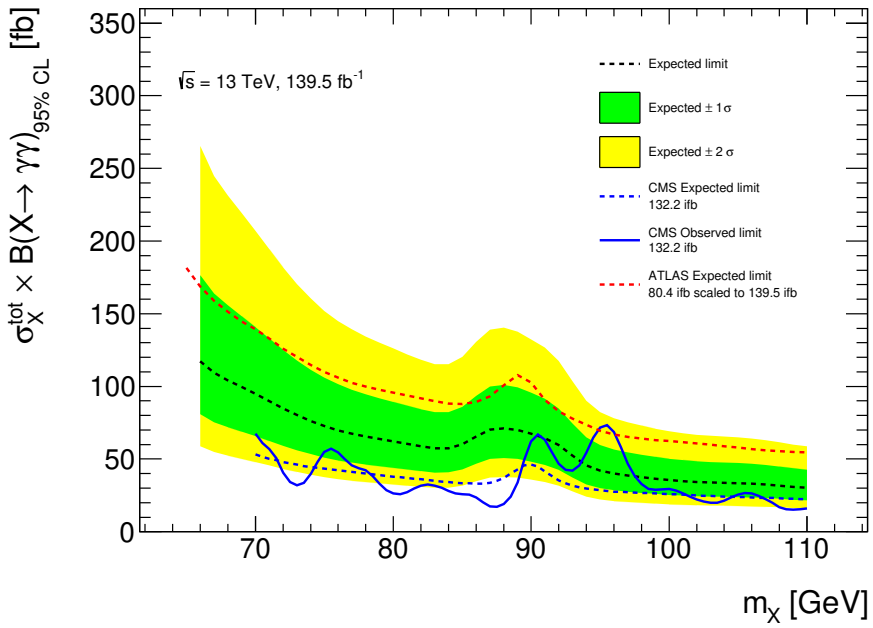

Figure 8.5: Expected limit on the total production cross-section times branching ratio to two photons for a Higgs-like resonance as a function of the resonance mass m_X for the model-independent method. Central values of the expected and observed limit from the recent CMS analysis [48] and the expected limit from the previous ATLAS analysis [55] using 80.4 fb^{-1} scaled to 139.5 fb^{-1} are shown for comparison. The expected limit here considers all systematic uncertainties and an integrated luminosity of 139.5 fb^{-1}.

8.4 Observed Limits and Results

8.4.1 Distributions of $m_{\gamma\gamma}$ in Data

The data distribution with the full dataset in the signal region is first compared to the background templates described in Section 7.3.2 to ensure agreement in the modeling.

♦ **Model-Dependent Method** The data and the background models have good agreement for the model-dependent method. The data distribution with the full dataset is shown in Figure 8.6 along with the background-only fits. The peak of the DY resonance background is clearly visible in the UC1, CC1, CC2, and CC3 categories in Figures 8.6d, 8.6g, 8.6h, and 8.6i, respectively, where the resonance background resides. No significant structures are seen in the residuals, indicating good modeling across the entire $m_{\gamma\gamma}$ range.

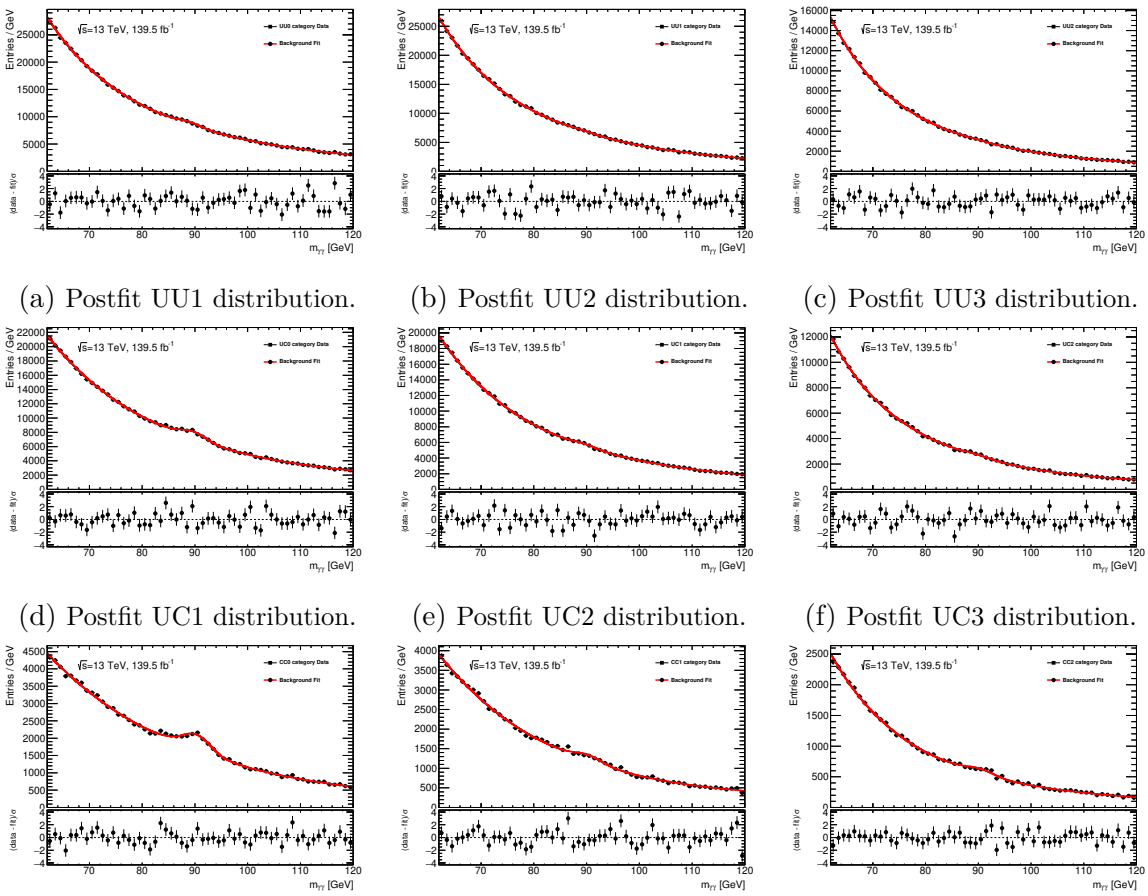

(a) Postfit UU1 distribution. (b) Postfit UU2 distribution. (c) Postfit UU3 distribution.

(d) Postfit UC1 distribution. (e) Postfit UC2 distribution. (f) Postfit UC3 distribution.

(g) Postfit CC1 distribution. (h) Postfit CC2 distribution. (i) Postfit CC3 distribution.

Figure 8.6: Data distributions of $m_{\gamma\gamma}$ overlaid with background-only fits for each model-dependent category. The bottom panels correspond to the difference between data and the the fit.

◊ **Model-Independent Method** The data and the background models also have good agreement for the model-independent method. The data distribution with the full dataset is shown in Figure 8.7 along with the background-only fits. The peak of the DY resonance background is clearly visible in the UC and CC categories in Figures 8.7b and 8.7b, respectively, where the resonance background resides. No significant structures are seen in the residuals, indicating good modeling across the entire $m_{\gamma\gamma}$ range.

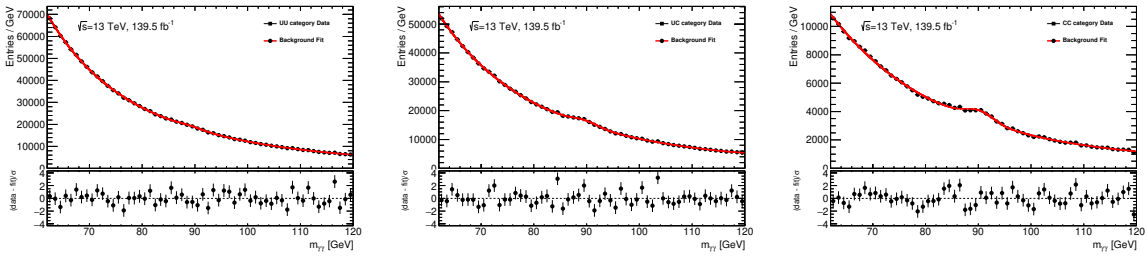

(a) Postfit UU distribution. (b) Postfit UC distribution. (c) Postfit CC distribution.

Figure 8.7: Data distributions of $m_{\gamma\gamma}$ overlaid with background-only fits for each model-independent category. The bottom panels correspond to the difference between data and the the fit.

8.4.2 Resonance Discovery p-value

To compute the acceptable level of local fluctuation within in the search range, global significance formulas can be used to approximate the local significance Z_{local} such that $Z_{\text{global}} = 0$:

$$\Phi(Z_{\text{global}}) = p_{\text{global}} = 1 - (1 - p_{\text{local}})^{N_{\text{trials}}} \tag{8.7}$$

$$N_{\text{trials}} = 1 + \sqrt{\pi/2} \cdot N_{\text{indep}} \cdot Z_{\text{local}} \tag{8.8}$$

$$N_{\text{indep}} = \frac{\text{limit scan range}}{\text{signal peak width}} \tag{8.9}$$

The formula for $Z_{\text{global}} = 0$ can then be given as follows:

$$\Phi(Z_{\text{global}} = 0) = (1 - \Phi(Z_{\text{local}}))^{1+\sqrt{\pi/2} \cdot N_{\text{indep}} \cdot Z_{\text{local}}} = 0.5. \tag{8.10}$$

For this analysis, a search range of 44 GeV and a signal width of approximately 1.5 GeV gives an expected fluctuation of 2.4σ on average.

♦ **Model-Dependent Method** The p-value scan with the full dataset using the model-dependent method is shown in Figure 8.8. The most significant local excess is seen at $m_X = 95.4$ GeV with a 1.7σ deviation in the data which is within the expected local fluctuation of this analysis. However, this local excess is in agreement with the 2.8σ local excess at 95.3 GeV as seen by the search results of CMS [47]. Since the systematic uncertainties of the model-dependent method have been minimized by using various statistical and modeling techniques, any further increase in sensitivity for the diphoton resonance search in this invariant mass regime will mostly come from having additional statistics gained by collecting more data in the LHC Run 3 period.

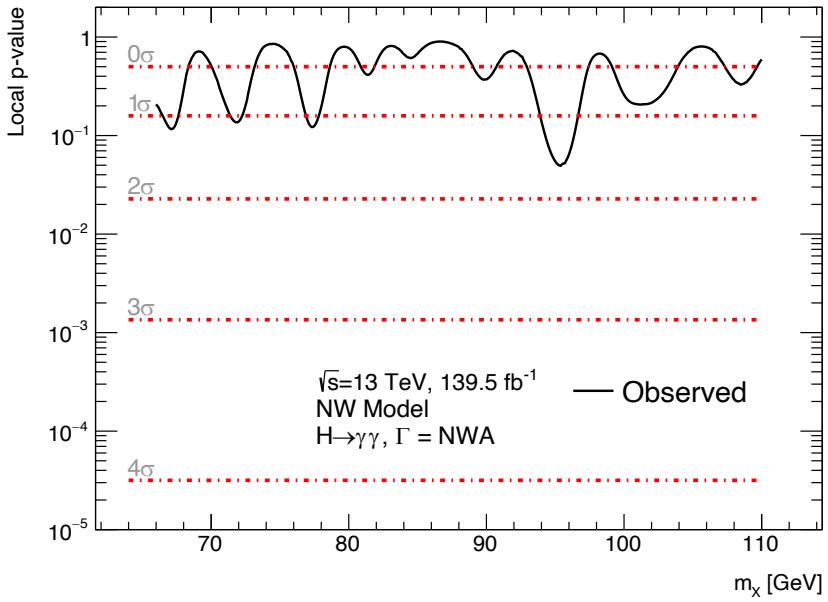

Figure 8.8: The observed p-value for the background-only hypothesis in the logarithmic scale as a function of the resonance mass m_X using the model-dependent method.

◊ **Model-Independent Method** The p-value scan with the full dataset using the model-independent method is shown in Figure 8.9. The most significant local excess is seen at $m_X = 71$ GeV with a 2.2σ deviation in the data which is also within the expected local fluctuation of this analysis.

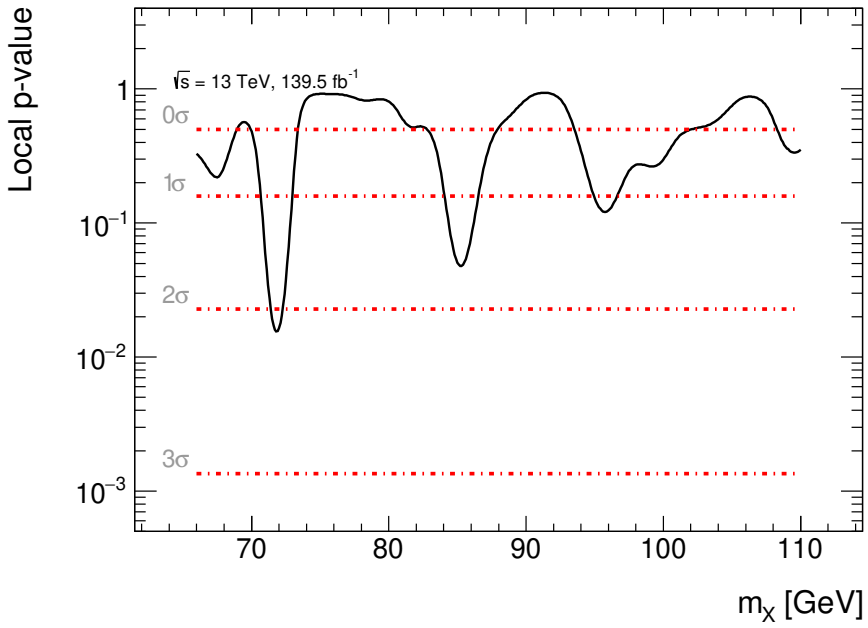

Figure 8.9: The observed p-value for the background-only hypothesis in the logarithmic scale as a function of the resonance mass m_X using the model-independent method.

8.4.3 Limits on Fiducial and Total Cross-Section

The observed cross section values are calculated across the m_X range of [66, 110] GeV in 0.1 GeV steps using the likelihood method described in Section 8.1. The results of each signal resonance model is presented below.

♦ **Model-Dependent Method** The expected and observed limits on the total cross section for the model-dependent method are shown in Figure 8.10. The observed cross section values in the m_X range of [66, 110] GeV all fall within the 2σ uncertainty band of the expected cross section limits.

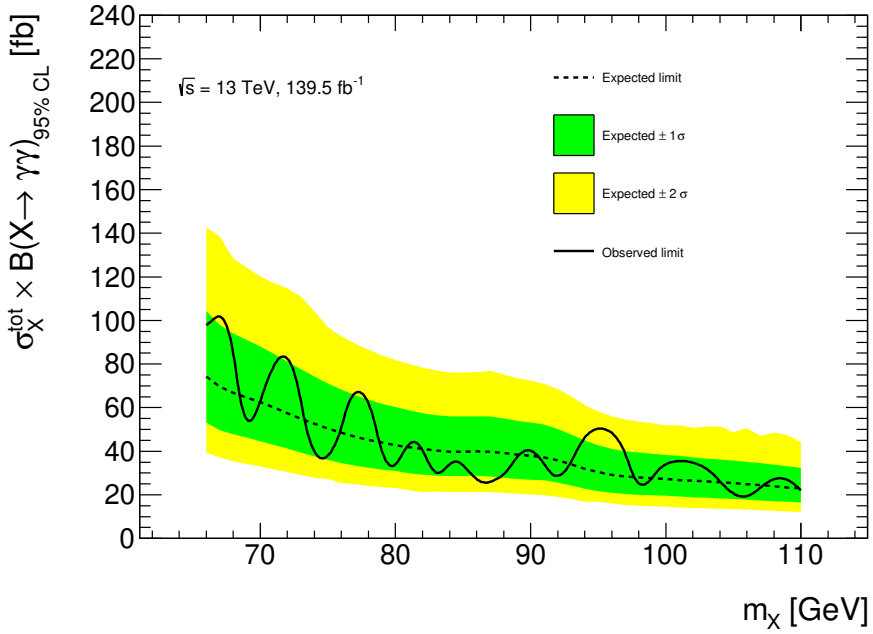

Figure 8.10: The expected and observed limits on the total production cross section $\sigma_{\text{fid}} \cdot \text{BR}(X \to \gamma\gamma)$ of a scalar resonance as a function of the resonance mass m_X in the 66 – 110 GeV diphoton invariant mass range for the model-dependent method. The green and yellow bands show the $\pm 1\sigma$ and $\pm 2\sigma$ uncertainties on the expected limit.

The expected and observed limits are compared to the results of other similar scalar resonance searches in Figure 8.11. The expected cross section limits are comparable to those of the recent resonance search performed by CMS, indicating

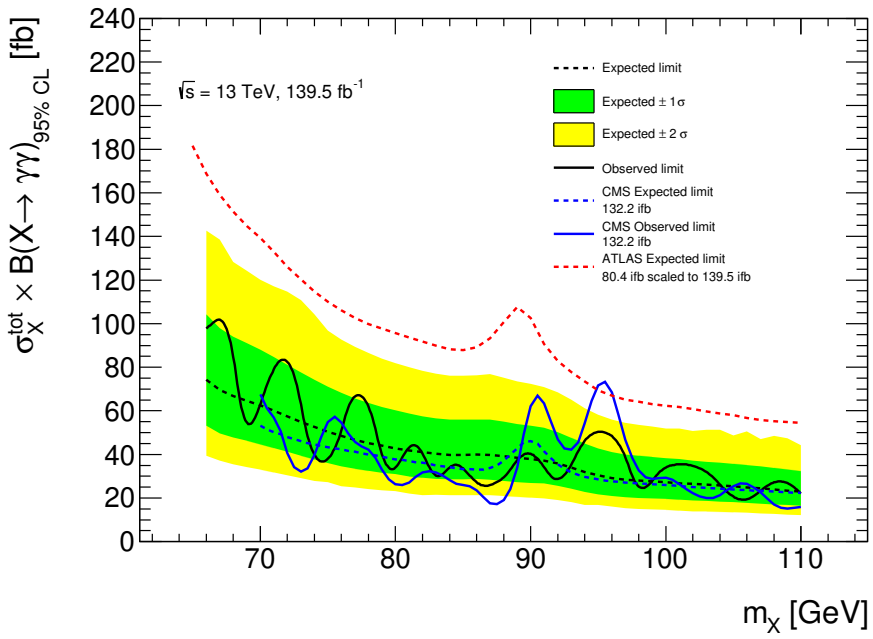

Figure 8.11: The expected and observed limits on the total production cross section for the model-dependent method overlaid with results from other similar scalar resonance searches. The resonance search previously performed by ATLAS [55] is shown in red. The resonance search recently performed by CMS [48] is shown in blue. The green and yellow bands show the $\pm 1\sigma$ and $\pm 2\sigma$ uncertainties on the expected limit.

that the two analyses have similar signal-to-background sensitivity to potential new scalars in this diphoton invariant mass regime. In the resonant background region of $m_{\gamma\gamma} \in [88, 92]$, the sensitivity of this analysis is better than that of CMS as indicated by the lower expected limits of this analysis. This enhancement is achieved in large part by the removal of ambiguous electron fakes as described in Section 6.3.6. The local excess of 1.7σ at $m_X = 95.4$ GeV for the model-dependent method from the p-value scan coincides with the excess seen in the recent resonance search performed by CMS [48] with a cross section of $\sigma_X^{\text{tot}} \approx 50.2\,\text{fb}$. Using the Fisher method [54], the combined significance of the two excesses is approximately 3σ, just reaching the traditional threshold for "evidence" of a signal detection.

◊ **Model-Independent Method** The expected and observed limits on the fiducial cross section for the model-independent method are shown in Figure 8.12. The observed cross section values in the m_X range of [66, 110] GeV all fall within the 2σ uncertainty band of the expected cross section limits.

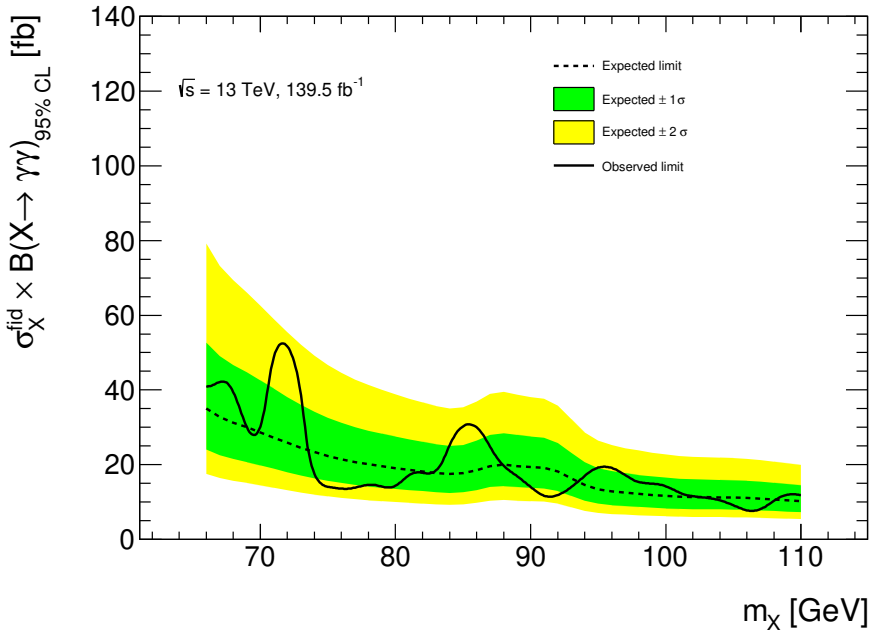

Figure 8.12: The expected and observed limits on the fiducial production cross section $\sigma_{\text{fid}} \cdot \text{BR}(X \to \gamma\gamma)$ of a scalar resonance as a function of the resonance mass m_X in the 66 – 110 GeV diphoton invariant mass range for the model-independent method. The green and yellow bands show the $\pm 1\sigma$ and $\pm 2\sigma$ uncertainties on the expected limit.

The expected and observed limits on the total cross section are compared to the results of other similar scalar resonance searches in Figure 8.13. The limits for the fiducial cross section are scaled by the A_X factor for the ggH production mode in Section 7.2.2 to provide total cross section limits. Although the p-value scan shows a local excess of 2.2σ at $m_X = 71$ GeV for the model-independent method, the previous diphoton resonance searches performed by ATLAS [55] and by CMS [47] both exclude the possibility of a new scalar resonance with a cross section of $\sigma_X^{\text{tot}} \approx 170\,\text{fb}$ at $m_X \approx 71$ GeV.

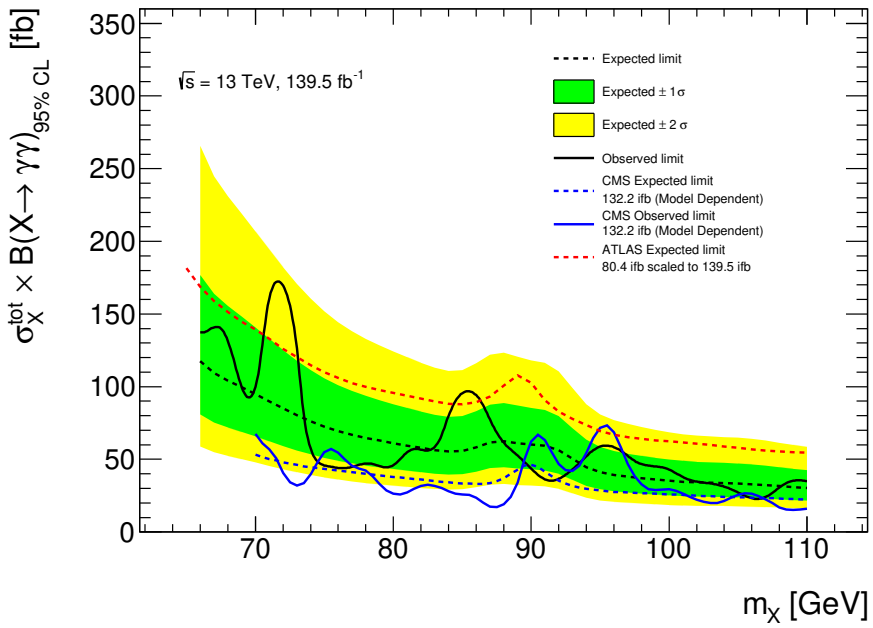

Figure 8.13: The expected and observed limits on the total production cross section for the model-independent method overlaid with results from other similar scalar resonance searches. The resonance search previously performed by ATLAS [55] is shown in red. The resonance search recently performed by CMS [48] is shown in blue. The green and yellow bands show the $\pm 1\sigma$ and $\pm 2\sigma$ uncertainties on the expected limit.

CHAPTER IX

Conclusion

A resonance search was performed for a BSM scalar decaying to two photons in the diphoton invariant mass range of 66 – 110 GeV. Data for pp collisions was recorded by the ATLAS particle detector at the LHC during the Run 2 data-taking period. Algorithms and multivariate analysis techniques were optimized to efficiently reconstruct collision events with two photons in the final state and create signal and background templates for the resonance search. Both MC samples and data-driven methods were used to construct the model for the signal and expected background components. Multiple sources of systematic variations to the models arising from detector and reconstruction effects as well as from control region definitions were studied to provide a systematic uncertainty for the final results.

All constructed background models for both the model-dependent and model-independent method of the analysis were found to be compatible with the dataset. No significant excesses were found within the mass range of the search. The total cross section of a SM-like Higgs-like scalar is excluded down to approximately 50 fb in the mass range of 66 – 110 GeV. Additionally, the total cross section of a model-independent Higgs-like scalar is excluded down to approximately 70 fb in the same mass range. Any potential BSM scalar that could exist within this mass range would need to have a total production cross section below these sets of limits.

A small 1.7σ local excess was observed in the model-dependent method at $m_X = 95.4$ GeV that coincides with the 2.8σ local excess at $m_X = 95.3$ GeV seen by CMS [47]. The combined significance for the two excesses is calculated to be approximately 3σ, just reaching the threshold for "evidence" of a new physics signature. However, the deviation found in this analysis is within the expected local fluctuation in the data. The total cross section limits are set between 75 and 20 fb using the expected value for a SM-like model-dependent search. A second small local excess of 2.2σ was observed in the model-independent method at $m_X = 71$ GeV, but the deviation is also within the expected local fluctuation in the data. The fiducial cross section limits are set between 35 and 10 fb using the expected value for a model-independent search.

At the time of writing this dissertation, the LHC Run 3 data-taking period has already begun and is expected to conclude in 2026. The additional 350 $\text{fb}^{-1}$of integrated luminosity will provide a large enough dataset that allows a subsequent resonance search to either exclude or confirm each of the two small local excesses observed in this analysis. On a more distant timescale, the construction of larger hadronic and leptonic colliders have been proposed by the particle physics community to pursue particle collisions at even higher energies [22] [4]. Additional resonance searches on data collected at these future colliders can provide further evidence of possible BSM physics and set more sensitive limits on BSM cross sections.

Alternatively, methods and techniques developed in this analysis can be used in resonance searches at other invariant mass ranges for the diphoton decay channel. An effort for performing a search in the intermediate mass regime of approximately 110 – 175 GeV using the full Run 2 dataset is already underway. This search would encounter a similar combination of background components where the resonant background model is constructed for the SM Higgs boson. The results of the intermediate mass resonance search will bridge the cross section limits set by the analysis in this dissertation and by the high mass resonance search [83].

APPENDIX

APPENDIX A

Muon Spectrometer Phase II Upgrade: sMDT Chambers

As mentioned in Section 3.2.5, the muon spectrometer consists of a central barrel and two end-caps on each end of the ATLAS detector. In the barrel region, the muons are tracked in the three concentric layers of edge-overlapping Barrel-Inner-Small (BIS) with Barrel-Inner-Large (BIL), Barrel-Middle-Small (BMS) with Barrel-Middle-Large (BML), and Barrel-Outer-Small (BOS) with Barrel-Outer-Large (BOL) MDT module-type pairs as shown in Figures A.1 and A.2. Each concentric layer consists of eight chambers of each module-type. The dense array of isolated and independent drift tubes used in each MDT chamber allows for a muon tracking resolution of $\Delta z = 35\,\mu\text{m}$.

To accommodate the higher pp interaction rate of the High Luminosity LHC (HL-LHC), the ATLAS muon spectrometer will be upgraded during Long Shutdown 3 (LS3) [12]. A new thin Resistive Plate Chamber (tRPC) trigger system in the inner barrel region will be installed to improve the L1 muon trigger efficiency in the high luminosity environment. As a result, the MDT chambers located at the inner barrel region of will be replaced by new muon tracking chambers composed of sMDT tubes with diameters half that of the previously used MDT tubes. The smaller tube radius reduces the maximum drift time from 750 ns to 180 ns. The tube cross section is also

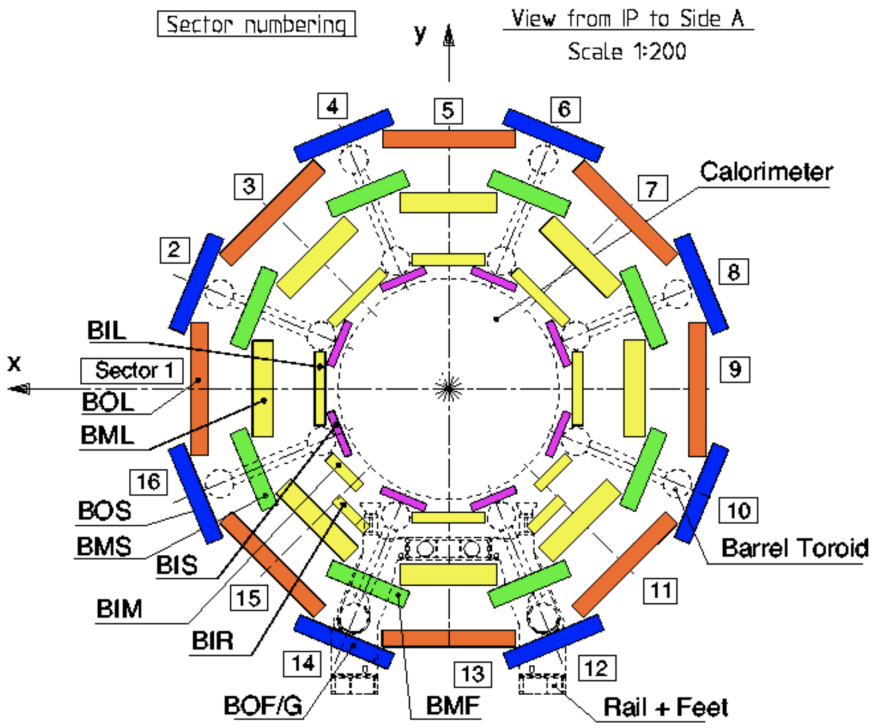

Figure A.1: A cross-sectional diagram of the muon spectrometer in the barrel region of the ATLAS detector in the $x - y$ plane.

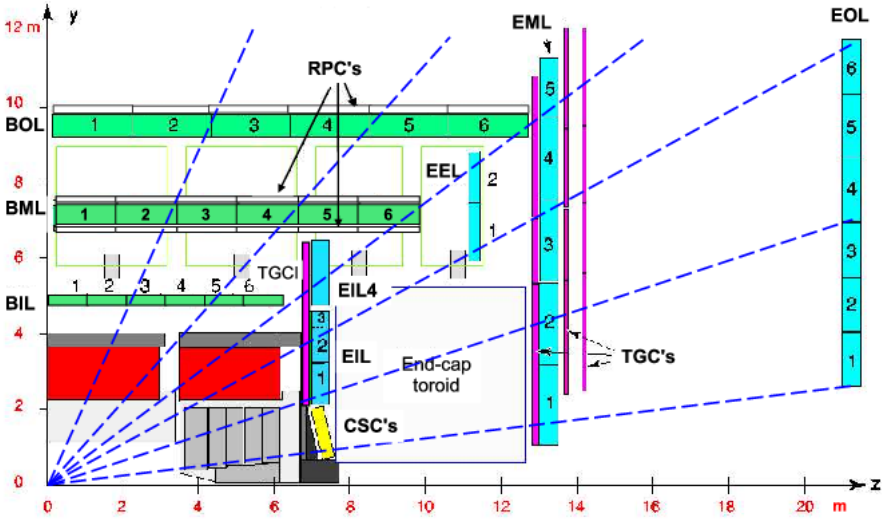

Figure A.2: A cross-sectional diagram of the muon spectrometer in the barrel and end-cap regions of the ATLAS detector in the $y - z$ plane.

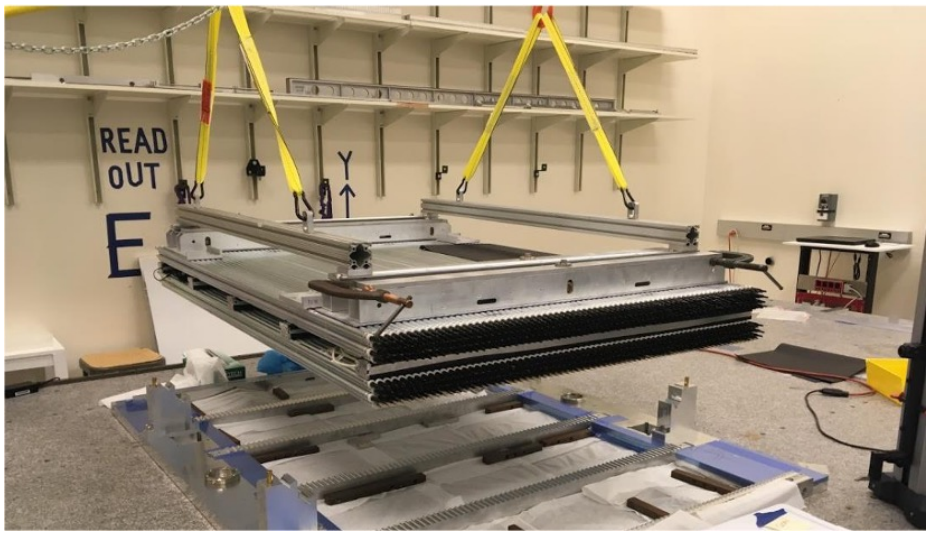

Figure A.3: One of the 96 sMDT chambers consisting of approximately 500 individual sMDT tubes. The tubes are mostly constructed at MSU and tested at UM. Each sMDT chamber is constructed and tested at UM before being delivered to CERN.

reduced by four-fold, lowering the tube occupancy by a factor of 8 for improved muon tracking performance.

A total of 96 new sMDT chambers will be built to replace the muon spectrometer BIS 1 through 6 MDT chambers. Half of these chambers will be constructed at the Max Planck Institute for Physics, Munich (MPI) in Germany while the other half at UM and Michigan State University (MSU) in the United States (US). An example of one sMDT chamber consisting of approximately 500 individual sMDT tubes is shown in Figure A.3. A total of 26000 sMDT tubes will be needed for the US chamber production: MSU will be responsible for the tube assembly and initial quality assurance and quality control (QAQC) tests, and UM will be responsible for the verification of all design specifications on each tube. The assembly and initial QAQC tests for the sMDT chambers will also be performed at UM.

During the sMDT chamber construction period in the US, approximately 2600 tubes were also built and tested at UM [101]: approximately 500 tubes were used for research and development (R&D) in 2018, and approximately 2100 tubes were used for chamber production in 2021. This appendix will focus on the latter effort,

including the overall workflow, the tube construction process, and the QAQC tests used.

A.1 Infrastructure and Workflow

A positive pressure room (referred to as the "tube room") measuring 12 m × 8 m is set up at the UM site with multiple work stations dedicated to the sMDT assembly and QAQC testing. Each station is built on a flat optical table, and large storage structures are built to accommodate up to around 3000 tubes during mass tube testing for sMDT chamber construction. All work stations are arranged such that they can be operated simultaneously by individual students and researchers to optimize tube construction and testing efficiencies. These work stations are listed in Table A.1 along with their purpose and tube capacity.

Station Name	Purpose	Tubes per station
Wire stringing and tensioning	construction	single
Swaging end-plug onto tube	construction	single
Length and tension measurement	QAQC	single
Straightness measurement	QAQC	single
Gas leak measurement	QAQC	single
Dark current measurement	QAQC	48
Negative high voltage (HV) treatment	QAQC	48

Table A.1: UM tube room stations.

The tube construction infrastructure and test stations were designed and built at UM during the R&D phase of the ATLAS muon detector upgrade project in 2018-2020. Approximately 500 sMDT tubes were constructed at the time and were tested for commissioning and verifying both the tube construction and chamber construction infrastructure and tooling. These preliminary tubes were later used to build a prototype sMDT chamber at UM for demonstration purposes. The knowledge and technologies used for tube production and testing were shared with MSU to ensure successful large-scale tube production. An additional batch of around 2100 tubes were built at UM in 2021 to supplement the tube construction effort at MSU to meet the early US sMDT chamber production schedule.

Material	Parameter
Tube material	Aluminium AW6060-T6/AlMgSi
Tube surface	Surtec 650 chromatization
Tube outer diameter	15 mm
Tube wall thickness	0.4 mm
Tube length	1615 mm
Wire material	W:Re (97:3)
Wire diameter	50 µm
Wire resistance	$44\,\Omega\,\mathrm{m}^{-1}$
Wire potential	2730 V
Gas mixture	Ar:CO2 (93:7)
Gas pressure	3 bar absolute
Gas gain	2×10^4
Test Measurement	**Threshold**
Tube straightness	< 0.5 mm
Wire tension	350 ± 15 g
Gas leak rate limit	$< 1 \times 10^{-8}\,\mathrm{mbar\,cm^3\,s^{-1}}$
Dark current	< 2 nA

Table A.2: Nominal parameters for sMDT tube materials and nominal criteria for test measurements.

The tube construction process can be divided into three main steps: the preparation of raw aluminum tubes and end-plug components, the tube assembly process, and the QAQC tests for each constructed tube. The nominal material parameters and test criteria for each constructed sMDT tube are listed in Table A.2.

A.2 Preparation of Materials

A.2.1 Tube Straightness Measurement

The raw aluminum tubes used to construct the sMDT tubes are supplied by the manufacturer Mifa Aluminium B.V. (Mifa) and are specified to have no more than 0.5 mm deviation at the sagitta when the tube is resting on a flat surface. To measure the straightness of a tube, an optical technique was developed using a digital microscope. The setup consisted of a straight V-shape bar with surfaces that deviate by no more than 0.05 mm to keep the center-line of the tube at the focal point of the microscope. The microscope is aimed at the center bottom of the tube where it should touch the flat surface of the V-bar. The tube is rotated in the V-bar to find the angular position with the maximum distance between the tube and the surface. The microscope has a built-in screen which is set to 20-times magnification as shown in Figure A.4.

This technique assumes that the deviation will be at the center along the length of a given tube. The fraction of tubes accepted in two batches of tubes received in 2020 and 2021 that pass various tube straightness criteria is shown in Figure A.5. Approximately 87% of the tubes met the nominal tube straightness requirement of 0.5 mm. These measurements motivated a relaxation of the nominal criteria 0.8 mm such that approximately 6% of those delivered in 2020 and 2021 were rejected. These rejected tubes were returned to Mifa for tube straightening treatment and were received in the US at the end of 2021. This tube straightness test has become a routine check performed in the large-scale sMDT tube production.

A.2.2 Aluminum Tube Preparation

Although the aluminum tubes are cleaned at the time of manufacture, additional cleaning was found to reduce the dark current drawn by tubes as described in Section

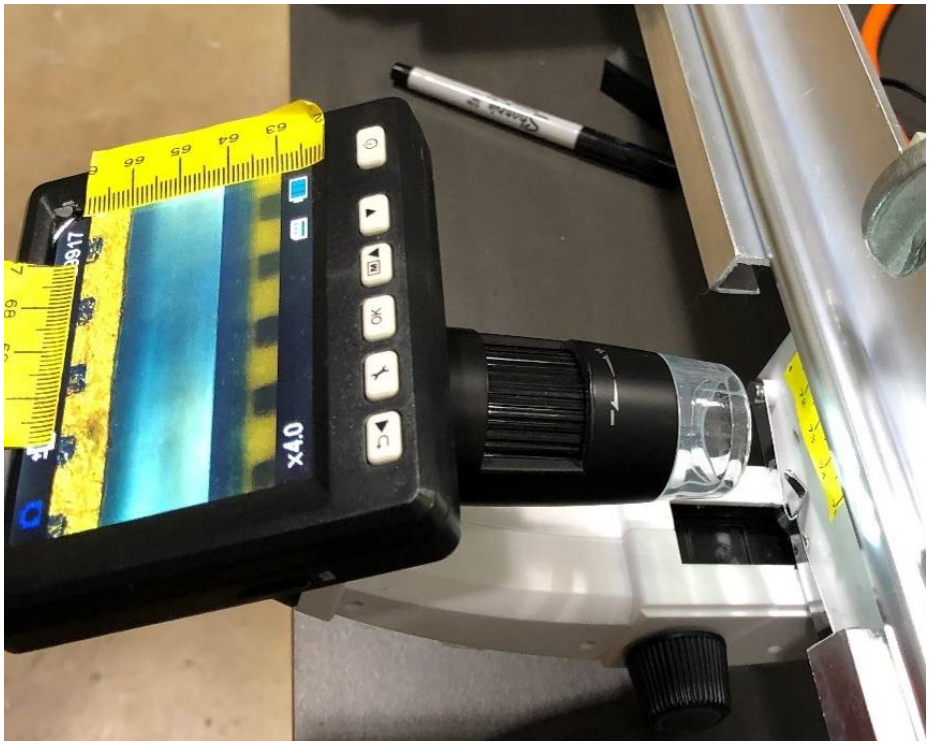

Figure A.4: Tube straightness measurement station with the digital microscope aimed at the middle of the aluminum tube sitting on the V-bar.

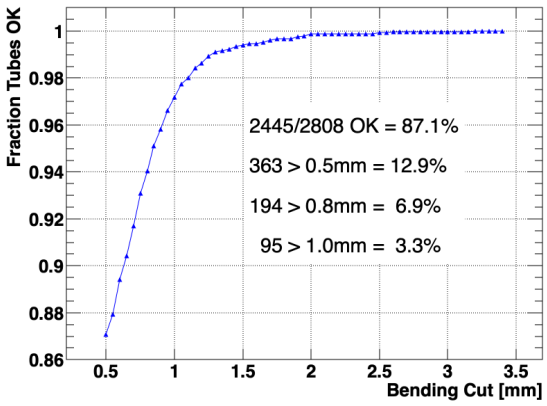

(a) Data from tubes built in 2020.

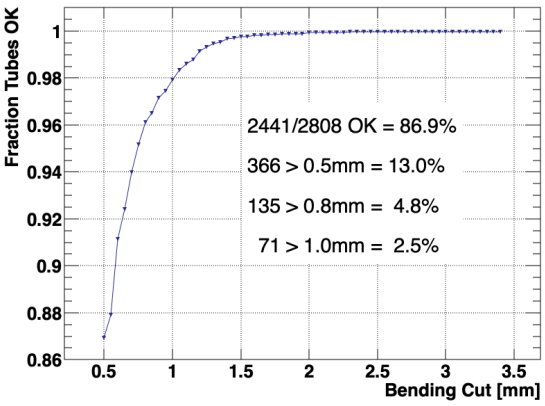

(b) Data from tubes built in 2021.

Figure A.5: The fraction of aluminum tubes delivered in 2020 and 2021 that pass various tube straightness criteria.

A.4.4. In the initial stages of the R&D tube production, approximately 12% of aluminum tubes were found to exceed the nominal dark current criteria. To reduce this high failure rate for the dark current test, the 2105 aluminum tubes used for the summer 2021 tube production at UM were each cleaned again upon arrival. The interior of each tube is swept three times with a cleaning plug consisting of a lint-free wipe wrapped around a small cylindrical piece of foam and soaked in isopropyl alcohol (IPA). The cleaning plug fit snugly inside the tube and was pushed through with a clean acrylic rod to ensure the entire length of the interior was wiped clean. The exterior is also cleaned with lint-free wipes soaked in IPA.

The cleaned tubes are stacked on foam saddles from the original packaging, and the ends were lightly covered with lint-free wipes to allow any residual IPA to evaporate completely. After all the tubes are cleaned and dried, the two ends of each tube are temporarily closed with clean rubber caps to keep the interior free of dust. The thoroughly cleaned tubes showed a failure rate of approximately 3% in the dark current test, significantly lower than that observed in the previous tests. In addition, the negative HV treatment described in Section A.4.5 was found to successfully treat any tubes that fail the dark current test.

A.2.3 End-Plug Preparation

The end-plugs attached to each end of an aluminum tube are designed to carry gas to and from the tubes through the gas manifolds mounted on the sMDT chamber. The end-plugs consist of a precision brass wire locator (referred to as a twister) fit inside a central brass insert, both of which are manufactured by the manufacturer Poschl. The central brass insert is molded into a polybutylene terephthalate (PBT) plastic body, and the twister is locked in place by plastic stoppers, both of which are manufactured by the Institute for High-Energy Physics (IHEP) at the Kurchatov Institute in Protvino, Russia. Copper crimp tubes, also manufactured by IHEP, are

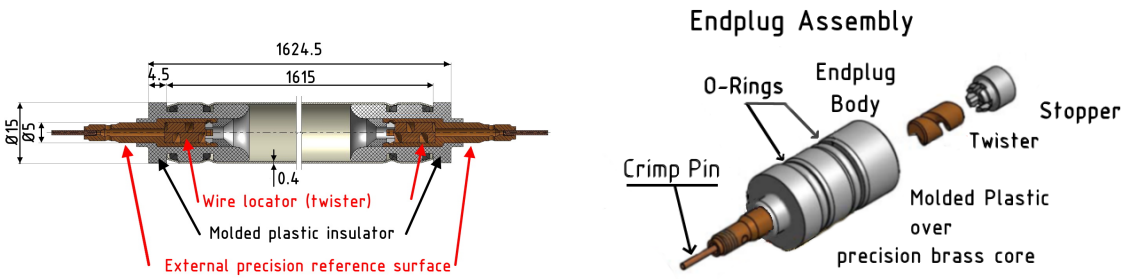

(a) sMDT tube design.

(b) End-plug and its components.

Figure A.6: Tube design with an exploded view of the end-plug components [68]. All length measurements are in mm.

used to secure the wire and hold it under tension. Two grooves on the outer surface of the plastic body each hold a rubber o-ring to make a gas-tight seal between the end-plug and the inner wall of the aluminum tube. The entire end-plug assembly is shown in Figure A.6.

Individual parts are given an initial wash for 15 minutes in an ultrasonic bath filled with IPA before assembly. A second wash for 5 minute is performed after assembly. The assembled end-plugs are stored in clean plastic packaging after drying in ambient air.

A.3 Tube Assembly

A.3.1 Wiring Station

The first station used in tube assembly is the wiring station as shown in Figure A.7. Two vacuum chucks, each fitted with a pneumatically controlled end-plate, rigidly align the aluminum tube with the wire feed before the tungsten-rhenium wire is strung through the tube. Each end-plate is mounted with a pair of hand-operated crimp jaws as shown in Figure A.8 to squeeze the 1.0 mm diameter crimp pin down to 0.7 mm. The spool of wire is mounted on a magnetically damped spindle on one end of the station to allow for a smooth pulling during tube construction. A three wheel tension-meter and a linear actuator is positioned at the other end to stretch the wire to the nominal tension as shown in Figure A.8.

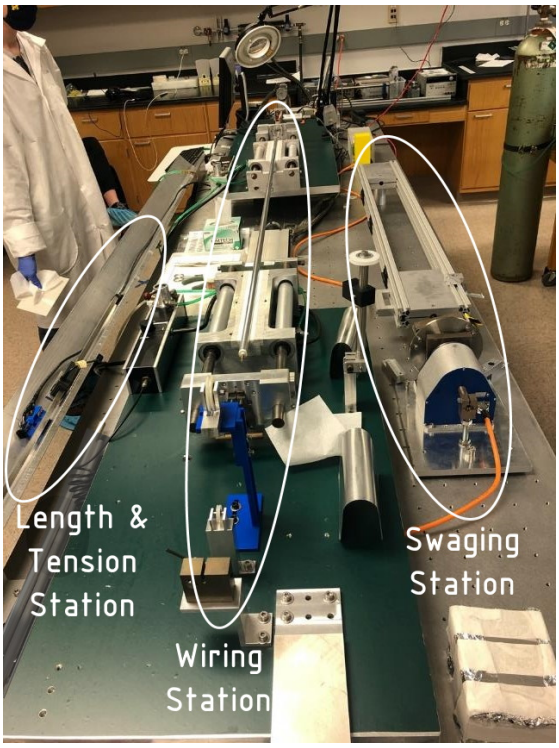

(a) Wiring station setup.

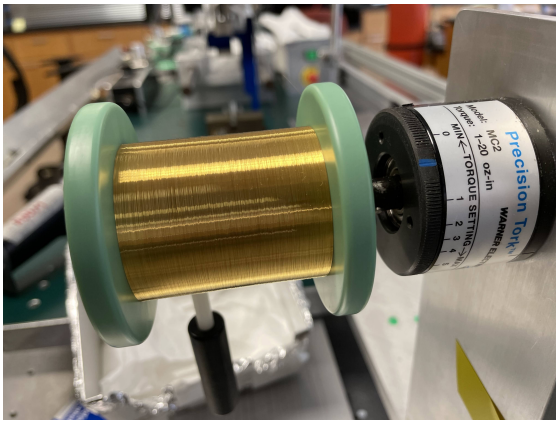

(b) Wire spool with magnetic brake.

Figure A.7: Setup used to string the tungsten-rhenium wire through the aluminum tube.

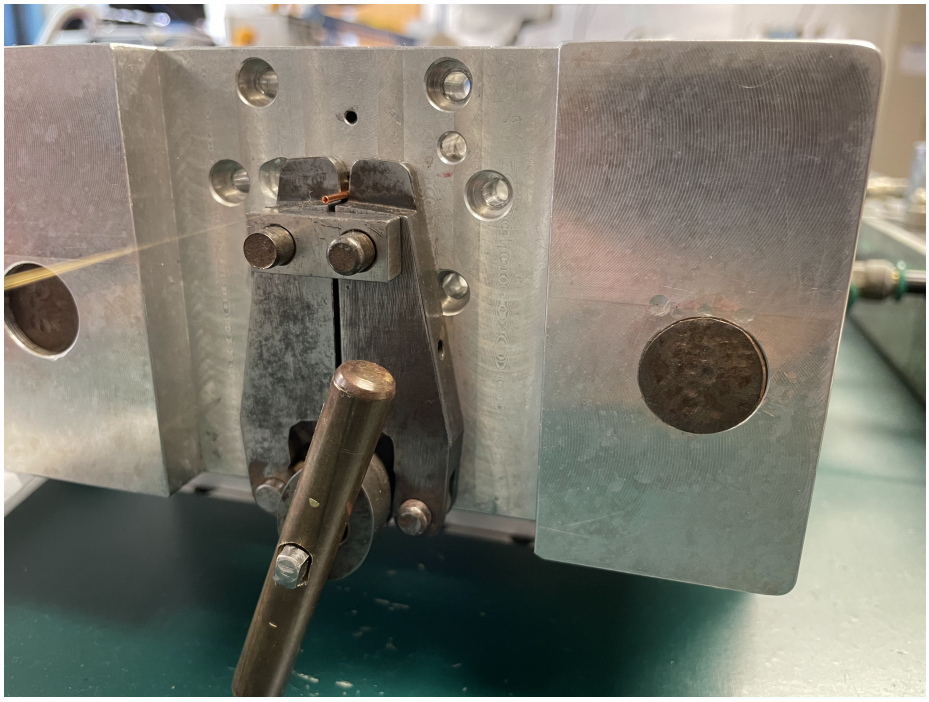

(a) Wire crimp jaw.

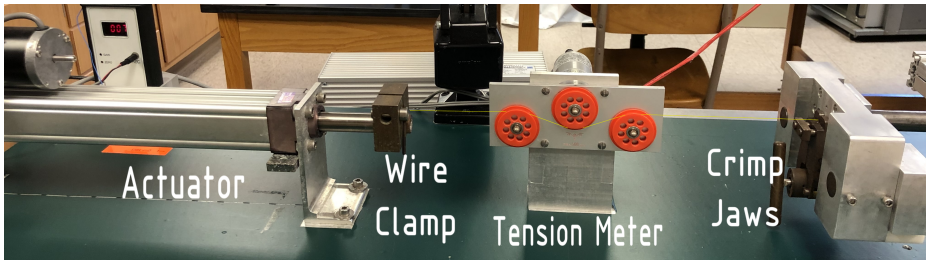

(b) Wire actuator and tension-meter.

Figure A.8: Setup used stretch the wire and hold the wire at the nominal tension.

A.3.2 Swaging Station

The second station used in tube construction is the swaging station as shown in Figure A.9. The custom-built rotary device (referred to as the swaging head) gradually forces 3 roller heads radially inward as they rotate around the tube. The thin walls of the tube are deformed (referred to as swaged) to compress and seal the tube against the o-rings on the end-plugs. The rotational head was designed at MPI, was built at MSU, and is driven by a rotary motor. An additional support structure is positioned to hold the tube in place when inserting it into the rotational head.

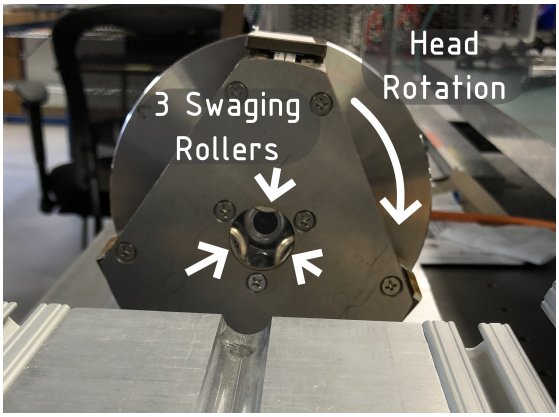

(a) Swaging rotational head.

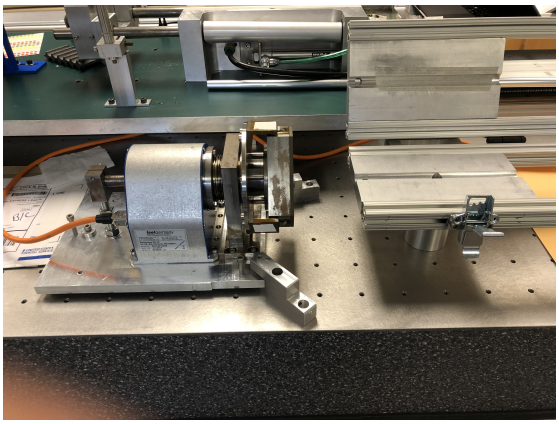

(b) Side view of swaging set up.

Figure A.9: The rotary swaging head for creating grooves around the tube at the end-plug o-ring locations.

A.3.3 Assembly procedure

The tube construction process starts with placing an aluminum tube on the vacuum chuck to hold the tube securely. The tube interior is then vacuumed to remove any residual dust. The tungsten-rhenium wire is secured to a shuttle and is carefully pulled through the tube using a gentle vacuum. The wire is drawn over a system of pulleys to prevent the wire from making contact with the wall of the aluminum tube during the stringing process. A magnetic brake controls the rate at which the wire is drawn from the spool to prevent the wire from tangling. The wire is then cut such that an excess length of 0.5 m is left protruding from each end of the aluminum tube. The wire ends are threaded through an end-plug at each end of the tube, and the end-plugs are then inserted into the ends of the tube until seated. Crimp pins are threaded onto each wire end and inserted into the end-plugs. One end of the wire is then secured with a stationary clamp. The other end of the wire is fed through the tension monitor, stretched by hand to around 200 g, and secured to another clamp attached to the actuator as shown in Figure A.8. The crimp pin on the end with the stationary clamp is crimped first to secure one end of the wire.

An online control program based on LabView [26] moves the actuator and monitors

the wire tension while the wire is gradually pulled to a tension of 400 g. This tension is held for 30 s, and the tension is slowly reduced to 325 g afterwards. The tube swaging that occurs later in the tube assembly process will increase the wire tension to 350 g. The second crimp pin is pushed into the end-plug until it comes in contact with the brass core. This adjustment ensures the tension is not altered by the movement of the crimp pin after it is crimped. The second crimp pin is crimped with the clamp on the actuator side of the tube to secure the wire inside the tube. The thickness of each crimp pin is measured to ensure a thickness of no more than 0.71 mm. This threshold ensures that the wire is held securely inside the tube and does not slip. Any excess wire protruding from the crimp-pins is cut such that a small excess length of 2 mm is left on each end of the sMDT tube.

After the tube is wired and the crimp pins are crimped, the wire tension is measured in the tension test station described later in Section A.4.3 to verify the tension value. At this point, a tube with an insufficient wire tension can easily be disassembled and all components, except the wire and crimp pins, can be reused for another tube assembly attempt.

Each end of the wired tube is then mechanically deformed in the swaging station to lock the end-plugs in place and produce an air-tight seal between the plastic end-plug and the interior wall of the tube. The rotating set of three rounded rollers create smooth indents around the circumference of the tube at each of the two o-ring locations as shown in Figure A.9a. The indent is made such that the width of the tube in the groove measures no more than 13.7 mm. This swaging process introduces an additional 25 g of tension in the wire due to the slight stretching of the aluminum tube. After swaging the two ends of the sMDT tube, a final tension test is performed to confirm that the wire inside the constructed tube has a tension of 350 ± 20 g. Once the two end-plugs are swaged, the tube assembly process is complete, and a bar code sticker with a unique serial number is placed on the aluminum tube for identification.

A.4 Quality Assurance and Quality Control Tests

The QAQC tests on all constructed tubes include visual inspections on all components, tube straightness, gas tightness, final assembled tube length, wire tension, and dark current measurements. The detailed procedures and test results tubes constructed at MSU and at UM are described in the following sections.

A.4.1 Visual Inspection

The fully assembled sMDT tubes are first given an visual inspection for locating any defects, such as dents or cracks in the tube wall, poorly or incorrectly swaged end-plugs, or severely bent crimp pins. Any crimp pins that appear to be bent are carefully straightened. All sMDT tubes with issues that cannot be resolved are rejected and flagged in the database described later in Section A.5.

A.4.2 Gas Tightness Test

The assembled sMDT tube is required to be air-tight with an upper limit on the leakage rate of $1 \times 10^{-8}\,\mathrm{mbar\,cm^3\,s^{-1}}$ when the gas inside the tube is at 3 bar absolute pressure. The leak rate test is performed with a helium leak detector connected to a vacuum vessel with an inner diameter of 25 mm and a length of 1.8 m as shown in Figure A.10. One end of the tube being tested is sealed shut with a brass cap and an o-ring. The other is screwed into the cap of the vacuum vessel which allows the tube to be pressurized with helium to 3 bar absolute. The cross section of the connection of the sMDT tube to the helium gas input while the tube is in the vacuum vessel is shown in figure A.11. The o-ring seals on each brass cap are lubricated with IPA to prevent twisting in the o-rings. IPA is used as the lubricant since it completely evaporates and leaves no residue that might contaminate the leak gas. The sMDT tube is inserted into the vessel, the end flange is sealed, and the leak detector is started to pump out the air inside the vessel. When the background helium level

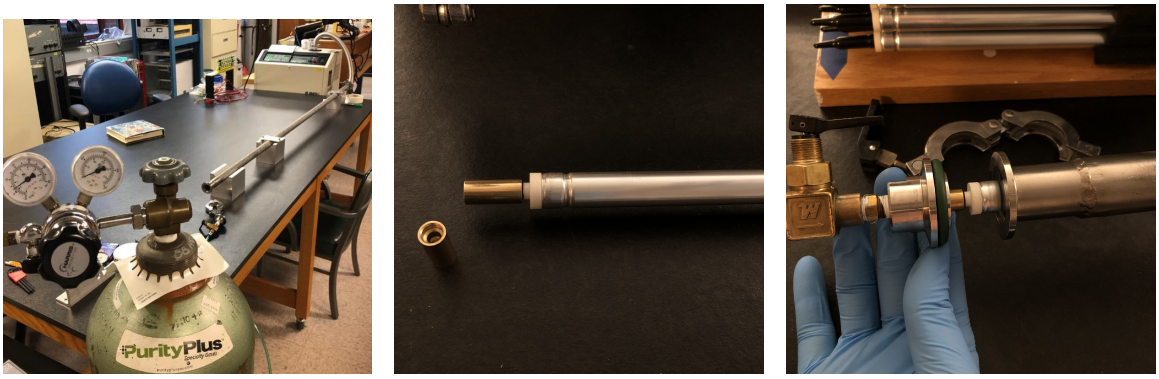

(a) Gas tightness test station. (b) Interior side of tube. (c) Vacuum side of tube.

Figure A.10: Set up of the tube leak test station. The tube is placed inside the vacuum vessel and pressurized with Helium to 3 bar absolute.

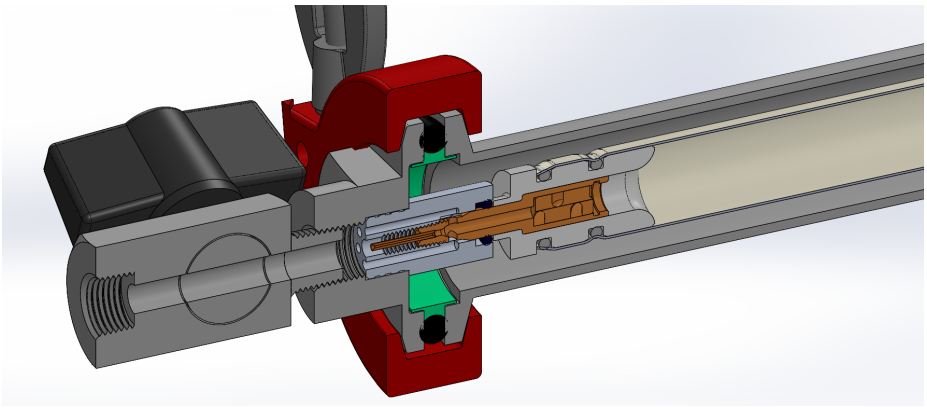

Figure A.11: Helium gas input connected to a sMDT tube placed inside the vacuum vessel for the gas tightness test.

reads approximately $1 \times 10^{-6}\,\mathrm{mbar\,cm^3\,s^{-1}}$, the tube is filled with Helium gas to a pressure of 3 bar absolute. Leaks can be detected within 30 seconds of starting the vacuum pump. When this test is completed, the helium is vented through a snorkel to outside the building.

The only measurement made for the gas tightness test is whether a given tube passes or fails the nominal tightness criteria. All the tubes built at UM passed the ATLAS gas tightness requirement.

A.4.3 Length and Wire Tension Measurements

The tube length and the wire tension are measured using the station shown in Figure A.12. A sMDT tube is placed in the V-shaped aluminum bar with its midpoint inside a U-shape magnet. A digital linear gauge is used to precisely measure the length of the sMDT tube to $\pm 10\,\mu m$. Before any length measurement is made, the digital gauge is calibrated with an aluminum rod of length $1624.5 \pm 0.1\,mm$. A tube is then placed into the V-shaped bar with the two ends resting in 3D printed saddles as shown in Figure A.12 such that one end is pressed against a stationary stopper and the other end is measured by the gauge. Good electrical contact must be made at both saddles to ensure the tube is grounded and the wire connected the electrical circuit.

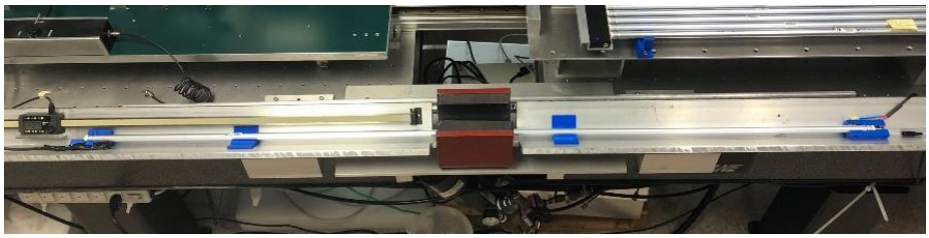

Figure A.12: Testing station for tube length and wire tension measurements.

The measured length distribution of the tubes built at UM is shown in Figure A.13. The maximum difference in tube length from the nominal specification is found to be slightly larger than 1 mm. All of the tubes built at UM meet the nominal length specification.

Wire tension is measured using the same set up with a separate set of procedures. The aluminum tube is grounded on the V-shaped bar and the wire is connected to the custom multiplexing circuit shown in Figure A.14. The circuit consists of an analog multiplexer, a signal generator, an instrumentation amplifier, and the sMDT itself. The multiplexing circuit induces vibrations in the sMDT wire by directing pulses from the signal generator to the sMDT. The signal from the discharging sMDT is then sent by the multiplexing circuit to the instrumentation amplifier. The instru-

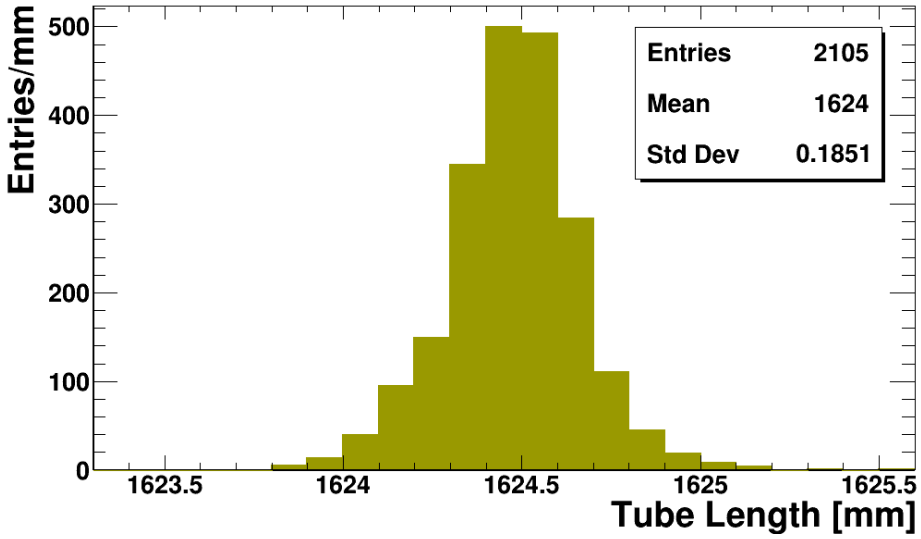

Figure A.13: Distribution of the measured length of the tubes built at UM.

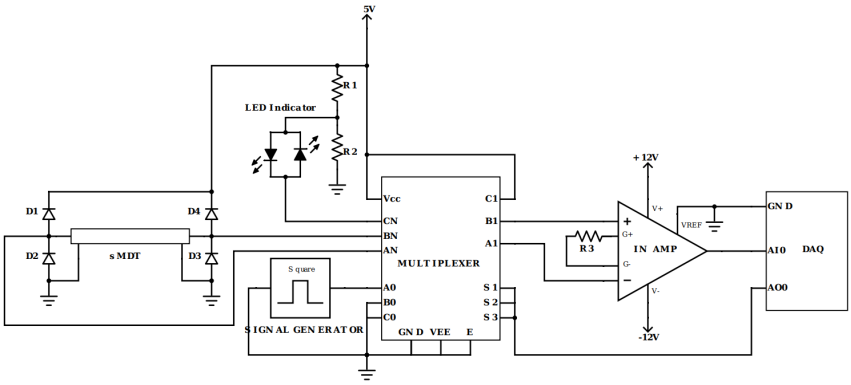

Figure A.14: Circuit for wire tension test.

mentation amplifier is connected to a DAQ system which consists of an multipurpose input/output (I/O) device interfaced to a computer. A LabView software program with a graphical user interface (GUI) was developed to set the wire tension measurement parameters, such as the measured tube length, and to perform real time analysis and wire tension measurements.

After the external pulse from the multiplexing circuit is stopped, the wire oscillates at its natural nth resonant frequency [67]:

$$f_n = \frac{n}{2L}\sqrt{\frac{T}{\mu}} \tag{A.1}$$

where L is the length of the oscillating portion of the wire, T is the tension in the wire, and μ is the linear density of the wire. Equation A.1 can be rearranged to calculate the tension in the wire from parameters measured on the sMDT tube and specifications on the wire itself:

$$T = \pi L^2 d^2 f_1^2 \rho / g, \tag{A.2}$$

where d is the diameter of the wire, ρ is the volumetric density of the wire material, and T is the tension expressed in grams such that the same amount of mass hung by the wire would achieve the same amount of tension force. The nominal sMDT wire parameters are as follows:

$$L = 1597\,\mathrm{mm}, \tag{A.3}$$

$$d = 50\,\mu\mathrm{m}, \tag{A.4}$$

$$\rho = 19.7\,\mathrm{g\,cm^{-3}}, \tag{A.5}$$

$$g = 9.81\,\mathrm{m\,s^{-2}}. \tag{A.6}$$

The first resonant frequency of 93.3 Hz corresponds to a wire tension of 350 g. The first resonant frequency is found using a fast Fourier Transform (FFT) and used to calculate the wire tension. In order to have a standardized calculation of the wire tension for comparing the results measured at UM with those measured at MSU during the tube construction process, the fixed nominal length of 1597 mm is used such that the only measured parameter used in the tension calculation is the first resonant frequency f_1.

A second tension measurement is made at least two weeks after the first measurement to check for any significant drop in tension. The sMDT tube is rejected if a drop in wire tension larger than 18 g in 2 weeks is found. The results of the wire

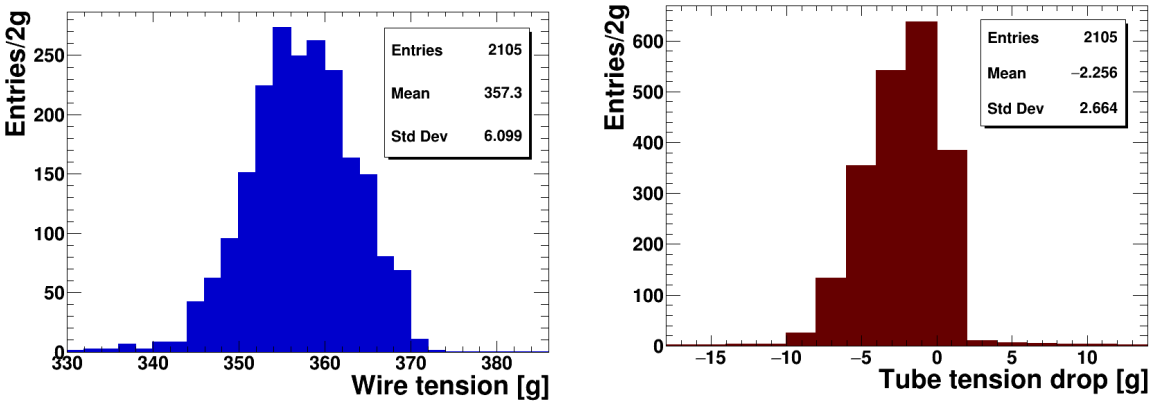

(a) sMDT tube wire tension.

(b) Wire tension drop after at least 2 weeks.

Figure A.15: Distribution of wire tension in the tubes built at UM.

tension measurements for sMDT tubes made at UM are shown in Figure A.15. A total of 2 tubes out of the 2105 built at UM (0.09% failure rate) did not pass the tension criteria.

A.4.4 Dark current measurement

The HV test station at UM holds 4 rows of 12 tubes each as shown in Figure A.16. Each row of tubes are inserted into a set of gas-manifold blocks to pressurize them to 3 atm absolute with the working gas mixture Ar:CO2 at a 93:7 ratio. The gas-manifold blocks are machined from polyoxymethylene (POM) acytal plastic and allow 12 tubes to be installed simultaneously with a lever handle to make the tube mounting process simple and quick. The 5 mm cylindrical precision brass part of the end-plugs in each of the 12 tubes are inserted into thick rubber o-rings installed inside the gas-manifold to make a gas-tight seal. The design of the HV setup is shown in Figure A.17.

The input gas pressure is regulated to 3 bar absolute and distributed to the 4 gas-manifold blocks, each with its own input and output shutoff valves. The output of the 4 blocks is combined into a single flow meter and a bubbler. The flow is initially set to a high flow rate of 3 standard cubic feet per hour (SCFH) for an hour to flush

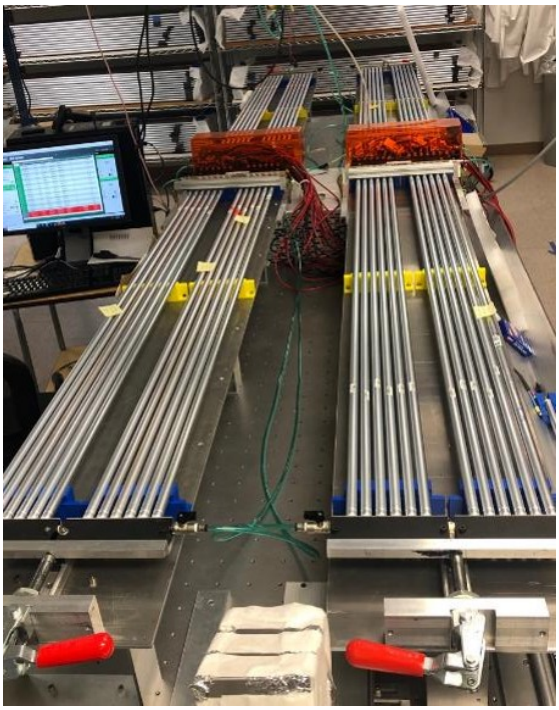

(a) HV test station.

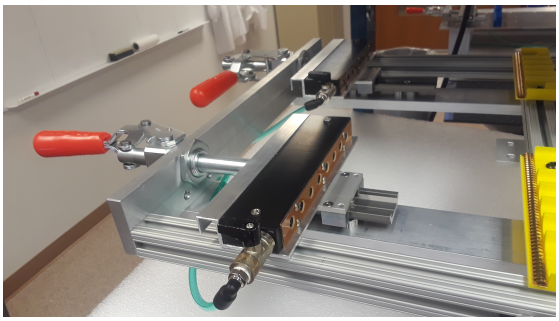

(b) HV gas-manifold blocks.

Figure A.16: HV test and dark current measurement setup.

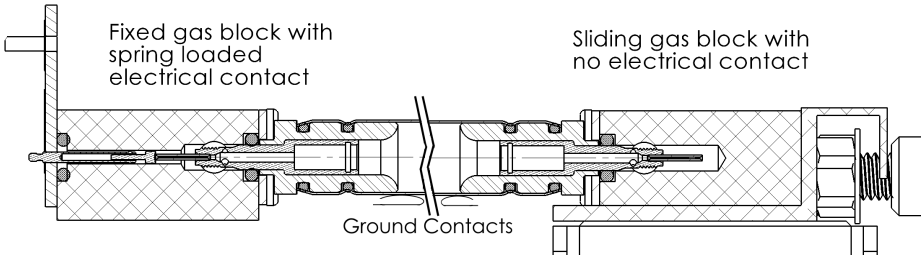

Figure A.17: Cross section of the tube mounting diagram for the dark current test station.

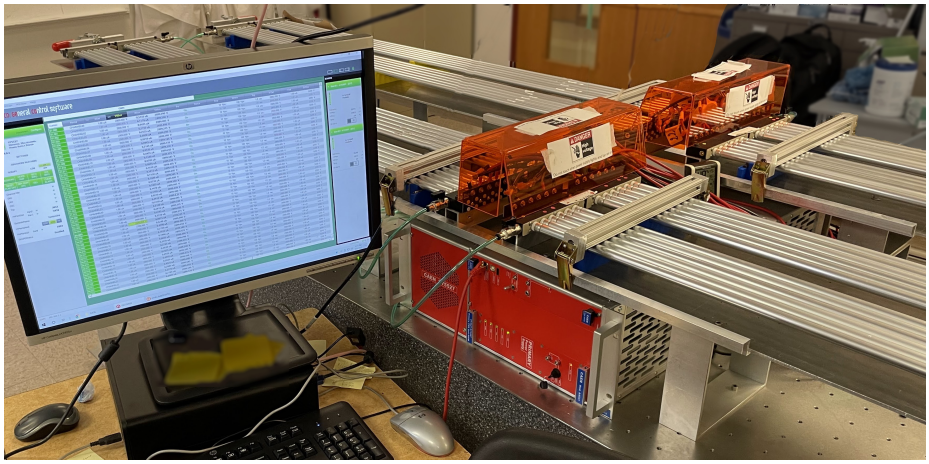

Figure A.18: HV test stand with a total capacity of 48 tubes. The CAEN SY5527 mainframe with the CAEN GECO monitoring program is running on the connected computer.

at least 3 volumes of gas through the tubes. The flow is then turned down such that approximately one gas volume passes through the tubes per day during testing.

The power supply system consists of a CAEN SY5527 mainframe which hosts two 24-channel AG7326 HV modules. Each module is able to deliver up to 3.5 kV per channel with 500 pA resolution for current measurements using the GEneral COntrol (GECO) monitoring and DAQ software. The dark current measurement setup is shown in Figure A.18. Two locations along the tubes are held rigidly using bar clamps to ensure good contact with a grounding strip. One of the two gas-manifolds in each row of tubes is fitted with spring-loaded contacts for applying high voltage to the wire. The spring contacts are hard-wired to HV cables that are separately connected to each of the 48 individual channels across the two modules of the CAEN HV power supply. For an accurate dark current measurement, the pedestal current level for each channel must be subtracted from its current measurement. The pedestals values are measured by turning on the HV with no tubes connected and measuring the average current on each channel for a period of one hour. The pedestals are stable up to a change in humidity and must be recalibrated frequently if the relative humidity exceeds 50%.

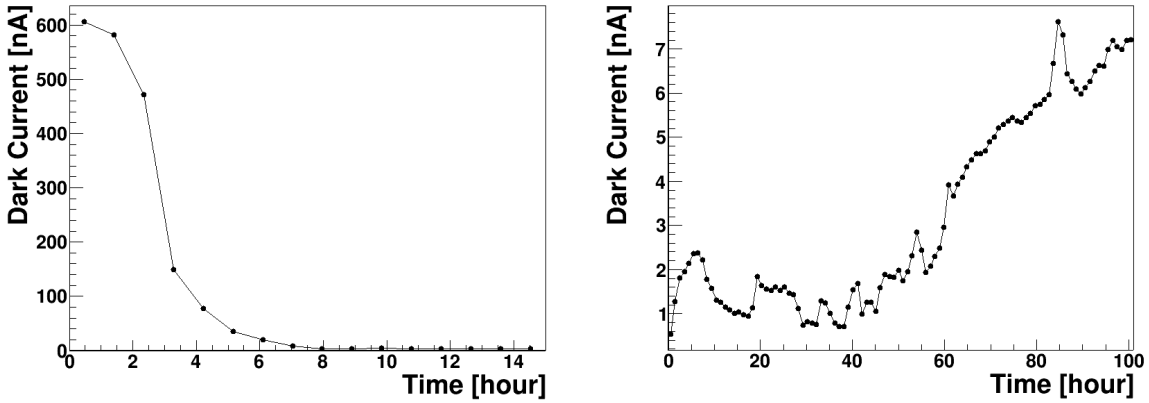

(a) Recovery from high dark current measurements.

(b) Development of increasing dark current measurements.

Figure A.19: Examples of one tube that recovered from initial high dark current measurements and one that developed higher and higher dark current over time. Note the different scales.

The sMDT tubes are placed in the gas-manifolds and the voltage is increased to 2900 V before dark current measurements are recorded for at least 4 hours. The tube satisfies the dark current criteria if its average current over the last hour of the test is less than 2 nA, Some tubes have dark current measurements above the limit in the first few hours after the HV is turned on and show a quickly decreasing trend afterwards as shown in Figure A.19. Some other tubes show the dark current measurements increasing in time, eventually leading to a tube failing the dark current test as also shown in Figure A.19. The latter case can be caused by foreign material such as dust inside the tube which sticks to the wire and causes discharge. This debris can be burned off over time (referred to as burn-in), resulting in a reduction in the measured dark current to an acceptable level. The dark current is measured again for all sMDT tubes received from MSU to ensure they are fully burned-in before being used in sMDT chamber construction.

A.4.5 Negative HV Treatment

The sMDT tubes that fail the dark current criteria are treated with a negative HV of −3 kV for 30 – 60 minute intervals on a separate HV station and reassessed using the standard HV testing procedure. The tubes that continue to fail the dark current criteria are treated with negative HV repeatedly until necessary. All tubes with high dark current values have responded to this treatment such that not a single tube was rejected in the dark current test and treatment procedure.

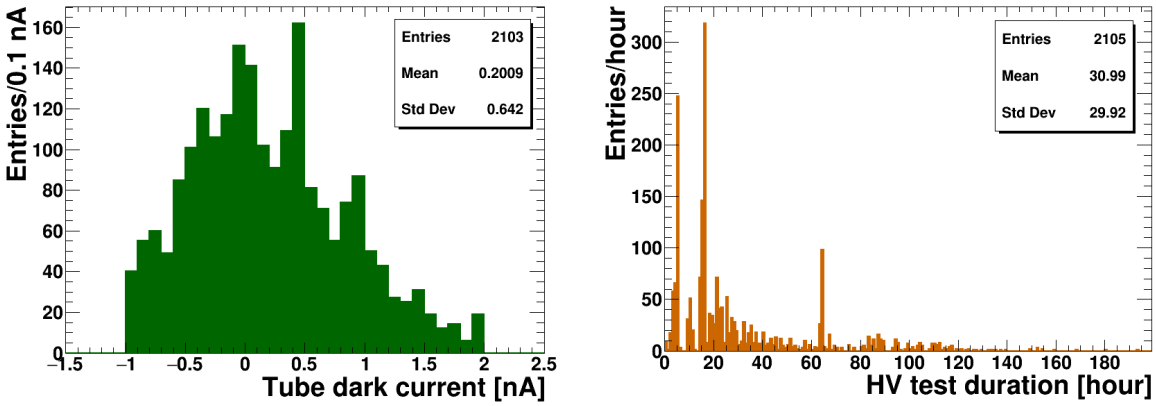

(a) Final dark current measurements.

(b) Total burn-in time.

Figure A.20: Distribution of the final dark current measurement and the burn-in time for the tubes built at UM. The three peaks in the burn-in time distribution correspond to the most common test lengths used for measuring the dark current: day time (just a few hours), overnight (typically about 15-16 hours) and over the weekend (normally around 64 hours).

In the 2105 tubes built at UM in the summer of 2021, a total of 67 tubes (corresponding to a 3.2% failure rate) were initially measured to have dark current above 2 nA. All of these sMDT tubes were treated either with longer HV burn-in time or with the negative HV process. The measured dark current distributions of the UM built tubes and the tube burn-in time distributions are shown in Figure A.20.

A.5 Tube Production Database

All the information gathered in tube production and testing is recorded into a local database for production QAQC monitoring. A subset of this data is uploaded to a master chamber production database encompassing all chambers built either in the US or at MPI. UM receives the QAQC measurements for the tubes delivered by MSU. This data is used as the first set of data in the data history of each tube. The results collected from tests and measurements performed at UM are shared with MSU for cross-checks and validation. All the test results from the UM test stations are saved in text files.

The most natural choice for storing all of the test results and measurements is a relational database since all information to be saved is related to many single tubes, each with its own history of production information and test results. The bar code serial number is used as the primary key for retrieving information in the tube database. The bar code is also the link between the entries of the tubes layout in a sMDT chamber and the associated test results.

ROOT [30], an analysis framework used commonly in high energy physics, is chosen to store, retrieve, and quickly produce distributions of test results locally. A few C++ classes have been developed to read the station measurement results and convert them into a set of text files for each tube. At the end of the process, all the test conditions and data relative to a tube are saved into a "TTree" data structure within a ROOT file with an entry for each tube. To easily access to tube test results, separate TTrees have also been created for each station Furthermore, there is a master TTree with all of the tube results from all tests and measurements. While filling each TTree with results, a standard set of distributions for each test is automatically generated and saved. A local web page is automatically created to show the results history of all tests.

All the production and test information will be uploaded to the CERN sMDT

production database which records information for all of the detectors to be installed on the ATLAS detector.

A.6 Conclusion

Fully functional stations for sMDT tube production and testing were designed, built, and used at the UM for the ATLAS HL-LHC muon detector upgrade project. A total of 2105 tubes were built at UM and tested for sMDT chamber production. The rejection rate of the UM constructed tubes is below 0.1% as indicated by the QAQC tests. In addition, over 14000 tubes built at MSU have been fully tested at UM.

Tubes passing all tests have been used to construct 30 sMDT chambers out of the 50 total chambers needed for the whole sMDT production task. All the chambers meet the stringent precision and performance requirements set forth by the Muon Spectrometer Phase II Upgrade plan.

BIBLIOGRAPHY

BIBLIOGRAPHY

[1] Jahred Adelman, Daniela Boerner, Frued Braren, Lydia Brenner, Louis D'eramo, Nils Ernst Klaus Gillwald, Yanping Huang, Joey Huston, Rachel Hyneman, Fabio Lucio Lucio Alves, Gangcheng Lu, Giovanni Marchiori, Ioannis Nomidis, Ivan Pogrebnyak, Brianna Lynn Stamas, Kerstin Tackmann, Ahmed Tarek Abouelfadl Mohamed, Ruggero Turra, Jean-Baptiste De Vivie De Regie, Mario Lamberti, Yi Fan Hu, Jinfei Wu, Xinchou Lou, and Shan Jin. Measurement of fiducial and differential cross sections in the $H \to \gamma\gamma$ decay channel with 140 fb^{-1} of 13 TeV proton–proton collision data with the ATLAS detector. Technical report, CERN, Geneva, 4 2020. (cit. on p. 157).

[2] ALICE. ALICE: Physics Performance Report. ALICE physics performance : Technical Design Report, 2005. revised version submitted on 2006-05-29 15:15:40. (cit. on p. 25).

[3] Simone Alioli, Paolo Nason, Carlo Oleari, and Emanuele Re. A general framework for implementing NLO calculations in shower Monte Carlo programs: the POWHEG BOX. *JHEP*, 06:043, 2010. (cit. on p. 63).

[4] Fenfen An, Yu Bai, Chunhui Chen, Xin Chen, Zhenxing Chen, Joao Guimaraes Da Costa, Zhenwei Cui, Yaquan Fang, Chengdong Fu, Jun Gao, et al. Precision higgs physics at the cepc. *Chinese Physics C*, 43(4):043002, 2019. (cit. on p. 228).

[5] ATLAS Collaboration. The ATLAS Simulation Infrastructure. *Eur. Phys. J. C*, 70:823, 2010. (cit. on p. 65).

[6] ATLAS Collaboration. The simulation principle and performance of the ATLAS fast calorimeter simulation FastCaloSim. ATL-PHYS-PUB-2010-013, 2010. (cit. on p. 65).

[7] ATLAS Collaboration. Observation of a new particle in the search for the Standard Model Higgs boson with the ATLAS detector at the LHC. *Phys. Lett. B*, 716:1–29, 2012. Comments: 24 pages plus author list (38 pages total), 12 figures, 7 tables, revised author list. (cit. on pp. 1 and 11).

[8] ATLAS Collaboration. ATLAS Pythia 8 tunes to 7 TeV data. Technical report, CERN, Geneva, 2014. All figures including auxiliary figures are available at https://atlas.web.cern.ch/Atlas/GROUPS/PHYSICS/PUBNOTES/ATL-PHYS-PUB-2014-021. (cit. on p. 63).

[9] ATLAS Collaboration. Estimate of the m_H shift due to interference between signal and background processes in the $H \to \gamma\gamma$ channel, for the $\sqrt{s} = 8$ TeV dataset recorded by ATLAS. ATL-PHYS-PUB-2016-009, 2016. (cit. on p. 64).

[10] ATLAS Collaboration. ATLAS simulation of boson plus jets processes in Run 2. ATL-PHYS-PUB-2017-006, 2017. (cit. on p. 66).

[11] ATLAS Collaboration. Electron and photon reconstruction and performance in ATLAS using a dynamical, topological cell clustering-based approach. Technical report, CERN, Geneva, 2017. All figures including auxiliary figures are available at https://atlas.web.cern.ch/Atlas/GROUPS/PHYSICS/PUBNOTES/ATL-PHYS-PUB-2017-022. (cit. on p. 46).

[12] ATLAS Collaboration. Technical Design Report for the Phase-II Upgrade of the ATLAS Muon Spectrometer. Technical report, CERN, Geneva, 2017. (cit. on p. 230).

[13] ATLAS Collaboration. Topological cell clustering in the ATLAS calorimeters and its performance in LHC Run 1. Topological cell clustering in the ATLAS calorimeters and its performance in LHC Run 1. *Eur. Phys. J. C*, 77:490, 2017. Comments: 64 pages plus author list + cover page (87 pages in total), 41 figures, 3 tables, submitted to EPJC. All figures including auxiliary figures are available at http://atlas.web.cern.ch/Atlas/GROUPS/PHYSICS/PAPERS/PERF-2014-07/. (cit. on p. 46).

[14] ATLAS Collaboration. Electron and photon performance measurements with the ATLAS detector using the 2015-2017 LHC proton-proton collision data. *JINST*, 14(12):P12006, 2019. 31 figures, 3 tables. All figures including auxiliary figures are available at https://atlas.web.cern.ch/Atlas/GROUPS/PHYSICS/PAPERS/EGAM-2018-01. (cit. on pp. ix, 51, 52, and 72).

[15] ATLAS Collaboration. Measurement of the photon identification efficiencies with the ATLAS detector using LHC Run 2 data collected in 2015 and 2016. *Eur. Phys. J. C*, 79(3):205, 2019. 55 pages in total, author list starting page 39, 18 figures, 2 tables, published in EPJC. All figures including auxiliary figures are available at http://atlas.web.cern.ch/Atlas/GROUPS/PHYSICS/PAPERS/PERF-2017-02. (cit. on p. 72).

[16] ATLAS Collaboration. Performance of electron and photon triggers in ATLAS during LHC Run 2. *Eur. Phys. J. C*, 80(1):47, 2020. 56 pages in total, author list starting page 40, 26 figures, 10 tables, published in EPJC. All figures including auxiliary figures are available at https://atlas.web.cern.ch/Atlas/GROUPS/PHYSICS/PAPERS/TRIG-2018-05. (cit. on p. 68).

[17] ATLAS Collaboration. Luminosity determination in pp collisions at $\sqrt{s} = 13$ TeV using the ATLAS detector at the LHC, 2022. (cit. on pp. 25, 27, and 29).

[18] Richard D. Ball et al. Parton distributions with LHC data. *Nucl. Phys. B*, 867:244, 2013. (cit. on p. 64).

[19] Richard D. Ball et al. Parton distributions for the LHC run II. *JHEP*, 04:040, 2015. (cit. on p. 65).

[20] I Bejar Alonso and L Rossi. HiLumi LHC Technical Design Report: Deliverable: D1.10. Technical report, CERN, 2015. (cit. on p. 25).

[21] Alexander Belyaev, Giacomo Cacciapaglia, Haiying Cai, Thomas Flacke, Alberto Parolini, and Hugo Serôdio. Singlets in composite Higgs models in light of the LHC 750 GeV diphoton excess. *Physical Review D*, 94(1), jul 2016. (cit. on p. 14).

[22] Michael Benedikt and Frank Zimmermann. Future circular colliders. *Proc. Int. Sch. Phys. Fermi*, 194:73–80, 2016. (cit. on p. 228).

[23] D. Berdine, N. Kauer, and D. Rainwater. Breakdown of the narrow width approximation for new physics. *Physical Review Letters*, 99(11), sep 2007. (cit. on p. 63).

[24] Disha Bhatia, Ushoshi Maitra, and Saurabh Niyogi. Discovery prospects of a light Higgs boson at the LHC in type-I 2HDM. *Physical Review D*, 97(5), Mar 2018. (cit. on pp. viii, 2, 17, 18, and 20).

[25] T. Biekötter, M. Chakraborti, and S. Heinemeyer. A 96 GeV Higgs boson in the N2HDM. *The European Physical Journal C*, 80(1), jan 2020. (cit. on p. 14).

[26] Rick Bitter, Taqi Mohiuddin, and Matt Nawrocki. *LabVIEW: Advanced programming techniques*. Crc Press, 2006. (cit. on p. 242).

[27] Enrico Bothmann et al. Event generation with Sherpa 2.2. *SciPost Phys.*, 7(3):034, 2019. (cit. on p. 65).

[28] G.C. Branco, P.M. Ferreira, L. Lavoura, M.N. Rebelo, Marc Sher, and João P. Silva. Theory and phenomenology of two-Higgs-doublet models. *Physics Reports*, 516(1-2):1–102, jul 2012. (cit. on pp. 1 and 14).

[29] Maximilien Brice. Aerial View of the CERN taken in 2008. 2008. (cit. on pp. viii and 24).

[30] Rene Brun and Fons Rademakers. ROOT—An object oriented data analysis framework. *Nuclear instruments and methods in physics research section A: accelerators, spectrometers, detectors and associated equipment*, 389(1-2):81–86, 1997. (cit. on pp. 92 and 254).

[31] Oliver Sim Brüning, Paul Collier, P Lebrun, Stephen Myers, Ranko Ostojic, John Poole, and Paul Proudlock. *LHC Design Report*. CERN Yellow Reports: Monographs. CERN, Geneva, 2004. (cit. on pp. 2 and 25).

[32] J Butterworth, E Dobson, U Klein, B Mellado Garcia, T Nunnemann, J Qian, D Rebuzzi, and R Tanaka. Single Boson and Diboson Production Cross Sections in *pp* Collisions at $\sqrt{s} = 7$ TeV. Technical report, CERN, Geneva, 2010. (cit. on pp. xxi and 67).

[33] Matteo Cacciari, Gavin P Salam, and Sebastian Sapeta. On the characterisation of the underlying event. *Journal of High Energy Physics*, 2010(4):1–42, 2010. (cit. on p. 73).

[34] Matteo Cacciari, Gavin P Salam, and Gregory Soyez. The catchment area of jets. *Journal of High Energy Physics*, 2008(04):005, 2008. (cit. on p. 73).

[35] L Carminati, M Delmastro, M Kataoka, M Kuna, R Lafaye, S Laplace, J Leveque, K Liu, G Marchiori, I Nikolic, J Ocariz, L Roos, J Schaarschmidt, M Schwoerer, and L Yuan. Measurement of the isolated di-photon cross section in 4.9 fb-1 of pp collisions at $\sqrt{S} = 7$ TeV with the ATLAS detector. Technical Report ATL-COM-PHYS-2012-592, CERN, Geneva, 5 2012. (cit. on p. 141).

[36] S. Catani, F. Krauss, B. R. Webber, and R. Kuhn. QCD Matrix Elements + Parton Showers. *JHEP*, 11:063, 2001. (cit. on p. 65).

[37] CERN. LHC run 3: Physics at record energy starts Tomorrow, Jul 2022. (cit. on p. 28).

[38] CMS. CMS Physics: Technical Design Report Volume 1: Detector Performance and Software. Technical report, CERN, Geneva, 2006. There is an error on cover due to a technical problem for some items. (cit. on p. 25).

[39] CMS Collaboration. Observation of a new boson at a mass of 125 GeV with the CMS experiment at the LHC. *Phys. Lett. B*, 716:30–61, 2012. (cit. on pp. 1 and 11).

[40] ATLAS Collaboration. The ATLAS Experiment at the CERN Large Hadron Collider, 2008. Also published by CERN Geneva in 2010. (cit. on pp. ix, 2, 25, 29, 30, 31, 33, 34, 36, and 40).

[41] ATLAS Collaboration. Improved electron reconstruction in ATLAS using the Gaussian Sum Filter-based model for bremsstrahlung. Technical report, CERN, Geneva, 2012. All figures including auxiliary figures are available at https://atlas.web.cern.ch/Atlas/GROUPS/PHYSICS/CONFNOTES/ATLAS-CONF-2012-047. (cit. on p. 48).

[42] ATLAS Collaboration. Search for scalar diphoton resonances in the mass range $65-600$ GeV with the atlas detector in *pp* collision data at $\sqrt{s} = 8$ TeV. *Physical review letters*, 113(17):171801, 2014. (cit. on p. 19).

[43] ATLAS Collaboration. Performance of the ATLAS Track Reconstruction Algorithms in Dense Environments in LHC run 2. Performance of the ATLAS Track

Reconstruction Algorithms in Dense Environments in LHC run 2. *Eur. Phys. J. C*, 77(10):673, 2017. 44 pages in total, author list starting page 28, 17 figures, 1 table, submitted to EPJC, All figures including auxiliary figures are available at http://atlas.web.cern.ch/Atlas/GROUPS/PHYSICS/PAPERS/PERF-2015-08/. (cit. on pp. 47 and 49).

[44] ATLAS Collaboration. Reconstruction of primary vertices at the ATLAS experiment in Run 1 proton–proton collisions at the LHC. Reconstruction of primary vertices at the ATLAS experiment in Run 1 proton-proton collisions at the LHC. *Eur. Phys. J. C*, 77(5):332, 2017. (cit. on p. 54).

[45] ATLAS Collaboration. Measurements of Photon efficiencies in *pp* collision data collected in 2015, 2016 and 2017 at $\sqrt{s} = 13$ TeV with the ATLAS detector. Technical Report ATL-COM-PHYS-2018-1604, CERN, Geneva, 11 2018. (cit. on pp. xxii and 142).

[46] CMS Collaboration. Search for new resonances in the diphoton final state in the mass range between 80 and 110 GeV in pp collisions at $\sqrt{s} = 8$ TeV. Technical Report CMS-PAS-HIG-14-037, CERN, Geneva, 2015. (cit. on p. 19).

[47] CMS Collaboration. Search for new resonances in the diphoton final state in the mass range between 70 and 110 GeV in pp collisions at $\sqrt{s} = 8$ and 13 TeV. Technical Report CMS-PAS-HIG-17-013, CERN, Geneva, 2017. (cit. on pp. viii, 19, 21, 76, 220, 225, and 228).

[48] CMS Collaboration. Search for a standard model-like Higgs boson in the mass range between 70 and 110 GeV in the diphoton final state in proton-proton collisions at $\sqrt{s} = 13$ TeV. Technical report, CERN, Geneva, 2023. (cit. on pp. xvii, xviii, 19, 211, 213, 214, 216, 224, and 226).

[49] T Cornelissen, M Elsing, I Gavrilenko, W Liebig, E Moyse, and A Salzburger. The new ATLAS track reconstruction (NEWT). *J. Phys.: Conf. Ser.*, 119:032014, 2008. (cit. on p. 47).

[50] T G Cornelissen, M Elsing, I Gavrilenko, J F Laporte, W Liebig, M Limper, K Nikolopoulos, A Poppleton, and A Salzburger. The global χ^2 track fitter in ATLAS. *J. Phys.: Conf. Ser.*, 119:032013, 2008. (cit. on p. 48).

[51] GI Dimov. Use of hydrogen negative ions in particle accelerators. *Review of scientific instruments*, 67(10):3393–3404, 1996. (cit. on p. 25).

[52] Paul Adrien Maurice Dirac. The quantum theory of the electron. *Proceedings of the Royal Society of London. Series A, Containing Papers of a Mathematical and Physical Character*, 117(778):610–624, 1928. (cit. on p. 5).

[53] FASER. Technical Proposal for FASER: ForwArd Search ExpeRiment at the LHC. Technical report, CERN, Geneva, 2018. (cit. on p. 27).

[54] R. A. Fisher. *Statistical Methods for Research Workers*. Springer New York, New York, NY, 1992. (cit. on p. 224).

[55] Rob Roy Mac Gregor Fletcher, Asma Hadef, Yuya Kano, Christopher Meyer, Ioannis Nomidis, Elisabeth Petit, Sergii Raspopov, Ruggero Turra, Alexis Roger Louis Vallier, Yufeng Wang, Lydia Roos, Yanwen Liu, Nicolas Berger, Remi Lafaye, Ryan Christopher Edgar, Dante Eric Amidei, Joe Kroll, Tianjue Min, Yasuyuki Okumura, Haichen Wang, and Yu Zhang. Search for new phenomena in low-mass diphoton events with the ATLAS detector at $\sqrt{s} = 13$ TeV. Technical report, CERN, Geneva, 2018. (cit. on pp. x, xvii, xviii, 19, 85, 87, 157, 211, 213, 214, 216, 224, 225, and 226).

[56] Patrick J. Fox and Neal Weiner. Light signals from a lighter Higgs. *Journal of High Energy Physics*, 2018(8), aug 2018. (cit. on pp. 2 and 14).

[57] H. Fritzsch, M. Gell-Mann, and H. Leutwyler. Advantages of the color octet gluon picture. *Physics Letters B*, 47(4):365–368, 1973. (cit. on p. 6).

[58] Stefano Frixione, Paolo Nason, and Carlo Oleari. Matching NLO QCD computations with parton shower simulations: the POWHEG method. *JHEP*, 11:070, 2007. (cit. on p. 63).

[59] Rudolf Frühwirth. Application of Kalman filtering to track and vertex fitting. *Nuclear Instruments and Methods in Physics Research Section A: Accelerators, Spectrometers, Detectors and Associated Equipment*, 262(2-3):444–450, 1987. (cit. on p. 48).

[60] John Erthal Gaiser. *Charmonium spectroscopy from radiative decays of the J/psi and psi'*. PhD thesis, Stanford University, 1982. (cit. on p. 107).

[61] T. Gleisberg, S. Höche, F. Krauss, M. Schönherr, S. Schumann, F. Siegert, and Winter J. Event generation with SHERPA 1.1. *JHEP*, 02:007, 2009. (cit. on p. 65).

[62] Stefan Höche, Frank Krauss, Marek Schönherr, and Frank Siegert. A critical appraisal of NLO+PS matching methods. *JHEP*, 09:049, 2012. (cit. on p. 65).

[63] Stefan Höche, Frank Krauss, Marek Schönherr, and Frank Siegert. QCD matrix elements + parton showers. The NLO case. *JHEP*, 04:027, 2013. (cit. on p. 65).

[64] Stefan Höche, Frank Krauss, Steffen Schumann, and Frank Siegert. QCD matrix elements and truncated showers. *JHEP*, 05:053, 2009. (cit. on p. 65).

[65] Andreas Hoecker, Peter Speckmayer, Joerg Stelzer, Jan Therhaag, Eckhard von Toerne, Helge Voss, M Backes, T Carli, O Cohen, A Christov, et al. TMVA-toolkit for multivariate data analysis, 2007. (cit. on pp. 92 and 93).

[66] Guolin Ke, Qi Meng, Thomas Finley, Taifeng Wang, Wei Chen, Weidong Ma, Qiwei Ye, and Tie-Yan Liu. LightGBM: A Highly Efficient Gradient Boosting Decision Tree. *Advances in Neural Information Processing Systems*, 30, 2017. (cit. on p. 85).

[67] J.Ting K.Lang and V. Vassilakopoulos. A technique of direct tension measurement of a strung fine wire. *Nucl. Instr. and Meth. A 420*, page 392, 1999. (cit. on p. 247).

[68] H. Kroha, R. Fakhrutdinov, and A. Kozhin. New High-Precision Drift-Tube Detectors for the ATLAS Muon Spectrometer. *JINST*, 12(MPP-2017-96):12, 2017. MPP-2017-96, https://cds.cern.ch/record/2268241, proceedings of INSTR17 conference, Novosibirsk, Russia, February 2017, extended version, to be published in Journal of Instrumentation. (cit. on pp. xviii and 239).

[69] W Lampl, S Laplace, D Lelas, P Loch, H Ma, S Menke, S Rajagopalan, D Rousseau, S Snyder, and G Unal. Calorimeter Clustering Algorithms: Description and Performance. Technical report, CERN, Geneva, 2008. All figures including auxiliary figures are available at https://atlas.web.cern.ch/Atlas/GROUPS/PHYSICS/PUBNOTES/ATL-LARG-PUB-2008-002. (cit. on pp. 47 and 73).

[70] Ernest O Lawrence. The evolution of the cyclotron. *Nobel Lecture*, 1951. (cit. on p. 23).

[71] Bruno Lenzi and David Delgove. Selection of the diphoton production vertex using multivariate techniques for $H \to \gamma\gamma$ and other analyses. Technical report, CERN, Geneva, 2015. (cit. on p. 71).

[72] LEP Collaboration. *LEP design report*. CERN, Geneva, 1984. Copies shelved as reports in LEP, PS and SPS libraries. (cit. on p. 24).

[73] LHC Higgs Cross Section Working Group. Handbook of LHC Higgs Cross Sections: 4. Deciphering the Nature of the Higgs Sector, 2017. 869 pages, 295 figures, 248 tables and 1645 citations. Working Group web page: https://twiki.cern.ch/twiki/bin/view/LHCPhysics/LHCHXSWG. (cit. on pp. xx, 10, 11, 12, 58, and 108).

[74] LHCb. LHCb reoptimized detector design and performance: Technical Design Report, 2003. (cit. on p. 25).

[75] LHCf. LHCf experiment: Technical Design Report. Technical report, CERN, Geneva, 2006. (cit. on p. 25).

[76] G.G. Lorentz. *Bernstein Polynomials*. Mathematical expositions. University of Toronto Press, 1953. (cit. on p. 171).

[77] Alberto Mariotti, Diego Redigolo, Filippo Sala, and Kohsaku Tobioka. New LHC bound on low-mass diphoton resonances. *Physics Letters B*, 783:13–18, aug 2018. (cit. on p. 14).

[78] B Mikulec, A Blas, C Carli, A Findlay, K Hanke, G Rumolo, and J Tan. LHC Beams from the CERN PS Booster. Technical report, CERN, 2010. (cit. on p. 25).

[79] Tianjue Min, Christopher Meyer, Ruggero Turra, Haichen Wang, and Yu Zhang. Selection and performance for the $H \to \gamma\gamma$ 2018 analyses using 2015+16+17 pp collision data at $\sqrt{s} = 13$ TeV with the ATLAS detector. Technical Report ATL-COM-PHYS-2018-250, CERN, Geneva, 3 2018. (cit. on p. 66).

[80] Esma Mobs. The CERN accelerator complex. Complexe des accélérateurs du CERN, 2016. General Photo. (cit. on pp. viii and 26).

[81] MoEDAL. Technical Design Report of the MoEDAL Experiment. Technical report, CERN, 2009. (cit. on p. 25).

[82] Paolo Nason. A new method for combining NLO QCD with shower Monte Carlo algorithms. *JHEP*, 11:040, 2004. (cit. on p. 63).

[83] Ioannis Nomidis, Remi Lafaye, Dante Eric Amidei, Nicolas Berger, Christopher Grud, Asma Hadef, Yanwen Liu, Lydia Roos, Yufeng Wang, Kevin Nelson, Christopher Hayes, Andy Chen, and Elisabeth Petit. Supporting note: High-mass diphoton resonance search using 139 fb^{-1} of 13 TeV pp collision data with the ATLAS detector. Technical report, CERN, Geneva, 4 2019. (cit. on pp. 19, 76, 144, 169, and 228).

[84] Mark Joseph Oreglia. *A Study of the Reactions psi prime → gamma gamma psi*. PhD thesis, Stanford University, 1980. (cit. on p. 107).

[85] Luis Pascual Dominguez, Jose Ocariz, Diego Redigolo, Ioannis Nomidis, Rachel Hyneman, Yuval Yitzhak Frid, Nicolas Berger, Liron Barak, Maria Josefina Alconada Verzini, Michael Aaron Kagan, Remi Lafaye, and Christopher Robyn Hayes. Very-low-mass diphoton resonance search using 139 fb^{-1} of 13 TeV pp collision data with the ATLAS detector. Technical report, CERN, Geneva, 2020. (cit. on pp. 19, 74, 157, and 167).

[86] Carl Edward Rasmussen and Christopher K. I. Williams. *Gaussian Processes for Machine Learning*. MIT Press, 2006. (cit. on p. 168).

[87] Alexander L. Read. Presentation of search results: the CL_S technique. *J. Phys. G*, 28:2693, 2002. (cit. on p. 202).

[88] A Renau. Current capabilities and future needs for semiconductor ion implantation. *Review of Scientific Instruments*, 81(2):02B907, 2010. (cit. on p. 23).

[89] L Rossi. The LHC Superconducting Magnets. Technical report, CERN, 2003. (cit. on p. 24).

[90] Filippo Sala. Higgs and flavour as doors to new physics. *The European Physical Journal Plus*, 131(4), Apr 2016. (cit. on p. 2).

[91] S. Schael, R. Barate, R. Brunelière, I. De Bonis, D. Decamp, C. Goy, S. Jézéquel, J.-P. Lees, F. Martin, and et al. Search for neutral MSSM Higgs bosons at LEP. *The European Physical Journal C*, 47(3), Jul 2006. (cit. on p. 19).

[92] Steffen Schumann and Frank Krauss. A parton shower algorithm based on Catani–Seymour dipole factorisation. *JHEP*, 03:038, 2008. (cit. on p. 65).

[93] Marco Silari. Applications of particle accelerators in medicine. *Radiation protection dosimetry*, 146(4):440–450, 2011. (cit. on p. 23).

[94] Torbjörn Sjöstrand, Stefan Ask, Jesper R. Christiansen, Richard Corke, Nishita Desai, Philip Ilten, Stephen Mrenna, Stefan Prestel, Christine O. Rasmussen, and Peter Z. Skands. An introduction to PYTHIA 8.2. *Comput. Phys. Commun.*, 191:159, 2015. (cit. on p. 63).

[95] Tomasz Skwarnicki. *A study of the radiative cascade transitions between the Upsilon-prime and Upsilon resonances*. PhD thesis, Institute of Nuclear Physics Polish Academy of Sciences, 1986. (cit. on p. 107).

[96] Nikolai Vasil'evich Smirnov and IV Dunin-Barkovskii. Short course of mathematical statistics for technical applications. *Moscow, Fizmatgiz*, 1959. (cit. on p. 184).

[97] SND. SND at LHC - Scattering and Neutrino Detector at the LHC. Technical report, CERN, Geneva, 2021. (cit. on p. 27).

[98] M. Tanabashi, K. Hagiwara, K. Hikasa, K. Nakamura, Y. Sumino, F. Takahashi, J. Tanaka, K. Agashe, G. Aielli, C. Amsler, M. Antonelli, D. M. Asner, H. Baer, Sw. Banerjee, R. M. Barnett, T. Basaglia, C. W. Bauer, J. J. Beatty, V. I. Belousov, J. Beringer, S. Bethke, A. Bettini, H. Bichsel, O. Biebel, K. M. Black, E. Blucher, O. Buchmuller, V. Burkert, M. A. Bychkov, R. N. Cahn, M. Carena, A. Ceccucci, A. Cerri, D. Chakraborty, M.-C. Chen, R. S. Chivukula, G. Cowan, O. Dahl, G. D'Ambrosio, T. Damour, D. de Florian, A. de Gouvêa, T. DeGrand, P. de Jong, G. Dissertori, B. A. Dobrescu, M. D'Onofrio, M. Doser, M. Drees, H. K. Dreiner, D. A. Dwyer, P. Eerola, S. Eidelman, J. Ellis, J. Erler, V. V. Ezhela, W. Fetscher, B. D. Fields, R. Firestone, B. Foster, A. Freitas, H. Gallagher, L. Garren, H.-J. Gerber, G. Gerbier, T. Gershon, Y. Gershtein, T. Gherghetta, A. A. Godizov, M. Goodman, C. Grab, A. V. Gritsan, C. Grojean, D. E. Groom, M. Grünewald, A. Gurtu, T. Gutsche, H. E. Haber, C. Hanhart, S. Hashimoto, Y. Hayato, K. G. Hayes, A. Hebecker, S. Heinemeyer, B. Heltsley, J. J. Hernández-Rey, J. Hisano, A. Höcker, J. Holder, A. Holtkamp, T. Hyodo, K. D. Irwin, K. F. Johnson, M. Kado, M. Karliner,

U. F. Katz, S. R. Klein, E. Klempt, R. V. Kowalewski, F. Krauss, M. Kreps, B. Krusche, Yu. V. Kuyanov, Y. Kwon, O. Lahav, J. Laiho, J. Lesgourgues, A. Liddle, Z. Ligeti, C.-J. Lin, C. Lippmann, T. M. Liss, L. Littenberg, K. S. Lugovsky, S. B. Lugovsky, A. Lusiani, Y. Makida, F. Maltoni, T. Mannel, A. V. Manohar, W. J. Marciano, A. D. Martin, A. Masoni, J. Matthews, U.-G. Meißner, D. Milstead, R. E. Mitchell, K. Mönig, P. Molaro, F. Moortgat, M. Moskovic, H. Murayama, M. Narain, P. Nason, S. Navas, M. Neubert, P. Nevski, Y. Nir, K. A. Olive, S. Pagan Griso, J. Parsons, C. Patrignani, J. A. Peacock, M. Pennington, S. T. Petcov, V. A. Petrov, E. Pianori, A. Piepke, A. Pomarol, A. Quadt, J. Rademacker, G. Raffelt, B. N. Ratcliff, P. Richardson, A. Ringwald, S. Roesler, S. Rolli, A. Romaniouk, L. J. Rosenberg, J. L. Rosner, G. Rybka, R. A. Ryutin, C. T. Sachrajda, Y. Sakai, G. P. Salam, S. Sarkar, F. Sauli, O. Schneider, K. Scholberg, A. J. Schwartz, D. Scott, V. Sharma, S. R. Sharpe, T. Shutt, M. Silari, T. Sjöstrand, P. Skands, T. Skwarnicki, J. G. Smith, G. F. Smoot, S. Spanier, H. Spieler, C. Spiering, A. Stahl, S. L. Stone, T. Sumiyoshi, M. J. Syphers, K. Terashi, J. Terning, U. Thoma, R. S. Thorne, L. Tiator, M. Titov, N. P. Tkachenko, N. A. Törnqvist, D. R. Tovey, G. Valencia, R. Van de Water, N. Varelas, G. Venanzoni, L. Verde, M. G. Vincter, P. Vogel, A. Vogt, S. P. Wakely, W. Walkowiak, C. W. Walter, D. Wands, D. R. Ward, M. O. Wascko, G. Weiglein, D. H. Weinberg, E. J. Weinberg, M. White, L. R. Wiencke, S. Willocq, C. G. Wohl, J. Womersley, C. L. Woody, R. L. Workman, W.-M. Yao, G. P. Zeller, O. V. Zenin, R.-Y. Zhu, S.-L. Zhu, F. Zimmermann, P. A. Zyla, J. Anderson, L. Fuller, V. S. Lugovsky, and P. Schaffner. Review of Particle Physics. *Phys. Rev. D*, 98:030001, Aug 2018. (cit. on pp. xx and 5).

[99] TOTEM. Total cross-section, elastic scattering and diffraction dissociation at the Large Hadron Collider at CERN: TOTEM Technical Design Report, 2004. (cit. on p. 25).

[100] Andreas Visibile. Master's thesis. Master's thesis, Istituto Nazionale Fisica Nucleare (INFN), 2021. (cit. on p. 85).

[101] C Wei, A Chen, D Amidei, N Anderson, E Carpenter, L Cooperrider, T Dai, E Diehl, C Ferretti, J Li, et al. Construction and testing of sMDT tubes at the University of Michigan for the ATLAS Muon Spectrometer upgrade. *Journal of Instrumentation*, 17(10):P10010, 2022. (cit. on p. 232).

[102] Herman Winick. The Stanford Synchrotron Radiation Project (SSRP). In *Proc. of Internat. Accel. Conf., SLAC*, 1974. (cit. on p. 23).